The Author

Since her childhood, Fay has been fascinated with nature. She followed up on this fascination in her studies Soil, Water and Atmosphere (B.Sc.) and Earth and Environment (M.Sc.) at Wageningen University. She finalised her studies by researching how incorporating *Plantago lanceolata* in peatland meadows affected N_2O land-atmosphere exchange for her master thesis. After her studies, she worked temporarily as an assistant researcher and as a soil quality consultant before starting a PhD position at the University of Hamburg. She worked on her dissertation within the working group of Prof. Dr. Lars Kutzbach and as part of the Research Training Group 2530. She examined CH_4 and N_2O land-atmosphere exchange in tidal wetlands of the Elbe estuary, supporting the RTG-2530 research aim of elucidating estuarine carbon cycling.

Verein zur Förderung der Bodenkunde Hamburg
c/o Institut für Bodenkunde - Universität Hamburg
https://www.geo.uni-hamburg.de/de/bodenkunde.html

Hamburger Bodenkundliche Arbeiten

2026
F. N. Lexmond
Band 107
HBA

Fay Niobe Lexmond

Land-atmosphere methane and nitrous oxide exchange of tidal wetlands in the Elbe estuary

Band 107
2026

ISSN: 0724-6382

Hamburger Bodenkundliche Arbeiten

Land-atmosphere methane and nitrous oxide exchange of tidal wetlands in the Elbe estuary

DISSERTATION

With the aim of achieving a doctoral degree
at the Faculty of Mathematics, Informatics and Natural Sciences
Department of Earth System Sciences
Universität Hamburg

Submitted by

Fay Niobe Lexmond

Hamburg, 2026

Accepted as Dissertation at the Department of Earth System Sciences

Date of Oral Defense:	10th November 2025
Supervision Panel:	Prof. Dr. Lars Kutzbach Prof. Dr. Philipp Porada Prof. Dr. Kathrin Dausmann Prof. Dr. Klaus-Holger Knorr
Reviewers:	Prof. Dr. Lars Kutzbach Jun.-Prof. Dr. Peter Müller
Members of the examination commission:	Prof. Dr. Lars Kutzbach Dr. Birgit Gaye Prof. Dr. Kathrin Dausmann Jun.-Prof. Dr. Peter Müller Prof. Dr. Philipp Porada
Chair of the Subject Doctoral Committee Department of Earth System Sciences:	Prof. Dr. Hermann Held
Dean MIN Faculty:	Prof. Dr.-Ing. Norbert Ritter

Published as

Hamburger Bodenkundliche Arbeiten, Volume 107

ISSN: 0724-6382

Editor: Verein zur Förderung der Bodenkunde Hamburg
Allende-Platz 2, 20146 Hamburg
https://www.geo.uni-hamburg.de/bodenkunde/ueber-das-institut/hba.html

Editorship: Dr. Klaus Berger

Abstract

Tidal wetlands are important ecosystems for climate change mitigation targets. Their high productivity and ability to build up carbon stocks offer pathways to enhance atmospheric carbon removal. Furthermore, tidal salt marshes are associated with low emissions of the potent greenhouse gas methane. On the other hand, their fresh water counterparts are associated with high methane emissions. While, natural tidal wetlands are nitrogen limited, those situated in intensively used agricultural and industrial areas are exposed to enhanced nitrogen loading. Consequently, large ranges in CH_4 and N_2O land-atmosphere flux magnitudes can occur in estuaries. Uncertainty remains in the spatiotemporal variability of these flux magnitudes as observational data is still limited. Furthermore, the controls of CH_4 and N_2O flux magnitude and variability and the effect of their interactions are not fully understood in the dynamic tidal wetland ecosystems. In this dissertation, soil-atmosphere-vegetation interactions have been investigated for the tidal wetlands in the Elbe estuary, with the aim to increase our understanding of CH_4 and N_2O land-atmosphere exchange in these ecosystems.

The research focused on the Elbe estuary, which was assessed by considering three different salinity zones; a fresh water, a brackish and a salt marsh and three different flooding frequency zones: a pioneer zone, a low marsh and a high marsh. Each tidal wetland zone was identified based on key plant species inhabiting the marshes. Additionally, the salt marsh included a managed, sheep grazed and open channel drained, high marsh. The soils and soil redox conditions were characterized and compared for the ten tidal wetland zones to investigate their variability within the estuary. The soil characterization relied on the WRB (2022) Soil Reference Group classification of a prepared soil pit per tidal wetland zone. The soils were classified as Gleysols, and at the unmanaged higher salt marsh as a gleyic Solonchak. Variation in soil physicochemical characteristics was mainly driven by soil textural differences, followed by chemical characteristics of the tidal floods according to Principal Component analyses. The soil redox conditions were studied through three different characterization methods; the redox reactions associated WRB diagnostics, the Indicator of Reducing conditions In Soils (IRIS) method and redox potential sensors. The latter two covered five replicates per tidal wetland zone with monthly sampling for IRIS and continuous potential measurements with the sensors over the course of 11 four-week blocks. The soil redox conditions shifted towards more strongly reducing conditions upstream the Elbe river, with higher flooding frequency and over soil depth. The aggregated results of all three characterization methods supported these general findings. The observed discrepancies emphasize the complexity, variability and heterogeneity of soil redox conditions.

The quantification of CH_4 and N_2O land-atmosphere fluxes and their spatiotemporal variability focused solely on the pioneer zones at each salinity zone and the four flooding frequency zones. The land-atmosphere fluxes were approximated by measuring bi-weekly to monthly the headspace gas concentration changes over a five-minute enclosure time with the manual closed chamber method at each of the five replicate plots per tidal wetland zone. The concentration measurements were supplemented with measurements of soil

temperature, volumetric water content, electrical conductivity, headspace air temperature, photosynthetic active radiation inside the flux chamber. The obtained raw data was processed with linear regression to calculate the mass flux of the gases in mg GHG m^{-2} h^{-1} and the average mass fluxes were compared among the different tidal wetland zones with non-parametric tests. There were significant magnitude increases in the average CH_4 and N_2O land-atmosphere fluxes towards the less saline zones in the estuary. Where the difference between the brackish and the fresh water marsh was significant for CH_4, it was not for N_2O land-atmosphere fluxes. The flux magnitude differences coincided with decreasing ground water salinity, increasing soil reducing conditions and increasing Elbe river mineral nitrogen load from down to upstream the estuary. Within the salt marsh, the average spring CH_4 flux indicated that the low marsh acted as a net sink and this negative flux was significantly different from fluxes at the pioneer zone and the unmanaged high marsh. The spring and summer average N_2O fluxes were significantly smaller at the pioneer zone compared to the other three flooding frequency zones. Furthermore, the average spring N_2O flux was significantly larger at the unmanaged high marsh in comparison to the managed high marsh, while the average autumn N_2O flux was significantly larger at the managed high marsh compared to the low marsh and pioneer zone.

Uncertainty of the obtained fluxes with respect to the quantification of the calculation variables was assessed with sensitivity analyses and propagation of quantification errors. The sensitivity analyses of the flux calculation to adaptations in headspace volume and input air temperature indicated a bidirectional response of the calculated flux magnitudes, leading to both larger and smaller differences among hourly fluxes of the different flux replicate plots and repeated measurements. However, these flux magnitude changes were smaller than the flux spatial and temporal variability. The propagated uncertainty indicated that the flux errors were potentially too modest for peak growing season fluxes. Recalculating the flux errors with updated error variables indicated flux errors in the same range as the observed spatial and temporal variabilities.

The results presented in this dissertation contribute to the increase of observational GHG land-atmosphere flux data from temperate tidal wetland soils. Furthermore, the presented results and discussion point to the importance of abiotic and biotic controls in driving GHG fluxes, but more research is required to elucidate the fundamental processes and effect of interactions among the environmental drivers.

Zusammenfassung

Gezeitenfeuchtgebiete sind wichtige Ökosysteme im Hinblick auf die Eindämmung des Klimawandels. Ihre hohe Produktivität und ihre Fähigkeit, Kohlenstoffvorräte aufzubauen, bieten Möglichkeiten, den Entzug von Kohlenstoff aus der Atmosphäre zu verstärken. Zudem sind Salzmarschen im Gezeitenbereich mit geringen Emissionen des starken Treibhausgases Methan verbunden, während ihre Süßwasser-Pendants hohe Methanemissionen aufweisen. Während natürliche Gezeitengebiete stickstofflimitiert sind, sind jene in intensiv landwirtschaftlich oder industriell genutzten Gebieten einer erhöhten Stickstoffbelastung ausgesetzt. Folglich können in Ästuaren große Schwankungsbreiten bei den Flüssen von CH_4 und N_2O zwischen Boden und Atmosphäre auftreten. Hinsichtlich der räumlich-zeitlichen Variabilität dieser Flussgrößen bestehen weiterhin Unsicherheiten, da die Beobachtungsdaten begrenzt sind. Zudem sind die steuernden Faktoren für die Höhe und Variabilität der CH_4- und N_2O-Flüsse sowie die Auswirkungen ihrer Wechselwirkungen in diesen Ökosystemen noch nicht vollständig geklärt. In dieser Dissertation wurden die Wechselwirkungen zwischen Boden, Atmosphäre und Vegetation in den Gezeitengebieten des Elbeästuars untersucht, mit dem Ziel, das Verständnis des Austauschs von CH_4 und N_2O zwischen Land und Atmosphäre in diesen Ökosystemen zu erweitern.

Der Schwerpunkt der Untersuchung lag auf dem Elbeästuar; dabei wurden drei Salzgehaltszonen (Süßwasser-, Brackwasser- und Salzmarschbereich) sowie drei Zonen unterschiedlicher Überflutungshäufigkeit (Pionierzone, untere Marsch und obere Marsch) berücksichtigt. Die jeweilige Zone wurde anhand von Schlüsselpflanzenarten identifiziert. Zusätzlich umfasste der Salzmarschbereich eine bewirtschaftete, mit Schafen beweidete und durch offene Gräben entwässerte Fläche der oberen Marsch. Die Böden und die Redoxbedingungen im Boden wurden für die zehn Zonen charakterisiert und verglichen, um deren Variabilität innerhalb des Ästuars zu untersuchen. Die Bodencharakterisierung basierte auf der Klassifizierung nach der World Reference Base for Soil Resources („WRB“, 2022) anhand eines Bodenprofils pro Zone. Die Böden wurden als Gleysols klassifiziert, mit Ausnahme der unbewirtschafteten, höher gelegenen Salzmarschfläche, die als Gleyic Solonchak klassifiziert wurde. Hauptursache für die Variation der physikochemischen Bodeneigenschaften waren – laut Hauptkomponentenanalyse – Unterschiede in der Bodenart (Textur), gefolgt von den chemischen Eigenschaften des Gezeitenwassers. Die Redoxbedingungen im Boden wurden mit drei verschiedenen Methoden untersucht: der WRB-Diagnostik auf Basis von Redoxreaktionen, der IRIS-Methode („Indicator of Reducing conditions In Soils“) sowie Redoxpotenzialsensoren. Die Redoxbedingungen im Boden verschoben sich in Richtung stärker reduzierender Verhältnisse, flussaufwärts entlang der Elbe, mit zunehmender Überflutungshäufigkeit und mit der Bodentiefe. Die zusammengeführten Ergebnisse aller drei Charakterisierungsmethoden bestätigten diese allgemeinen Befunde. Die beobachteten Abweichungen unterstreichen die Komplexität, Variabilität und Heterogenität der Redoxbedingungen im Boden.

Die Quantifizierung der CH_4- und N_2O-Flüsse zwischen Land und Atmosphäre sowie deren räumlich-zeitliche Variabilität konzentrierten sich ausschließlich auf die Pionierzonen der drei verschiedenen Salzgehaltsbereiche sowie auf die vier Zonen unterschiedlicher Überflutungshäufigkeit in der Salzmarsch. Die Flüsse wurden durch zweiwöchentliche bis

monatliche Messungen der Gaskonzentrationsänderungen im Gasraum (Headspace) über einen Zeitraum von fünf Minuten mit der Methode der „manuellen geschlossenen Haube“ bestimmt; pro Gezeitenfeuchtgebietszone wurden fünf Replikatsflächen untersucht. Ergänzend zu den Konzentrationsmessungen im Haubengasraum wurden Bodentemperatur, volumetrischer Wassergehalt, elektrische Leitfähigkeit, Lufttemperatur im Gasraum sowie die photosynthetisch aktive Strahlung innerhalb der Messhaube erfasst. Die Rohdaten wurden mittels linearer Regression ausgewertet, um den Massenfluss der Gase in mg m^{-2} h^{-1} zu berechnen; die mittleren Massenflüsse der verschiedenen Zonen wurden anschließend mithilfe nichtparametrischer Tests verglichen. Es zeigten sich signifikante Anstiege der mittleren CH_4- und N_2O-Flüsse in Richtung der Zonen mit geringerem Salzgehalt im Ästuar. Während der Unterschied zwischen der Brackwasser- und der Süßwassermarsch bei CH_4 signifikant war, traf dies für die N_2O-Flüsse nicht zu. Die Unterschiede in der Flussstärke korrelierten mit einem abnehmenden Salzgehalt des Grundwassers, zunehmenden reduzierenden Bedingungen im Boden sowie einer steigenden mineralischen Stickstoffbelastung durch die Elbe in Richtung flussaufwärts. Innerhalb der Salzmarsch deutete der mittlere CH_4-Fluss im Frühjahr darauf hin, dass die untere Marsch als Netto-Senke fungierte; dieser negative Fluss unterschied sich signifikant von den Flüssen in der Pionierzone und der unbewirtschafteten oberen Marsch. Die mittleren N_2O-Flüsse im Frühjahr und Sommer waren in der Pionierzone der Salzmarsch signifikant geringer als in den drei anderen Zonen unterschiedlicher Überflutungshäufigkeit. Zudem war der mittlere N_2O-Fluss im Frühjahr in der unbewirtschafteten oberen Marsch signifikant höher als in der bewirtschafteten oberen Marsch, während der mittlere N_2O-Fluss im Herbst in der bewirtschafteten oberen Marsch signifikant höher ausfiel als in der unteren Marsch und der Pionierzone.

Die Unsicherheit der ermittelten Flüsse hinsichtlich der Quantifizierung der Berechnungsvariablen wurde mittels Sensitivitätsanalysen und Fehlerfortpflanzung abgeschätzt. Die Sensitivitätsanalysen der Flussberechnung gegenüber Anpassungen des Gasraumvolumens und der Eingangslufttemperatur zeigten eine bidirektionale Reaktion der berechneten Flussstärken; dies führte sowohl zu größeren als auch zu kleineren Unterschieden zwischen den stündlichen Flüssen der verschiedenen Wiederholungsflächen und den wiederholten Messungen. Diese Änderungen der Flussstärke waren jedoch geringer als die räumliche und zeitliche Variabilität der Flüsse. Die Fehlerfortpflanzung deutete darauf hin, dass die Fehlerabschätzungen für die Spitzenflüsse während der Vegetationsperiode möglicherweise zu niedrig waren. Die Neuberechnung der Flussfehler unter Verwendung aktualisierter Fehlervariablen ergab Fehlerwerte in einer Größenordnung, die der beobachteten räumlichen und zeitlichen Variabilität entsprach.

Die in dieser Dissertation vorgestellten Ergebnisse tragen zur Erweiterung der Datenbasis zu beobachteten Treibhausgasflüssen zwischen Boden und Atmosphäre in gemäßigten Gezeitenfeuchtgebieten bei. Darüber hinaus unterstreichen die Ergebnisse und ihre Diskussion die Bedeutung abiotischer und biotischer Steuerfaktoren für die Treibhausgasflüsse. Es bedarf jedoch noch weiterer Forschung, um die grundlegenden Prozesse sowie die Auswirkungen von Wechselwirkungen zwischen den antreibenden Umweltfaktoren zu klären.

Contents

Abstract 3
Zusammenfassung 5
Contents 7
List of abbreviations and symbols 10

Chapter 1 Introduction 11
1.1 Turning tides: tidal wetlands and climate change mitigation 11
1.2 Production and consumption of methane and nitrous oxide in tidal wetland soils 12
1.3 Quantification of methane and nitrous oxide land-atmosphere exchange 14
1.4 Dissertation objectives and research questions 16
Chapter 2 Materials and methods 19
2.1 Study sites 19
2.2 Characterization of the tidal wetland soils 21
2.3 Characterization of tidal wetland soil redox conditions 23
2.3.1 Reductimorphic and oxymorphic soil features 23
2.3.2 Indicator of Reduction in Soils 23
2.3.3 Soil redox potential sensors 24
2.3.4 Comparison of soil redox condition characterization methods 25
2.4 Greenhouse gas land-atmosphere fluxes 26
2.4.1 Manual closed chamber method 26
2.4.2 Greenhouse gas flux calculations 30
2.4.3 Greenhouse gas flux data analyses 32
Chapter 3 Results 41
3.1 Characteristics of tidal wetland soils in the Elbe estuary 41
3.2 Characteristics of tidal wetland soil redox conditions in the Elbe estuary 45
3.3 Soil redox characterization methods 47
3.4 Greenhouse gas land-atmosphere fluxes in the Elbe estuary 49
3.4.1 Methane dataset 49
3.4.2 Nitrous oxide dataset 51
3.4.3 Greenhouse gas fluxes from different tidal wetland zones 52
3.4.4 Temporal trends in methane and nitrous oxide land-atmosphere fluxes 57
3.4.5 Correlations between methane and nitrous oxide land-atmosphere fluxes and tidal wetland environmental conditions 61
3.4.6 Vegetation characteristics at the greenhouse gas plots 68
3.4.7 Greenhouse gas flux uncertainty and sensitivity analyses 69

Chapter 4 Discussion 75
4.1 Characteristics of tidal wetland soils in the Elbe estuary 75
4.2 Characteristics of soil redox conditions in the Elbe estuary 77
4.3 Methane land-atmosphere fluxes from Elbe tidal wetland soils 80
4.4 Nitrous oxide land-atmosphere fluxes from Elbe tidal wetland soils 82
4.5 Methane and nitrous oxide flux calculations uncertainties and flux data set assessment 84
Chapter 5 Conclusions 89

List of publications 92

References 93
Software 100
Manuals and books 101
Reports 102
Maps 102
Online sources 102
Preprints 102

Appendices 103
A. Contributions to this dissertation 103
B. Collar installation and collar details 105
C. Manual closed flux chamber design of Chamber1 106
D. Manual closed flux chamber design of Chamber2 107
E. Manual closed flux chamber small and large extensions 108
F. Flux chamber measurement dates 109
G. Flux chamber measurement procedure 110
H. Example plot of (potential) false negative flux 111
I. RMSE details for CH_4 and N_2O full data sets 112
J. Example of deformed collar 114
K. Friedman tests covered measurement days 115
L. Soil description forms 116
M. Soil horizon characteristics 126
N. PCA results soil physicochemical analyses 130
O. Pearson correlations of physicochemical soil properties 131
P. Reduction index per soil horizon 132
Q. Sensor redox potential (Eh) and partial hydrogen pressure (rH) 133
R. Gaussian distribution tests of land-atmosphere flux data 136
S. Methane and nitrous oxide land-atmosphere flux data 137

T. Spearman's correlations of methane and nitrous oxide land-atmosphere fluxes and tidal wetland environmental variables 149
U. Vegetation community composition and details 153
V. Greenhouse gas flux uncertainty and sensitivity analyses.....155

Acknowledgements.....159

List of abbreviations and symbols

#i	number of individuals
%w/w	percentage weight to weight
1st Q	first quantile
3rd Q	third quantile
A_{LEAVE}	average leave area
ANOVA	analysis of variance
avg	average
BM	brackish marsh
BM_{AG}	above ground biomass
CEC	cation exchange capacity
CH_4	methane
CO_2	carbon dioxide
C_{org}	organic carbon
C_{tot}	total carbon
DFG	Deutsche Forschungsgemeinschaft
DL	detection limit
DLK	bioavailable K calcium-lactate extracted
DLP	bioavailable P calcium-lactate extracted
dS	decisiemens
DS	disturbed sampling block
DW	dry weight
EC	electrical conductivity
EC_{se}	electrical conductivity of saturation extract
EC_{ms}	electrical conductivity of fresh soil sample
Eh	redox potential
err_{P_A}	applied air pressure error
err_{P_ACT}	corrected air pressure error
FAO	Food and Agriculture Organization of the United Nations
Fe_{dit}	dithionite extract iron
FM	fresh water marsh
GHG	greenhouse gas
HMg	managed high marsh
HMu	unmanaged high marsh
IRIS	Indicator of Reduction in Soil
K_{calac}	calcium-lactate extracted potassium
KCl	potassium chloride
kPa	kilopascal
LAR	leaf area ratio
LKN.SH	Landesbetrieb für Küstenschutz, Nationalpark und Meeresschutz Schleswig-Holstein
LM	low marsh
max	maximum
med	median
MHT	mean high tide
min	minimum
mmolc	millimols of charge
Mn_{dit}	dithionite extract magnesium
mV	millivolt
N_2O	nitrous oxide
NA	not available
NH_4^+-N	nitrogen in ammonium complex
NO_3^-N	nitrogen in nitrate complex
NS	not significant
N_{tot}	total nitrogen
P_A	assumed air pressure
PAR_{in}	photoactive radiation inside flux chamber
PAR_{out}	photoactive radiation received at top of flux chamber
PC	principal-component
PCA	principal-component-analysis
pH_{CaCl2}	pH of air-dried soil sample 2 M CaCl2 extract
pH_{H2O}	pH of fresh soil sample water extract
P_{calac}	calcium-lactate extracted phosphorus
P_{olsen}	Olsen-extracted phosphorus
PVC	poly-vinyl chloride
PZ	pioneer zone
QL	quality level of calculated GHG flux
$RC_{morphology}$	reduction class based on soil morphological features
RC_{sensor}	reduction class based on rH values
redox	reduction-oxidation
rH	hydrogen partial pressure
RH_{in}	relative air humidity inside flux chamber
RI	reduction index
RI_{10cm}	reduction index in 10 centimeter sections
$RI_{horizon}$	reduction index of soil horizon
RI_{sensor}	reduction index of sensor depth soil section
RI_{tot}	reduction index over 60 centimeter soil depth
RMSE	root mean square error
RTG	research training group
sd	standard deviation
se	standard error
SHE	standard hydrogen electrode
SLA	specific leaf area
SM	salt marsh
SMV	stem mass per volume
T_{air_in}	air temperature inside flux chamber
TIC	total inorganic carbon
T_{in_man}	manually measured air temperature inside flux chamber
T_{soil}	soil temperature
UM	undisturbed measurement block
VWC	volumetric water content
WC_{se}	water content of saturation extract
WFPS	water filled pore space
WRB	World Reference Base for Soil Resources

Chapter 1 Introduction

With the goal of unearthing some of the invisible collaborations that happen underground, we will dive with this dissertation into atmosphere-vegetation-soil interactions in tidal wetlands.

1.1 Turning tides: tidal wetlands and climate change mitigation

Greenhouse gases (GHG) are atmospheric components that play a major role in the climate change crisis. These gases absorb and reemit part of the outgoing long-wave radiation back to the earth's surface and consequently have a warming effect (Armour et al., 2021; Jain, 1993). Three major and potent GHG are carbon dioxide (CO_2), methane (CH_4) and nitrous oxide (N_2O) (Armour et al., 2021; Jain, 1993). In 2024, the globally averaged annual atmospheric concentrations were 423 ppm CO_2, 1930 ppb CH_4 and 338 ppb N_2O, compared to respectively 379 ppm, 1774 ppb and 319 ppb in 2005 (Lan, Thoning and Dlugokencky, 2025-06, Solomon et al., 2007). These numbers show that globally, the average atmospheric concentrations have risen, even though the urgency to put a stop to the rise has gained public attention with the publication of the IPCC Fourth Assessment Report in 2007 and the Paris Agreement, in act since November 2015. A variety of measures are proposed to reduce emissions of GHGs and enhance the removal of atmospheric carbon. One suggested measure is to support carbon sequestration in soils (Shukla et al., 2019). Tidal wetlands are interesting ecosystems in this regard due to their carbon sequestration potentials and near zero emissions of N_2O and in case of salt marshes of CH_4 too (Chmura, Anisfeld, Cahoon, & Lynch, 2003; Kroeger, Crooks, Moseman-Valtierra, & Tang, 2017). However, data and fundamental understanding of CH_4 as well as N_2O land-atmosphere fluxes, their spatiotemporal variability and drivers is still limited for tidal wetlands (Huertas, Flecha, Navarro, Perez, & de la Paz, 2018; Koontz et al., 2024; Livesley & Andrusiak, 2012; Macreadie et al., 2019; Rosentreter, Al-Haj, Fulweiler, & Williamson, 2021; Yang & Silver, 2016).

The carbon sequestrating potential of tidal wetlands is associated with vertical accretion, which is the natural growth process of tidal marshes (Chmura et al., 2003; Duarte, Middelburg, & Caraco, 2005). Incoming sediments, brought in by floods, are deposited and stabilized at the soil surface by the vegetations standing stock. As a result, the marsh expands in horizontal and vertical direction (Bakker, 2014; Schoutens et al., 2019). The ongoing supply of sediments continuously creates new space for vegetation to grow. The produced biomass and washed up allochthonous organic carbon get incorporated in the soil organic carbon pool when buried with deposited sediments (Chmura, 2013; Xin et al., 2022). The removal rate of carbon from the soil organic carbon pool is small, as decomposition rates are hampered under the dominantly wet and reducing soil conditions (Freeman, Ostle, & Kang, 2001; Mcleod et al., 2011; Megonigal, Hines, & Visscher, 2004). The remaining soil organic carbon can be stabilized through binding to other soil compounds and in this way become sequestered in the soil carbon pool.

The near-zero to even negative land-atmosphere CH_4 fluxes from salt marshes, the high fluxes from their fresh counterparts and small N_2O land-atmosphere fluxes from tidal wetland soils were mainly observed from marshes in the United States of America, China, Australia and within Europe mainly at coast of the United Kingdom of Great Britain and Northern Ireland (Bartlett, Bartlett, Harriss, & Sebacher, 1987; Bartlett & Harriss, 1993; Cadier, Waltham, Canning, Fry, & Adame, 2023; Capooci & Vargas, 2022; Chmura, Kellman, & Guntenspergen, 2011; Kroeger et al., 2017; Livesley & Andrusiak, 2012; Moseman-Valtierra et al., 2011; Z. Sun, Wang, Mou, Jiang, & Sun, 2014). To our knowledge, information on CH_4 and N_2O flux magnitudes and spatiotemporal variability is lacking for tidal wetlands along the Wadden Sea coast and adjacent estuaries.

1.2 Production and consumption of methane and nitrous oxide in tidal wetland soils

The prolonged and extensive saturated conditions in large parts of tidal wetland soils create unsuitable conditions for aerobic decomposition. Oxygen becomes quickly limited in the saturated soil as its diffusion rate into soil pore water is low compared to its relative quick consumption by soil microbes (Ponnamperuma, 1972). However, there are anaerobe specialist microbes who can use alternative electron acceptors for their metabolic activity, although at the expense of a lower energy yield compared to aerobic metabolism (Megonigal et al., 2004). Generally, the following ranking reflects the most to least energetically favorable electron acceptors after oxygen (O_2): nitrate (NO_3^-), manganese (MnO_2, Mn_8O_{14}, MnOOH), iron-hydroxide ($Fe(OH)_3$), sulfate (SO_4^{2-}), iron oxide-hydroxide (FeOOH), carbonate (HCO_3^-) and iron-oxide (Fe_3O_4) (Bethke, Sanford, Kirk, Jin, & Flynn, 2011).

Microbial competition for substrates is steered by the relative energy yield from electron transfer between acceptor and donor species. Soil microbes reducing higher energy yielding electron acceptors have a competitive benefit over the microbes relying on less energy yielding acceptors, as long as the environmental conditions support the thermodynamic optimum for the respective half reactions (Bethke et al., 2011; Derby, Needelman, Roden, & Megonigal, 2021; Megonigal et al., 2004).

Methanogens rely on the energetically least beneficial electron acceptors. Hydrogenotrophic methanogens and acetoclastic methanogens can be outcompeted by the competitively stronger sulfate reducers as they rely on the same substrates (Le Mer & Roger, 2001; Segers, 1998; Seyfferth et al., 2020).

The competition between these two microbial groups is believed to be the main process leading to the earlier mentioned minor CH_4 land-atmosphere fluxes from salt marshes. As soil salinity reflects the dissolved salt concentrations in the soil pore water, an increase in salinity pairs with an increase in sulfate, as long as SO_4^{2-} is among the anions that constitute the saline soil solution. Sulfate reducers haven been found to suppress methanogens at salinities of 10 ppt and higher (Wang, Tong, Chambers, & Liu, 2017) and a variety of studies have reported strong correlations between CH_4 land-atmosphere fluxes and soil salinity.

These studies found lower fluxes from polyhaline marshes (> 18 ppt) compared to mesohaline (5 ppt to 18 ppt), oligohaline (0.5 ppt to 5 ppt) and fresh water marshes (< 0.5 ppt) (Arias-Ortiz et al., 2024; Bartlett et al., 1987; Bartlett & Harriss, 1993; Hartman et al., 2024; Poffenbarger, Needelman, & Megonigal, 2011).

Previous studies also pointed out the high variability in CH_4 flux magnitudes, especially in the fresh water and oligohaline marshes (Arias-Ortiz et al., 2024; Poffenbarger et al., 2011). This relative larger variability could indicate the stronger effect of the interplay of environmental variables in driving the CH_4 land-atmosphere fluxes. As for the salt marsh soils, while hydrogenotrophic and acetoclastic methanogens can be outcompeted by sulfate reducers for substrates, methylotrophic methanogens rely on other substrates and do not compete with sulfate reducers (Capooci et al., 2024; Seyfferth et al., 2020). Consequently, methanogenesis can take place even at high SO_4^{2-} pore water concentrations when the amount of methylated compounds supports the metabolic requirements of methylotrophic methanogens. The CH_4 land-atmosphere exchange along salinity gradients proof to be complex and a large uncertainty in CH_4 budgets of tidal wetlands remain (Bartlett et al., 1987; Le Mer & Roger, 2001; Poffenbarger et al., 2011).

While methanogenesis occurs in anaerobic conditions, methanotrophs can oxidize CH_4 in the presence of O_2 (Segers, 1998). Half to nearly all of the produced CH_4 in wetlands soils can be oxidized in aerobic layers of the soils (Capooci et al., 2024; Le Mer & Roger, 2001). Von Fischer and Hedin (2007) showed that net soil emissions of CH_4 significantly increased at a water filled pore space (WFPS) of 60 % and higher. On the other hand, CH_4 oxidation was still observed at WFPS levels of 90 % (Von Fischer & Hedin, 2007). The WFPS can vary highly in tidal wetland soils, depending on flooding frequency, infiltration rate and depth of the flood, ground water dynamics and rhizosphere processes. Furthermore, the tidal floods supply a variety of compounds to the soil pore system, but can also contribute to substitutes removal from the soil pore system of for example of dissolved CH_4 and N_2O (Capooci et al., 2024; Chanton, Martens, & Kelley, 1989; Murray, Erler, & Eyre, 2015; Trifunovic et al., 2020). Knowledge gaps prevail with regard to characterization of CH_4 land-atmosphere exchange by WFPS and flooding and more observations are required from different flooding conditions in space and time to reduce uncertainties in CH_4 budgets of tidal wetlands (Arias-Ortiz et al., 2024; Huertas et al., 2018).

Natural tidal wetland soils are associated with being nitrogen limited due to the high primary productivity and hampered decomposition of organic matter (Bai, Gao, Xiao, Wang, & Huang, 2012; Kiehl, Esselink, & Bakker, 1997; Megonigal & Neubauer, 2019) However, many tidal wetlands are enriched in nitrogen as a consequence of widespread eutrophication of surface waters and atmospheric nitrogen deposition (Rockström, 2009; Steffen et al., 2015; Van Beusekom et al., 2019). Multiple studies found a rise in N_2O emission following increased mineral nitrogen loading (Moseman-Valtierra et al., 2011; Murray et al., 2015; Roughan, Kellman, Smith, & Chmura, 2018).

The reduction of nitrate is thermodynamically more favorable than the reduction of sulfate, as reflected in the earlier introduced relative energy yield ranking. Consequently, the availability of sulfate in the soil pore solution is not expected to create a competitive disadvantage for denitrifiers and therefore no trends would be expected in denitrification rates with salinity gradients. Denitrification can lead to release of the potent greenhouse

gas N_2O when the environmental conditions limit further reduction to N_2 (Butterbach-Bahl, Baggs, Dannenmann, Kiese, & Zechmeister-Boltenstern, 2013; Firestone & Davidson, 1989). The ratio of intermediate to final denitrification product (N_2O : N_2) depends on the active denitrifier species, availability of O_2, organic substrate and mineral nitrogen as well as soil pH and temperature (K. E. Dobbie & Smith, 2003; Firestone & Davidson, 1989; Skiba & Smith, 2000). While no direct effect of sulfate on denitrification rates would be expected, soil pore water salinity might indirectly affect N_2O production by affecting the controls of N_2O : N_2 production (Bai et al., 2012; Wang et al., 2017). N_2O land-atmosphere fluxes from soils with different salinity levels have been observed to be highly variable and had no clear relation with salinity (Chmura, Kellman, Van Ardenne, & Guntenspergen, 2016; Murray et al., 2015; Roughan et al., 2018; Yang & Silver, 2016). Data availability is limited and increasing the number of N_2O land-atmosphere flux observations in space and time from tidal wetland soils is required to further advance our fundamental understanding of N_2O flux dynamics in these ecosystems (Murray et al., 2015).

Not only denitrification, but also nitrification can lead to N_2O production. When the oxidation of ammonium (NH_4^+) is limited by the availability of O_2, the bacteria can use the intermediate product nitrite (NO_2^-) in nitrifier-denitrification. During nitrifier-denitrification, N_2O can also be lost as a by-product similarly as with the denitrification process (Butterbach-Bahl et al., 2013; Firestone & Davidson, 1989). Produced N_2O that moves away from its point of production can still be reduced to N_2 when passing anaerobic soil layers (Murray et al., 2015). The functional gen marker *nosZ,* commonly referred to as proxy for N_2O reduction, has been detected in both anoxic as well as oxic marine water layers (X. Sun et al., 2021). Possibly, the potential for N_2O reduction is not limited to zones of permanently anaerobic conditions in soils and N_2O reduction might occur in aerobic zones when these undergo deoxygenation, for example following tidal flooding. A range of 70 % to 85 % soil WFPS has been found as most supportive for N_2O emissions (K. Dobbie, McTaggart, & Smith, 1999; Velthof & Oenema, 1995), but the dynamic character of WFPS in tidal wetland soils supports high variability of N_2O production. Roughan and colleagues showed that scaling up measured land-atmosphere N_2O fluxes from a specific tidal stage led to false daily estimates (Roughan et al., 2018). Moreover, the effect of a tidal flood on N_2O emissions can also be related to incoming and outgoing compounds such as mineral nitrogen (Murray et al., 2015). As for CH_4, do knowledge gaps also remain with regard to characterization of N_2O land-atmosphere exchange by flooding and flood chemical characteristics.

1.3 Quantification of methane and nitrous oxide land-atmosphere exchange

Increasing our fundamental understanding of CH_4 and N_2O cycling in tidal wetlands requires the quantification of land-atmosphere fluxes, for example to improve estimates of budgets and balances, predictive models or management strategies. Manual closed flux chambers are widely applied for the quantification of land-atmosphere GHG exchange, because they

cover intermediate spatial scales, are a relative flexible and versatile field method and often come with low costs and limited electrical requirements (Kutzbach et al., 2007; Pérez-Priego et al., 2015; Pihlatie et al., 2013; Philippe Rochette, 2011).

The manual closed chamber method relies on gas exchange between the soil surface, vegetation cover and a closed chamber headspace during a certain time frame. The gas concentration change in the headspace can be determined *in-situ* by connecting the flux chamber to a portable trace gas analyzer, allowing the headspace air to circulate in a closed loop between analyzer and flux chamber (Denmead, 2008; P Rochette et al., 1997). The measured concentration change over the predetermined time frame is used to approximate a flux rate through regression analyses (Maier et al., 2022; Pérez-Priego et al., 2015).

Often linear regression is applied to approximate the land-atmosphere flux rates (Pihlatie et al., 2013), although various studies report the underestimation of linearly calculated fluxes (Anthony, Hutchinson, & Livingston, 1995; Kutzbach et al., 2007; Levy et al., 2011; Oertel, Matschullat, Zurba, Zimmermann, & Erasmi, 2016; Pihlatie et al., 2013). This underestimation has been linked to various processes causing non-linear behavior of land-atmosphere fluxes (Kutzbach et al., 2007; Philippe Rochette, 2011), such as the buildup of the GHG in the headspace altering the concentration gradient between soil or plant and headspace air, consequently affecting the diffusion rates of the gas (Kutzbach et al., 2007). A wide array of alternative, non-linear, models have been developed to reach a more accurate approximation of the true land-atmosphere flux (Maier et al., 2022). This created opportunities but also challenges, as multiple studies argued that a better statistical performance of a regression model does not inherently equal lower flux uncertainty (Levy et al., 2011; Pérez-Priego et al., 2015; Pihlatie et al., 2013). Venterea, Spokas and Baker (2009) recommend the use of linear regression for treatment-based studies focusing on relative differences.

The estimated slope from the regression analysis is combined with the ideal gas law to approximate a molar or mass flux for the respective GHG. Therefore, the uncertainty of the final approximated flux also depends on uncertainties in the quantification of the ideal law gas variables, being air pressure and temperature in the headspace, headspace volume and surface area. Levy and colleagues (2011) concluded from their meta-analyses on measured trace gas uncertainty that the selection of the regression model and its lack-of-fit were the largest contributors to the flux uncertainty. However, they pointed out that some of the other uncertainty inducing variables were hard to assess, as these are often assumed, based on ambient conditions, considered a constant or even neglected. For example, vegetation volume is often not included in quantification of the headspace volume, but has been shown to significantly affect calculated flux sizes (Morton & Heinemeyer, 2018). Even with the many recent advances in the manual closed chamber method, trace gas analyzers and chamber data processing, the retrieved datasets are often subject to large uncertainties.

GHG land-atmosphere exchange hypotheses testing further requires quantification of the dominant controls in a field-based study in order to discuss and interpret the quantified fluxes. Main established controls for CH_4 and N_2O emissions are soil organic carbon, mineral nitrogen, temperature, pH, redox potential, bulk density, texture, salinity and moisture as well as presence of vascular plant species and species with aerenchyma

(Bartlett et al., 1987; Bartlett & Harriss, 1993; Fiedler & Sommer, 2000; Le Mer & Roger, 2001; Li et al., 2020; Livesley & Andrusiak, 2012; Megonigal et al., 2004; Segers, 1998; L. Sun, Song, Miao, Qiao, & Gong, 2013; Täumer et al., 2021; Wagner, Pfeiffer, & Bock, 1999).

The World Reference Base (WRB, 2022) offers a soil classification system that allows comprehensively characterizing soils all over the world and relies on *in-situ* description of diagnostics and supplementary laboratory analyses. The characterization of soil redox conditions can also be based on the WRB (2022) by focusing on the diagnostics associated with redox processes: characterizing and quantifying reducti- and oximorphic features, assessing the presence of free Fe(II), sulfides and methane gas and quantifying the hydrogen partial pressure (Blume & Schwertmann, 1969; Rabenhorst & Parikh, 2000; Veneman, Spokas, & Lindbo, 1998; Vepraskas & Richardson, 2001). The obtained characterization reflects seasonal to inter-annual prevailing redox conditions and gives limited insights on shorter timescales.

Alternatively, the IRIS (Indicator of Reduction in Soils) method makes use of indicator sticks to assess the cumulative effect of reducing conditions on the sticks' ferrihydrite coating (Castenson & Rabenhorst, 2006; BJ Jenkinson & Franzmeier, 2006). The longer reducing conditions prevail, the more coating is removed from the sticks as the insoluble Fe(III) in the ferrihydrite paint is reduced to the more soluble Fe(II). The integration time of this indicative method typically ranges from 21 to 30 days (Castenson & Rabenhorst, 2006; Sapkota, Duball, Vaughan, Rabenhorst, & Berkowitz, 2022). While the IRIS method reflects whether the redox conditions supported the reduction of Fe(III) to Fe(II) or not, a more specific characterization can be obtained with redox potential sensors. An inert, for example platinum (Pt), electrode and a reference electrode are integrated in a soil probe and can be installed *in-situ* at point of interest, the measured voltage reflects instantaneously but for a limited spatial reach the integrated effect of processes contributing to the abundance of oxidized and reduced chemical substances (Fiedler, Vepraskas, & Richardson, 2007). In order to close our knowledge gaps in the mechanism driving biogeochemical cycling and CH_4 and N_2O fluxes in tidal wetlands soils, there is a need for more observations and descriptions of tidal wetland soil and soil redox condition characteristics.

1.4 Dissertation objectives and research questions

Currently, the availability of CH_4 and N_2O land-atmosphere flux data is limited for the tidal wetland soils in Northern Europe. More observations are required in space and time to evaluate what CH_4 and N_2O land-atmosphere flux magnitudes occur along salinity gradients and from different flooding conditions to further elucidate the fundamental processes steering the land-atmosphere exchange (Arias-Ortiz et al., 2024; Capooci et al., 2024; Chmura et al., 2011; Huertas et al., 2018; Koontz et al., 2024; Le Mer & Roger, 2001; Murray et al., 2015; Poffenbarger et al., 2011). Therefore, the leading question in this dissertation is "What CH_4 and N_2O land-atmosphere flux magnitudes, directions and spatiotemporal variability originate from tidal wetlands located in the intensively used Elbe estuary?".

This main research question will be addressed by studying the following supporting research questions:

a. What soil forming processes and physicochemical properties characterize tidal wetland soils in different salinity zones and different flooding frequency zones in the Elbe estuary according to the World Reference Base (WRB) classification?
b. What soil redox conditions characterize the tidal wetland soils in different salinity zones and different flooding frequency zones in the Elbe estuary?
c. How does the soil redox condition characterization from soil descriptive, IRIS and redox potential sensor approaches compare when aggregating the obtained results over the measurement area over a year?
d. How do CH_4 and N_2O flux magnitudes, flux directions and spatiotemporal variability compare between the pioneer zones of the three salinity zones and the flooding frequency zones within the salt marsh located in the Elbe estuary over the course of 15 months?
e. What are the key controlling environmental variables for flux magnitude, flux direction and spatiotemporal variability and how do these vary among the tidal wetland zones in the Elbe estuary?
f. What is the uncertainty in the obtained CH_4 and N_2O land-atmosphere exchange dataset considering the quantification of the fluxes, flux errors and how do these compare to the spatiotemporal variability of fluxes in the tidal wetland zones.

Chapter 2 Materials and methods

2.1 Study sites

Data collection took place in the Elbe estuary located in the north of Germany (figure 1). A salt (SM), brackish (BM) and fresh water (FM) marsh were selected as research sites in order to cover different salinity zones within the estuary (figure 1, table 1). Each research site was equipped with three research stations in different flooding frequency zones (figure 1, table 1). These flooding zones were selected based on the presence of indicator species associated with flooding exposures. Pioneer zone (PZ) vegetation develops below the mean high tide level (MHT level), whereas the low marshes (LM) and high marshes (HM) develop above the MHT level (Bakker, 2014).

In total nine research stations covered the estuarian gradients (figure 1, table 1). An additional, tenth research station was set up in a managed high marsh (HMg) area in the salt marsh. This area is grazed by sheep from late spring to autumn and drained with a passive, open-channel drainage network. As these two practices affect soil conditions and vegetation community (Bakker, 2014), the area was considered as a separate tidal wetland zone. The SM HMg is only included in the research questions addressing GHG land-atmosphere exchange and was left out of the soils and soil redox conditions study.

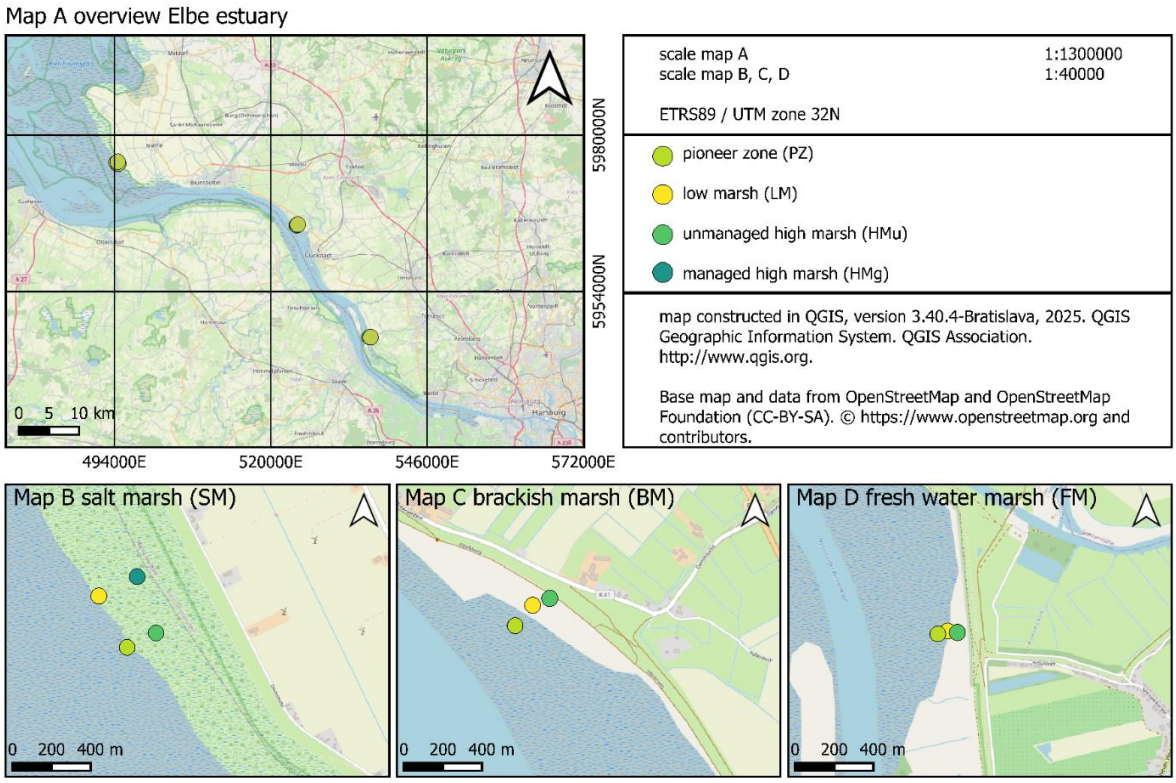

Figure 1 Overview of the studied tidal wetland zones along the Elbe river. Map A shows where the three salinity zone representing research sites are located within the Elbe estuary and map B, C and D show where the research stations are located of each flooding frequency zone per salinity zone.

Table 1 Specifications of the different research sites, referred to as salinity zones, and different research stations per flooding frequency zone, referred to as tidal wetland zones.

salinity zone	**ground water salinity[1]**	**tidal wetland zone**	**flooding frequency[1,2]**	**indicator species**
fresh water marsh (FM)	0.9 ppt (0.7 - 1.5 ppt)	FM PZ	0.9 days	*Typha angustifolia*
		FM LM		*Phragmites australis*
		FM HMu	3 days	*Phragmites australis*
brackish marsh (BM)	1.8 ppt (0.8 - 2.5 ppt)	BM PZ	0.5 days	*Bolboschoenus maritimus*
		BM LM		*Phragmites australis*
		BM HMu	100 days	*Phragmites australis*
salt marsh (SM)	16.8 ppt (12.0 – 20.0 ppt)	SM PZ	1.4 days	*Salicornia* ssp. and *Spartina anglica*
		SM LM		*Puccinellia maritima* and *Atriplex portulacoides*
		SM HMu	10 days	*Elymus athericus*
		SM HMg		*Festuca rubra*

[1] *preprint* Branoff et al., 2024

[2] flooding frequency expressed in time between consecutive floods of soil surface

Each research station covers 6.5 by 10 meters. The stations were split into three blocks of 2 by 10 meter (figure 2), with two blocks for disturbed sampling (DS) and undisturbed measurements (UM) of soil and vegetation and one block for greenhouse gas flux measurements (GHG). Each of the three blocks consists of 5 replicate plots of 2 by 2 meters (figure 2). All stations are equipped with boardwalks to limit the disturbance to soil and vegetation by treading on the ground, except for SM HMu and SM HMg where the general conditions were considered not to be affected by accessing during data collection. The research stations were orientated such that the replicate plots are parallel to the Elbe river bed.

Plant community surveys and above ground biomass measurements were performed at each of the research stations once a year. The surveys consisted of assessing percentages of species coverage, bare soil and litter within two subplots of 60 by 60 cm per UM block and aboveground biomass was harvested from two 20 by 20 cm sub sections per replicate plot within the DS blocks (figure 2). Both the survey and harvest took place yearly at end of July or beginning of August.

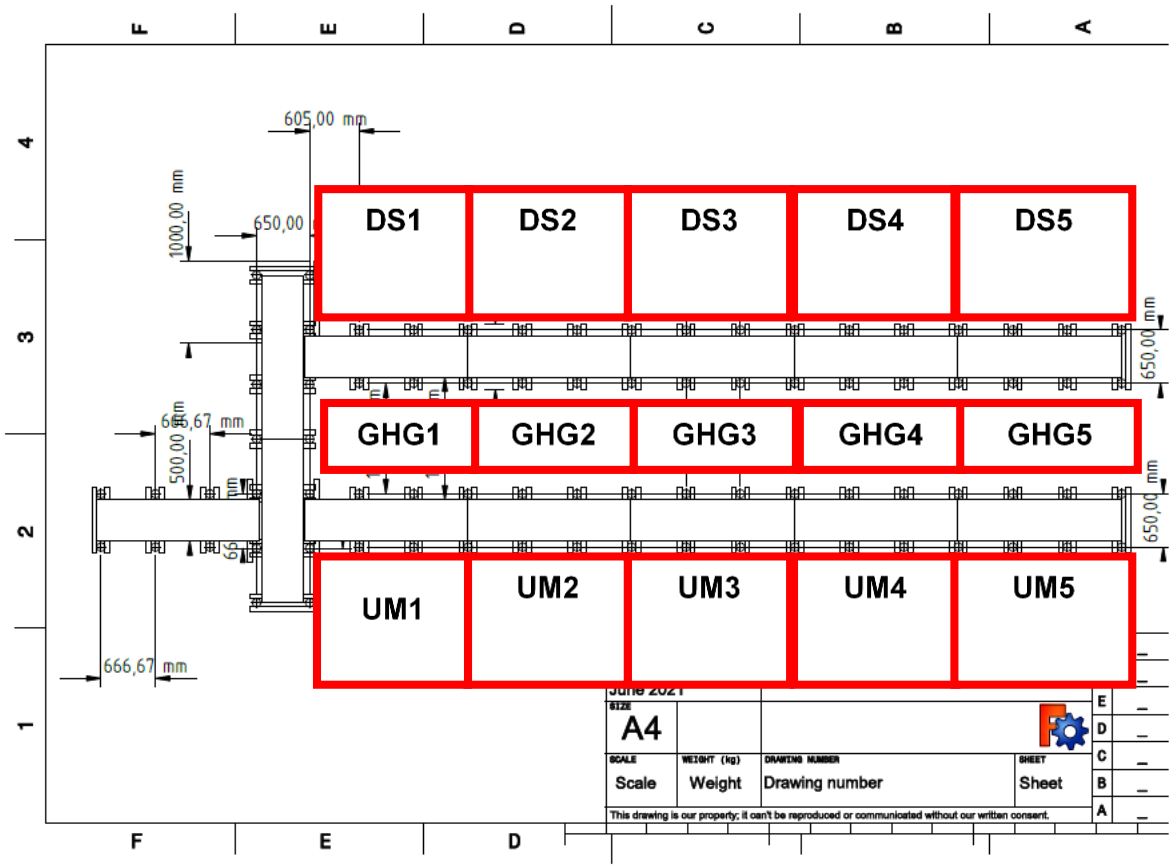

Figure 2 Overview of research station design with red boxes indicating replicate plots for disturbed sampling (DS) greenhouse gas flux measurements (GHG) and undisturbed measurements (UM). Research stations were systematically set up, having the DS replicate plots on the riverbed side of the station and the UM plots on the dike side. This figure is adapted from the original by N. Rüggen 2021.

2.2 Characterization of the tidal wetland soils

The soils were described and sampled for physicochemical analyses at the different tidal wetland zones on the 23rd and 24th of November 2021, 22nd, 23rd and 24th of February 2022 and 2nd March 2022. One soil profile per research station was prepared by digging a 1 meter wide by 1.5 meter deep soil pit. Soil descriptions and reference soil group (RSG) classification were based on the latest World Reference Base for Soil Resources (WRB, 2022) with additional consulting of Food and Agriculture Organization of the United Nation's (FAO) guidelines for soil description, 2006 (Jahn, Blume, Asio, Spaargaren, & Schad, 2006; WRB, 2022).

Two mixed, homogenized, soil samples were taken from each identified horizon per soil profile. One soil sample was processed fresh and the other was first air dried, then oven-dried at 105 °C for further analyses. Additionally, five replicate undisturbed soil cores were taken using metal rings of 100 mm^3 for soil physical property analyses at 5 cm, 10 cm, 30 cm and 60 cm depths. The soil cores were used to determine the soil bulk density (in g m^{-3} soil) by weighing the samples before and after drying at 105 °C.

Soil chemical analyses included: I) pH_{H2O} of the fresh soil sample in H_2O extract and pH_{CaCl2} of the air-dried soil sample in 0.01 M $CaCl_2$ extract (Mettler Toledo FiveEasy, Mettler-Toledo GmbH, Germany), II) electrical conductivity of the fresh soil sample (EC_{ms} in dS m^{-1}, WTW Cond 3110 Set 1, Xylem Analytics Germany Sales GmbH & Co. KG, Germany), III) total carbon, $C_{tot,}$ and total nitrogen, N_{tot}, contents of the at 105 °C dried, 2 mm sieved soil sample (% w/w, vario Max cube, Elementar Analysensysteme GmbH, Germany), IV) inorganic carbon, TIC, content of the at 105 °C dried, 2 mm sieved soil sample in 10 % H_3PO_4 extract (% w/w, soli TOC® cube, Elementar Analysensysteme GmbH, Germany), V) the mineral nitrogen in ammonium, NH_4-N, content in the soil sample according to DIN 38406 (mg kg^{-1} dry soil, DR 5000, Hach Lange GmbH, Germany), VI) soil cation-exchange-capacity, CEC, of the soil sample according to DIN EN ISO 11260 ($mmol_c$ kg^{-1} soil, Varian AA 280FS, Agilent Technologies Inc., USA), VII) bioavailable, Ca^{2+}-lactate extracted potassium, K_{calac}, content in the soil sample according to VDLUFA, 1991 (mg kg^{-1} soil, Varian AA 280FS, Agilent Technologies Inc., USA), VIII) bioavailable Ca^{2+}-lactate extracted phosphor, P_{calac}, content in the soil sample according to DIN 38405 (mg kg^{-1} soil, DR 5000, Hach Lange GmbH, Germany), IX) phosphorus content in the soil sample with Olsen-extraction, P_{olsen} (mg kg^{-1} soil, DR 5000, Hach Lange GmbH, Germany) (Olsen, 1954), X) mineral nitrogen in nitrate, NO_3-N and total nitrate, NO_3^- in H_2O extract of the fresh soil samples (mg kg^{-1} soil, HPLC Agilent 1200 Serie, Agilent Technologies Inc., USA), XI) sulphate, SO_4^{2-}, bromide, Br^-, chloride, Cl^- contents in H_2O extract of the fresh soil samples (mg kg^{-1} soil, Methrom Compact Flex 930 with Sampler 858, Metrohm Deutschland GmbH & Co. KG, Germany), XII) dithionite extracted iron, Fe_{dit}, and manganese, Mn_{dit}, in the soil sample according to ISO 12782 (mg kg^{-1}, Varian AA 280FS, Agilent Technologies Inc., USA).

Furthermore, soil textures were determined in mass-percentage from the air-dried samples through the sieving method and sedimentation method (DIN-ISO 11277, DIN 18123, DIN 19683). Soil organic carbon was calculated as the remainder of C_{tot} minus TIC. The NH_4-N content in the salt marsh soil samples was obtained based on the in-house protocol of the Helmholtz-Zentrum Hereon (T. Sanders) using the same reagents but applied in three separate solutions instead of two, as the high salt levels did not allow to analyses according to the standard protocol.

In order to identify the presence of salic horizons in tidal wetland soils, information is required on the soil electrical conductivity in the saturated extract, ECse. The parameter ECse (dS m-1) can be calculated using ECse = 250 * EC2.5 * (WCse)-1 with WCse based on the estimation scheme reported in table 8.69, chapter 8.4.28 of the WRB (2022). The ECse acts as a proxy for the amount of available soluble salts.

The chemical analyses results were visualized and studied through the principal-component-analyses (PCA) (Greenacre et al., 2022). The PCA was performed in R (R Core Team, 2020) through RStudio (RStudio Team, 2021 version 1.4.1103) with the packages “factoextra” (Kassambara and Mundt, 2020), “ggplot2” (Wickham, 2016) and “stats” (R Core Team, 2020). The variables were centered and scaled before the principal components (PC) were constructed.

2.3 Characterization of tidal wetland soil redox conditions

2.3.1 Reductimorphic and oxymorphic soil features

Part of the describing soils for RSG-classification is the identification, quantification and qualification of redoximorphic features. This is achieved by comparing the soils matrix color with colors of present concretions and patches based on the Munsell color charts as described in chapter 8.4.20 of WRB (2022). These descriptions include abundance, size, cementation and location of concretions in addition to their assigned color codes. The concretion, or mottle, descriptions are supplemented by field observations of fresh soil samples reactions to the addition of 0.2% α,α-dipyridyl in 1 *N* NH_4OAc (pH 7) solution and 10% HCl solutions. Reducing conditions are indicated by color change of the soil sample, or H_2S gas formation, following the exposure to these reactants (Chapter, 8.4.21, (WRB, 2022)). The combination of these descriptions is translated to a reduction class ($RC_{morphology}$) for each described soil horizon according to table 2.

Table 2 Classification guide for the soil horizon "reduction class" ($RC_{morphology}$) adapted from WRB 2022. RC are based on criteria described in chapter 8.4.21, table 8.59.

RC	**criteria** (based on chapter 8.4.21, p. 198, WRB 2022)
R2	The fresh soil sample has flammable CH_4, presence of FeS indicated by release of H_2S with 10% HCl test or presence of free Fe^{2+} indicated with α,α-dipyridyl test soil matrix has Munsell-hue N (due to presence of metal sulfides)
R3	Soil matrix has Munsell-hues either 10Y, 5GY, 10GY, 5G, 10G, 5BG, 10BG, 5B, 10B or 5PB, alternatively soil matrix hue of 5Y or 2.5Y with chroma ≤ 2
R4	The exposed soil in the soil pit reveals presence of oximorphic Fe features with Munsell colors as described by Scheinost and Schwertmann (1999)
R5	The exposed soil in the soil pit is absent of redoximorphic features as described for R4, but can have oximorphic Mn features visible as black concretions, soil pores have temporally no free O_2, conditions can support denitrification or are even completely aerobic conditions

2.3.2 Indicator of Reduction in Soils

The Indicator of Reduction in Soils, IRIS, method was used as a second approach to quantify soil redox conditions. The method is based on the microbial iron(III) reduction process. It was first described by Jenkinson (2002) and further developed by Castenson and Rabenhorst (2006) and Rabenhorst (2013). The method applied here closely resembles the described approach by Mittmann-Goetsch and colleagues in 2024. 60-cm long PVC plates (60 cm x 5 cm x 0.28cm) were sanded (180 grid), cleaned with acetone and painted with a ferrihydrite-goethite paint mixture on both sides. These sticks were installed at each of the five replicate plots in the UM blocks at the nine research stations, excluding the managed high salt marsh. The sticks were exchanged every 4 weeks for 11 campaigns in 2022 and 2023 (table 3). At the start of the experiment a pilot hole was prepared by hammering a metal bar with similar dimensions as the IRIS sticks into the soil. At the end of each measurement campaign, the sticks were replaced with fresh ones. The

harvested sticks were transported back to the lab, manually cleaned by rinsing off soil and other debris with tap water and left to dry for one day before being stored in the dark. All collected sticks were scanned at the end of the 11 measurement campaigns. These scans were analyzed per 10 cm and 1 cm sections on paint removal through image processing with ArcGIS Pro as described by Mittmann-Goetsch et al. (2024). The dimensionless reduction index (RI) was obtained by dividing the number of pixels with paint removed, corrected for errors by total number of pixels (Mittmann-Goetsch et al., 2024). The RI, can range from 0 to 1, with a RI of 0 indicating no paint removal and therefore no suitable conditions for iron(III) reduction over the integration period and depth. Whereas RI of 1 indicating full paint removal, supporting suitable conditions for Fe^{3+} reduction over the integration period and depth. Three RI variables are constructed with RI_{tot} reporting the averaged RI over the maximum 60 cm reach of the IRIS sticks, RI_{10cm} reporting the RI results per 10 cm soil depth increment and RI_{1cm} reporting the RI results per 1 cm soil depth increment.

Table 3 Sampling campaigns for the IRIS method and averaging time windows applied for redox sensors readings.

campaign	date	campaign	date
1	2022-05-30 to 2022-06-27	7	2022-11-14 to 2022-12-12
2	2022-06-27 to 2022-07-25	8	2022-12-12 to 2023-01-09
3	2022-07-25 to 2022-08-24	9	2023-01-09 to 2023-02-07
4	2022-08-24 to 2022-09-19	10	2023-02-07 to 2023-03-06
5	2022-09-19 to 2022-10-20	11	2023-03-06 to 2023-03-30
6	2022-10-20 to 2022-11-14		

The RI results were visualized in boxplots with “ggplot2” package (Wickham, 2016) in R (R Core Team, 2020) through RStudio (RStudio Team, 2021 version 1.4.1103). Additionally, a mixed linear effect model was constructed for predicting RI_{10cm} (scaled and centered), with fixed effects salinity zone (FM, BM, SM), flooding frequency zone (PZ, LM, HMu), depth below soil surface (0 – 10 cm, 10 – 20 cm, 20 – 30 cm, 30 – 40 cm, 40 – 50 cm and 50 - 60 cm), measurement campaign (table 3) and with IRIS stick ID codes as random effect. The model was assessed with ANOVAs. Mixed effects model construction and statistical analyses were performed using “ggeffects” (Luedecke, 2018), “lme4” (Bates et al., 2015), “lmerTest” (Kuznetsova, Brockhoff and Christensen, 2017) and “stats” packages (R Core Team, 2020). Additionally, non-parametric tests were conducted to compare the RItot between the three salinity zones with Kruskal-Wallis and pairwise Wilcoxon tests through the “stats” package (R Core Team, 2020) in R (R Core Team, 2020) using RStudio (RStudio Team, 2021 version 1.4.1103).

2.3.3 Soil redox potential sensors

The third method relied on soil redox potential sensors to quantify soil redox conditions. Customized analogue soil redox potential probes (customized ORP-60-4-A, SWAP instruments B.V., Netherlands) were installed in each replicate plot in the UM blocks of the

SM PZ, SM LM and SM HMu. The other tidal wetland zones were not equipped with sensors due to the high costs. The probes had a total length of 69 cm and a diameter of 1.4 cm, a casing of epoxy glass fiber and POM-c top and tip. They are equipped with platinum electrodes mounted at depths of 5 cm, 10 cm, 30 cm and 60 cm below soil surface. The probes were installed by manually inserting them gradually into the soil with gentle constant forcing. One Ag/AgCl reference electrode in 3 M KCl gel was deployed at SM PZ, SM LM and SM HMu. The raw output of the sensors was converted to standard hydrogen electrode (SHE) reference by adding 213 mV to the measured voltage, as specified by the manufacturer. The sensor output after conversion is the redox potential, Eh, expressed in mV. The Eh was averaged for each sensor depth over the IRIS installation periods (table 3). The averaged Eh values were converted into hydrogen partial pressure, rH, according to rH = (2 Eh / 59) + 2 pH as described in chapter 8.4.21 of the WRB (2022) using the soil pH measured at the corresponding depth obtained from the earlier described soil physicochemical dataset (WRB, 2022). The 11 four week block average redox potentials were visualized in scatter plots with “ggplot2” package (Wickham, 2016) in R (R Core Team, 2020) through RStudio (RStudio Team, 2021 version 1.4.1103).

A mixed effects model was constructed for the prediction of average redox potential (scaled, centered) with fixed effects flooding frequency zone (PZ, LM, HMu), depth increment (5 cm, 10 cm, 30 cm and 60 cm), measurement campaign (table 3) and with redox sensor ID codes as random effect. The model was assessed with ANOVAs. Mixed effects model construction and statistical analyses were performed using “ggeffects” (Luedecke, 2018), “lme4” (Bates et al., 2015), “lmerTest” (Kuznetsova, Brockhoff and Christensen, 2017) and “stats” packages (R Core Team, 2020) in R (R Core Team, 2020) through RStudio (RStudio Team, 2021 version 1.4.1103).

2.3.4 Comparison of soil redox condition characterization methods

Redox conditions reflected per soil horizon were compared between the assigned $RC_{morphology}$ from soil redox diagnostics and corresponding $RI_{horizon}$ from IRIS. The $RI_{horizon}$ values were obtained by averaging RI_{1cm} over the soil horizon layer thickness. ANOVAs were conducted on square root transformed $RI_{horizon}$ per $RC_{morphology}$ with the “stats” package (R Core Team, 2020) and Tukey HSD post hoc tests were conducted with the “rstatix” package (Kassambara, 2021) in R (R Core team, 2020), through RStudio (RStudio Team, 2021 version 1.4.1103). The transformation of the $RI_{horizon}$ was needed to meet the ANOVA assumptions as Shapiro-Wilk normality test reported a p value of 0.006. Upon the square root transformation p value became 0.066. Additionally, the transformed RI values resulted in normal distributed residuals as reflected by Shapiro-Wilk normality test of linear model $\sqrt{(RI_{horizon})} \sim RC_{morphology}$ reporting p value of 0.17 and homogeneity of variance, with LeveneTest of $\sqrt{(RI_{horizon})} \sim RC_{morphology}$ F-statistic of 1.48 on 3 and 36 and p 0.24. The results of the comparison are summarized in descriptive tables.

Redox conditions reflected per redox sensor depth were compared between the calculated rH values, corresponding reduction classes (RC_{sensor}) and reduction index (RI_{sensor}). RC_{sensor} was assigned based on ranges of rH value associated with the reduction classes as reported in table 4. RI_{sensor} values were calculated for the four sensor depths

(5 cm, 10 cm, 30 cm and 60 cm) by averaging RI_{1cm} results over the depth sections 3 – 7 cm, 8 – 12 cm, 28 – 32 cm and 58 – 60 cm respectively.

Table 4 Classification guide for the soil horizon "reduction class" ($RC_{morphology}$) adapted from table 8.59, chapter 8.4.21, WRB 2022. The corresponding rH value ranges are reported for the associated processes per RC class (table 8.59, chapter 8.4.21, WRB 2022).

RC	**criteria** (WRB 2022, 8.4.21, p198)	**rH value range**
R2	The fresh soil sample has flammable CH_4, presence of FeS indicated by release of H_2S with 10% HCl test or presence of free Fe^{2+} indicated with α,α-dipyridyl test soil matrix has Munsell-hue N (due to presence of metal sulfides)	<13
R3	Soil matrix has Munsell-hues either 10Y, 5GY, 10GY, 5G, 10G, 5BG, 10BG, 5B, 10B or 5PB, alternatively soil matrix hue of 5Y or 2.5Y with chroma ≤2	13-20
R4	The exposed soil in the soil pit reveals presence of oximorphic Fe features with Munsell colors as described by Scheinost and Schwertmann (1999)	temporarily <20
R5	The exposed soil in the soil pit is absent of redoximorphic features as described for R4, but can have oximorphic Mn features as black concretions, soil pores have temporally no free O_2, conditions can support denitrification or are even completely aerobic conditions	temporarily ranging 20 - 29 (Mn oxides) or >29 and <33 (denitrification) or >33 (aerobic)

2.4 Greenhouse gas land-atmosphere fluxes

2.4.1 Manual closed chamber method

The GHG land-atmosphere fluxes were quantified with the manual closed chamber method. The data collection and analyses focused on the three pioneer zones at each salinity zones (FM PZ, BM PZ, SM PZ) and on the three flooding zones plus managed high marsh zone within the SM (SM PZ, SM LM, SM HMu, SM HMg) (figure 1). Time, material and labor support were too limited to collect sufficient data of the other tidal wetland zones (BM LM, BM HMu, FM LM and FM HMu) to address the research questions raised in this project.

Collars

The GHG measurement blocks were prepared for the flux chamber measurements by inserting square shaped PVC collars (80 cm x 80 cm x 15 cm) into the soil to a depth of approximately 12 to 13 cm (figure 2, appendix B figure 24). One collar was positioned in the middle of each of the five flux replicate plot. The use of inserted collars is common practice in the manual closed chamber method as they minimalize the disturbance of the soil system by chamber placement, block lateral diffusion of gases in and out of the measurement area and ensure sampling of the exact same area for repeated measures (Maier et al., 2022; Philippe Rochette, 2011; P Rochette et al., 1997). The relatively large measurement area of 80 cm by 80 cm was chosen for this project as a large surface area allows coverage of

small-scale variability of these dynamic ecosystems. A large base area also allowed the use of taller flux chambers that were required to enclose *Typha angustifolia* while maintaining the stability of the measurement set up.

The collars were constructed by riveting four 80 cm x 15 cm x 0.5 cm PVC plates (PVC-U) together with 5 cm x 5 cm x 0.5 cm alumina L-shaped profiles (AlMgSi0.5) using 3 mm x 14 mm alumina rivets (DIN 7337) and sealing the connections with silicon (DIN 32622) (appendix B, figure 25). Collars were installed three months before flux measurements started in January and February 2022. Regular checks were performed on the levelness and state of the collars. Corrections to the collars were made when needed and reported in the field log book. Notes on the collar state included for example ponding in the collar, erosion around the collar or relevelling of the collar and were used in the flux quality assessment addressed later.

Transparent flux chamber

Two versions of transparent flux chambers were constructed. Both designs were made from non-reactive, air-tight materials to secure a fixed volume of headspace air for the approximation of CH_4 and N_2O land-atmosphere fluxes. The first-generation flux chamber (Chamber1) consisted of an aluminum frame (80 cm x 80 cm x 83 cm, 0.555 m^3) manually assembled from separate U-, T and L- profiles fixed with steel squares using flanch lock nuts and glued together tightly (appendix C, figure 26). The U-shaped bottom of the chamber was embedded with a cellular rubber sealant (EPDM-basic, ISO-7715) to seal the chamber-collar contact from the atmosphere. The chamber frame was covered with transparent foil (polyethylene, 200 µm thick, 88 to 90 % sunlight transmissivity) and on one side equipped with two 5 mm thick acrylic plates (PMMA). In both acrylic plates two connection ports (6 mm diameter) were installed, two in the upper plate and two in the lower plate, to connect the chamber with tubes (6 mm outer, 4 mm inner diameter, polyurethane) to the portable trace gas analyzers. All contact points between the aluminum parts were sealed with silicon (DIN 32622). Strips of a polyethylene sheet were added around the chamber to cover the chamber-collar connection in order prevent exposure of the sealant wind gusts. Additionally, before a measurement started the chamber was strapped with bungee cords to the board walk or to tent pegs present in the soil to ensure enough pressure on the cellular rubber foam to seal the chamber-collar connection.

Chamber1 was equipped with four fans (5 cm x 5 cm x 1 cm, 5700 RPM, 22.08 m^3 / h, DC 12V, model EE-50101S2-1000U-999, Sunonwealth Electric Machine Industry Co., Ltd., Taiwan) to ensure homogenously mixed air in the chamber headspace and prevent the buildup of a concentration gradient. Homogenous mixture of the headspace air is required to obtain a representative sample of the complete chamber headspace air (P Rochette et al., 1997). A pressure release vent was drilled in the lower acrylic plate to minimize the pressure effect of placing the chamber onto the collar (P Rochette et al., 1997). The vent was closed with a butylene stop after the chamber placement, right before a measurement would start. A thermometer (DET1R, Voltcraft, Conrad Electronic SE, Germany) was attached to the butylene stop to record the headspace air temperature ($T_{air_in_man}$). The fans were powered with rechargeable 9 V nickel-metal hydride batteries. Damages to the

chamber foil were repaired with transparent tape (polyethylene). The first-generation chamber (Chamber1) was used from April 2022 until October 2022. In June 2022, a combined air temperature (T_{air_in}) and humidity (RH_{air_in}) sensor (HMP45C, Campbell Scientific, Inc., USA) and a photosynthetic active radiation (PAR_{in}) sensor (full spectrum PAR quantum sensor SQ-521, Apogee Instruments, Inc., USA) were mounted inside the flux chamber. Manual temperature measurements continued till October 2022, as long as Chamber1 was used for the flux measurements. The four fans were switched for two bigger fans (120 mm x 120 mm x 25 mm, 12V DC, 1800 rpm, 32.13 cfm, Fan 103, LogiLink 2direct GmbH, Germany) in June 2022 as well. Two additional connection ports were installed to lead the sensors' cables to the logger (CR10000X, Campbell scientific, Inc., USA) and provide a power cable from the external battery (lead-acid 12V battery, NPV-12, Yuasa Battery, Inc., USA) to the two new fans.

The second-generation flux chamber (Chamber2) was of similar design but the base chamber was less tall, 83 cm x 83 cm x 40 cm (0.296 m^3), and all chamber walls were made of 5 mm thick acrylic glass panels connected by the alumina frame (appendix D, figure 27). All connections between the separate parts, acrylic glass panels, U-, T- and L-profiles, screws and flanch lock nuts, were sealed again with silicon (DIN 32622). A cellular rubber sealant (EPDM-basic, ISO-7715) was glued in the U-profile chamber bottom. Chamber2 was not further adapted to cover the chamber-collar connection as its larger weight compressed the cellular rubber sufficiently to seal it off. Chamber2 was equipped with photosynthetic active radiation sensors inside (PAR_{in}) and on top (PAR_{out}) of the flux chamber (full spectrum PAR quantum sensor, Apogee Instruments, Inc., USA), a combined air temperature (T_{air_in}) and humidity (RH_{in}) sensor inside the flux chamber (HMP45C, Campbell Scientific, Inc., USA) and a port to connect the air pressure (p_{air_in}) sensor (Model 278, Setra Systems, USA) with a tube (6 mm outer and 4 mm inner diameter, polyurethane) to the flux chamber. Additionally, six connection ports (6 mm diameter) were installed in the acrylic glass panels to connect the chamber headspace volume to the measurement cell of the trace gas analyzers with tubing (6 mm outer and 4 mm inner diameter, polyurethane), enable power supply (two lead-acid, 12V batteries, NPV-12, Yuasa Battery, Inc., USA) and data transfer (CR10000X, Campbell scientific, Inc., USA).

Four small (0.293 m^3) and one larger (0.572 m^3) chamber extensions were constructed that could be stacked by connecting U-shaped chamber bottom and T-shaped chamber tops (appendix E, figure 28). The construction procedure and materials are equal to that of Chamber2. The extensions were required to fit the growing vegetation within the head-space. Two fans were added for each extra 0.6 m^3 of chamber volume, thus, there were two fans in two of the four small extensions and two fans in the large extension (120 mm x 120 mm x 25 mm, 12 V DC, 32.13 cfm, 1800 rpm, Fan 103, LogiLink, 2direct GmbH, Germany).

The chamber constructions were tested for leakages and air mixing by deploying smoke cartridges and visually assessing the air mixture inside the flux chamber. There were no indications of insufficient sealing or insufficient air mixing for either chamber designs.

Table 5 summarizes the applied set of flux chamber constructions for the different measurement periods. The initial measurement planning aimed at addressing all tidal wetland zones biweekly. However, limitations put up for nature protection, absence and

unavailability of staff and weather conditions limited the actual amount of performed measurement campaigns. Further details on measurement date specifics are given in appendix F, table 24. The flux chamber measurements were conducted between 9:00 and 17:00 local time.

Table 5 Overview of flux chamber and extension (small, large) used during flux chamber measurements, with associated headspace volume per combination and the measurement time windows for which each specific combination was used.

tidal wetland zone	flux chamber combinations	headspace volume[1] (m^3)	measurement period[2]
FM PZ	Chamber1	0.555	2022-04, 2022-05
	Chamber1 + 2 small extensions	1.151	2022-09, 2022-10
	Chamber2	0.296	2023-02, 2023-03, 2023-04
	Chamber2 + small extension	0.589	2023-05
	Chamber2 + large extension	0.869	2023-01
	Chamber2 + small + large extensions	1.162	2023-06
	Chamber2 + 2 small + large extensions	1.455	2023-07
BM PZ	Chamber1	0.555	2022-04, 2022-05
	Chamber1 + large extension	1.146	2022-06
	Chamber2	0.296	2023-01 until 2023-05
	Chamber2 + large extension	0.869	2023-06
SM PZ	Chamber1	0.555	2022-04 until 2022-10
	Chamber2	0.296	2023-01 until 2023-06
SM LM	Chamber1	0.555	2022-04 until 2022-10
	Chamber2	0.296	2023-02 until 2023-06
SM HMu	Chamber1	0.555	2022-04 until 2022-10
	Chamber2	0.296	2022-12 until 2023-05
	Chamber2 + small extension	0.589	2023-06
SM HMg	Chamber1	0.555	2022-04 until 2022-10
	Chamber2	0.296	2022-12 until 2023-06

[1] BM PZ flux chamber headspace volumes were corrected for soil surface unevenness in the flux calculations when there was no ponding in the collars. Details are given in chapter 2.4.3.

[2] Full overview of measurement dates are given in the appendix F, table 24.

Auxiliary measurements of soil and atmosphere

A variety of environmental variables were measured simultaneously with the flux chamber measurements. Volumetric water content (VWC), soil temperature (T_{soil}) and soil electrical conductivity (EC) were measured with TEROS-12 soil probes (METER group, USA). Four TEROS-12 probes were installed around the collar, one at roughly 20 cm distance of each of the corners, shortly before the start of a flux chamber measurement and removed briefly after. The sensors inside and on top of the flux chambers as well as the soil probes were connected to the datalogger (CR1000X, Campbell scientific, Inc., USA) and to one (Chamber1) or two 12V acid-lead batteries (Chamber2). The Chamber1 set-up had the logger and battery both inside a logger box (GEOS-series for Industry and Outdoor, Spelsberg, Germany) attached to a carrier backpack. Whilst the set-up for Chamber2 had the two batteries in a separate rechargeable battery pack field case (5C-14 11080003 field case rechargeable battery pack, S::CAN, Austria).

Auxiliary measurements of vegetation at the flux replicate plots

Vegetation development in each flux replicate plot was tracked with a top view picture of the collar at the end of each measurement day. The pictures were used to describe the plant community composition and estimate coverages per species (%) and bare soil (%). The information was combined with the findings from the main RTG2530 vegetation surveys to calculate the above ground biomass (g dry and fresh weight) by scaling the surveyed sub plots to the dimensions of the replicate flux plots and correcting for present species and coverages. These results are used for correcting headspace volume and for the sensitivity analyses of the GHG flux calculation introduced later. Furthermore, the vegetation information was used in the discussion of observed flux magnitude differences.

Flux chamber measurement procedure

Flux chamber measurements were conducted with portable trace gas analyzers LI-7810 (CH_4 / CO_2 / H_2O) and LI-7820 (N_2O / H_2O) (LI-COR, Inc., USA). The LI-78XX analyzers rely on optical feedback cavity enhanced adsorption spectroscopy and sample at a 1 Hz frequency. Different flow rates can be selected but during were kept constant at the standard configuration of 250 sccm in this project. Measurement ranges reach from 0 to 100 ppm with a precision of 0.60 ppb at 2000ppb (1 second averaging) for CH_4, 0 to 10,000 ppm with a precision of 3.5 ppm at 400 ppm (1 second averaging) for CO_2 and 0 to 100 ppm with a precision of 0.4 ppb at 330 ppb (1 second averaging) for N_2O (LI-COR, Inc., publications: 984-17414 and 984-19432). Polyurethane tubing (6 mm outer, 4 mm inner diameter) was used to connect the flux chamber to the analyzers. 6 mm Ports connected the flux chamber and tubing and Swageloks connected the tubing with analyzer. Additionally, a dust filter was incorporated in the inlet tubing.

One chamber measurement took 5 minutes to complete, which was a predetermined time frame based on the consideration of the high analyzer precisions and the effect of enclosure of the system on GHG land-atmosphere exchange, but also considering the possibility of near zero GHG land-atmosphere fluxes. Specific attention was paid to not disturb the set-up when measurements were running. Shading of the flux chamber, touching of the flux chamber or tugging of cables were considered among those disturbances. If such a disturbance did occur, it was noted down. Similarly, changes in the weather and surroundings were noted in the field log book. These included for example recent mowing, ponding, erosion, and sedimentation. A detailed description is given of the flux chamber measurement procedure in appendix G.

2.4.2 Greenhouse gas flux calculations

Flux chamber data (.data file) was converted into CSV-files with “pandas” (The pandas development team, 2025) in Python programming language (Python Software Foundation, version Python 3). The converted raw chamber data file consisted of a timestamp column (dd:mm:yyyy hh:mm:ss), the measured gas concentrations of H_2O (ppm), N_2O (ppb) or H_2O (ppm), CO_2 (ppm) and CH_4 (ppb). A meta data file was prepared containing each measurement start and end time (dd:mm:yyyy hh:mm:ss), measurement ID, specification of light (0)

or dark (1) measurement, sample number, chamber headspace volume (m^3), collar surface area (m^2), air temperature (°C). The air temperature used in the flux calculations was T_{air_in} when available or $T_{air_in_man}$, as four-minute averaged temperature over the four-minute gas concentration change slope. Fluxes (in µg N_2O or CH_4 per m^{-2} s^{-1}) were calculated in MATLAB (The MathWorks Inc, 2022, version: R2022a) with the script "chamberflux" (Eckhardt & Kutzbach, 2016) version v15 (Holl, 2022-11). Land-atmosphere CH_4 and N_2O fluxes were calculated with the linear regression model provided in "chamberflux" after consideration of its limitations in comparison to the other provided regression models.

The linear gas flux formula and gas flux absolute error are given in EQ1 and EQ2. Input data for the calculations comprised of the first 4 minutes of each flux chamber measurement. The dry fraction for the gases was used and a fixed, assumed, air pressure of 101.3 kPa. This assumed air pressure was used as other air pressure data availability was limited at the study sites for the considered time frame. The headspace volume depended on the combination of chamber version used and extensions. The volume was corrected for the high variability in soil surface elevation at the PZ BM (chapter 2.4.3). The calculated fluxes were converted to mg m^{-2} h^{-1} for further analyses.

Flux errors (EQ2) were calculated based on the in-house flux chamber design of Working Group Soils in the Climate System, Institute of Soil Science, University Hamburg. The error variables used were: air pressure error (err_p) of 0.15 kPa, headspace volume (err_V) of 0.00721 m^3, surface area (err_A) of 0.0012 m^2 and air temperature (err_T) of 0.1 K. The error variables err_V and err_A are based on the assumed uncertainty in determining flux chamber and collar sizes of 0.001 m. The calculated flux errors were also converted to mg m^{-2} h^{-1}.

EQ1 $$flux_{lin} = (p_{air} * V_{chamber} * M_{gas}) / (R * T_{air_in} * A_{collar}) * slope_{lin}$$

$flux_{lin}$	linear GHG land-atmosphere flux (µg m^{-2} s^{-1})
P_{air}	air pressure in the headspace (kPa)
$V_{chamber}$	headspace volume (m^3)
M_{gas}	molar mass of the gas of interest (g mol^{-1})
R	ideal gas constant (8.31447 J K^{-1} $µmol^{-1}$)
T_{air}	air temperature inside the flux chamber (K)
A_{collar}	surface area over which the flux is calculated (m^2)
$slope_{lin}$	coefficient from the linear regression model representing the concentration change δC/δt

EQ2 $$flux_{lin_abs_err} = \sqrt{((M_{gas}^2 * R^2) * (V_{chamber} * slope_{lin}^{-1} * T_{air_in}^{-1})^2 * err_p^2 + (p_{air} * slope_{lin} * A_{collar}^{-1} * T_{air_in}^{-1})^2 * err_V^2 - (p_{air} * V_{chamber} * slope_{lin} * A_{collar}^{-2} * T_{air_in}^{-1})^2 * err_A^2 - (p_{air} * V_{chamber} * slope_{lin} * A_{collar}^{-1} * T_{air_in}^{-2})^2 * err_T^2 + (p_{air} * V_{chamber} * A_{collar}^{-1} * T_{air_in}^{-1})^2 * se_{lin}^2))}$$

P_{air}	air pressure in the headspace (kPa)
$V_{chamber}$	headspace volume (m^3)
M_{gas}	molar mass of the gas of interest (g mol^{-1})
R	ideal gas constant (8.31447 J K^{-1} $µmol^{-1}$)
T_{air}	air temperature inside the flux chamber (K)
A_{collar}	surface area over which the flux is calculated (m^2)

$slope_{lin}$ coefficient from the linear regression model representing the concentration change δC/δt
err_p (0.15 kPa), err_V (0.00721 m^3), err_A (0.0012 m^2), err_T (0.1 K) assumed random errors for the respective variables

2.4.3 Greenhouse gas flux data analyses

Quality levels for calculated greenhouse gas land-atmosphere fluxes

The calculated land-atmosphere fluxes received a quality level (QL1 to QL4) based on calculation model and measurement performance. First, root mean square errors (RMSE) were plotted as boxplots per gas type and salinity zone. The boxplots' fourth quantile was selected as a quality level threshold, leading to the following thresholds: a) FM $RMSE_{CH4}$ > 261.0 ppb, $RMSE_{CO2}$ > 1.1 ppm, $RMSE_{N2O}$ > 0.4 ppb, b) BM $RMSE_{CH4}$ > 12.1 ppb, $RMSE_{CO2}$ > 4.3 ppm, $RMSE_{N2O}$ > 0.4 ppb and c) SM $RMSE_{CH4}$ > 0.4 ppb, $RMSE_{CO2}$ > 3.5 ppm, $RMSE_{N2O}$ > 0.3 ppb. Calculated fluxes below the thresholds were labelled with preliminary quality level 1 and fluxes above the threshold with preliminary quality level 2.

The second step involved studying each negative CH_4 and N_2O flux individually. The decrease in GHG concentration was compared to the ambient concentration and starting headspace concentration. This assessment step was required as some flux measurements showed a large initial jump in gas concentration upon chamber placement, followed by a negative slope in the plotted headspace gas concentration. When the concentrations dropped below ambient gas concentrations, the flux was considered a true uptake flux. In the other cases, it could not be determined if the negative flux reflected natural uptake. One case is shown in the appendices as example (appendix H, figure 29). The linear flux calculated for this measurement case was -2.30 (± 0.06) µg CH_4 m^{-2} s^{-1}, with R^2 of 0.98, RMSE of 75.22, however the regression model intercept was 8397.7 ppb compared to the ambient concentration of about 2100 ppb. When a negative calculated flux had such an initial jump and it would not reach or drop below ambient concentrations during the four-minute interval, it received a quality level QL3.

The final consideration were the field notes. When the notes indicated something occurred that did not meet the protocol, the calculated flux would receive a +1 onto its preliminary quality level. A few examples are malfunctioning of the fans during the measurement, shading of the flux chamber by standing to near and insects flying over landing on the sensors or damages to vegetation during chamber placement. These events could affect the performance of the methodology.

Table 6 shows an overview of flux observations per quality level. Only QL1 and QL2 labelled measurements were used in the statistical analyses of this study, as QL3 and QL4 were associated with elevated uncertainty. The 79 QL3 and QL4 fluxes comprised of 15 % of the observations from SM plots, 20 % of the observations from BM plots and 10 % of observations from FM plots. A summary of the four QL groups, with their mean RMSEs and mean CH_4 and N_2O land-atmosphere fluxes are given in the appendix I, tables 25 to 28. The change of RMSE with land-atmosphere flux magnitudes are visualized in appendix I, figure 30.

Table 6 Number of flux observations in each quality level class

salinity zone	QL1	QL2	QL3	QL4	Total
FM	n = 62	n = 21	n = 6	n = 3	n = 92
BM	n = 43	n = 22	n = 14	n = 2	n = 81
SM	n = 181	n = 129	n = 50	n = 4	n = 364

Statistical analyses of greenhouse gas land-atmosphere flux data

The calculated hourly CH_4 and N_2O land-atmosphere fluxes, labelled QL1 or QL2, were plotted in boxplots to visualize their spread and identify extreme outliers. A flux observation was considered an extreme outlier when it was 3 times smaller than the first or 3 times larger than the third interquartile. The CH_4 and N_2O flux data was tested for Gaussian distributions with the Shapiro-Wilk test at different grouping levels: fluxes per flux replicate plot, per tidal wetland zone and as averages over time per tidal wetland zone. Additionally, the CH_4 and N_2O flux datasets were split up into the meteorological seasons with spring covering measurements from April, May and June, summer measurements from June, July and August, autumn measurements from September, October, and November and winter measurements from December, January and February. Data distributions were also tested for all observations grouped per tidal wetland zone and aggregated as averaged hourly flux per flux replicate plot per tidal wetland zone for each meteorological season. Generally, the CH_4 and N_2O flux data did not show a Gaussian distribution, although there were a few exceptions (appendix R, tables 35 to 38). Therefore, the statistical testing has been conducted with non-parametric tests. Differences in land-atmosphere flux magnitudes between replicate flux plots were assessed with Kruskal-Wallis tests followed by pairwise Wilcoxon with Bonferroni ($p_{bonferroni}$) and Benjamini-Hochberg method (p_{BH}) p value adjustments.

The average land-atmosphere fluxes were compared with Kruskal-Wallis and pairwise Wilcoxon tests to study difference between three PZs and among the four flooding frequency zones within SM per season and over the total 16 months of chamber measurements. The land-atmosphere flux magnitudes were compared over time at the tidal wetland zones separately with Friedman tests followed by post hoc testing through pairwise Wilcoxon and Sign tests. The post hoc tests p values were adjusted with Bonferroni method ($p_{bonferroni}$) and Benjamini-Hochberg method (p_{BH}). Not all measurement days covered complete observations of the five replicate plots as result of the quality filtering. The measurement dates included in the Friedman tests are reported in appendix K, table 29.

The measured environmental conditions (VWC, EC, T_{soil}, T_{air_in}, PAR_{in} and RI) were tested for correlations with hourly land-atmosphere fluxes of CH_4 and N_2O using Spearman's rank correlations. The complete datasets were used to test for correlations among the three gases, CO_2, CH_4 and N_2O. Chamber design based subsets of flux observations were used to test for correlations between CH_4 or N_2O and T_{air_in} and PAR_{in}, due to missing data for these environmental variables in the first measurement year. The observations retrieved with the TEROS-12 probes were tested for correlations with CH_4 and N_2O land-atmosphere fluxes per tidal wetland zone separately due to the large effect of the soil salt content on the output of the sensors. Finally, the RI results from the IRIS-sticks were tested for correlations with the CH_4 and N_2O land-atmosphere fluxes with regard to complete set

of datapoints and with regard to the separate meteorological seasons. The correlation coefficients were evaluated as being weak when Spearman's rho ($\rho_{spearman}$) < 0.4, moderate when $\rho_{spearman}$ = 0.4 to 0.7, strong when $\rho_{spearman}$ = 0.7 to 0.9 and perfect $\rho_{spearman}$ > 0.9.

The statistical tests were performed in R (R Core Team, 2020) through RStudio (RStudio Team, 2021 version 1.4.1103) with the following packages: Shapiro-Wilk tests, Friedman tests and Sign test with "rstatix" (Kassambara, 2021), Kruskal-Wallis tests, pairwise Wilcoxon, Spearman's rank correlations with "stats" (R Core Team, 2020). CH_4 and N_2O land-atmosphere flux boxplots were constructed with "ggplot2" (Wickham, 2016), "viridisLite" (Garnier et al., 2021) and "ggpubr" (Kassambara, 2020). The correlation plots were constructed with "corrplot" (Wei & Simko, 2021).

Greenhouse gas flux uncertainty and sensitivity analyses

The discussion of land-atmosphere GHG fluxes in tidal wetlands is supported by reviewing the uncertainty in the quantification of land-atmosphere fluxes and corresponding errors (EQ1, EQ2). Sensitivity analyses of the flux calculation were conducted to test the effects of changes to the flux chamber headspace volume on the quantified flux. The contribution of soil surface unevenness and vegetation standing stock to the headspace volume are assessed and the calculations to obtain these volumes are described in the following sections. Additional sensitivity analysis was performed to test the effect of the input temperature. The headspace air temperature as four-minute average (T_{air_in}) was switched for the initial temperature ($T_{initial}$) in this analysis. $T_{initial}$ was calculated as mean temperature of the first 6 seconds of a flux measurement. The combined effect of changes in these two variables to the calculated gas flux magnitudes was tested in a third sensitivity analysis of EQ1. All three sensitivity analyses were done with chamber flux data measured in June and July 2023 at FM PZ, BM PZ and SM HMu.

The uncertainty in the quantification was also assessed for headspace volume, temperature and surface area. The headspace volume quantification uncertainty was propagated from the quantification of construction dimensions, soil surface to collar rim volume and vegetation standing stock volume. Additionally, it was considered how wind gusts affected the volume of Chamber1. The surface area quantification uncertainty was addressed by assessing the quantification of collar dimensions. Additionally, it was considered how deformation of the collar affected the surface area. These topics will be further explained in the following sections. Finally, the propagated uncertainties and thermometer sensor precision (± 0.2 °C at 20 °C) were compared to the applied error variables of EQ2.

Flux chamber headspace volume

The uncertainty in flux chamber headspace is based on the estimated random error (u_{dim}) of 0.001 m when measuring the construction dimensions with a ruler. A propagated uncertainty (e_{Vdim}, EQ3) was calculated for each specific chamber construction (Chamber1 and Chamber2), as well as for construction combinations with the extensions.

EQ3 $e_{Vdim} = \sqrt{(\sqrt{((u_{dim} / l_{body})^2 + (u_{dim} / w_{body})^2 + (u_{dim} / h_{body})^2) * (l_{body} * w_{body} * h_{body}))^2 + \sqrt{((u_{dim} / l_{top})^2 + (u_{dim} / w_{top})^2 + (u_{dim} / h_{top})^2) * (l_{top} * w_{top} * h_{top}))^2 + \sqrt{((u_{dim} / l_{bottom})^2 + (u_{dim} / w_{bottom})^2 + (u_{dim} / h_{bottom})^2) * (l_{bottom} * w_{bottom} * h_{bottom}))^2)}$

u_{dim} represents the uncertainty in flux chamber dimensions of 0.001 m (Eckhardt & Kutzbach, 2016)
l_{body}, l_{top}, l_{bottom} represent length dimension of chamber body, chamber top and chamber bottom
w_{body}, w_{top}, w_{bottom} represent width dimension of chamber body, chamber top and chamber bottom
h_{body}, h_{top}, h_{bottom} represent height dimension of chamber body, chamber top and chamber bottom
(appendices C, D, E tables 21, 22, 23)

Soil surface to collar rim volume

Soil surface elevation was measured in comparison to the collar rim to determine the headspace volume gained or lost from the flux chamber by the unevenness of the soil surface. The headspace volumes of the FM PZ flux chamber measurements were not further addressed in this section, as the soil surface unevenness was small and due to permanent ponding in the lows negligible. The soils in the collars at the PZ BM were surveyed through a 16-reference-points grid pattern. The height of the soil surface to collar rim was measured with a ruler up to the millimeter at each of the reference points. These 16 reference points were used to calculate the headspace volume above nine subsections according to EQ4. EQ5 describes how the headspace volume was corrected for the surface elevation unevenness (V_{sse}). V_{sse_BM} was determined for each flux replicate plot and each flux measurement campaign and combined with information on ponding in the collar to correct the headspace volume used in EQ1.

EQ4 $V_{subsectioncollar}1 = h1 * h2 * h3 * h4 / 4 * L_{collarX} * L_{collarY}$

h1, h2, h3, h4 etc. height in millimeters of reference point 1, 2, 3, 4, and forth
$L_{collarX/Y}$ length of collar subsection in X or Y direction, 300 mm or 200 mm

EQ5 $V_{sse_BM} = V_{subsectioncollar}1 * P + V_{subsectioncollar}2 * P + V_{subsectioncollar}3 * P + V_{subsectioncollar}4 * P + V_{subsectioncollar}5 * P + V_{subsectioncollar}6 * P + V_{subsectioncollar}7 * P + V_{subsectioncollar}8 * P + V_{subsectioncollar}9 * P$

$V_{subsectioncollar}1$ is volume above respective subsections (1 to 9)
P presence of ponding above subsection for respective measurement, 0 for not present, 1 for present

Additionally, a standard error (σ_{sse_BM}) was calculated for the volume change based on the 9 subsection volumes. This error was added to the error e_{Vdim} for measurements taken at PZ BM according to EQ6.

EQ6 $e_{Vdim_sse_BM} = \sqrt{(\sqrt{((u_{dim} / l_{body})^2 + (u_{dim} / w_{body})^2 + (u_{dim} / h_{body})^2) * (l_{body} * w_{body} * h_{body}))^2 + \sqrt{((u_{dim} / l_{top})^2 + (u_{dim} / w_{top})^2 + (u_{dim} / h_{top})^2) * (l_{top} * w_{top} * h_{top}))^2 + \sqrt{((u_{dim} / l_{bottom})^2 + (u_{dim} / w_{bottom})^2 + (u_{dim} / h_{bottom})^2) * (l_{bottom} * w_{bottom} * h_{bottom}))^2 + \sigma_{sse_BM}^2)}$

U_{dim} represents the uncertainty in flux chamber dimensions of 0.001 m (Eckhardt & Kutzbach, 2016)
l_{body}, l_{top}, l_{bottom} represent length dimension of chamber body, chamber top and chamber bottom
w_{body}, w_{top}, w_{bottom} represent width dimension of chamber body, chamber top and chamber bottom
h_{body}, h_{top}, h_{bottom} represent height dimension of chamber body, chamber top and chamber bottom

A similar survey was conducted at the salt marsh tidal wetland zones. However, there the survey was done to a lesser spatial extent because of limited resources and the much smaller relief within the collars. Four reference points were surveyed by measuring the heights of soil surface to collar rim with a ruler, similarly to BM PZ (EQ4). Mean height (μ_{sse_SM}) of the four reference points was included in the height dimension (h) of the flux chamber per flux replicate plot and tidal wetland zone separately (EQ7). The standard error (σ_{sse_SM}) was included in $e_{Vdim_sse_SM}$ as the extra uncertainty in the flux chamber height dimension (EQ7). The headspace volumes were not corrected for the gain or loss from soil surface unevenness in the land-atmosphere flux calculations (EQ1) as the unevenness was considered small. The effect of not correcting the headspace volume was tested in the sensitivity analyses.

EQ7 $e_{Vdim_sse_SM} = \sqrt{(\sqrt{((u_{dim} / l_{body})^2 + (u_{dim} / w_{body})^2 + ((u_{dim} + \sigma_{sse_SM}) / (h_{body} + \mu_{sse_SM})^2) * (l_{body} * w_{body} * (h_{body} + \mu_{sse_SM})))^2 + \sqrt{((u_{dim} / l_{top})^2 + (u_{dim} / w_{top})^2 + (u_{dim} / h_{top})^2) * (l_{top} * w_{top} * h_{top}))^2 + \sqrt{((u_{dim} / l_{bottom})^2 + (u_{dim} / w_{bottom})^2 + (u_{dim} / h_{bottom})^2) * (l_{bottom} * w_{bottom} * h_{bottom}))^2)}$

U_{dim} represents the uncertainty in flux chamber dimensions of 0.001 m (Eckhardt & Kutzbach, 2016)
σ_{sse_SM} standard error of soil surface to collar height from four reference height points
μ_{sse_SM} mean soil surface to collar height calculated from four reference height points
l_{body}, l_{top}, l_{bottom} represent length dimension of chamber body, chamber top and chamber bottom
w_{body}, w_{top}, w_{bottom} represent width dimension of chamber body, chamber top and chamber bottom
h_{body}, h_{top}, h_{bottom} represent height dimension of chamber body, chamber top and chamber bottom

Vegetation standing stock volume

The above ground vegetation volume was estimated to assess the effect of ignoring vegetation standing stock volume in headspace on calculated flux magnitude. The volume

estimation is based on the above ground biomass information retrieved with the earlier mentioned RTG vegetation surveys combined with flux replicate plot specific information collected during each measurement campaign and vegetation properties from literature. The collected information was too limited to make a well supported approximation for the vegetation standings stock volume at SM PZ, SM LM and SM HMg. Therefore, it was only calculated for the SM HMu tidal wetland zone.

First, the collected biomass data (BM_{AG_SUB}) from the two sampling plots of 20 by 20 cm ($A_{subplot}$) was scaled to the flux plot size (A_{collar}) to find the total above ground biomass (BM_{AG}, EQ8).

EQ8 $BM_{AG} = \mu(BM_{AG_SUB}) * A_{collar} / (A_{subplot})$

with $A_{collar} = 0.632\ m^2$ and $A_{subplot}\ 0.04\ m^2$

BM_{AG} above ground biomass on flux measurement plot in grams
BM_{AG_SUB} biomass survey data from subplots in grams
A_{collar} surface area collar
$A_{subplot}$ surface area subplot

The vegetation biomass in dry weight was then translated into vegetation volume using properties reported by Rozema and colleagues (1997), Schulze and colleagues (2019) and Schulte Ostermann and colleagues (2021).

The plot specific vegetation volume at FM PZ was calculated according to equation EQ9 for the dominant species *Typha angustifolia* (i1), with counted number of individuals (n_{i1}), average leave area ($A_{leave} = 497.48\ cm^2$)^A and its standard deviation ($sd_{leave} = 90.68\ cm^2$)^A, above ground biomass per individual (BM_{AG_i1}, 38.56 ± 13.22 g)^A, stem mass per volume (M_{stem_V}, $0.79 \pm 0.04\ g\ cm^{-3}$)^A and an assumed leave width of 0.05 cm. Both a minimum and a maximum vegetation volume were calculated by addition and subtraction of the standard deviations as described in EQ9.

EQ9 $V_{veg_FM1} = n_{i1} * (A_{leave1} \pm sd_{Aleave1}) * 0.05 + (n_i * (BM_{AG_i1} \pm sd_{BMAGi1})) / (M_{stem_V1} \pm sd_{Mstem_V1})$

V_{veg_FM1} *Typha angustifolia* above ground volume
n_{i1} number of *Typha angustifolia* individuals
$A_{leave} \pm sd_{leave}$ average and standard deviation leave area ($497.48 \pm 90.68\ cm^2$)^A
BM_{AG_i1} above ground biomass per individual (38.56 ± 13.22 g)^A
M_{stem_V} stem mass per volume ($0.79 \pm 0.04\ g\ cm^{-3}$)^A
^{A} (Schulte Ostermann et al., 2021)

The plant community at FM PZ flux plots comprised also of *Caltha palustric*. The volume of *Caltha palustric* (i2) was estimated based on number of individuals per plot (n_{i2}) derived from plot total BM_{AG}, $BMAG_{i1,}$ the ratio of *Thypha angustifolia (i1)* to other species at each plot ($ratio_{i1:o}$) and as approximation the averaged above ground biomass of the species *Lythrum salicaria*; *Cirsium arvense*; *Myostis scorpioides* (μBM_{AG_o})^A as described in EQ10. Minimum and maximum volumes were calculated according to EQ11 and EQ12, using A_{leave_o} of $848.46 \pm 370.29\ cm^{2A}$ and $M_{stem_V_o}$ of $1.03 \pm 0.05\ g\ cm^{-3A}$.

EQ10 $n_{i2} = (BM_{AG} – (BM_{AGi1} * ratio_{i1:o})) / \mu BM_{AG_o}$

with $BM_{AG_o} = BM_{AG} – (BM_{AGi2} * ratio_{i1:o})$

n_{i2} number of *Caltha palustric* individuals
$ratio_{i1:o}$ ratio of *Thypha angustifolia* to other species (*Lythrum salicaria*; *Cirsium arvense*; *Myostis scorpioides*)
μBM_{AG_o} literature derived averaged individuals' above ground biomass (*Lythrum salicaria*; *Cirsium arvense*; *Myostis scorpioides*)

EQ11 $V_{veg_FM2} = n_{i2} * (A_{leave_o} \pm sd_{Aleave_o}) * 0.05 + BM_{AG_o} / (M_{stem_V_o} \pm sd_{Mstem_V_o})$

V_{veg_FM2} *Caltha palustric* above ground volume
A_{leave_o} leave area (848.46 ± 370.29 cm^2)[A]
$M_{stem_V_o}$ stem mass per volume (1.03 ± 0.05 g cm^{-3})[A]

EQ12 $V_{veg_FM} = V_{veg_FM1} + V_{veg_FM2}$

V_{veg_FM} final vegetation volume at FM PZ flux replicate plot
[A] (Schulte Ostermann et al., 2021)

Vegetation volume at BM PZ was calculated in a similar manner using properties of the sole specie present at the plots: *Bolboschoenus maritimus* (EQ13, EQ14). The volume was calculated using plot specific above ground biomass (BM_{AG}), literature-based individual BM_{AG_i3} of 6.70 ± 2.03 g[A], total A_{leave} of 144.92 ± 48.72 cm^{2A} and M_{stem_V} of 0.81 ± 0.07 g cm^{-3A} and in this case also the plots above ground fresh weight (BM_{Fresh}).

EQ13 $n_{i3} = BM_{AG} / (BM_{AG_i3} \pm sd_{BMAG_i3})$

n_{i3} number of *Bolboschoenus maritimus* individuals
BM_{AG} above ground biomass on flux measurement plot in grams
$BM_{AG_i3} \pm sd_{BMAG_i3}$ above ground biomass with standard deviation per *Bolbuschoenus maritimus* individual (6.70 ± 2.03 g)[A]

EQ14 $V_{veg_BM} = n_{i3} * (A_{leave} \pm sd_{leave}) * 0.05 + (BM_{Fresh} / (M_{stem_V} \pm sd_{Mstem_V})$

V_{veg_BM} final vegetation volume at BM PZ flux replicate plot
n_{i3} number of *Bolboschoenus maritimus* individuals
A_{leave} (± sd_{leave}) mean leave area (144.92 cm^2) and standard deviation leave area (± 48.72 cm^2)[A]
BM_{Fresh} plot specific above ground biomass in grams fresh weight
$M_{stem_}V$ (± sdM_{stem_V}) mean stem mass per volume (0.81 g cm^{-3}) with standard deviation stem mass volume (± 0.07 g cm^{-3})[A]
[A] (Schulte Ostermann et al., 2021)

Vegetation standing stock volume at SM HMu followed two separate approaches to find minimum, maximum and mean vegetation volume of dominant species *Elymus athericus* (i4). First, the number of individuals (n_{i4A} and n_{i4B}) per plot were determined according to equation (EQ15) and (EQ16), using $BM_{AG_i4_literature}$ of 1.35 g[B], $n_{i4_literature}$[B] of 883 individuals per m^2 from literature and plot specific biomass BM_{AGi4} and ratio *Elymus athericus* to bare soil (cov_{i4}). Next, the minimum and maximum volumes (V_{veg_SM1} and V_{veg_SM2}) were calculated using a radius ($r_{i4_literature}$) of 0.11 cm[B], a stem length ($l_{i4_literature}$) of 79 cm[B], a leave area ratio ($A_{leave:BM_i4_literature}$) of 8.2 * 10^4 cm^2 kg^{-1} [C], a leave to weight mass ratio

($M_{leave:BM_i4_literature}$) of 0.34[C], specific leaf area ($SLA_{i4_literature}$) of 23.8 * 10^4 cm^2 kg^{-1} [C] from literature and assumed leave width of 0.05 cm as described in EQ17 and EQ18.

EQ15 $n_{i4A} = BM_{AGi4} / BM_{AGi4_literature}$

EQ16 $n_{i4B} = n_{i4_literature} * (A_{collar} * cov_{i4})$

n_{i4} number *Elymus athericus* individuals calculated with approach A (EQ14) or B (EQ15)
BM_{AGi4} flux replicate plot total above ground biomass
$BM_{AGi4_literature}$ above ground biomass of *Elymus athericus* individual (1.35 g)[B]
$n_{i4_literature}$ number of individuals per m^2 (883 m^{-2})[B]
A_{collar} surface area collar (0.632 m^2)
cov_{i4} ratio *Elymus athericus* to bare soil coverage at flux replicate plot

EQ17 $V_{veg_SM1} = n_{i4A} * \pi * r_{i4_literature}^2 * l_{i4_literature} + (BM_{AGi4} * A_{leave:BM_i4_literature}) * SLA_{i4_literature} * 0.05$

$r_{i4_literature}$ *Elymus athericus* stem radius (0.11 cm)[B]
$l_{i4_literature}$ *Elymus athericus* stem length (0.79 cm)[B]
$A_{leave:BM_i4_literature}$ *Elymus athericus* leave area ratio (8.2 * 10^4 cm^2 kg^{-1})[C]
$SLA_{i4_literature}$ *Elymus athericus* specific leave area (23.8 * 10^4 cm^2 kg^{-1})[C]

EQ18 $V_{veg_SM2} = n_{i5B} * \pi * r_{i4_literature}^2 * l_{i4_literature} + (BM_{AGi4} * M_{leave:BM_i4_literature}) * SLA_{i4_literature} * 0.05$

$r_{i4_literature}$ *Elymus athericus* stem radius (0.11 cm)[B]
$l_{i4_literature}$ *Elymus athericus* stem length (0.79 cm)[B]
$M_{leave:BM_i4_literature}$ *Elymus athericus* leave to weight mass ratio (0.34)[C]
$SLA_{i4_literature}$ *Elymus athericus* specific leave area (23.8 * 10^4 cm^2 kg^{-1})[C]
[B] (D. Schulze, Rupprecht, Nolte, & Jensen, 2019)
[C] (Rozema et al., 1997)

The difference between the earlier described maximum and minimum vegetation volume estimates were used as a third headspace volume quantification uncertainty and used in a final propagated uncertainty for headspace volume as described by EQ19, EQ20 and EQ21.

EQ19 $e_{V_total_FM} = \sqrt{(e_{VdimFM}^2 + e_{VvegFM}^2)}$

EQ20 $e_{V_total_BM} = \sqrt{(e_{VdimBM}^2 + e_{VessBM}^2 + e_{VvegBM}^2)}$

EQ21 $e_{V_total_SM} = \sqrt{(e_{VdimSM}^2 + e_{VessSM}^2 + e_{VvegSM}^2)}$

Headspace volume affected by windgusts

The effect of wind gusts was estimated for Chamber1 headspace volume uncertainty with EQ22 (e_{V_wind}). The maximum possible headspace volume change was approximated by assuming an inward movement of the chamber wall at the wind facing side of 3 cm and no outward counter movement from the other four chamber walls. The wind-facing chamber wall was assumed to reshape from a plane to a dome, with height (h_D) of 3 cm at its central

point. The base area of the dome (a) was corrected for the curve of the sheet in the calculation (EQ22).

EQ22 $e_{V_wind} = 1/6 * \pi * h_D (3 * a + h_D^2)$

with $a = (0.802 – 0.03 / 2) * (0.827 – 0.03 / 2)$

h_D height of the domeshaped concaving sheet
a base area of the domeshaped concaving sheet (m^2)

Surface area

A propagated uncertainty was calculated for surface area (e_{Adim}) based on the quantification of its dimensions according to EQ23.

EQ23 $e_{Adim} = \sqrt{(\sqrt{((u_{dim} / l_1)^2 + (u_{dim} / l_2)^2) * (l_1 * l_2)})^2}$

u_{dim} represents the uncertainty in flux chamber dimensions of 0.001 m (Eckhardt & Kutzbach, 2016)
l_1, l_2 represent collar length dimension of the two directions L_1 and L_2 (appendices B table 20)

Additionally, the collar square shape was assessed after installation. Collars located in PZ BM and the four SM zones showed deformation after installation. A maximum deformation margin (D) was measured of 1.6 cm for one PVC-U plate. The resulting change in collar dimensions (L_D) was calculated with Pythagoras theorem (EQ24). The gain or loss in surface area due to the maximum potential deformation ($A_{collarD}$) was calculated according to EQ25. The deformed collar surface area ($A_{collarD}$) was considered as increased uncertainty in the surface area error variable in EQ2 ($e_{s_Adim_def}$, EQ25) and compared to the applied error variable in EQ2. An example case of a deformed collar with the different variables is given in appendix J, figure 31.

EQ24 $L_D = L_{collar} – 2 * B$

following $A^2 + B^2 = C^2$

with $C = ½ L_{collar} = 0.3975$ m and $A = D = 0.016$ m

EQ25 $e_{S_Adim_def} = \sqrt{(A_{collarD} * \sqrt{((D/L_{collar})^2 * 2)^2 + A_D}}$

with $A_D = ½ * \pi * 2L_D * D$ and $A_{collarD} = L_A * L_A \pm A_D$

$e_{S_Adim_def}$ error in surface area resulting from collar dimensions and collar deformation
$A_{collarD}$ surface area of deformed collar
D deformation margin (1.6 cm)
L_{collar} length of PVC-U plate
A_D surface area between original position PVC-U plate and deformed PVC-U plate

Chapter 3 Results

3.1 Characteristics of tidal wetland soils in the Elbe estuary

Two Reference Soil Groups were identified within the tidal marshes of the Elbe estuary, Gleysols and Solonchaks (table 7, appendix L). The main principal qualifiers assigned to each tidal wetland soil are summarized in table 7 and the full soil names can be found in appendix L. All soils showed to some extent diagnostics associated with ground water dynamics (gleyic), but the SM HMu soil was dominantly characterized by the large amount of available soluble salts (table 7, appendices L and M).

Table 7 Reference Soil Group and principal qualifiers per tidal wetland zone. "X" indicates that the criteria of the principal qualifier was met. "proto" indicates protosalic, suggesting elevated soluble salt content but not meeting all criteria to qualify as salic. "someri" indicates somerimollic suggesting a top soil with elevated organic carbon content, high base saturation and developed aggregates but not meeting all criteria to qualify as mollic. "ferric" indicating accumulation of Fe oxides from redox processes, but not having enough concretions or concretions were not cemented enough to be classify as pisoplinthic.

tidal wetland zone		RSG	gleyic	salic	stagnic	mollic	fluvic	reductic	tidalic	reducti-gleyic	piso-plinthic
FM	PZ	Gleysol	X		X		X	X	X	X	
	LM	Gleysol	X		X	X	X	X		X	
	HMu	Gleysol	X		X	someri	X				ferric
BM	PZ	Gleysol	X				X	X	X	X	
	LM	Gleysol	X	proto	X		X	X			ferric
	HMu	Gleysol	X		X	X	X	X			ferric
SM	PZ	Gleysol	X	X	X	X	X	X	X	X	
	LM	Gleysol	X	proto	X		X				X
	HMu	Solonchak	X	X	X		X				ferric

Generally, the readily available soluble salts in the soils decreased from the estuary mouth stream upwards (appendix M, table 30). The EC_{se} were 1.0 dS m^{-1}, 2.2 dS m^{-1}, 2.1 dS m^{-1} at FM PZ, FM LM and FM HMu, 3.0 dS m^{-1}, 4.9 dS m^{-1}, 1.6 dS m^{-1} at BM PZ, BM LM and BM HMu and 21.7 dS m^{-1}, 9.9 dS m^{-1}, 17.3 dS m^{-1} at SM PZ, SM LM and SM HMu, respectively, expressed as averages of the top 60 cm soil. The relatively high EC_{se} observed in the BM LM soil resulted mainly from a high EC_{se} (8.0 dS m^{-1}) in the Ahr (19 to 24 cm) horizon and ranged between 3.7 dS m^{-1} and 8.0 dS m^{-1} in the top 60 cm of the soil. The relatively lower EC_{se} at SM LM was mainly driven by its two upper horizons, Ah (0 – 2 cm) and Cr (2 – 31 cm) with 4.9 dS m^{-1} and 7.6 dS m^{-1} and ranged between 4.9 dS m^{-1} and 12.6 dS m^{-1} in the top 60 cm of the soil.

All soils consisted of fluvic materials and showed the associated characteristic layering with different soil textures. Buried horizons were present at all three salinity zones, according to diagnostic criteria for panpaic horizons (chapter 3.1.23, WRB 2022). Soil bulk density was lowest in the FM PZ (0.5 g cm^{-3}) soil, where the soil was clay dominated (42.9

% w/w) and had the highest organic carbon content (4.5 % w/w) of all nine tidal wetland soils. The highest soil bulk density was observed for the BM PZ soil (1.4 g cm^{-3}), being sand dominated (57.9 % w/w) and having the lowest organic carbon content (0.5 % w/w) among the studied soils (appendix M, table 30). Information on bulk density and organic carbon was lacking for the BM LM soil due to high amounts of rhizomes in the soil samples obstructing the analysis.

Soil structures did not suggest differences between the salinity zones, but showed clear differences between the three flooding zones. The high marsh soils showed more pronounced soil structures and had larger aggregates compared to the lower elevations (appendix M, table 30). Soil structures showed to be more developed in the more intensively rooted soil layers in the FM PZ and SM PZ soils (appendix M, table 30). Whereas, in the older and higher elevated soils this contrast was not clearly visible based on the performed descriptions. The roots reached till a depth of at least 50 cm in all soils (appendix M, table 30). Extensive layers of rhizomes were present in the soils of the FM and BM sites (appendix M, table 30).

A two-dimensional PC representation explained 56 % (PC1: 36.7 % and PC2: 19.6 %) of the variability present in the tidal wetland soils physicochemical dataset. The following PC's, number 3 to 25, explained individually no more than 8.7 % of the variation (appendix N, figure 32). The PCA-biplot (figure 3) shows a clear separation between the three tidal wetland zones as can be seen from the depicted site averages (large points) and ellipses. The most important variables in dimensions 1 and 2 are reported in table 8, these had the highest contribution (%) to and were best depicted (cos2) on the PCs, suggesting that these best explained the variation within the dataset.

Table 8 Main variables for the construction of PC1 and PC2 and their representation (cos2) reflecting the representation on PC1 and PC2 ranging from 0 to 1, with 1 a perfect representation. The variables contribution reflects how much of the variability in PC1 and PC2 is account for by the respective variable.

variable	representation (cos2)	contribution (%)
C_{tot}	0.94	6.7
N_{tot}	0.93	6.6
C_{org}	0.91	6.5
CEC	0.90	6.4
EC_{ms}	0.86	6.1
K^+ Ca-Lactate	0.81	5.8
Sand	0.79	5.6
Clay	0.78	5.6

PC1 is mainly driven by the variables C_{tot}, N_{tot}, C_{org}, CEC and clay content, which all had negative coordinates of < - 0.85 and by sand content with a positive coordinate of > 0.85. Therefore, all soil horizons projected on the left side of the PCA plot origin are characterized by relatively high levels of C_{tot}, N_{tot}, C_{org}, CEC and clay and low levels of sand (figure 3). These are horizons of the FM PZ, the FM LM and FM HMu top soils, the BM LM Ahl2 horizon, SM top soils as well as SM HMu Bl2 (appendix M, table 30) The horizons of BM soils are depicted on the right side of the PCA plot, and thus characterized by relatively high

sand contents and low clay contents, low CEC, low C and N levels (figure 3). Other relative sandy horizons were those of FM LM soil between 18 and 48 cm depth, horizons of FM HMu below 30 cm depth and the Cr horizon of SM HMu (appendix M, table 30).

PC2 is mainly contrasted by EC (both EC_{ms} and EC_{se}), pH_{CaCl2} and Cl^-, which all had positive coordinates of > 0.75. Therefore, soil horizons projected on the upper half of the PCA plot are characterized by higher than the average level of these variables. This shows to be the case for the salt marsh soils (figure 3).

The PCA results suggest strong positive correlations among the variables EC_{ms}, pH_{CaCl2}, Cl^- and between TIC and Ca-lactate extracted K^+ (K_{calac}), as well as among CEC, C_{org} and N_{tot}. Pearson correlations support these observations, but showed that the strongest correlations for these individual variables are: EC_{ms} with Cl^- ($\rho = 0.94$), pH_{CaCl2} with EC_{ms} ($\rho_{pearson} = 0.71$), TIC with pH_{CaCl2} ($\rho_{pearson} = 0.70$), K_{calac} with Cl^- ($\rho_{pearson} = 0.88$), CEC with N_{tot} ($\rho_{pearson} = 0.95$), N_{tot} with C_{org} ($\rho_{pearson} = 0.99$) and C_{org} with C_{tot} ($\rho_{pearson} = 0.99$). All correlations are summarized in a correlation plot in appendix O, figure 33.

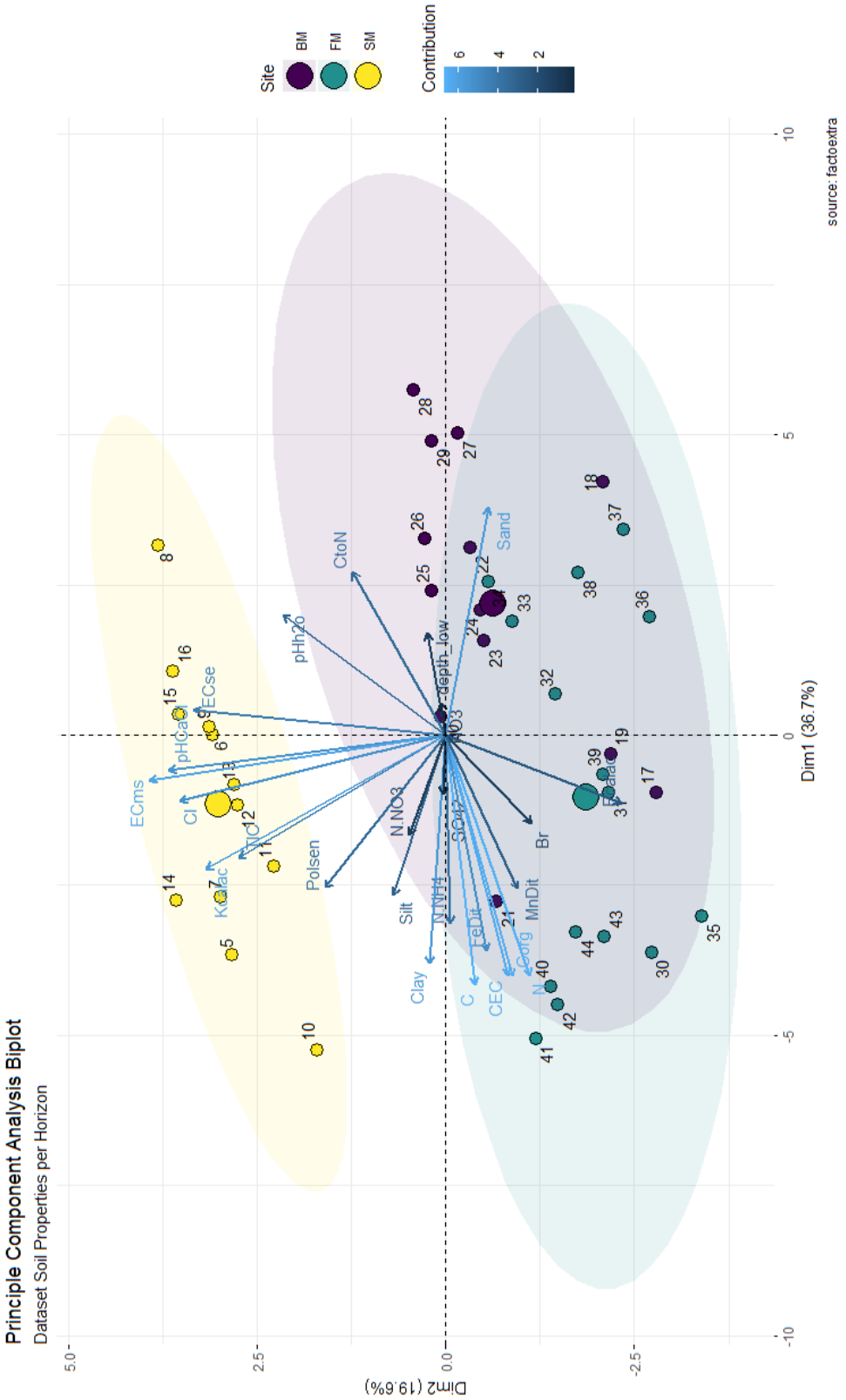

Figure 3 PCA biplot depicting the soil horizon observations as points (corresponding horizon numbers are given in appendix M, table 30) and variables (chemicals analyses, appendix M table 30, 31 and 32) as eigenvectors. The three large points correspond to the mean values per tidal wetland zone (FM, BM, SM). Arrow lengths depict the quality of the variable representations. The arrow color, blue scale, indicates contribution in % of variables to the defined dimensions

3.2 Characteristics of tidal wetland soil redox conditions in the Elbe estuary

The tidal wetland soils showed a change in reduction class ($RC_{morphology}$) from the less reducing R5 and R4 towards the more reducing R3 and R2 over soil depth (appendix M, table 30). There were two exceptions to this monotonous decrease as the R3 classified Cr-horizons in SM HMu and SM LM, starting at 58 cm and 2 cm depths respectively, were located above less strongly reducing (R4) horizons.

The top soils classified from aerated to temporarily without free oxygen (R5 and R4). An exception was the SM PZ top soil, which fell in the R3 class. The R3 class is associated with permanent presence of Fe^{2+} ions and thus suggesting continuous reducing conditions in the SM PZ top soil. However, this specific top soil was assigned until 30 cm below soil surface, in contrast to the other top soils which were assigned to only a few centimeters of soil depth (appendix M, table 30).

All following soil horizons below the top soils classified as R2, associated with sulfide and methane formation, in the pioneer zones. In the low and high marsh soils (permanently) reducing conditions (R3) were observed below 2 cm, 19 cm and 23 cm depth in the respectively SM LM, BM LM and FM LM soils and below 60 cm, 40 cm and 30 cm depth in respectively the SM HMu, BM HMu and FM HMu soils.

The reduction index (RI_{tot}) results showed a general increase in reducing conditions stream upwards the Elbe river (figure 4). Furthermore, the tidal wetland soils showed larger RI_{tot} values with increasing flooding frequency, from HMu to LM to PZ (figure 4). The constructed mixed effects model for predicting RI_{10cm} gave a significant contribution for the interaction of the four fixed effects according to the ANOVA test. The salinity zones (FM, BM, SM), flooding frequency zones (PZ, LM, HMu), depth increments (0 – 10 cm, 10 – 20 cm, 20 – 30 cm, 30 – 40 cm, 40 - 50 cm and 50 - 60 cm), measurement campaigns (table 3) resulted in a significant p value of < 0.01 with SSQ of 7.4, mean SQ 0.04, degree of freedom 198 and F-statistic 1.70. Additionally, the IRIS sticks themselves as random effects explained 7.5% of the total variance in the dataset.

The Kruskal-Wallis test, followed by unpaired Wilcoxon test, indicated that the SM site had a smaller RI_{tot} in 10 of 11 tested campaigns ($p < 0.05$) compared to BM with an averaged difference of -0.18 and FM with an average difference of -0.19. The three sites were not significantly different from each other during campaign 6. The BM showed a significantly ($p < 0.05$) smaller RI_{tot} compared to FM, with an averaged difference of -0.10, during campaign 5, 10 and 11, but a significantly larger RI_{tot}, with an averaged difference of 0.06 during campaign 3, 6 and 8. The BM and FM were not significantly different during the other tested months.

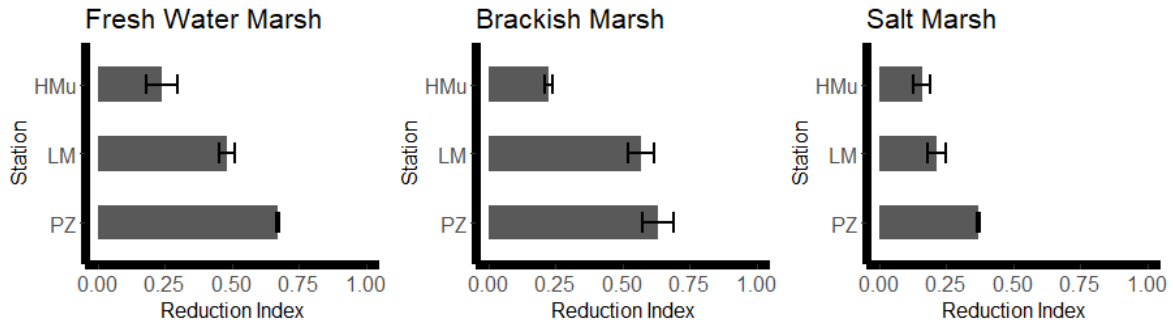

Figure 4: Reduction index (RI_{tot}) as median of 60 cm depth of 5 replicate plots measured at 11 measurement campaigns with MAD as error bars (n = 5). Larger RI value suggests stronger reducing conditions.

Redox potentials (Eh) in the SM soils decreased from HMu, to LM to PZ (figure 5). The ANOVA test of the mixed effect model predicting the campaign average redox potential (table 3) gave a significant contribution for the interaction of the three tested fixed effects: flooding frequency zone (HMu, LM, PZ), sensor depth (5 cm, 10 cm, 30 cm and 60 cm) and measurement campaign (table 3), with a p value of < 0.01, SSQ of 50.6, mean SQ 0.56, F-statistic 3.07 on 90 and 688 degree freedom. The different sensors themselves, as random effects, explained 25% of the total variance in the data set.

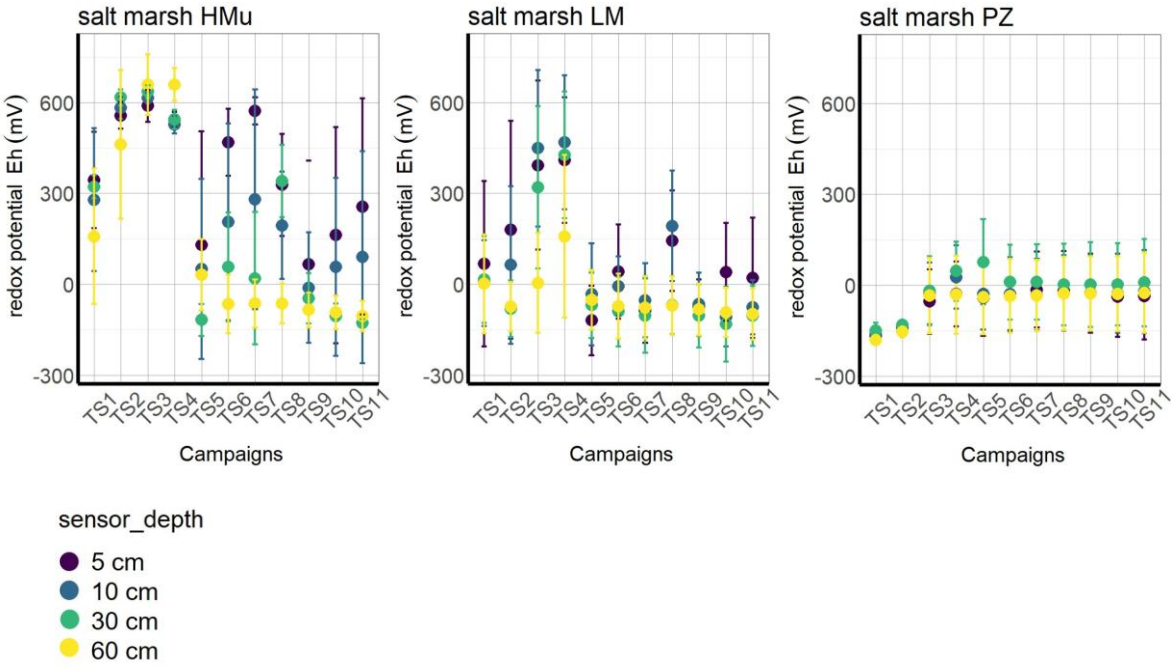

Figure 5 mean redox potentials (mV) per campaign, with campaigns indicating the averaging windows for the sensor output (ts1 to ts11 corresponding to campaigns 1 to 11, table 3). Error bars depict standard errors.

3.3 Soil redox characterization methods

Results from $RC_{morphology}$ aligned with those from $RI_{horizon}$ as larger RI values were observed in soil horizons with reduction classes R2 and R3 compared to R4 and R5 (appendix P, table 33). The $RI_{horizon}$ medians of the 11 campaigns ranged between 0.11 and 0.96 and the averages between 0.17 and 0.85 for the R2 and R3 horizons. In comparison R4 had median RI ranging between 0.00 and 0.36 and averages between 0.06 and 0.36, while R5 horizons showed even smaller RI medians, ranging from 0.00 to 0.12, and averages, ranging from 0.04 to 0.15 (appendix P, table 33). ANOVA tests of the square root transformed $RI_{horizon}$ indicated significant ($p < 0.01$, degrees of freedom 4 on 35, F-statistic value 18.7) differences among the four $RC_{morphology}$ groups, with R2 horizons having larger $RI_{horizon}$ compared to R3, R4 and R5 and R3 horizons having larger $RI_{horizon}$ compared to R4 and R5.

A striking observation was the decrease in $RI_{horizon}$ values from second-last to last horizon in the soil profiles of FM PZ, FM LM, BM PZ, BM HMu, SM LM and SM HMu. This decrease ranged between 0.07 and 0.24 (or median values 0.01 and 0.17) and it occurred at different depths in respect to the soil surface and horizon types (appendix P, table 33). In most cases the two adjacent horizons fell in the same $RC_{morphology}$, however in BM HMu, SM LM and SM HMu the decrease in $RI_{horizon}$ was contrasted by a lowering of $RC_{morphology}$. While the $RI_{horizon}$ suggested less iron reduction, the $RC_{morphology}$ reflected stronger reducing conditions in these three cases. The lower $RI_{horizon}$ values deeper in the soils of SM LM and SM HMu were also observed when calculating the RI for the soil at the sensor depths (RI_{30cm_sensor} and RI_{60cm_sensor}, table 9) but were contrasted by the sensor results which showed a decrease in hydrogen partial pressure (rH_{30cm} and rH_{60cm}, table 10).

Most of the RI_{sensor} results supported the previously described increase in reducing conditions from pioneer zone to low marsh, to high marsh (chapter 3.2) but the standard deviations were large and standard errors indicated overlap between the different flooding frequency zones in the salt marsh (table 9). The RI_{5cm_sensor} was higher for the SM LM and SM HMu compared to SM PZ (table 9), indicating more iron paint was reduced at 5 cm soil depth in the SM LM and SM HMu compared to the SM PZ. The RI_{5cm_sensor} results do not match the observations from the RC_{sensor}, as the lower rH value in SM PZ indicates stronger reducing conditions compared to SM LM and SM HMu (table 10). The, RI_{30cm_sensor} and RI_{60cm_sensor} values increased from SM PZ to SM LM to SM HMu.

Table 9 RI_{sensor} values as average over 60 cm depth. RI values per sensor depth retrieved from 1 cm increments (RI_{1cm}) in following ranges: 5 cm: 3 cm to 7 cm, 10 cm: 8 cm to 12 cm, 30 cm: 28 cm to 32 cm and 60 cm: 58 cm to 60 cm. Mean value with ± se and (sd) and median (med.) of the 55 observations.

	RI_{sensor}	**RI_{5cm_sensor}**	**RI_{10cm_sensor}**	**RI_{30cm_sensor}**	**RI_{60cm_sensor}**
PZ	0.34 ± 0.04 (sd)	0.04 ± 0.01 (0.08) med.: 0.01	0.10 ± 0.02 (0.13) med.:0.04	0.41 ± 0.04 (0.30) med.:0.25	0.60 ± 0.03 (0.20) med.: 0.64
LM	0.22 ± 0.03 (sd)	0.11 ± 0.03 (0.21) med.: 0.01	0.13 ± 0.03 (0.22) med.: 0.03	0.37 ± 0.03 (0.25) med.: 0.31	0.31 ± 0.03 (0.20) med.: 0.29
HMu	0.16 ± 0.04 (sd)	0.08 ± 0.02 (0.18) med.: 0.01	0.10 ± 0.03 (0.20) med.: 0.01	0.34 ± 0.04 (0.29) med.: 0.22	0.19 ± 0.02 (0.19) med.: 0.12

Table 10 summarizes the calculated rH results retrieved from redox potentials. The full overview is given in appendix Q, tables 34 A to C, summarizing the calculated mean redox potentials, corresponding soil temperature and soil pH per campaign and measurement point and the resulting calculated rH. The results show a change in reducing conditions from SM PZ to SM LM to SM HMu, with stronger reducing conditions in more frequently flooded zones. A high variability in rH existed over time as reflected by the large standard deviations. The assigned RC_{sensor} aligned with the assigned $RC_{morphology}$, based on aggregated results of the four redox sensor depths and the 11 campaigns (table 10).

*Table 10 rH values derived from sensor data (transformed according to rH = (2*Eh / 59) + 2*pH, (WRB, 2022)). rH_{avg} gives averaged values of four sensor depths for the 11 campaigns (table 3) with standard deviations per tidal marsh zone. RC_{sensor} reports RC corresponding to the averaged rH to reflect the full 60 cm soil depth over the course of the measurement year. $RC_{morphology}$ reports assigned RC based on morphological description. rH_{5cm}, rH_{10cm}, rH_{30cm}, rH_{60cm} report averaged rH values per sensor depth as average of the 11 campaigns with standard deviations. RC_{5cm_sensor}, RC_{10cm_sensor}, RC_{30cm_sensor}, RC_{60cm_sensor} report the assigned RC per sensor depth separately.*

	rH_{avg}	**RC_{sensor}**	**$RC_{morph-ology}$**	**rH_{5cm} $RC_{5cm\ sensor}$**	**rH_{10cm} $RC_{10cm\ sensor}$**	**rH_{30cm} $RC_{30cm\ sensor}$**	**rH_{60cm} $RC_{60cm\ sensor}$**
PZ	13.7 ± 0.3 (2.0)	R3 / R2	R3 / R2[1]	12.8 ± 0.5 (1.7) R3 / R2	13.1 ± 0.6 (1.9) R3 / R2	14.8 ± 0.7 (2.3) R3 / R2	14.1 ± 0.6 (1.9) R3 / R2
LM	17.7 ± 0.9 (5.8)	R4*	R4[2]	19.5 ± 1.8 (6.0) R4*	19.4 ± 2.1 (7.0) R4*	16.8 ± 1.9 (6.4) R4*	15.2 ± 0.8 (2.5) R3
HMu	24.0 ± 1.4 (8.9)	R4*	R4 / R3[2]	28.0 ± 2.0 (6.5) R4*	25.0 ± 2.3 (7.6) R4*	22.2 ± 3.1 (10.3) R4*	21.0 ± 3.1 (10.4) R4*

Class R4* is assigned when during some of the campaigns the rH values reached below or exceeded rH of 20.

[1] The deepest located soil horizons Cr1 and Cr2 in the soil profile were assigned to this class.

[2] The deeper located soil horizons Cr in the soil profile was assigned to this class.

When comparing the RC_{sensor} per separate sensor depth with the $RC_{morphology}$ (appendix M table 30, appendix Q tables 34 A to C), it can be seen that SM PZ RC_{5cm_sensor} and RC_{10cm_sensor}, inhabiting a R3 horizon, were temporarily more reducing than suggested by $RC_{morphology}$. During some of the campaigns, rH values fell below the rH threshold of 13, associated with the R2 level of $RC_{morphology}$.

The SM PZ sensors at 30 cm depth are situated at the boundary of the R3 classified Ahlr and R2 classified Cr horizons (appendix M table 30). The RC_{30cm_sensor} classified also as R3 / R2 due a large standard deviation but the mean rH value was higher compared to means of rH_{5cm} and rH_{10cm}, also when taking into account the standard errors (table 10). Similarly, the SM PZ sensors at 60 cm depth had higher rH values compared to rH_{5cm}, but still classified as R3 / R2 and fell into $RC_{morphology}$ R2 class.

SM LM sensors results of 5 cm, 10 cm and 30 cm soil depths classified as R4, but based on $RC_{morphology}$ these three depths were classified as R3, as all three fell in the R3 Cr

horizon. Soil within the Brbl horizon was classified with R3 by both RC_{60cm_sensor} and $RC_{morphology}$ in the SM LM.

At all sensor depths, the HMu soil was classified with R4 conditions. This was in agreement with $RC_{morphology}$ except for the 60 cm soil depth which was classified as R3 with $RC_{morphology}$.

3.4 Greenhouse gas land-atmosphere fluxes in the Elbe estuary

3.4.1 Methane dataset

The boxplots in figure 6 show all the QL1 and QL2 labelled average hourly CH_4 land-atmosphere fluxes collected at the five flux replicate plots per pioneer zone of each salinity zone and per flooding frequency zone within the salt marsh. 21 CH_4 fluxes identified as extremes, these were observed between end of May and end of October (figure 6, table 11). The extreme FM PZ CH_4 fluxes had larger flux magnitudes compared to the median of fluxes observed at this tidal wetland zone, as was the case for the one extreme BM PZ flux. 10 Extreme fluxes were identified among the fluxes measured at SM PZ and these were mainly observed at plot 5. Two extreme flux observations found at SM LM were relatively strong negative fluxes compared to the median of fluxes observed at the four zones within the SM. The three extremes found for SM HMg were in one case a relatively strong negative, as was the extreme flux observed at SM HMu, and the other two cases at SM HMg were relatively strong positive fluxes compared to the median flux observed at the SM. There were no arguments to consider these 21 land-atmosphere CH_4 flux extremes as outliers as there were no flux calculative or measurement associated indications that implied a mistake, error or increased uncertainty. They were not removed from the dataset in the further statistical analyses. In appendix R tables 35 and 36 summarizes the Shapiro-Wilk Normality test results, indicating generally a non-normal distribution of the hourly CH_4 land-atmosphere flux data. Appendix S reports the complete dataset of calculated CH_4 land-atmosphere fluxes.

Kruskal-Wallis tests indicated significantly different hourly CH_4 flux magnitudes among the flux replicate plots of FM PZ (n = 10 to 12, Kruskal-Wallis' $chi^2 = 12.08$, df = 4, p = 0.02) and pairwise Wilcoxon revealed that the land-atmosphere CH_4 fluxes from plot 2 were significantly lower than fluxes from plot 4 (p_{BH} / $p_{bonferroni}$ = 0.04). Similarly, CH_4 flux magnitudes significantly differed among the flux replicate plots of SM PZ (n = 16 to 18, chi^2 = 14.93, df = 4, p = 0.01) and the pairwise Wilcoxon revealed that flux magnitudes from plots 1 and 2 were significantly lower than fluxes from plot 5 (p_{BH} = 0.01, $p_{bonferroni}$=0.02, p_{BH} / $p_{bonferroni}$ = 0.02 respectively).

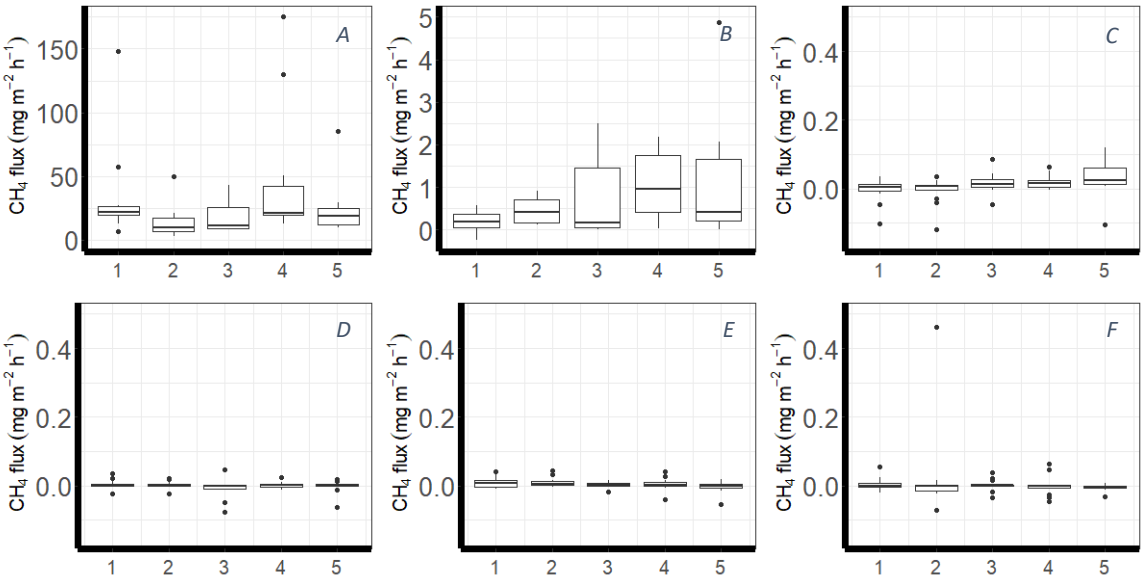

Figure 6 Boxplots of the CH_4 land-atmosphere fluxes (in mg CH_4 m^{-2} h^{-1}) measured at the flux replicate plots (nr 1 to 5) within each of the tidal wetland zones (A: FM PZ, B: BM PZ, C: SM PZ, D: SM LM, E: SM HMu, F: SM HMg).

Table 11 CH_4 land-atmosphere flux extremes, according to 3 times the interquartile > Q3 or < Q1, with data points visualized in figure 6. Environmental conditions are reported with each respective extreme flux.

salinity zone	plot	date	T_{air_in} (°C)	VWC (m^3 m^{-3})	EC (µS cm^{-1})	T_{soil} (°C)	PARin (µmols^{-1} m^{-2})	CH_4 (mg m^{-2} h^{-1})
FM	4 (PZ)	17.05.2022	20.0	0.554	1036	17.4	NA	175.56
	5 (PZ)	27.09.2022	14.4	NA	NA	NA	NA	85.63
	4 (PZ)	11.07.2023	33.3	NA	NA	NA	NA	129.80
	1 (PZ)	11.07.2023	33.4	NA	NA	NA	NA	148.39
BM	5 (PZ)	28.06.2023	26.4	0.407	1118	21.9	1375	4.88
SM	5 (LM)	25.05.2022	24.7	0.617	3673	17.1	NA	-0.06
	5 (PZ)	03.06.2022	33.2	0.644	12682	19.5	NA	0.08
	2 (HMg)	03.06.2022	31.4	0.588	4987	26.7	NA	0.46
	1 (PZ)	05.07.2022	31.1	0.662	22216	18.2	1297	-0.10
	5 (PZ)	12.07.2022	19.7	0.649	8538	17.4	271	0.08
	5 (PZ)	02.08.2022	27.3	NA	NA	NA	NA	0.11
	5 (PZ)	10.08.2022	34.0	0.653	4681	19.8	1094	0.12
	5 (PZ)	30.08.2022	21.8	NA	NA	NA	NA	0.06
	3 (PZ)	30.08.2022	21.3	NA	NA	NA	NA	0.09
	2 (PZ)	30.08.2022	28.6	NA	NA	NA	NA	-0.12
	5 (PZ)	12.09.2022	27.0	NA	NA	NA	NA	-0.10
	4 (PZ)	12.09.2022	27.3	NA	NA	NA	NA	0.07
	5 (HMu)	26.10.2022	17.7	0.492	3828	12.5	363	-0.05
	4 (HMg)	23.05.2023	14.6	0.372	988	14.0	356	0.07
	2 (HMg)	15.06.2023	30.3	0.177	364	25.4	1018	-0.07
	3 (LM)	15.06.2023	25.3	0.518	4075	20.9	260	-0.08

3.4.2 Nitrous oxide dataset

Boxplots of QL1 and QL2 labelled hourly N_2O land-atmosphere exchange showed the occurrence of extreme fluxes at all three salinity zones (figure 7, table 12). 19 N_2O fluxes were identified as extreme, these were observed between the end of April and mid-July (figure 7, table 12). The extreme FM PZ and BM PZ N_2O fluxes were all observed during specific measurement campaigns: the 11th of July and the 14th of June 2023 respectively. These extremes were larger positive fluxes compared to the median of fluxes observed at the respective tidal wetland zone. The observed extreme N_2O fluxes at the SM were from HMu and in one case from LM, all these extreme fluxes were also relatively stronger positive fluxes compared to median of fluxes observed at SM. Similarly, as for CH_4, there were no arguments to consider the identified extreme N_2O land-atmosphere fluxes as outliers in further data analyses. Appendix R tables 37 and 38 summarizes the Shapiro-Wilk Normality test results, indicating generally non-normal distribution of the hourly N_2O land-atmosphere flux data. Appendix S reports the complete dataset of calculated N_2O land-atmosphere fluxes.

The hourly N_2O land-atmosphere fluxes from the five flux replicate plots were compared and no significant difference were found between the replicates at any of the tidal wetland zones based on Kruskal-Wallis tests.

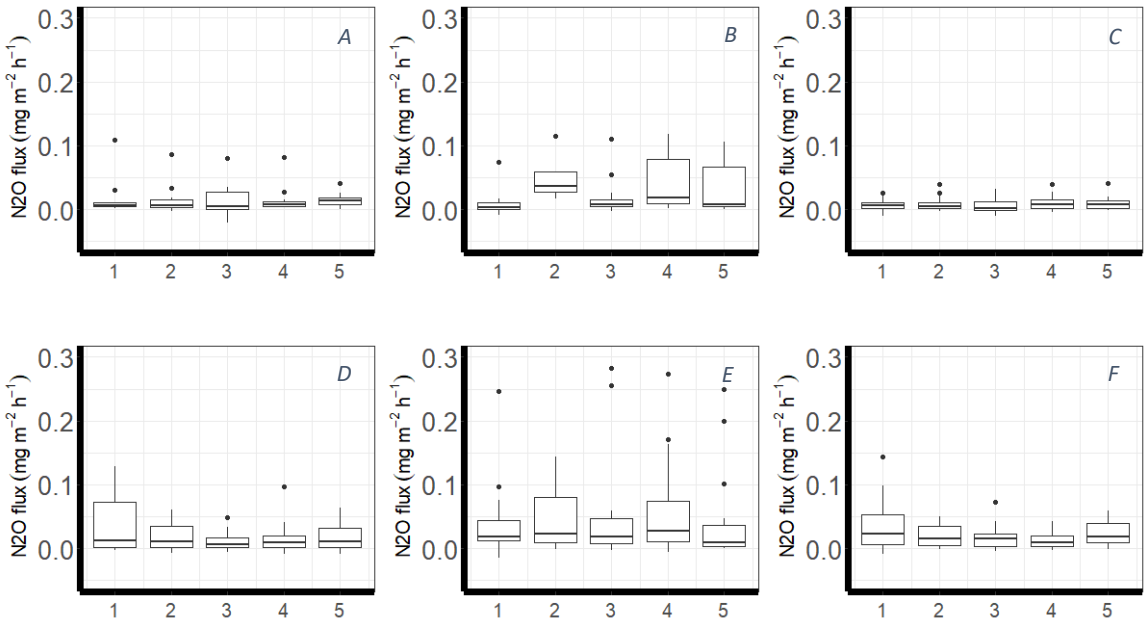

Figure 7 Boxplots of the N_2O land-atmosphere fluxes (in mg N_2O m^{-2} h^{-1}) measured at the flux replicate plots (nr 1 to 5) within each of the tidal wetland zones (A: FM PZ, B: BM PZ, C: SM PZ, D: SM LM, E: SM HMu, F: SM HMg).

Table 12 N_2O land-atmosphere flux extremes, according to 3 times the interquartile > Q3 or < Q1, with data points visualized in figure 7. Environmental conditions are reported with each respective extreme flux.

salinity zone	plot	date	T_{air_in} (°C)	VWC ($m^3\ m^{-3}$)	EC ($\mu S\ cm^{-1}$)	T_{soil} (°C)	PAR_{in} ($\mu mols^{-1}\ m^{-2}$)	N_2O ($mg\ m^{-2}\ h^{-1}$)
FM	4	11.07.2023	33.3	NA	NA	NA	1187	0.08
	3		34.8	NA	NA	NA	1265	0.08
	2		34.5	NA	NA	NA	1013	0.09
	1		33.4	NA	NA	NA	1049	0.11
BM	2	14.06.2023	34.8	0.410	1081	22.8	1724	0.11
	3		29.0	0.389	947	21.5	1372	0.11
	4		31.3	0.395	901	21.2	1243	0.12
SM	1 (HMg)	28.04.2022	26.9	0.287	1512	16.6	NA	0.14
	1 (HMu)	12.05.2022	27.9	0.614	3599	18.2	NA	0.25
	3 (HMu)	12.05.2022	28.0	0.602	3301	19.5	NA	0.28
	4 (HMu)	12.05.2022	26.9	0.575	3264	18.7	NA	0.16
	2 (HMu)	25.05.2022	29.1	0.433	1979	18.5	NA	0.14
	1 (LM)	01.06.2023	15.2	0.557	5466	13.2	504	0.13
	3 (HMu)	01.06.2023	16.3	0.173	646	14.6	588	0.26
	4 (HMu)		16.1	0.119	329	14.4	545	0.17
	5 (HMu)		16.9	0.146	291	15.1	496	0.20
	2 (HMu)	15.06.2023	28.4	0.090	218	23.0	822	0.12
	4 (HMu)		27.6	0.076	96	22.4	1359	0.27
	5 (HMu)		26.7	0.072	81	21.7	737	0.25

3.4.3 Greenhouse gas fluxes from different tidal wetland zones

The average hourly CH_4 land-atmosphere fluxes significantly differed between SM PZ, BM PZ and FM PZ according to the Kruskal-Wallis test (Kruskal-Wallis' $chi^2 = 12.5$, $p < 0.01$) and pairwise comparisons with Wilcoxon test ($p_{BH} = 0.01$, $p_{bonferroni} = 0.02$) revealed larger flux magnitudes from FM PZ, followed by BM PZ and smallest flux magnitudes from SM PZ (table 13, figure 8). The average hourly CH_4 fluxes per season also significantly differed among the three PZs according to the Kruskal-Wallis test (spring and summer: Kruskal-Wallis' $chi^2 = 12.5$, $p = < 0.01$, autumn Kruskal-Wallis' $chi^2 = 6.82$, $df = 1$, $p = 0.01$, winter Kruskal-Wallis' $chi^2 = 10.5$, $p = 0.01$, table 14, figure 10). Wilcoxon showed significantly different spring and summer CH_4 flux magnitudes among the three PZs ($p_{BH} = 0.01$, $p_{bonferroni} = 0.02$), with larger flux magnitudes from FM PZ followed by BM PZ and smallest from SM PZ. The winter flux magnitudes were only significantly different between SM PZ and FM PZ ($p_{BH} = 0.02$, $p_{bonferroni} = 0.02$), with larger flux magnitudes from FM PZ. A difference in winter flux magnitudes between FM PZ : BM PZ and BM PZ : SM PZ was observed when applying Benjamini-Hochberg p value adjustment but not when using Bonferroni ($p_{BH} = 0.04$, $p_{bonferroni} = 0.11$).

The average hourly CH_4 land-atmosphere fluxes from the salt marsh flooding frequency zones did not significantly differ from each other according to Kruskal-Wallis testing (Kruskal-Wallis' $chi^2 = 2.90$, $df = 3$, $p = 0.41$, table 13, figure 9). However, the average spring hourly fluxes were significantly different (Kruskal-Wallis' $chi^2 = 11$, $df = 3$, $p = 0.01$, table 14, figure 11) and the pairwise Wilcoxon test revealed significant larger flux magnitudes from

PZ compared to LM ($p_{BH} < 0.05$, $p_{bonferroni} < 0.05$). When considering Benjamini-Hochberg p value adjustment, HMu spring CH_4 fluxes were significantly larger in magnitude compared to LM spring fluxes, but not when applying the Bonferroni adjustment ($p_{BH} < 0.05$, $p_{Bonferroni} = 0.10$).

Table 13 Average hourly CH_4 land-atmosphere fluxes with standard errors (SE, ±xxx) per tidal wetland zone as average of 5 the flux replicate plots (n = 5) and average hourly CH_4 land-atmosphere fluxes with standard deviations (SD, ±xxx) per flux replicate plot averaged over the full measurement period (n = number of measurements in time).

tidal wetland zone	**mean** (mg CH_4 m^{-2} h^{-1})	**plot 1** (mg CH_4 m^{-2} h^{-1})	**plot 2** (mg CH_4 m^{-2} h^{-1})	**plot 3** (mg CH_4 m^{-2} h^{-1})	**plot 4** (mg CH_4 m^{-2} h^{-1})	**plot 5** (mg CH_4 m^{-2} h^{-1})
FM PZ	27.3 ± 5.7	34.66 ± 39.79 n = 11	14.39 ± 12.76 n = 12	18.29 ± 12.79 n = 10	45.73 ± 51. n = 12	23.61 ± 21.66 n = 11
BM PZ	0.7 ± 0.2	0.19 ± 0.28 n = 7	0.46 ± 0.39 n = 4	0.70 ± 0.96 n = 16	1.07 ± 0.90 n = 5	1.10 ± 1.52 n = 10
SM PZ	$13.3 * 10^{-3}$ ± $6.7*10^{-3}$	-0.0023 ± 0.0326 n = 16	-0.0008 ± 0.0346 n = 18	0.0167 ± 0.0278 n = 16	0.0198 ± 0.0204 n = 18	0.0333 ± 0.0486 n = 18
SM LM	$-0.3*10^{-3}$ ± $1.9*10^{-3}$	0.0040 ± 0.0140 n = 13	0.0016 ± 0.0121 n = 16	-0.0069 ± 0.0275 n = 14	0.0019 ± 0.0092 n = 12	-0.0020 ± 0.0188 n = 14
SM HMu	$5.0*10^{-3}$ ± $2.5*10^{-3}$	0.0105 ± 0.0172 n = 15	0.0095 ± 0.0138 n = 15	0.0033 ± 0.0087 n = 14	0.0050 ± 0.0174 n = 15	-0.0032 ± 0.0148 n = 17
SM HMg	$4.4*10^{-3}$ ± $4.3*10^{-3}$	0.0044 ± 0.0181 n = 17	0.0204 ± 0.1152 n = 17	0.0020 ± 0.0172 n = 14	-0.0003 ± 0.0272 n = 15	-0.0045 ± 0.0087 n = 16

Table 14 Average hourly CH_4 land-atmosphere fluxes per meteorological season with standard errors (SE, ±xxx) per tidal wetland zone with n = 5.

tidal wetland zone	**spring** (mg CH_4 m^{-2} h^{-1})	**summer** (mg CH_4 m^{-2} h^{-1})	**autumn** (mg CH_4 m^{-2} h^{-1})	**winter** (mg CH_4 m^{-2} h^{-1})
FM PZ	23 ± 9.20	47 ± 13.43	23 ± 3.54	22 ± 4.16
BM PZ	0.3 ± 0.07	1.6 ± 0.43	NA	0.1 ± 0.06
SM PZ	$10.4*10^{-3} \pm 2.3*10^{-3}$	$22.2*10^{-3} \pm 11.3*10^{-3}$	$-17.7*10^{-3} \pm 20.9*10^{-3}$	$8.7*10^{-3} \pm 4.3*10^{-3}$
SM LM	$-7.2*10^{-3} \pm 3.0*10^{-3}$	$2.4*10^{-3} \pm 2.6*10^{-3}$	$-1.4*10^{-3} \pm 2.9*10^{-3}$	$8.6*10^{-3} \pm 6.6*10^{-3}$
SM HMu	$5.0*10^{-3} \pm 1.7*10^{-3}$	$5.0*10^{-3} \pm 1.6*10^{-3}$	$4.6*10^{-3} \pm 21.3*10^{-3}$	$7.9*10^{-3} \pm 9.5*10^{-3}$
SM HMg	$1.1*10^{-3} \pm 3.4*10^{-3}$	$10.9*10^{-3} \pm 11.6*10^{-3}$	$-9.2*10^{-3} \pm 2.9*10^{-3}$	$1.4*10^{-3} \pm 5.6*10^{-3}$

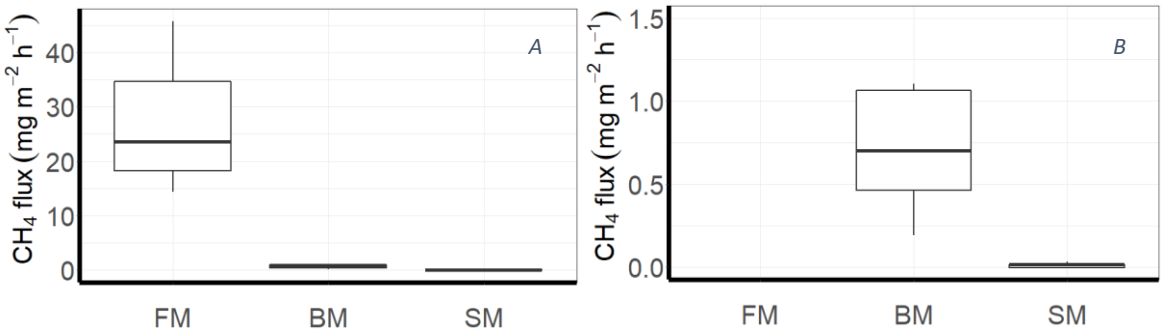

Figure 8 Average hourly CH_4 land-atmosphere fluxes (in mg CH_4 m^{-2} h^{-1}) from fresh marsh pioneer zone (FM PZ), brackish marsh pioneer zone (BM PZ) and salt marsh pioneer zone (SM PZ) in the Elbe estuary. Boxplots constructed from average hourly fluxes of the five flux replicate plots per tidal wetland zone (n = 5). Graph A shows all flux magnitudes, graph B shows fluxes between 0 and 1.5 mg CH_4 m^{-2} h^{-1}.

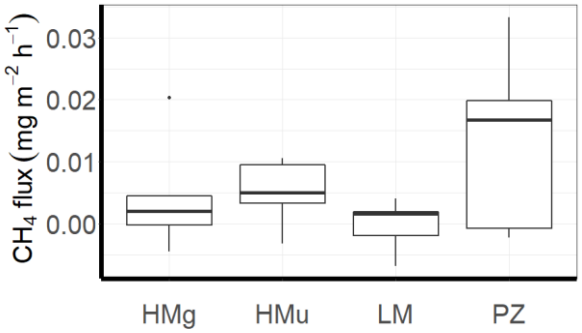

Figure 9 Average hourly CH_4 land-atmosphere fluxes (in mg CH_4 m^{-2} h^{-1}) from the grazed high marsh (HMg), ungrazed high marsh (HMu), low marsh (LM) and pioneer zone (PZ) within the salt marsh (SM) in the Elbe estuary. Boxplots constructed from average hourly fluxes of the five flux replicate plots per tidal wetland zone (n = 5).

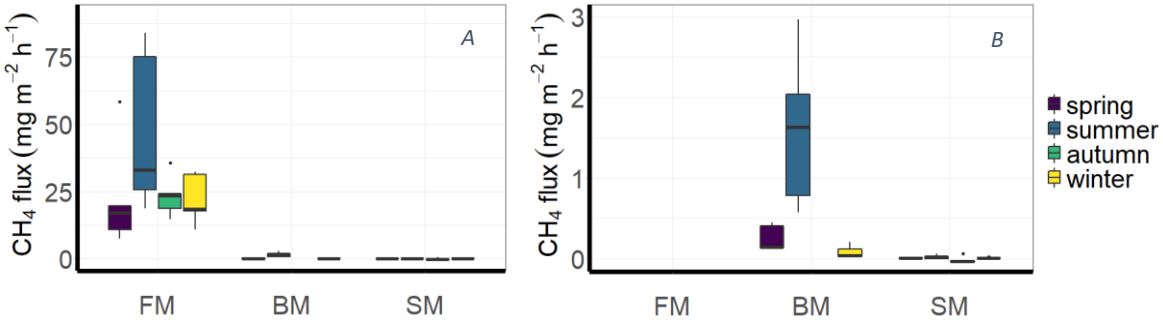

Figure 10 Average hourly CH_4 land-atmosphere fluxes (in mg CH_4 m^{-2} h^{-1}) per meteorological season from pioneer zones at the fresh water marsh (FM), brackish marsh (BM) and salt marsh (SM) in the Elbe estuary. Boxplots constructed from average hourly fluxes of the five flux replicate plots per tidal wetland zone (n = 5). Graph A shows all flux magnitudes, graph B shows fluxes between 0 and 3 mg CH_4 m^{-2} h^{-1}.

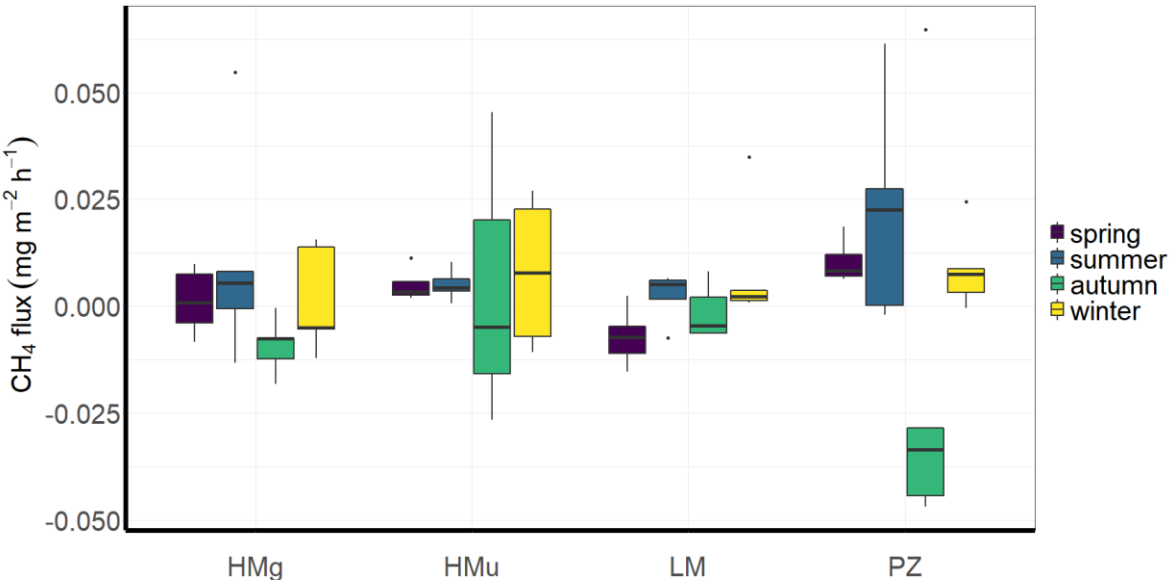

Figure 11 Average hourly CH_4 land-atmosphere fluxes (in mg CH_4 m^{-2} h^{-1}) per meteorological season from the grazed high marsh (HMg), ungrazed high marsh (HMu), low marsh (LM) and pioneer zone (PZ) within the salt marsh (SM) in the Elbe estuary. Boxplots constructed from average hourly fluxes of the five flux replicate plots per tidal wetland zone (n = 5).

The average hourly N_2O flux magnitudes significantly differed between FM PZ and SM PZ as well as between BM PZ and SM PZ, with in both cases smaller flux magnitudes from the SM PZ (Kruskal-Wallis' $chi^2 = 10.22$, $p = 0.01$, pairwise Wilcoxon test $p_{BH} = 0.01$, $p_{bonferroni} = 0.02$, figure 12 and table 15). The average hourly N_2O fluxes per meteorological seasons revealed significantly smaller N_2O SM PZ summer fluxes compared to FM PZ and BM PZ summer fluxes (Kruskal-Wallis' $chi^2 = 10.82$, $p < 0.01$, pairwise Wilcoxon test $p_{BH} = 0.01$, $p_{bonferroni} = 0.02$). Similarly, the N_2O SM PZ winter fluxes were significantly smaller compared to FM PZ winter fluxes but not compared to BM PZ winter fluxes (Kruskal-Wallis' $chi^2 = 8.08$, $p = 0.02$, pairwise Wilcoxon test $p_{BH} = 0.01$, $p_{bonferroni} = 0.02$). The average hourly N_2O spring and autumn fluxes were not significantly different among the three PZ.

Within the SM, the average hourly land-atmosphere N_2O flux magnitudes differed significantly between the four flooding frequency zones (Kruskal-Wallis' $chi^2 = 16.07$, $p < 0.01$). The HMu N_2O fluxes were significantly larger than the fluxes from the other three zones, as revealed by pairwise Wilcoxon test ($p_{BH} = 0.01$, $p_{bonferroni} < 0.05$). Furthermore, the N_2O SM PZ fluxes were significantly smaller compared to the fluxes from all three other flooding frequency zones ($p_{BH} = 0.01$, $p_{bonferroni} < 0.05$).

The average spring, summer and autumn hourly N_2O land-atmosphere flux magnitudes were significantly different between the four flooding frequency zones within the salt marsh, however average hourly winter fluxes were not (spring: Kruskal-Wallis' $chi^2 = 14.14$, $p < 0.01$, summer: Kruskal-Wallis' $chi^2 = 13.26$, $p < 0.01$, autumn: Kruskal-Wallis' $chi^2 = 10.13$, $p = 0.02$, winter: Kruskal-Wallis' $chi^2 = 7.04$, $p = 0.07$). Pairwise comparison with Wilcoxon revealed that HMu spring N_2O fluxes were significantly larger compared to HMg and PZ spring N_2O fluxes (HMg versus HMu $p_{BH} < 0.05$, $p_{bonferroni} = 0.19$, HMu versus PZ $p_{BH} = 0.02$, $p_{bonferroni} < 0.05$), but not compared to LM spring fluxes. The PZ spring and summer N_2O

fluxes were significantly smaller than the spring and summer fluxes from the other three zones (spring: $p_{BH} = 0.02$, $p_{bonferroni} < 0.05$, summer: $p_{BH} = 0.02$, $p_{bonferroni} < 0.05$). Among, the SM LM, SM HMu and SM HMg no significant differences were observed in summer N_2O fluxes. However, HMg autumn N_2O fluxes were significantly larger compared to LM and PZ autumn fluxes ($p_{BH} < 0.05$, $p_{bonferroni} = 0.10$) but did not differ from HMu autumn flux magnitudes.

Table 15 Average hourly N_2O land-atmosphere fluxes with standard errors (SE, ±xxx per tidal wetland zone as average of 5 the flux replicate plots (n = 5) and average hourly N_2O land-atmosphere fluxes with standard deviations (SD, ±xxx) per flux replicate plot averaged over the full measurement period (n = number of measurements in time).

tidal wetland zone	**mean**	**plot 1**	**plot 2**	**plot 3**	**plot 4**	**plot 5**
	(all in mg N_2O m^{-2} h^{-1})					
FM PZ	$15.6 * 10^{-3}$	0.0179	0.0145	0.0160	0.0151	0.0145
	$\pm 0.6 * 10^{-3}$	± 0.0313	± 0.0245	± 0.0279	± 0.0219	± 0.0113
		n = 11	n = 12	n = 10	n = 12	n = 11
BM PZ	$32.0 * 10^{-3}$	0.0128	0.0508	0.0179	0.0455	0.0330
	$\pm 7.4 * 10^{-3}$	± 0.0281	± 0.0438	± 0.0280	± 0.0511	± 0.0421
		n = 7	n = 4	n = 16	n = 5	n = 10
SM PZ	$7.5 * 10^{-3}$	0.0075	0.0089	0.0049	0.0108	0.0093
	$\pm 1.0 * 10^{-3}$	± 0.0092	± 0.0114	± 0.0110	± 0.0114	± 0.0102
		n = 16	n = 17	n = 16	n = 18	n = 18
SM LM	$21.4 * 10^{-3}$	0.0370	0.0201	0.0121	0.0176	0.0202
	$\pm 4.2 * 10^{-3}$	± 0.0463	± 0.0243	± 0.0156	± 0.0284	± 0.0242
		n = 13	n = 16	n = 14	n = 12	n = 14
SM HMu	$49.9 * 10^{-3}$	0.0423	0.0446	0.0567	0.0634	0.0423
	$\pm 4.3 * 10^{-3}$	± 0.0636	± 0.0462	± 0.0921	± 0.0796	± 0.0736
		n = 15	n = 15	n = 14	n = 15	n = 17
SM HMg	$21.3 * 10^{-3}$	0.0349	0.0188	0.0172	0.0125	0.0232
	$\pm 3.8 * 10^{-3}$	± 0.0399	± 0.01687	± 0.0208	± 0.0132	± 0.0198
		n = 17	n = 17	n = 14	n = 15	n = 16

Table 16 Average hourly N_2O land-atmosphere fluxes per meteorological season with standard errors (SE, ±xxx) per tidal wetland zone with n= 5.

tidal wetland zone	**spring** (mg N_2O m^{-2} h^{-1})	**summer** (mg N_2O m^{-2} h^{-1})	**autumn** (mg N_2O m^{-2} h^{-1})	**winter** (mg N_2O m^{-2} h^{-1})
FM PZ	$4.5*10^{-3} \pm 1.2*10^{-3}$	$45.1*10^{-3} \pm 7.2*10^{-3}$	$9.6*10^{-3} \pm 1.2*10^{-3}$	$14.3*10^{-3} \pm 2.9*10^{-3}$
BM PZ	$11.4*10^{-3} \pm 4.1*10^{-3}$	$71.2*10^{-3} \pm 8.4*10^{-3}$	NA	$5.2*10^{-3} \pm 2.4*10^{-3}$
SM PZ	$4.2*10^{-3} \pm 1.2*10^{-3}$	$11.3*10^{-3} \pm 1.2*10^{-3}$	$8.5*10^{-3} \pm 5.1*10^{-3}$	$3.3*10^{-3} \pm 1.2*10^{-3}$
SM LM	$21.2*10^{-3} \pm 4.5*10^{-3}$	$29.6*10^{-3} \pm 7.0*10^{-3}$	$9.2*10^{-3} \pm 3.6*10^{-3}$	$0.8*10^{-3} \pm 1.5*10^{-3}$
SM HMu	$69.2*10^{-3} \pm 17.4*10^{-3}$	$53.0*10^{-3} \pm 8.8*10^{-3}$	$24.2*10^{-3} \pm 2.6*10^{-3}$	$-1.6*10^{-3} \pm 2.2*10^{-3}$
SM HMg	$22.0*10^{-3} \pm 7.0*10^{-3}$	$23.5*10^{-3} \pm 2.7*10^{-3}$	$33.2*10^{-3} \pm 5.3*10^{-3}$	$6.0*10^{-3} \pm 2.7*10^{-3}$

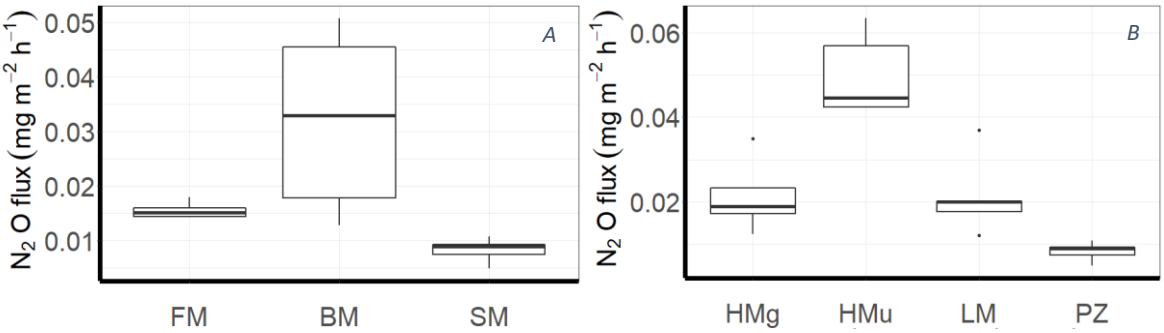

Figure 12 A) average hourly land-atmosphere N_2O fluxes (in mg N_2O m^{-2} h^{-1}) from fresh marsh pioneer zone (FM PZ), brackish marsh pioneer zone (BM PZ) and salt marsh pioneer zone (SM PZ) in the Elbe estuary. B) Average hourly N_2O land-atmosphere fluxes from the grazed high marsh (HMg), ungrazed high marsh (HMu), low marsh (LM) and pioneer zone (PZ) within salt (SM) region of the Elbe estuary. Boxplots constructed from average hourly fluxes of the five flux replicate plots per tidal wetland zone (n = 5).

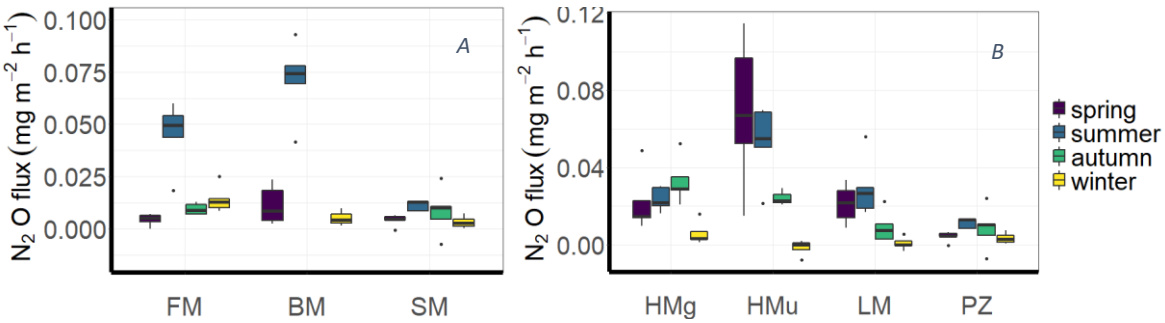

Figure 13 A) average hourly N_2O land-atmosphere fluxes (in mg N_2O m^{-2} h^{-1}) per meteorological season from pioneer zones at the fresh water marsh (FM), brackish marsh (BM) and salt marsh (SM) in the Elbe estuary. B) Average hourly N_2O land-atmosphere fluxes per meteorological season from the grazed high marsh (HMg), ungrazed high marsh (HMu), low marsh (LM) and pioneer zone (PZ) within the salt marsh (SM) region of the Elbe estuary. Boxplots constructed from average hourly fluxes of the five flux replicate plots per tidal wetland zone (n = 5).

3.4.4 Temporal trends in methane and nitrous oxide land-atmosphere fluxes

The hourly FM PZ CH_4 land-atmosphere fluxes did not significantly differ in magnitude between the tested measurement days (p = 0.28, df = 5, Friedman test, figure 14). Separate Friedman tests were conducted for the FM PZ without the observations from plot 2 (test a) and without the observations from plot 4 (test b) as a significant difference in flux magnitudes existed between these two plots (chapter 3.4.1). Both test a and b also did not show significant differences between the considered measurements days a: p = 0.25, df = 4, b: p = 0.27, df = 4). The BM PZ CH_4 land-atmosphere fluxes could not be tested due to the lack of complete cases.

The hourly SM PZ CH_4 land-atmosphere fluxes did significantly differ in magnitude among tested measurement days (p < 0.01, df = 5, Kendall's W: 0.53, figure 14) and the

Kendall's W of 0.53 indicated a marginally good agreement. However, further post hoc testing did not identify significantly different measurement pairs. The lowest non-adjusted p values from the paired Wilcoxon test were found when comparing CH_4 fluxes magnitudes from 3rd of June 2022 (DOY 154) to 12th of May 2022, 27th of July 2022, 26th of January 2022, 13th of April 2023 and 27th of June 2023 (DOYs 132, 208, 391, 468, 543, p = 0.06). The CH_4 flux magnitudes on the 3rd of June 2022 were larger, in positive direction, than flux magnitudes on these other dates.

Additionally, CH_4 flux magnitudes on 2nd of August 2022 (DOY 214) were larger, stronger positive, than flux magnitudes on 12th of May 2022, 27th of July 2022, 26th of January, 13th of April and 27th of June 2023 (DOYs 132, 208, 391, 468, 543) and comparing these combinations also resulted in non-adjusted p values of 0.06.

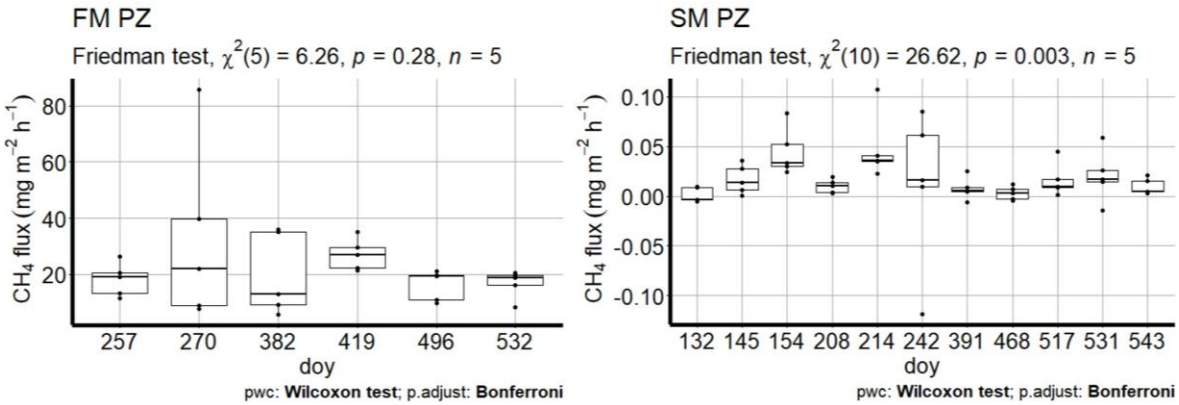

Figure 14 Boxplots of hourly CH_4 land-atmosphere fluxes (in mg CH_4 m^{-2} h^{-1}) from the fresh water marsh pioneer zone (FM PZ) and salt marsh pioneer zone (SM PZ). Boxplots cover flux observation from the five flux replicate plots. Friedman with Wilcoxon post hoc test results are plotted in the figure. DOY as day of the year with measurement year 2022 < 365 and 2023 > 366 (appendix K).

There were no significant differences in SM LM and SM HMu CH_4 hourly land-atmosphere flux magnitudes between the considered measurement days according to Friedman's test (figure 15). However, they did differ at the SM HMg (Friedman's test p = 0.03, figure 15). Although, the effect size was only moderate (Kendall's W: 0.42) and neither pairwise Wilcoxon test nor Sign Test identified significantly different measurement day pairs. When considering the non-adjusted p values from the paired Wilcoxon test, a low p value of 0.06 was found when comparing the hourly SM HMg CH_4 flux of 26th of October 2022 (DOY 299) with 12th of May 2022, 13th of June 2022, 27th of July 2022, 13th of September 2022, 20th of February 2023, 11th of April 2023 and 1st of June 2023 (DOYs 132, 164, 208, 256, 416, 466, 517). The hourly SM HMg CH_4 fluxes on 26th of October 2022 was a larger, in negative direction, flux compared to the fluxes on these other days. Additionally, the hourly SM HMg CH_4 flux magnitudes on 12th of May 2022 (DOY 132) were stronger in negative direction compared to the CH_4 fluxes on 27 July 2022, 13th of September 2022, 11th of April 2023 and 1st of June 2023 (DOYs 208, 256, 466, 517), these comparisons also resulted in non-adjusted p values of 0.06.

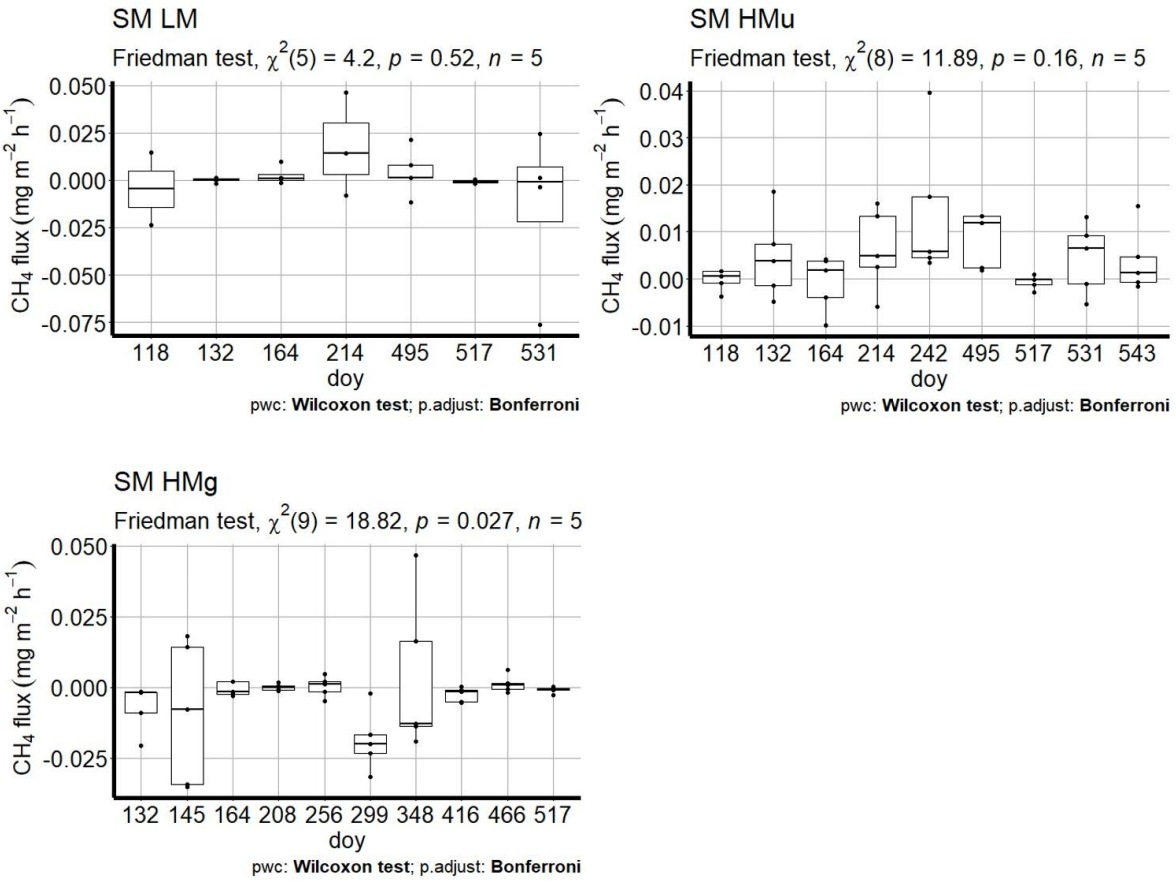

Figure 15 Boxplots of hourly CH_4 land-atmosphere fluxes (in mg CH_4 m^{-2} h^{-1}) from salt marsh low marsh (SM LM), salt marsh unmanaged high marsh (SM HMu) and salt marsh managed high marsh (SM HMg). Boxplots cover flux observation from the five flux replicate plots. Friedman with Wilcoxon post hoc test results are plotted in the figure. DOY as day of the year with measurement year 2022 < 365 and 2023 > 366 (appendix K).

The hourly FM PZ N_2O land-atmosphere fluxes significantly differed among the tested measurement dates with a large effect size ($p < 0.01$, Kendall's W: 0.70) as did the SM PZ N_2O fluxes with a moderate effect size ($p = 0.03$, Kendall's W: 0.42) (Figure 16). However, the post hoc testing did not identify significantly different measurement day pairs based on pairwise Wilcoxon test nor based on the Sign Test (figure 16). When considering the non-adjusted p values from the pairwise Wilcoxon test, again p values of 0.06 were found when comparing 23rd of February 2023 (DOY 419) to 14th of September 2022, 17th of January 2023 and 16th of June 2023 and 11th of May 2023 (DOY 496) compared to the 14th of September 2022, 17th of January 2023 and 16th of June 2023 (DOYs 257, 382, 532). Hourly FM PZ N_2O flux magnitudes were smaller, in positive direction, on the 23rd of February 2023 and 11th of May 2023 compared to these other dates.

The hourly SM PZ N_2O land-atmosphere fluxes were larger, in positive direction, on the 3rd of June 2022 (DOY 154) compared to 2nd of August 2022, 26th of January, 13th of April, 1st of June and 27th of June 2023 (DOYs 214, 391, 468, 517, 543) and on 30th of August 2022 (DOY 242) compared to 13th of April, 1st of June 2023 and 27th of June 2023 (DOYs 468, 517, 543) and both comparisons resulted in non-adjusted p values of 0.06.

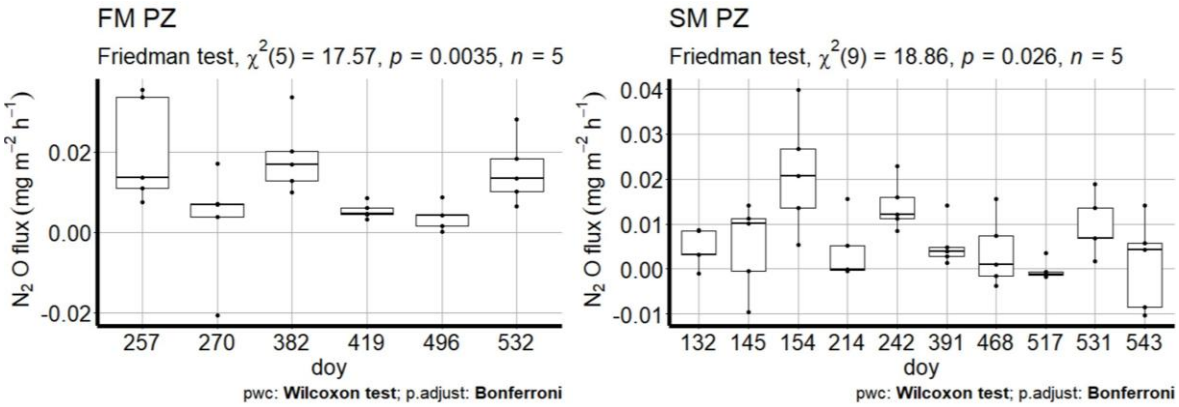

Figure 16 Boxplots of hourly N_2O land-atmosphere fluxes (in mg N_2O m^{-2} h^{-1}) from fresh marsh pioneer zone (FM PZ) and salt marsh pioneer zone (SM PZ). Boxplots cover flux observation from the five flux replicate plots. Friedman with Wilcoxon post hoc test results are plotted in the figure. DOY as day of the year with measurement year 2022 < 365 and 2023 > 366 (appendix K).

The hourly SM N_2O land-atmosphere flux magnitudes also significantly differed among the tested measurement days at the other three flooding frequency zones with respectively p values of < 0.01 (figure 17). The Kendall's W effect sizes were large for all three zones, with values of 0.85 for SM LM, 0.60 for SM HMu and 0.80 for SM HMg. However, again no significantly different measurement date pairs could be identified with the pairwise Wilcoxon test nor with the Sign Test. When considering the non-adjusted p values from the paired Wilcoxon test, values of 0.06 were found when comparing hourly SM LM N_2O fluxes from the 12th of May 2022 (DOY 132) with 26th of October 2022, 20th of February, 11th of April and 10th of May 2023 (DOYs 299, 416, 466, 495) and from the 1st of June 2023 with 20th of February, 11th of April and 10th of May 2023 (DOYs 416, 466, 495). The fluxes on 12th of May 2022 and 1st of June 2023 were larger, in positive direction compared to the respective listed other dates. The hourly SM HMu N_2O fluxes were larger, in positive direction, on 12th of May 2022 (DOY 132) compared to the 13th of June 2022, 2nd of August 2022, 30th of August 2022 and 10th of May 2023 (DOYs 164, 214, 242, 495) and on 1st of June 2023 and 15th of June 2023 (DOYs 517, 531) compared to 13th of June 2022, 2nd of August 2022 and 30th of August 2022 (DOYs 164, 214, 242), with all comparisons leading to non-adjusted p values of 0.06. Finally, the hourly SM HMg N_2O fluxes were smaller, in positive direction, on the 20th February, 11th of April and 1st of June 2023 (DOYs 416, 466, 517) compared to 12th of May 2022, 25th of May 2022, 27th of July 2022, 13th of September 2022 and 26th of October 2022 (DOYs 132, 145, 208, 256, 299) and on 13th of June 2022 (DOY 164) compared to 12th of May 2022, 25th of May 2022, 13th of September 2022 and 26th of October 2022 (DOYs 132, 145, 256, 299), with again the comparisons resulting in non-adjusted p values of 0.06.

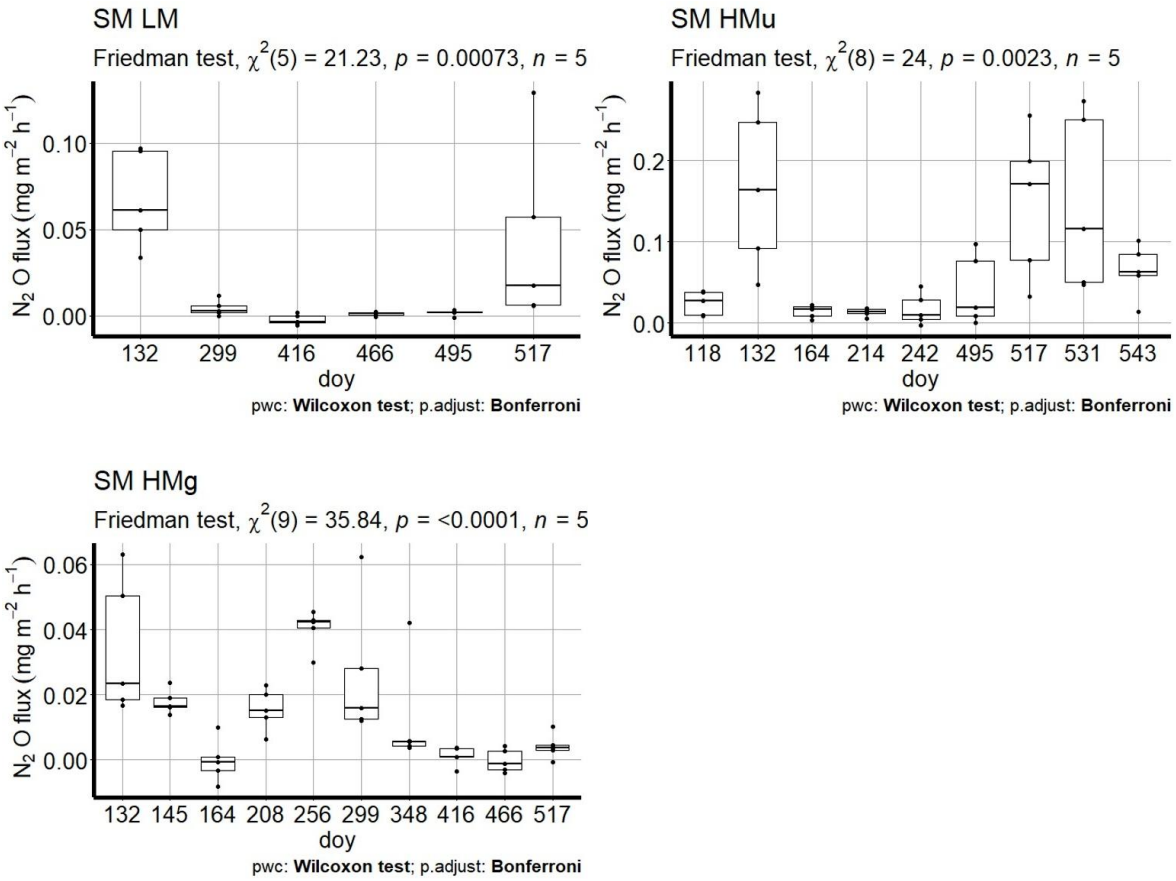

Figure 17 Boxplots of hourly N_2O land-atmosphere fluxes (in mg N_2O m^{-2} h^{-1}) from salt marsh low marsh (SM LM), salt marsh unmanaged high marsh (SM HMu) and salt marsh managed high marsh (SM HMg). Boxplots cover flux observation from the five flux replicate plots. Friedman with Wilcoxon post hoc test results are plotted in the figure. DOY as day of the year with measurement year 2022 < 365 and 2023 > 366 (appendix K).

3.4.5 Correlations between methane and nitrous oxide land-atmosphere fluxes and tidal wetland environmental conditions

Spearman's correlations of the CH_4 and N_2O complete datasets revealed significant but weak, negative correlation between hourly CO_2 and N_2O land-atmosphere fluxes ($\rho_{spearman}$ = - 0.31, $p < 0.01$), moderate, positive correlation between hourly N_2O land-atmosphere flux and T_{air_in} ($\rho_{spearman}$ = 0.50, $p < 0.01$) and moderate, positive correlation between hourly N_2O land-atmosphere flux and PAR_{in} ($\rho_{spearman}$ = 0.50, $p < 0.01$). Visualization of the N_2O flux, CO_2 flux, T_{air_in} and PAR_{in} observations are provide in the scatterplots of figure 18. The three tested environmental variables, CO_2 flux, T_{air_in} and PAR_{in}, are also correlated with each other. Moderate, negative Spearman's correlations were found between CO_2 flux and T_{air_in} and PAR_{in} with $\rho_{spearman}$ of - 0.45 and -0.56 and a strong, positive correlation between T_{air_in} and PAR_{in} with a $\rho_{spearman}$ of 0.78. The non significant correlations of the other tested variables are summarized in the appendix T, table 40.

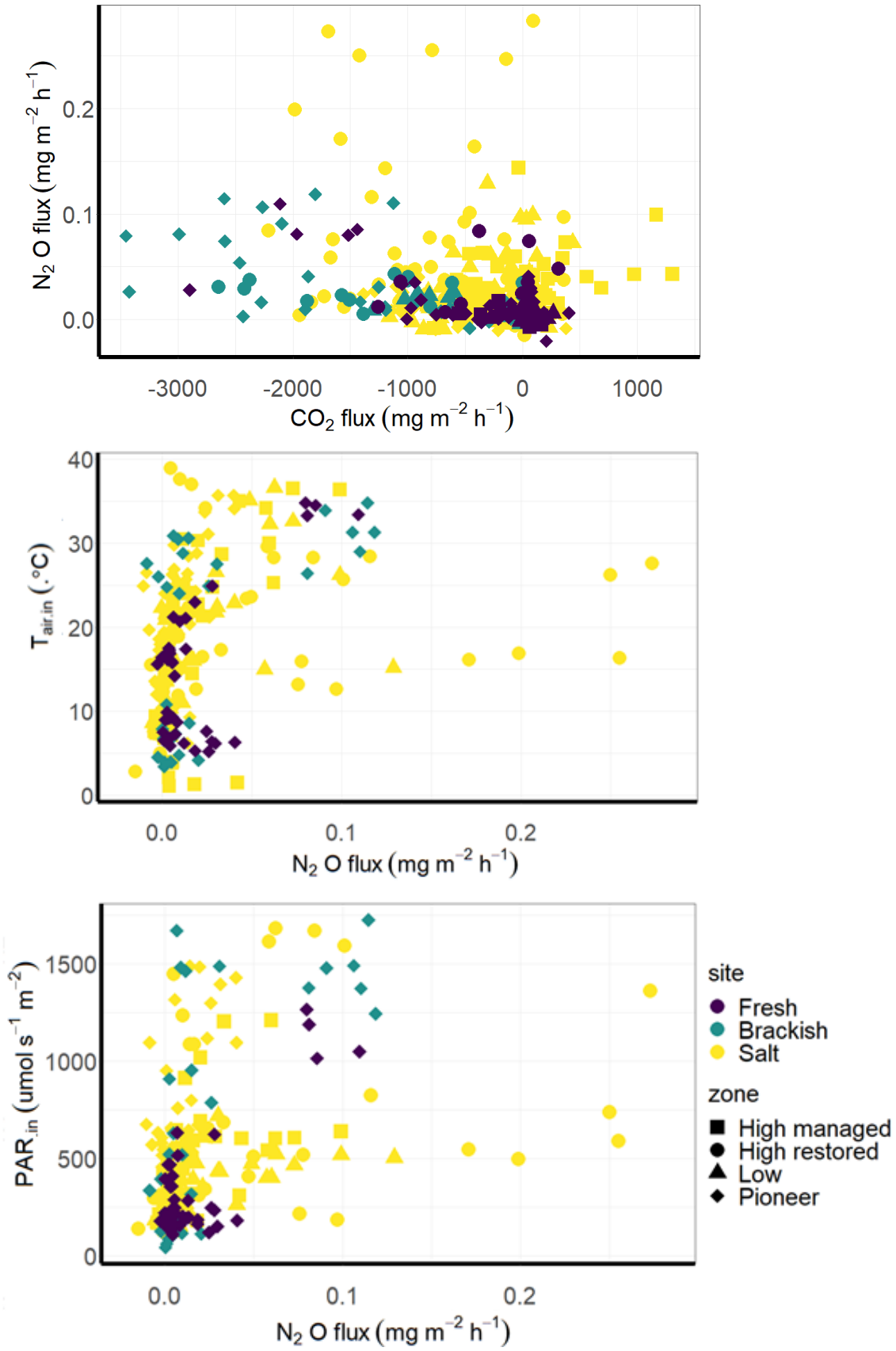

Figure 18 Scatter plots of (top left) hourly N_2O and CO_2 land-atmosphere fluxes (in mg m^{-2} h^{-1}), (top right) hourly N_2O land-atmosphere flux and T_{air_in} (°C) and (bottom) hourly N_2O land-atmosphere flux and PAR (µmol s^{-1} m^{-2}) for all observations collected in 2022 and 2023 at all tidal wetland zones.

Separate Spearman's rank correlation tests were conducted per tidal wetland zone, due to the large differences in the soil soluble salt content and its effect on the TEROS-12 readings. The analyses of the separate zones showed a significant but weak, positive correlation between hourly CH_4 and N_2O land-atmosphere fluxes at FM PZ (table 17, appendix T, table 40, figure 34). The hourly BM PZ CH_4 fluxes were significantly correlated with all tested environmental variables; having a strong, positive correlation with soil EC, moderate, positive correlations with hourly N_2O flux, T_{soil}, T_{air_in} and PAR_{in} (table 17, appendix T, table 40, figure 34). Additionally, a strong, negative correlation was found between hourly BM PZ CH_4 and CO_2 fluxes and a moderate, negative correlation between hourly BM PZ CH_4 flux and soil VWC (table 17, appendix T, table 40, figure 34). The hourly SM CH_4 land-atmosphere fluxes were only significantly correlated with environmental variables at SM LM and SM PZ. A significant weak, positive correlation was found between hourly SM LM CH_4 flux and soil EC and a significant weak, positive correlation between hourly PZ SM CH_4 flux and T_{soil} (table 17, appendix T, table 40, figure 35).

Table 17 Spearman's correlation coefficients (ρ) with p values and number of observations for hourly CH_4 land-atmosphere fluxes (mg m^{-2} h^{-1}) and the environmental variables: hourly N_2O flux, hourly CO_2 flux, soil volumetric water content (VWC), electrical conductivity (EC), temperature (T_{soil}) and headspace air temperature (T_{air_in}) as well as photosynthetic active radiation inside the flux chamber (PAR_{in}).

tidal wetland zone	**N_2O** (mg m^{-2} h^{-1})	**CO_2** (mg m^{-2} h^{-1})	**VWC** (m^{-3} m^{-3})	**EC** (µS cm^{-1})	**T_{soil}** (°C)	**T_{air_in}** (°C)	**PAR_{in}** (µmol s^{-1} m^{-2})
FM PZ	ρ = 0.33 p = 0.02 n = 56	NS	NS	NS	NS	NS	NS
BM PZ	ρ = 0.64 p < 0.01 n = 42	ρ = -0.74 p < 0.01 n = 42	ρ = -0.40 p < 0.01 n = 42	ρ = 0.68 p < 0.01 n = 42	ρ = 0.65 p < 0.01 n = 42	ρ = 0.56 p < 0.01 n = 32	ρ = 0.53 p < 0.01 n = 32
SM PZ	NS	NS	NS	NS	ρ = 0.24 p = 0.043 n = 72	NS	NS
SM LM	NS	NS	NS	ρ = 0.35 p < 0.01 n = 59	NS	NS	NS
SM HMu	NS	NS	NS	NS	NS	NS	NS
SM HMg	NS	NS	NS	NS	NS	NS	NS

The hourly N_2O land-atmosphere fluxes were significantly correlated with many of the tested environmental variables at most of the studied tidal wetland zones (table 18, appendix T, table 40, figure 34, figure 35). Significant, weak to moderate, positive correlations were found between hourly N_2O flux and T_{soil} at all tidal wetland zones except the FM PZ (table 18). In addition, moderate to strong, positive correlations were found between hourly N_2O flux and T_{air_in} and weak to strong, positive correlations with PAR_{in} at all tidal wetland zones with the exception of FM PZ (table 18). Furthermore, a significant, moderate, negative correlation was found between hourly BM PZ N_2O flux and VWC and weak negative correlations between hourly SM HMu and SM HMg N_2O fluxes and VWC (table 18). In contrast, a weak, positive correlation was found between hourly SM PZ N_2O flux and VWC

(table 18). The soil electrical conductivity had a moderate positive correlation with hourly BM PZ N_2O flux, but weak to moderate negative with hourly SM LM and SM HMu N_2O flux (table 18). Finally, hourly CO_2 land-atmosphere fluxes were moderately strong, negatively, correlated to hourly BM PZ, SM PZ and SM HMu N_2O fluxes but contrastingly, positively although weakly correlated to hourly SM HMg N_2O flux (table 18).

Table 18 Spearman's correlation coefficients (ρ) with p values and number of observations for hourly N_2O land-atmosphere fluxes (mg m^{-2} h^{-1}) and the environmental variables: hourly CH_4 flux, hourly CO_2 flux, soil volumetric water content (VWC), electrical conductivity (EC), temperature (T_{soil}) and headspace air temperature (T_{air_in}) as well as photosynthetic active radiation inside the flux chamber (PAR_{in}).

tidal wetland zone	**CH_4** (mg m^{-2} h^{-1})	**CO_2** (mg m^{-2} h^{-1})	**VWC** (m^{-3} m^{-3})	**EC** (µS cm^{-1})	**T_{soil}** (°C)	**T_{air_in}** (°C)	**PAR_{in}** (µmol s^{-1} m^{-2})
FM PZ	ρ = 0.33 p = 0.02 n = 56	NS	NS	NS	NS	NS	NS
BM PZ	ρ = 0.64 p < 0.01 n = 42	ρ = -0.69 p < 0.01 n= 42	ρ = -0.44 p = 0.003 n = 42	ρ = 0.53 p < 0.01 n = 42	ρ = 0.65 p < 0.01 n = 42	ρ = 0.59 p < 0.01 n = 32	ρ = 0.63 p < 0.01 n = 32
SM PZ	NS	ρ = -0.53 p < 0.01 n = 85	ρ = 0.35 p < 0.01 n = 71	NS	ρ = 0.37 p < 0.01 n = 71	ρ = 0.45 p < 0.01 n = 53	ρ = 0.39 p < 0.04 n = 53
SM LM	NS	NS	NS	ρ = -0.28 p = 0.03 n = 59	ρ = 0.44 p < 0.01 n = 59	ρ = 0.76 p < 0.01 n = 41	ρ = 0.78 p < 0.01 n = 41
SM HMu	NS	ρ = -0.49 p < 0.01 n = 76	ρ = -0.34 p < 0.01 n = 61	ρ = -0.44 p < 0.01 n = 61	ρ = 0.47 p < 0.01 n = 61	ρ = 0.50 p < 0.01 n = 41	ρ = 0.65 p < 0.01 n = 41
SM HMg	NS	ρ = 0.24 p = 0.03 n = 79	ρ = -0.29 p = 0.02 n = 67	NS	ρ = 0.53 p < 0.01 n = 67	ρ = 0.62 p < 0.01 n = 46	ρ = 0.73 p < 0.01 n = 46

Spearman's correlation plots for the hourly CH_4 and N_2O land-atmosphere fluxes and tested environmental variables are included in the appendix T figure 34 and 35. Due to lacking observations for some of the tested variables in time, the included number of data points is smaller and therefore the results reported in these correlation plots deviate slightly from those reported in tables 17 and 18 and table 42. Various of the environmental variables were correlated with each other. Soil EC showed significant weak to moderately strong, negative correlations with PAR_{in} and moderately strong, negative correlations with T_{soil} and T_{air_in} at SM LM, SM HMu and SM HMg. Within the SM HMu and SM HMg, soil EC was strong to perfectly, positively, correlated with soil VWC, in contrast to the BM PZ soil where a moderately strong, negative correlation was observed between EC and VWC. Soil VWC showed both positive and negative correlations with T_{soil} and T_{air_in} with a strong, positive correlation at SM PZ and moderate, positive correlation at SM LM. However, a strong negative strong correlation was found for the FM PZ soil and moderate negative correlation for the SM HMu soil. T_{soil} showed significant, perfect, positive correlations with T_{air_in} and moderate to strong, positive correlations with PAR_{in} at all tested tidal wetland zones.

Figure 19 shows the correlation plots of the maximum, average, median and minimum hourly CH_4 or N_2O land-atmosphere flux observed at each replicate flux plot per tidal wetland zone with the average and median RI_{tot} at each replicate plot per tidal wetland zone (n = 30). The correlation tests showed generally, a moderate to strong, positive correlation between hourly CH_4 flux and RI_{tot}, whilst for hourly N_2O fluxes, a moderate negative correlation was found and only between the median hourly N_2O flux and RI_{tot}.

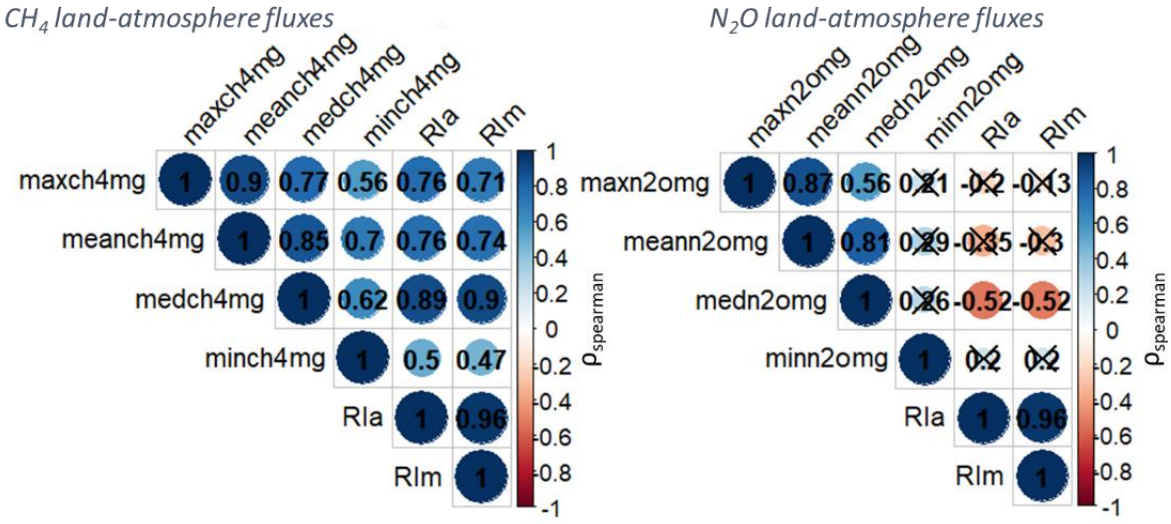

Figure 19 Spearman's correlations for hourly CH_4 (left) and N_2O (right) land-atmosphere fluxes as maximum (maxch4mg or maxn2omg), averaged (meanch4mg or meann2omg) median (medch4mg or medn2omg) and minimum (minch4mh or minn2omh) fluxes from the three pioneer zones along the Elbe river and the additional three salt marsh flooding frequency zones and RI_{tot} as mean (RIa) and median (RIm) over 60 cm depth, for all measurement campaigns. Number of observations is 30, with 5 replicate plots per tidal wetland zone and the 6 zones pooled together. An X in the correlation coefficient boxes indicates a non-significant correlation.

In figure 20 the results from the Spearman's correlation tests are visualized for average and median hourly CH_4 land-atmosphere fluxes and RI_{tot} at the replicate plots per meteorological season. The results show positive correlations with varying strengths. The correlations were moderately strong in autumn, strong in winter, moderately to strong in spring and strong in summer. The highest correlation coefficients are observed for the season median CH_4 fluxes with depth median, season average RI_{tot} in autumn, with depth average, season average RI_{tot} in winter, with depth median RI_{tot} in spring and with depth average RI_{tot} or depth median and time average RI_{tot} in summer.

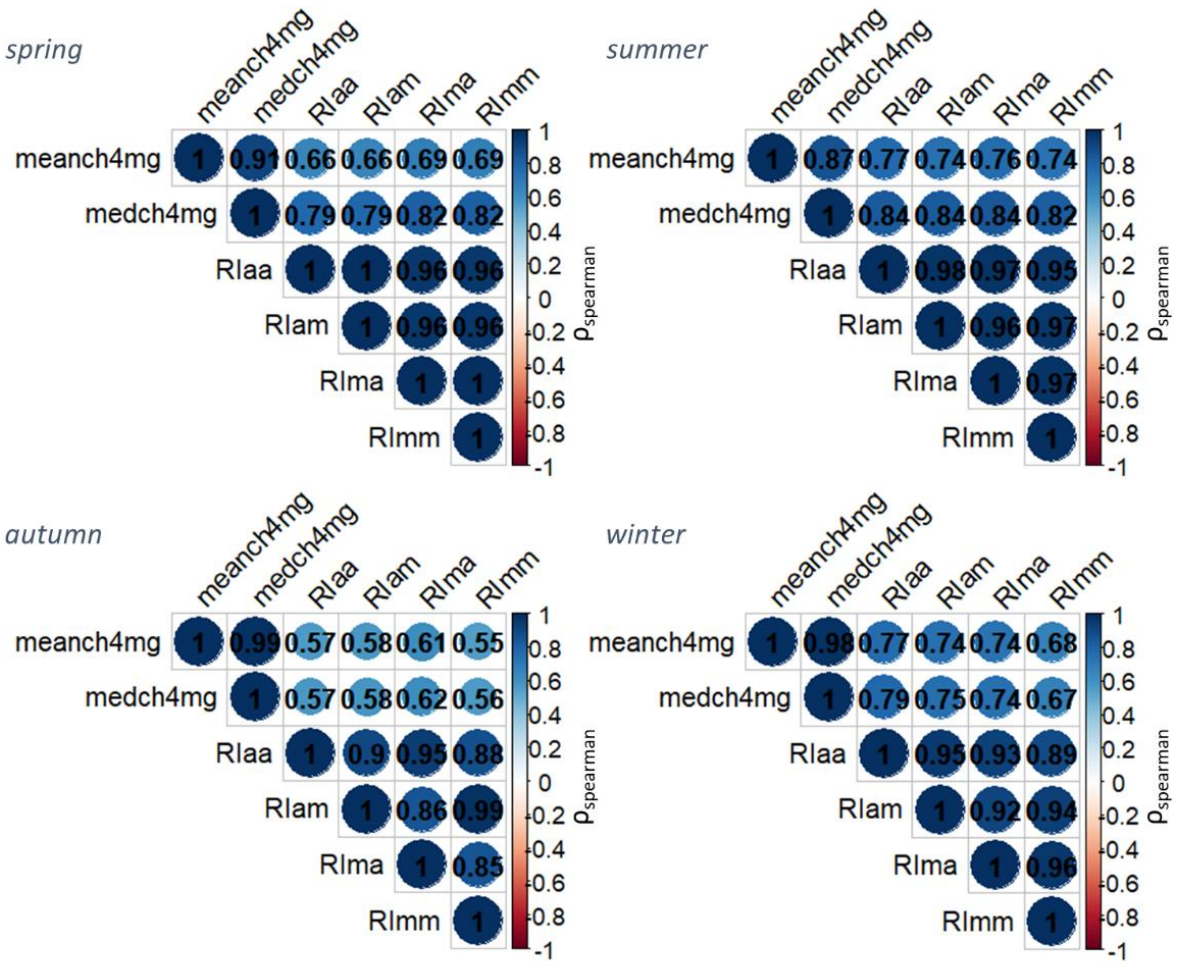

Figure 20 Spearman's correlations for hourly CH_4 land-atmosphere fluxes as average (meanch4mg) and median (medch4mg) CH_4 flux per meteorological season, from the three pioneer zones along the Elbe river and the additional three salt marsh flooding frequency zones, for all measurement campaigns, and RI as mean (RIaX) and median (RImX) over 60 cm depth and average (RIaa or RIma) or median (RIam or RImm) over the meteorological seasons. 30 Observations consisting of 5 replicate plots and 6 tidal wetlands zones pooled together for winter, spring and summer and 25 observations for autumn due to lacking flux chamber data from BM PZ during this season. An X in the correlation coefficient boxes indicates a non-significant correlation.

Figure 21 shows the results from the average and median hourly N_2O land-atmosphere Spearman's correlation tests with RI_{tot} at the replicate plots per meteorological season. The correlations were moderately strong between N_2O flux and RI_{tot} (figure 21) as was observed earlier when considering all flux data collected at each of the six tidal wetland zones (figure 19). The correlation sign altered between the seasons. In autumn and spring, the hourly N_2O land-atmosphere fluxes were negatively correlated with RI_{tot} and positively in winter and summer. The highest correlation coefficients were observed for median hourly N_2O fluxes with the depth and time averaged RI_{tot} in autumn and winter, but with depth averaged and season median RI_{tot} in summer. In spring, the highest correlation coefficient was found for the season averaged hourly N_2O flux and depth averaged RI_{tot}.

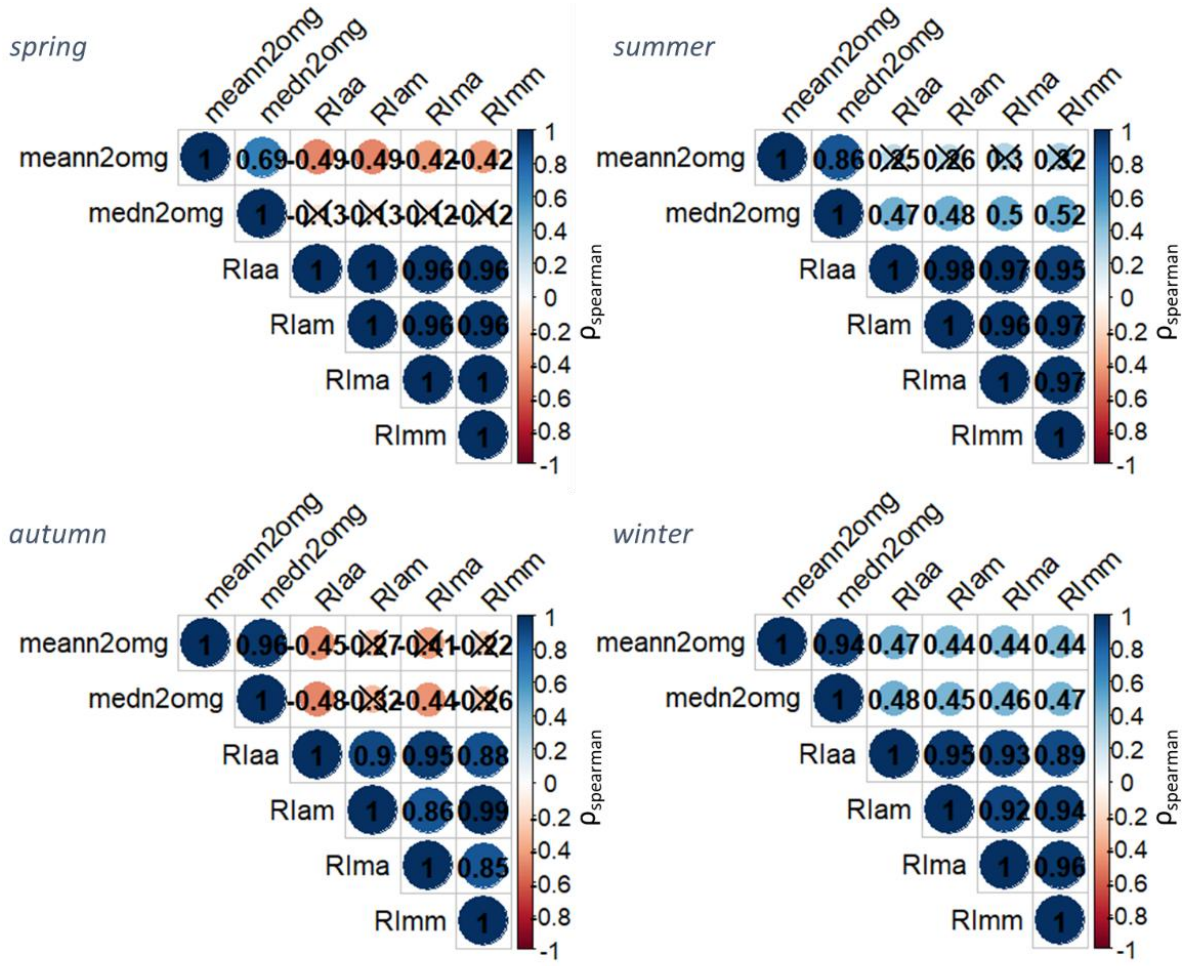

Figure 21 Spearman's correlations for N_2O land-atmosphere fluxes as average (meann2omg) and median (medn2omg) N_2O flux per meteorological season, from the three pioneer zones along the Elbe river and the additional three salt marsh flooding frequency zones, for all measurement campaigns, and RI as mean (RIax) and median (RImx) over 60 cm depth and average (RIaa or RIma) or median (RIam or RImm) over the meteorological seasons. 30 Observations consisting of 5 replicate plots and 6 tidal wetlands zones are included in winter, spring and summer and 25 observations for autumn due to lacking flux chamber data from BM PZ during this season. X in the correlation coefficient boxes indicates a non-significant correlation.

Figure 22 visualizes the significant Spearman's correlations between average and median hourly CH_4 land-atmosphere flux and RI_{10cm} at the replicate plots of BM PZ and SM PZ. The other tidal wetland zones, as well as the N_2O land-atmosphere fluxes did not result in significant correlations with RI_{10cm}. The average and median hourly BM PZ CH_4 flux showed a strong positive correlation with the upper two RI_{10cm} increments (RI010 and RI1020, figure 22). The average and median hourly SM PZ CH_4 flux was moderately, positive correlated with the middle RI10cm increments, starting at 20 cm up to 50 cm soil depth (RI2030, RI3040 and RI4050, figure 22). The highest correlation coefficients were observed for RI_{10cm} from 0 to 10 cm at BM PZ and 30 to 40 cm at SM PZ

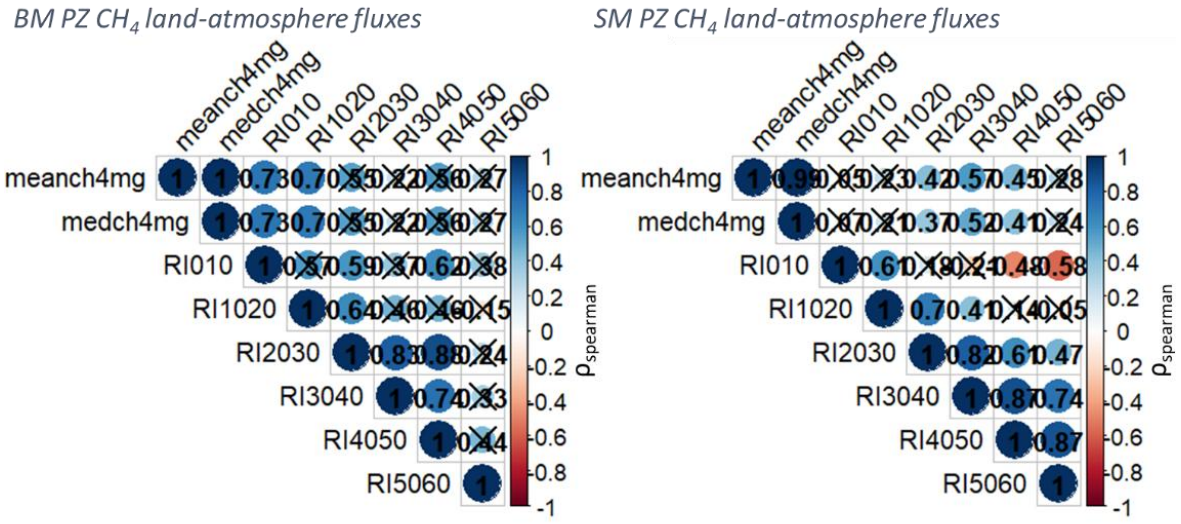

Figure 22 Spearman's correlations for CH_4 land-atmosphere fluxes as averaged (meanch4mg) and the median (medch4mg) monthly flux from BM PZ (left) and SM PZ (right) and RI_{10cm}, the RI values per 10 cm depth increment. 14 Observations are included in the correlation plot of the BM PZ and 37 observations in the correlation plot of SM PZ. X in the correlation coefficient boxes indicates a non-significant correlation.

3.4.6 Vegetation characteristics at the greenhouse gas plots

Different plant species inhabited the flux replicate plots of the different salinity zones and different flooding frequency zones. The FM PZ was dominated by *Typha angustifolia* and *Caltha palustris,* with plot 3 being dominantly covered with *Caltha palustris*, whereas the other plots were dominated by *Typha angustifolia* (appendix U table 41). The share of bare soil in the flux replicate plots as well as the above ground biomass also varied within the FM PZ. Flux replicate plot 3 was characterized by highest vegetation coverage, highest above ground biomass and lowest bare soil coverage and plot 4 by lowest vegetation coverage, lowest above ground biomass and highest bare soil coverage. The other plots ranked from high to low presence of vegetation: 2, 1 and 5. The plots at BM PZ were dominated by *Bolboschoenus maritimus* and varied in vegetation coverage and above ground biomass. Plots 1, 2 and 3 had larger vegetation coverage and biomass than plot 4 and plot 5 (appendix U table 41). The SM PZ plant community was more divers, with 4 to 6 species present compared to 1 to 2 species at the other two PZ. The SM PZ flux replicate plots were dominated by *Spartina anglica*, with increasing share of this species from 45 % at plot 1 to 80 % at plot 5. The number and occurrence of the other species, *Puccinellia maritima*, *Aster tripolium*, *Atriplex prostrata*, *Suaeda maritima*, *Triglochin maritima*, *Halimione portulacoides*, *Salicornia europaea*, increased from plot 5 to 1. The largest share of bare soil and lowest above ground biomass were found at plot 3 (appendix U table 41).

Within the salt marsh, the LM had highest species diversity with 9 to 11 species per flux replicate plot. *Puccinellia maritima* occurred in highest coverages but did not exceed 50 %. Additionally, *Aster tripolium* and *Festuca Rubra* were present in relatively large shares, ranging between 5 and 20 % (appendix U table 41). The HMu was dominated by *Elymus*

athericus, except for plot 3 which had a relatively high occurance of *Aster tripolium*, *Atriplex prostrata* and coverage of bare soil, which was reflected in the above ground biomass (appendix U table 41). Finally, the HMg was dominantly inhabited by grasses, especially *Festuca rubra* (35 to 75%) in addition to *Puccinellia maritima*, *Agrostis stolonifera* and *Lolium perenne*. The HMg had lowest above ground biomass but also lowest bare soil coverage among the flooding frequency zones.

3.4.7 Greenhouse gas flux uncertainty and sensitivity analyses

Flux chamber headspace volume

The calculated maximum headspace volume uncertainty, e_{Vdim}, for Chamber1 and Chamber2 was respectively 0.00129 m^3 and 0.00119 m^3 based on the quantification of flux chambers dimensions. The calculations showed that the larger the construction and the more separate parts, the larger the uncertainty (appendix V table 42). The highest uncertainty was found for the combination of Chamber2 plus two small and the large extension ($V_{headspace}$ = 1.455 m^3) with an e_{Vdim} of 0.00252 m^3 (appendix V table 42).

An additional uncertainty was caused by the flexible sheet-walls of Chamber1. In- and outward movement of the plastic sheet was observed on windy days. An approximation of the maximum possible volume change resulting from this phenomenon reached up to 5.4 % of the headspace volume, namely 0.030 m^3 upon 0.555 m^3.

Soil surface to collar rim volume

Headspace volumes for the BM PZ flux measurements were corrected for the additional volume gain or loss from the soil-surface-to-collar as earlier described. The associated maximum uncertainty in headspace volume ($e_{Vdim_sse_BM}$) was 0.00194 m^3 and was found for the combined construction of Chamber2 with large extension at plot 5 at BM PZ (appendix V table 43).

The maximum soil-surface-to-collar-rim volumes (V_{sse}) were 0.005 m^3, 0.019 m^3, 0.016 m^3, - 0.009 m^3 at SM PZ, SM LM, SM HMu and SM HMg respectively, observed at plots 4, 1, 4, 2 respectively (appendix V table 44). The corresponding maximum soil-surface-to-collar-rim height standard errors per SM zone were 0.70 cm, 1.05 cm, 1.10 cm and 0.52 cm at PZ, LM, HMu and HMg respectively, found for plots 1, 1, 4 and 5 respectively (appendix V table 44). The resulting highest e_{Vdim_sse} were 0.00601 m^3, 0.00855 m^3, 0.00895 m^3 and 0.00468 m^3 for Chamber2 measurements at SM PZ, SM LM, SM HMu and SM HMg, respectively, found for plots 1, 1, 4, 5 respectively (appendix V table 44). The addition of the large extension led to a maximum combined $e_{Vdim_sse_SM_HMu}$ of 0.00907 m^3 at SM HMu plot 4.

Vegetation standing stock volume

Vegetation standing stock volumes were estimated to be 3.45 * 10^{-3} ± 1.07 * 10^{-3} m^3 at PZ FM, 2.47 * 10^{-3} ± 0.35 * 10^{-3} m^3 at PZ BM and 4.94 * 10^{-3} ± 0.35 * 10^{-3} m^3 at HMu SM

(appendix V tables 45 and 46). The largest volumes were predicted for plot 3 at PZ FM, dominated by *Caltha Palustric,* plot 4 at PZ BM dominated by *Bolboschoenus maritimus* and plot 1 at HMu SM dominated by *Elymus athericus,* with respectively 7.61 * 10^{-3} (± 3.85 * 10^{-3}), 2.78 * 10^{-3} (± 1.31 * 10^{-3}) and 6.16 * 10^{-3} (± 8.95 * 10^{-4}) m^3. An overview of all the calculated volumes is given in the (appendix V table 46).

Adding the uncertainty in vegetation standing stock volume to the other two headspace uncertainties resulted in a final maximum combined uncertainty e_{V_total}, at FM PZ of 0.00371 m^3 (Chamber2 with 2 small and the large extension), at BM PZ of 0.00211 m^3 (Chamber2 with the large extension) and at SM HMu of 0.00907 (Chamber2 with one small extension) for the measurements conducted in June and July 2023 (appendix V table 46).

Headspace air temperature

The thermometer precisions differed between the manual and automatic thermometers as reported in the methods paragraphs. Both manual and automatic thermometers were used with Chamber1 during some measurement campaigns, from these results the maximum occurring difference was determined to be 0.4 ± 0.2 °C between the two thermometers.

The difference between the T_{air_in}, the four-minute average headspace air temperature, and $T_{initial}$, the initial headspace air temperature, are summarized in appendix V table 47. The maximum difference recorded was a 4.1 °C higher $T_{initial}$ compared to T_{air_in} and a 3.5 °C lower $T_{initial}$ compared to T_{air_in} for the considered measurement days in the summer of 2023. The standard deviations between the two temperatures were 2.7, 1.8 and 1.5 °C for FM PZ, BM PZ and SM HMu respectively.

Uncertainty in surface area

Surface area was associated with an uncertainty (e_{Adim}) of 0.0018 m^2. After the approximation of maximum potential collar deformation, the maximum combined e_{Adim_def} was 0.020 m^2 for collars at the BM PZ and SM HMu. Collars did not undergo deformation upon installation or over time at the FM PZ flux replicate plots.

Land-atmosphere flux calculation sensitivity analyses

Table 19 A and B and figure 23 summarize the results of the sensitivity analyses. The change in flux chamber headspace volume resulted in smaller calculated flux magnitudes, except for SM HMu fluxes from flux replicate plots 1, 3 and 4. These three cases had a net increase in headspace volume, since the gain from soil-surface-to-collar rim volume (V_{SSE}) exceeded the loss by vegetation standing stock volume (V_{veg}) and consequently led to larger flux magnitudes. The CH_4 flux magnitudes changed in response to the adapted headspace volume with maximally 0.4 %, 1.1 % and 5.5 % for the FM PZ, BM PZ and SM HMu fluxes respectively. FM PZ and BM PZ N_2O flux magnitudes were slightly more affected by volume correction, with respective maximum differences of 0.6 % and 1.8 % but SM HMu N_2O fluxes were slightly less affected with a maximum difference of 3.6 %. The V_{corr} led to a change in flux magnitude that was smaller than the flux error of the original calculated flux, with

exception of the BM PZ CH_4 flux at plot 2 on 14th June 2023 and SM HMu N_2O fluxes at plot 4 on 15th of June 2023 and on 27th of June 2023.

The effect of using the initial temperature ($T_{initial}$) in the flux calculations instead of the 4-minute average temperature (T_{air_in}), showed to generally lead to larger flux sizes (table 19). However, the calculated FM PZ fluxes from plot 4 and 5 on 11th of July 2023 had higher $T_{initial}$ than their T_{air_in} and consequently, resulted in smaller flux magnitudes upon recalculation. The highest relative changes in CH_4 flux magnitudes were respectively 1.3 %, 1.3 % and 4.6 % for FM PZ, BM PZ and SM HMu upon recalculating with $T_{initial}$. In comparison, highest relative change in N_2O flux magnitudes were 1.3 %, 1.3 % and 2.6 % for FM PZ, BM PZ and SM HMu respectively. The switch to $T_{initial}$ led to a change in flux magnitude that was smaller than the flux error of the original calculated flux, with exception of the FM PZ CH_4 flux at plot 5 on 11th July 2023 and the BM PZ CH_4 at plot 3 BM PZ on 28th of June 2023.

The combined volume change and temperature choice effect led in some cases to even larger changes in the calculated flux magnitudes compared to the individual effects, but in other cases the effects were balanced out (table 19). Maximum differences between CH_4 original and recalculated fluxes were 1.4 %, 1.1 % and 6.4 % at FM PZ, BM PZ and SM HMu respectively. As for N_2O, maximum differences were 1.4 %, 1.5 and 4.5 % at FM PZ, BM PZ and SM HMu respectively. The combination of V_{corr} and $T_{initial}$ led to a change in flux magnitude that was smaller than the flux error of the original calculated flux, with exception of FM PZ CH_4 flux at plot on 11th July 2023, BM PZ CH_4 flux at plot 3 on 28th of June 2023 and SM HMu CH_4 flux at plot 1 on 27th of June and the SM HMu N_2O fluxes at plot 4 on 15th June 2023 and 27th of June 2023.

Propagated flux variable uncertainty assessment

The flux chamber dimensions, soil surface unevenness and vegetation standing stock resulted in an approximated maximum uncertainty of 0.00371 m^3 at FM PZ, 0.00211 m^3 at BM PZ and 0.00907 m^3 at SM HMu. The applied err_V of 0.00721 m^3 showed to be conservative with respect to these approximated maximum uncertainties in flux chamber headspace volumes for June and July 2023 fluxes at FM PZ and BM PZ, but showed to be smaller than the approximated uncertainty for the measurements at SM HMu. Furthermore, the head space volume uncertainty increased when including the wind induced deformation of Chamber1, showing a change from 0.00129 m^3 to 0.030 m^3 for solely flux chamber size uncertainty. The maximum surface area uncertainty calculated was 0.0018 m^2, in comparison to the applied err_A of 0.0012 m^2. Furthermore, the uncertainty increased to 0.020 m^2 when including collar deformation. Finally, the HMP45C sensor precision of 0.2 to 0.3 °C in the range of 0 to 30 °C was higher than the err_T used in the flux error calculation (EQ2). The combination of these results suggests that the flux errors of the calculated fluxes in June and July of 2023 (table 19) represent too modest uncertainty windows for peak growing season fluxes.

Recalculating the flux errors with these propagated uncertainties for the fluxes reported in table 19 A and B indicated that the errors would range between 1.68 to 6.00 mg CH_4 m^{-2} h^{-1} at FM PZ, 3.51 * 10^{-2} to 18.7 * 10^{-2} mg CH_4 m^{-2} h^{-1} at BM PZ and 2.73 * 10^{-4} and 6.88

*10^{-4} mg CH_4 m^{-2} h^{-1} at SM HMu. Whereas for N_2O the errors ranged 4.86 * 10^{-3} to 6.74 * 10^{-3} mg N_2O m^{-2} h^{-1} at FM PZ, 2.51 * 10^{-3} to 5.52 * 10^{-3} mg N_2O m^{-2} h^{-1} at BM PZ and 2.32 * 10^{-3} to 11.06 * 10^{-3} mg N_2O m^{-2} h^{-1} at SM HMu.

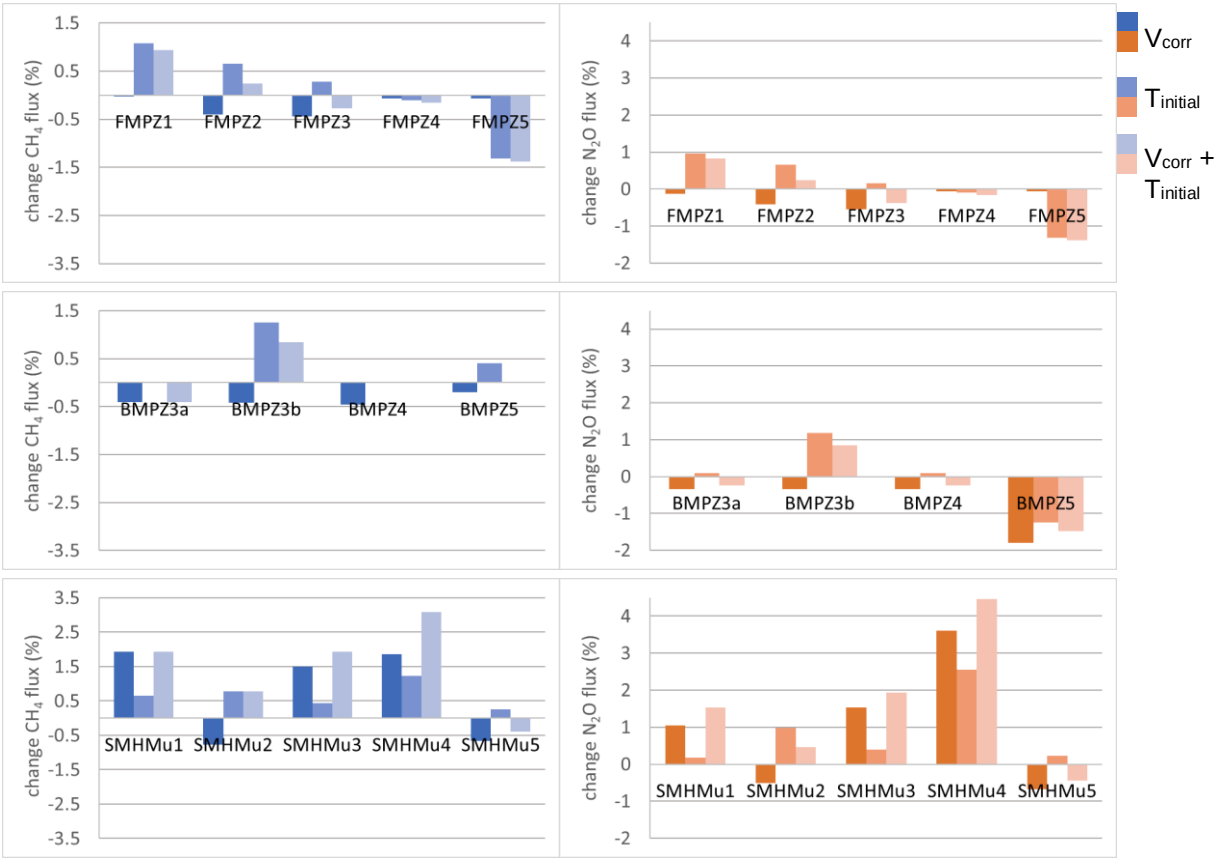

Figure 23 Change in hourly CH_4 (left, blue) and N_2O (right, red) land-atmosphere fluxes as result of correcting headspace volume for vegetation standing stock and soil-surface-to-collar-rim volume (V_{corr}), for changing input temperature from 4-minute average (T_{air_in}) to initial temperature ($T_{initial}$), and for the combined effect of V_{corr} and $T_{initial}$. FM PZ, BM PZ and SM HMu are presented from top to bottom graphs with corresponding plot numbers. Graphs include only the results of calculated fluxes from 27th, 28th of June and 11th of July 2023 (table 19).

Table 19 A) Overview of sensitivity analysis on hourly CH_4 land-atmosphere fluxes from adaptations to headspace volume and input temperature values. Base calculated fluxes and recalculated fluxes are reported, with the respective asolute volume and temperature change tested for the respective measurement dates considered.

flux ID	**change in V** (m^3) **and T** (°C)	**ORG CH_4 flux ± abs. error** (mg m^{-2} h^{-1})	**CH_4 flux $V_{corrected}$** (mg m^{-2} h^{-1})	**CH_4 flux $T_{initial}$** (mg m^{-2} h^{-1})	**CH_4 flux $V_{corrected}$ and $T_{initial}$** (mg m^{-2} h^{-1})
FM PZ 1	V - 0.002				
11.07.2023	T - 2.9	148.39 ± 1.97	148.35	149.98	149.77
FM PZ 2	V - 0.006				
11.07.2023	T - 2.0	50.11 ± 0.34	49.91	50.44	50.23
FM PZ 3	V - 0.008				
11.07.2023	T - 0.5	43.11 ± 0.38	42.92	43.23	42.99
FM PZ 4	V - 0.001				
11.07.2023	T + 0.3	129.80 ± 2.72	129.71	129.67	129.59
FM PZ 5	V - 0.001				
11.07.2023	T +4.1	73.56 ± 0.89*	73.51*	72.59*	72.54*
BM PZ 2	V - 0.003				
14.06.2023	T +2.3	0.92 ± 0.76 *10^{-2}	0.91	0.91	0.91
BM PZ 3	V - 0.003				
14.06.2023 a	T 0	2.18 ± 2.07 *10^{-2}	2.17	2.18	2.17
14.06.2023 b	T -0.8	1.34 ± 1.12 *10^{-2}	1.34	1.35	1.34
28.06.2023 a	T -0.3	2.49 ± 2.04 *10^{-2}	2.48	2.49	2.48
28.06.2023 b	T -3.5	2.39 ± 1.96 *10^{-2}	2.38	2.42	2.41
BM PZ 4	V - 0.003				
14.06.2023	T 0	1.75 ± 1.45 *10^{-2}	1.75	1.75	1.75
28.06.2023	T - 0.3	2.18 ± 1.81 *10^{-2}	2.17	2.18	2.18
BM PZ 5	V - 0.002				
14.06.2023 a	T + 1.8	2.06 ± 1.70 *10^{-2}	2.05	2.04	2.04
14.06.2023 b	T + 2.3	1.96 ± 1.62 *10^{-2}	1.96	1.95	1.94
28.06.2023	T - 1.0	4.88 ± 4.02 *10^{-2}	4.87	4.90	4.88
SM HMu 1	V +0.008				
15.06.2023	T -0.9	-5.44 * 10^{-3} ± 3.11 * 10^{-4}	-5.52 * 10^{-3}	-5.46 * 10^{-3}	-5.53 * 10^{-3}
27.06.2023	T -0.4	15.47 * 10^{-3} ± 3.57 * 10^{-4}	1.58 * 10^{-2}	1.56 * 10^{-2}	1.58 * 10^{-2}
SM HMu 2	V -0.003				
15.06.2023	T -0.8	9.27 * 10^{-3} ± 3.38 * 10^{-4}	9.22 * 10^{-3}	9.29 * 10^{-3}	9.25 * 10^{-3}
27.06.2023	T -2.9	1.30 * 10^{-3} ± 2.91 * 10^{-4}	1.29 * 10^{-3}	1.31 * 10^{-3}	1.31 * 10^{-3}
SM HMu 3	V +0.009				
15.06.2023	T -3.3	-1.09 * 10^{-3} ± 3.35 * 10^{-4}	-1.15 * 10^{-3}	-1.14 * 10^{-3}	-1.16 * 10^{-3}
27.06.2023	T -1.2	4.68 * 10^{-3} ± 2.85 * 10^{-4}	4.75 * 10^{-3}	4.70 * 10^{-3}	4.77 * 10^{-3}
SM HMu 4	V +0.011				
15.06.2023	T -0.5	1.31 * 10^{-2} ± 3.30 * 10^{-4}	1.33 * 10^{-2}	1.31 * 10^{-2}	1.33 * 10^{-2}
27.06.2023	T -2.5	-1.62 * 10^{-3} ± 2.66 * 10^{-4}	-1.65 * 10^{-3}	-1.64 * 10^{-3}	-1.67 * 10^{-3}
SM HMu 5	V -0.004				
15.06.2023	T +1.9	6.48 * 10^{-3} ± 2.66 * 10^{-4}	6.44 * 10^{-3}	6.44 * 10^{-3}	6.40 * 10^{-3}
27.06.2023	T -0.7	-0.76 * 10^{-3} ± 2.73 * 10^{-4}	-0.76 * 10^{-3}	-0.76 * 10^{-3}	-0.76 * 10^{-3}

* QL3, calculated land-atmosphere flux flagged with quality level 3 flux as determined in flux data quality assessment section

Table 19 B) Overview of sensitivity analysis on hourly N_2O land-atmosphere fluxes from adaptations to headspace volume and input temperature values. Base calculated fluxes and recalculated fluxes are reported, with the respective asolute volume and temperature change tested for the respective measurement dates considered.

flux ID	**change in V** (m^3) **and T** (°C)	**N_2O flux ± abs. error** (mg m^{-2} h^{-1})	**N_2O flux $V_{corrected}$** (mg m^{-2} h^{-1})	**N_2O flux $T_{initial}$** (mg m^{-2} h^{-1})	**N_2O flux $V_{corrected}$ and $T_{initial}$** (mg m^{-2} h^{-1})
FM PZ 1	V - 0.002				
11.07.2023	T - 2.9	$1.10 * 10^{-1} \pm 5.29 * 10^{-3}$	$1.09 * 10^{-1}$	$1.11 * 10^{-1}$	$1.10 * 10^{-1}$
FM PZ 2	V - 0.006				
11.07.2023	T - 2.0	$8.56 * 10^{-2} \pm 4.39 * 10^{-3}$	$8.52 * 10^{-2}$	$8.61 * 10^{-2}$	$8.58 * 10^{-2}$
FM PZ 3	V - 0.008				
11.07.2023	T - 0.5	$8.00 * 10^{-2} \pm 4.58 * 10^{-3}$	$7.96 * 10^{-2}$	$8.01 * 10^{-2}$	$7.97 * 10^{-2}$
FM PZ 4	V - 0.001				
11.07.2023	T + 0.3	$8.11 * 10^{-2} \pm 4.23 * 10^{-3}$	$8.11 * 10^{-2}$	$8.11 * 10^{-2}$	$8.10 * 10^{-2}$
FM PZ 5	V - 0.001				
11.07.2023	T +4.1	$7.20 * 10^{-2} \pm 4.01 * 10^{-3}$	$7.20 * 10^{-2}$	$7.11 * 10^{-2}$	$7.10 * 10^{-2}$
BM PZ 2	V - 0.003				
14.06.2023	T +2.3	$1.15 * 10^{-1} \pm 2.90 * 10^{-3}$	$1.14 * 10^{-1}$	$1.14 * 10^{-1}$	$1.13 * 10^{-1}$
BM PZ 3	V - 0.003				
14.06.2023 a	T 0	$1.49 * 10^{-2} \pm 3.31 * 10^{-3}$	$1.49 * 10^{-2}$	$1.49 * 10^{-2}$	$1.49 * 10^{-2}$
14.06.2023 b	T -0.8	$1.10 * 10^{-1} \pm 2.80 * 10^{-3}$	$1.10 * 10^{-1}$	$1.11 * 10^{-1}$	$1.10 * 10^{-1}$
28.06.2023 a	T -0.3	$2.63 * 10^{-2} \pm 2.53 * 10^{-3}$	$2.62 * 10^{-2}$	$2.63 * 10^{-2}$	$2.62 * 10^{-2}$
28.06.2023 b	T -3.5	$2.81 * 10^{-3} \pm 2.52 * 10^{-3}$	$2.80 * 10^{-3}$	$2.84 * 10^{-3}$	$2.83 * 10^{-3}$
BM PZ 4	V - 0.003				
14.06.2023	T 0	$1.19 * 10^{-1} \pm 3.27 * 10^{-3}$	$1.18 * 10^{-1}$	$1.19 * 10^{-1}$	$1.18 * 10^{-1}$
28.06.2023	T - 0.3	$9.80 * 10^{-3} \pm 2.59 * 10^{-3}$	$9.76 * 10^{-3}$	$9.81 * 10^{-3}$	$9.77 * 10^{-3}$
BM PZ 5	V - 0.002				
14.06.2023 a	T + 1.8	$9.10 * 10^{-2} \pm 2.93 * 10^{-3}$	$9.08 * 10^{-2}$	$9.05 * 10^{-2}$	$9.03 * 10^{-2}$
14.06.2023 b	T + 2.3	$1.06 * 10^{-1} \pm 2.78 * 10^{-3}$	$1.06 * 10^{-1}$	$1.06 * 10^{-1}$	$1.05 * 10^{-1}$
28.06.2023	T - 1.0	$8.10 * 10^{-2} \pm 3.26 * 10^{-3}$	$7.96 * 10^{-2}$	$8.00 * 10^{-2}$	$7.99 * 10^{-2}$
SM HMu 1	V +0.008				
15.06.2023	T -0.9	$4.98 * 10^{-2} \pm 1.78 * 10^{-3}$	$5.03 * 10^{-2}$	$4.98 * 10^{-2}$	$5.05 * 10^{-2}$
27.06.2023	T -0.4	$1.43 * 10^{-2} \pm 2.20 * 10^{-3}$	$1.45 * 10^{-2}$	$1.44 * 10^{-2}$	$1.46 * 10^{-2}$
SM HMu 2	V -0.003				
15.06.2023	T -0.8	$1.16 * 10^{-1} \pm 2.18 * 10^{-3}$	$1.16 * 10^{-1}$	$1.17 * 10^{-1}$	$1.16 * 10^{-1}$
27.06.2023	T -2.9	$8.42 * 10^{-2} \pm 2.23 * 10^{-3}$	$8.37 * 10^{-2}$	$8.50 * 10^{-2}$	$8.46 * 10^{-2}$
SM HMu 3	V +0.009				
15.06.2023	T -3.3	$4.73 * 10^{-2} \pm 4.16 * 10^{-3}$	$4.80 * 10^{-2}$	$4.78 * 10^{-2}$	$4.85 * 10^{-2}$
27.06.2023	T -1.2	$5.88 * 10^{-2} \pm 2.24 * 10^{-3}$	$5.97 * 10^{-2}$	$5.91 * 10^{-2}$	$6.00 * 10^{-2}$
SM HMu 4	V +0.011				
15.06.2023	T -0.5	$2.73 * 10^{-1} \pm 3.95 * 10^{-3}$	$2.78 * 10^{-1}$	$2.74 * 10^{-1}$	$2.79 * 10^{-1}$
27.06.2023	T -2.5	$6.24 * 10^{-2} \pm 1.83 * 10^{-3}$	$6.47 * 10^{-2}$	$6.40 * 10^{-2}$	$6.52 * 10^{-2}$
SM HMu 5	V -0.004				
15.06.2023	T +1.9	$2.50 * 10^{-1} \pm 3.53 * 10^{-3}$	$2.49 * 10^{-1}$	$2.49 * 10^{-1}$	$2.47 * 10^{-1}$
27.06.2023	T -0.7	$1.01 * 10^{-1} \pm 2.25 * 10^{-3}$	$1.00 * 10^{-1}$	$1.01 * 10^{-1}$	$1.00 * 10^{-1}$

Chapter 4 Discussion

4.1 Characteristics of tidal wetland soils in the Elbe estuary

Soil formation of all nine studied tidal wetland soils was characterized by dynamic behavior of groundwater. Aside of all soils having gleyic properties, the three high marsh soils and the BM LM had ferric horizons and SM LM had a pisoplinthic horizon. These diagnostic horizons and the gleyic properties reflect the presence and accumulation of oxi- and reductimorphic features resulting from the dynamic and relative shallow groundwater tables in these soils. The salt marsh soils were further characterized by high levels of soluble salts, even dominantly at SM HMu, classifying it as a Solonchak. The salt marsh soils were also separated from brackish and fresh water marsh soils driven by high soil EC, pH_{CaCl2} and Cl^- content in the PCA. As marine and terrestrial water differ in these properties, these results indicate that the fresh water and brackish marsh soils are subject to more terrestrial water characterized floods and the salt marsh soils to more marine water characterized floods.

Interestingly, the BM LM soil classified as protosalic and had especially high EC_{se} values in the relatively sandy, low in organic carbon content, Ahr horizon located at 19 to 24 cm soil depth. Whereas, the SM LM soil had relatively lower EC_{se} values compared to SM PZ and SM HMu. However, both LM soils did not show clear differentiation from the other soils of the same salinity zones based on the PCA. The relatively low EC_{se} observed in SM LM soil could be related to higher percolation of water through the well-developed soil structure. Vertical and lateral movement of water could have supported the transport of infiltrated flood water away from the upper 60 cm of the SM LM soil. Possibly, the SM LM soil is also more affected by tidal pumping due to the developed soil structure in comparison to the SM HMu and SM PZ soils. In the SM HMu and SM PZ soils highest EC_{se} values were observed in the massive structured soil horizons.

Although the marine associated chemical characteristics set the salt marsh soils apart from the other tidal wetland soils, it was soil texture associated chemical characteristics that explained most of the variation between the tidal wetland soils according to the PCA. The fresh water marsh soils characterized with high clay and organic carbon contents and low bulk densities compared to the sandier, low organic carbon and high bulk density brackish marsh soils. This contrast was especially pronounced in the pioneer zones. The difference in soil texture likely results from differences in the Elbe's morphology between the sites. The fresh water marsh is sheltered by two islands from the rivers' main channel and the river is also wider and shallower compared to the river section abutting the brackish marsh (ABPmer Ltd, report R.1805, 2011). Consequently, incoming tidal flood carries fewer coarse particles at the fresh water marsh compared to the brackish marsh. Lower flow velocity with retreating tidal flood also allows finer sediments to settle over the fresh water marsh soil surfaces compared to the brackish marsh.

Soil texture, especially clay content, has been found to explain differences in soil organic carbon content among soils (Gorham, Lavery, Kelleway, Salinas, & Serrano, 2021; Kelleway, Saintilan, Macreadie, & Ralph, 2016; Wiesmeier et al., 2019) and hence could explain this contrast between the two sites too. Neiske et al. (2025) showed supporting

evidence for this explanation, as they found the largest share of soil organic carbon present in mineral associated organic matter. Furthermore, clay content was a good predictor for the amount of soil organic carbon at the same research sites as studied in this work (Neiske et al., 2025).

Vegetation too plays a role in the texture driven differences between fresh and brackish marsh soils. Vegetation standing stock dissipates wave energy and flow velocity (Möller et al., 2014; Schoutens et al., 2019; Vuik, Jonkman, Borsje, & Suzuki, 2016; Ysebaert et al., 2011) and species specific traits control the energy and wave dissipation, such as plant height, stem diameter and flexibility (Marjoribanks et al., 2019; Ysebaert et al., 2011). Since, flow velocity and wave energy of the tidal flood affects sedimentation rates and particle size settling out, vegetation can indirectly exert influence by affecting these former two features. The two dominant pioneer zone species *Typha angustifolia* and *Bolboschoenus maritimus* at the studied sites differ with respect to these traits. *Typha angustifolia* is generally taller, heavier, stiffer and has a larger leave area per individual than *Bolboschoenus maritima* (Schulte Ostermann et al., 2021) and therefore affect flow velocity of the in- and outgoing tidal flood differently. Furthermore, these two pioneer species differ in below ground biomass production and ratio of root mass and rhizome mass to total below ground mass (Schulte Ostermann et al., 2021). These differences can add to the explanation of the difference in soil organic carbon content in the two pioneer zone soils.

The salt marsh soils were also characterized by finer textured soils in comparison to the brackish marsh soils, which was most pronounced in the top soils. The presence of the finer textured soils at the salt marsh is likely due to the extent tidal planes and the groynes present between the salt marsh and the main river channel (ABPmer Ltd, report R.1805, 2011). The flow velocity of the tidal flood is reduced by the constructions and the large intertidal flats before reaching the salt marsh pioneer zone. Therefore, the incoming sediment load consists of finer particles and the settling rate is larger compared to the brackish marsh pioneer zone.

Abrupt textural changes in tidal wetland soils can reflect alternations to the estuarian environment or the occurrence of an incidental event such as a large storm surge. The FM LM and FM HMu soils had relative sandier layers starting at 18 and 30 cm depth reaching to 48 and 60 cm, respectively. These layers could be a reflection of the changes made to a sand bank located in the Elbe river bed in front of the FM. Dredging material has been deposited onto this sand bank since 1922, with a strong increase in deposition volume between 2000 and 2004 (ABPmer Ltd, report R.1805, 2011). The additions were reduced to volumes of before 1999 after 2005 (ABPmer Ltd, report R.1805, 2011). These interventions affected the river morphology and possibly suspended sediment characteristics in front of the FM and likely have affected sediment grain size settling on the FM soil surfaces. In the SM HMu, also a relatively sandy layer was found located at 58 cm to 63 cm depth. This coarser textured layer could be a relic of a large storm surge. The horizon boundary between the sandier layer and the one below was defined as a lithic discontinuity, indicating an abrupt textural change, and as a panpaic horizon, indicating a buried former surface horizon. This suggests that the soil surface was buried with cover material of a different textural composition, which could have been the result of a flooding event with large water volumes and high flow velocity.

The results from the soil description and classification show the relevance of these methods when conducting ecological and biogeochemically focused field experiments. In order to test hypothesis within a field experimental setting it is required to measure the control variables that cannot be manipulated. Even though a lot of material is available for soil characteristics in northern Europe and North Germany, such as the BÜK200 (BGR, 2018), the projection scales are often too large or the measurement points are too far away for extrapolation to provide information at field or treatment scales in tidal wetlands. I recommend to conduct soil descriptions and classification as part of the preparations in designing field experiments when addressing biogeochemically focused research questions in dynamic and variable ecosystems such as tidal wetlands.

4.2 Characteristics of soil redox conditions in the Elbe estuary

The IRIS retrieved RI_{tot} results showed stronger reducing conditions upstream the Elbe river. The observed differences related to a combination of studied environmental conditions. Since, the IRIS method relies on the metabolic activity of iron reducing microbes, it is limited by the availability of organic substrate required by these microbes (BJ Jenkinson & Franzmeier, 2006; Vepraskas & Richardson, 2001). The observed soil organic carbon contents would support more iron reduction in the FM, followed by SM and least in the BM. However, not only substrate availability but also sufficiently reducing conditions are required by the soil microbes to activate the ferrihydrite reduction process fundamental to the IRIS method. The actual flooding frequency of the soils varied between the salinity zones for the same flooding frequency categories. The BM PZ flooded accordingly to the tidal cycle of 12 hours, whereas the FM PZ flooded about half as often and SM PZ about a third as often (Branoff et al., 2024, preprint). While the BM PZ was flooded most regularly, its soil texture supports a smaller water holding capacity due to the larger grainsize of its sandy loam, loamy sand texture compared to the silty clay, silty clay loam of FM PZ. Additionally, the lower soil organic carbon content in the BM PZ soils supports lower water holding capacity too. The SM PZ had also a finer soil texture, consisting of silty clay loam and loam, compared to BM PZ, but a lower soil organic carbon content compared to FM PZ. This situates the SM PZ between FM PZ and BM PZ with regard to expected water holding capacity. On the other hand, SM PZ had the most developed soil structure in its upper 30 cm among the three pioneer zone soils, which would support the drainage of percolating water. The combination of these characteristics suggests regular hot moments of anaerobic conditions in the BM PZ but the relatively lower availability of substrates might limit the iron reduction. Whereas, the FM PZ soil offers more substrate but experiences less frequent albeit more durable anaerobic conditions, supporting the relatively most ideal conditions for the iron reducing microbes. The SM PZ offers less regular inducement of anaerobic conditions compared to BM PZ and less durable anaerobic conditions in the upper 30 cm compared to FM PZ. This combination of these soil characteristics could explain the observed highest RI_{tot} at the FM PZ soil and lowest RI_{tot} at the SM PZ.

The redox characterization results all showed an increase in reducing conditions with the increase in flooding frequency, when considering the full soil depth and measurement

time. This is reflected in the decreasing soil depth at which the permanently reducing conditions classes R3 and R2 appeared. Furthermore, it was shown by the higher RI_{tot} values at the three PZ, followed by the LM and finally HMu and by the decreasing redox potentials following that same order.

Over soil depth, the redox conditions followed the general pattern from aerobic and temporarily or locally without free oxygen in the top soils, to alternatingly aerobic and anaerobic conditions, to permanently reduced in the deepest soil sections. This sequence is expected based on general understanding of oxygen diffusion rates, microbial metabolism and rhizosphere processes (Ponnamperuma, 1972, Bartlett & Harriss, 1993; Dean et al., 2018; Gilbert & Frenzel, 1995; Murray et al., 2015; Segers, 1998; Yuan et al., 2019). Two $RC_{morphology}$ exceptions were R3 horizons situated on top of R4 horizons in SM LM and SM HMu soils. In contrast, the IRIS method results showed more iron reduction in the R4 compared to the above laying R3 in the SM LM. This suggests a possible false $RC_{morphology}$ classification of either of the two horizons. The RI_{tot} depth limit of 60 cm did not allow to compare the IRIS results with the $RC_{morphology}$ for the observation in the SM HMu soil. The two R4 classified layers had too low Munsell-values to classify as R3. Their colors could have been obscured by other soil constituents. As the Munsell-value has a strong relation with organic matter content in fine textured soils (D. G. Schulze et al., 1993), the high C_{org} content of the SM HMu R4 horizon at 63 to 70 cm could have limited the assessment of this layer. However, the SM LM R4 horizon at 31 to 45 cm was not relatively elevated in C_{org} and therefore has been assessed with a similar contribution of Corg to the Munsell value as the other described horizons. The redox potential results contradicted the soil descriptive based R3 classification. RC_{sensor} classified the SM LM at 5 cm, 10 cm and 30 cm depth as R4, while $RC_{morphology}$ resulted in R3 (Cr, 2 – 31 cm depth). On the other hand, the RC_{sensor} of the SM HMu 60 cm depth classified as R4, while $RC_{morphology}$ of the corresponding Cr horizon (58 - 63 cm depth) classified as R3. Even more, the two R3 classified horizons contained commonly occurring medium sized mottles (appendix L), when these are not relicts, their presence would support a possible false classification with $RC_{morphology}$. The two explanations both show the challenge and limitations when relying on matrix color when classifying the reducing conditions in the tidal wetland soil.

Remarkably, the IRIS method ($RI_{horizon}$) indicated less strongly reducing conditions in many of the deepest assessed horizons compared to the ones above. This observation was made in the FM PZ, FM LM, BM PZ, BM HMu, SM LM and SM HMu soils. The redox potential results contradict these observations for the two SM soils. The rH_{30cm}, falling in shallower horizons, were less reducing compared to the rH_{60cm}, while the $RI_{sensors}$ indeed suggested the other way around. A similar conflict in the results of these two methods was found for the SM LM upper 10 cm. The IRIS SM LM RI_{10cm} results suggest stronger reducing conditions in comparison to the SM PZ RI_{10cm} and SM HMu RI_{10cm} but Rh_{10cm} showed otherwise. The contrasting findings can be explained by the fundamental basis of the IRIS method. As it reflects iron reduction specifically, the results show that the conditions were less suitable for Fe^{3+} reduction in the horizons around 60 cm compared to the ones located above. Soil temperature and C_{org} content control the metabolic activity of the iron reducers but were not believed to have caused the relatively less suitable conditions in the horizons around 60 cm soil depth (BJ Jenkinson & Franzmeier, 2006). A difference in pH could

explain the lower iron reduction, as iron reducers are more pH-dependent than sulphate reducers or methanogens due to the higher hydrogen ion demand of the iron reducing half reaction (Bethke et al., 2011). Bethke and colleagues (2011) reported a switch around pH 7.5 for which reduction of iron in the ferrihydrite complex does no longer yield more free energy than sulphate reduction, albeit this being at 25 °C and with 1 mmol SO_4^{2-} and Fe^{2+} kg^{-1}. pH also affects solubility of organic carbon and organic carbon-iron associations, mobility of iron ions, binding properties of clay minerals and nutrient-availability which could affect the iron reducer metabolic rates (Anisfeld & Benoit, 1997; Saidy, Smernik, Baldock, Kaiser, & Sanderman, 2013; Seyfferth et al., 2020). Possibly, the difference in pH affected the IRIS response to reducing conditions as there was a pH increase of 0.4 between the two SM HMu horizons, albeit it being a change from 7.8 to 8.2 with depth, which is both above the identified threshold from Bethke et al. (2011). In the other cases, pH differences were smaller and, in some cases, slightly decreased from the more to the lesser reducing horizons.

Another mismatch between methods was found when comparing the RC_{sensor} and $RC_{morphology}$ for the separate depths. In the SM PZ, the Ahlr horizon classified as R3 with $RC_{morphology}$ but the corresponding sensor depths suggested R3 / R2 with RC_{sensor}. Possibly, the few occurrences of R2 conditions were not expressed over the much longer integration time of $RC_{morphology}$. Alternatively, the small spatial reach of the sensors could reflect more strongly the local conditions such as presence of root excretions that can trigger microbial metabolism. Additionally, the disturbance of the sensor installation might have created more preferential root growth and infiltration paths that could enhance root development and water percolation directly around the sensors.

The integrated results of the three methods aligned when characterizing the soil redox conditions between the salinity and flooding frequency zones over depth. However, the discrepancies found here show the relevance of relying on multiple approaches, measuring with replicates and conducting repetitive sampling to characterize the soil redox conditions. The characterization of redox conditions based on soil description benefits from conducting the visual assessment by a well trained team, such that a data set is retrieved with replicate observations from multiple assessors. The variation among the results can help with the interpretation and assessment of the uncertainty in the observations for further characterizing the redox conditions. The visual assessed features should be backed up with associated chemical analyses of which especially soil constituents that affect the soil colors and those that are directly involved in redox reactions. The characterization with the IRIS methods should be considered within the context of iron reduction and therefore requires additional information of variables that can affect the microbial metabolic activity. I recommend to measure soil organic carbon content, soil texture, groundwater table dynamics, soil temperature and pH and determine the water filled pore space for the desired depth increments. When collecting this information, the sampling effort can efficiently be combined with the soil descriptions. Furthermore, I recommend taking sufficient repeated samples and using sufficient number of replicates to statistically test the spatial and temporal variability of the RI results in order to address hypotheses on treatment or system scales. The redox sensors offer valuable insights in soil redox conditions, especially when addressing fundamental research questions but require aggregation when comparing

between treatments or ecosystems. Their costs might limit the number of replicates and therefore combining the sensor approach with one of the other two methods and translating the results via for example the reduction classes allows to obtain information on large scales.

4.3 Methane land-atmosphere fluxes from Elbe tidal wetland soils

The average hourly CH_4 land-atmosphere fluxes significantly increased from the SM PZ at the estuary mouth towards the FM PZ upstream the Elbe river. This finding is in line with the findings of various reviews of soil methane emission from wetlands (Arias-Ortiz et al., 2024; Bartlett & Harriss, 1993; Poffenbarger et al., 2011). In these reviews, higher annual CH_4 emissions from soils with low pore and surface water salinities are explained by decreased substrate competition between methanogens and sulphate reducers (Arias-Ortiz et al., 2024; Bartlett & Harriss, 1993; Poffenbarger et al., 2011). The observed average hourly fluxes of 27.6 with se 4.5 mg CH_4 m^{-2} h^{-1}, 0.7 with se 0.2 mg CH_4 m^{-2} h^{-1} and 0.1 * 10^{-2} with se 4.9 * 10^{-3} mg CH_4 m^{-2} h^{-1} from the three pioneer zones were associated with average ground water salinities of 0.9 ppt, 1.8 ppt and 16.8 ppt respectively (table 1, Branoff et al., 2024, *preprint*). Therefore, the studied pioneer zones classify as oligohaline, in case of the FM and BM, and mesohaline, in case of SM, according to Corwardin's classification system (Cowardin, 1979). The measured hourly CH_4 flux magnitudes were significantly different between these two salinity classes, in contrast to the findings of Poffenbarger et al. (2011) and Arias-Ortiz et al. (2024). However, those two studies tested annual CH_4 fluxes, whereas we tested hourly fluxes. When Arias-Ortiz and colleagues (2024) assessed the fluxes expressed per second, they did find significant differences between emissions from the oligohaline and mesohaline marshes.

The two studied oligohaline pioneer zone marshes, FM PZ and BM PZ, also significantly differed from each other in the average hourly flux magnitudes, showing the wide range of flux magnitudes emitted from marshes within this salinity class. Other studies too found high variability in flux magnitudes within the oligohaline salinity class (Arias-Ortiz et al., 2024; Poffenbarger et al., 2011; Tong, Morris, Huang, Xu, & Wan, 2018). In this lower salinity range, the competition between sulfate reducers and methanogens might only be expressed at small spatial and temporal scales depending on sulfate replenishment and depletion (Arias-Ortiz et al., 2024). The other environmental variables become relatively more important controls of CH_4 flux magnitude variability. The earlier discussed differences in soil texture, flooding frequency and organic carbon content could explain the significantly smaller CH_4 land-atmosphere fluxes from the BM PZ in comparison to the FM PZ as it was relatively poorer in organic carbon and experienced more hot-moment like patterns in reducing conditions due to its regular flooding but lower water holding capacity.

The BM PZ CH_4 land-atmosphere fluxes showed a large number of significant correlations with the studied environmental variables. The negative correlation of CH_4 flux with CO_2 flux can be the result of variation in *Bolboschoenus maritimus* above ground biomass among the flux replicate plots and over time. *Bolboschoenus maritimus* stems

contain aerenchyma tissue (Schweingruber et al., 2020) which is known to enhance gas transport from soil to atmosphere (Bastviken et al., 2023; Kutzbach, Wagner, & Pfeiffer, 2004). With a larger number of *Bolboschoenus* individuals present on a flux plot, more aerenchyma pathways exist between soil and atmosphere and the consumption of CO_2 in the headspace will increase with more individuals conducting photosynthesis. Therefore, the negative correlation of CO_2 with CH_4 could be a reflection of plant-mediated transport of CH_4 from the soil to the atmosphere. Furthermore, the members of the Cyperaceae family can exudate organic compounds through their roots, these excretions provide the microbial community with organic substrates for their metabolic activity (Boschker, De Brouwer, & Cappenberg, 1999). Higher plant productivity might enhance the production and release of these organic excretions, which would enhance the microbial metabolic rates and therefore CH_4 production. The observed positive correlation between BM PZ CH_4 flux and PAR_{in} supports this reasoning. Arias-Ortiz et al. (2024) also found a correlation of peak CH_4 flux and incoming short-wave radiation. However, the correlation of PAR_{in} and CH_4 could also reflect the effect of incoming short-wave radiation on soil temperature and headspace air temperature. Indeed, these three variables were strongly correlated among each other at BM PZ (appendix T table 40). Various studies have shown the link between changes in temperature and in CH_4 flux emissions (Arias-Ortiz et al., 2024; Bartlett et al., 1987; Holm Jr et al., 2016; Li et al., 2020; Zheng et al., 2018). As soil temperature exerts a direct effect on the activity of microbes, it affects production and consumption rates of CH_4 (Butterbach-Bahl et al., 2013; Le Mer & Roger, 2001). Here we found a positive correlation of soil temperature and BM PZ CH_4 flux. Which suggests that production and transport of CH_4 were stronger positively affected by an increase in soil temperature than CH_4 consumption. Megonical and colleagues (2004) argued that the stronger effect of temperature on produced methane could be caused by quicker depletion of the more energetically favorable electron acceptors as well as by the sensitivity of some of the acetogenesis steps to temperature. On the other hand, headspace air temperature exerts indirect effects on CH_4 land-atmosphere fluxes, for example by affecting plant physiological processes, evapo-transpiration, soil moisture and oxygen concentrations (Butterbach-Bahl et al., 2013). The findings of a positive correlation between headspace air temperature and BM PZ CH_4 flux and a negative correlation between volumetric water content and BM PZ CH_4 flux highlight the complex response of final CH_4 land-atmosphere flux to changes in environmental conditions.

Within the salt marsh, the different salt marsh flooding frequency zones were not significantly different with regard to their average CH_4 land-atmosphere fluxes. The spatial and temporal variability in flux magnitudes among the flux replicate plots was larger than the differences flux magnitudes between the zones (table 13). However, the spring SM LM CH_4 fluxes were significantly different from the spring SM HMu and SM PZ CH_4 fluxes, where SM LM acted as a net sink while to other two acted as net sources of methane to the atmosphere. Although, uptake of CH_4 did occur also sporadically at both SM PZ and SM HMu, as did CH_4 release at SM LM (appendix S, table 39). Nevertheless, the general situation at SM LM in spring indicates that the CH_4 oxidation rates overruled CH_4 production and transport rates, at least at certain depths in the soil. Neither the correlations with auxiliary flux variables nor RI nor the redox sensor yielded insights that could explain the

contrast between SM LM, SM PZ and SM HMu CH_4 land-atmosphere flux directions. Possibly, CH_4 production rate was smaller in the SM LM soil, due to the presence of more energetically favorable electron acceptors other than sulfate. NO_3^- and denitrification products can inhibit CH_4 production as result of microbial competition for H_2 and the toxic effect of nitrite and nitric oxide (Balderston & Payne, 1976; Klüber & Conrad, 1998). Soil nitrate levels were higher in the upper 30 cm of the SM LM soil compared to the SM PZ and SM HMu (appendix M table 31), which could have contributed to lower CH_4 production rates. The N_2O hourly flux results could not support this explanation but standalone are neither a counter argument. The net uptake of atmospheric CH_4 by the SM LM soil could result from higher CH_4 oxidation, depleting the soil pore water CH_4 and supporting transport rates from atmosphere to soil. The oxidation of CH_4 under anaerobic conditions can take place coupled to the reduction of N_2O, NO_3^-, NO_2^-, birnessite, ferrihydrite and SO_4^{2-} (Beal, House, & Orphan, 2009; Gupta et al., 2013; Hallam et al., 2004; Segers, 1998). While the SM LM soil was relatively lower in its EC_{se} and SO_4^{2-} compared to SM PZ and HMu (appendix M table 30, table 32), anaerobic CH_4 oxidation could be linked to NO_3^- or Mn^{4+} in the SM LM soil. The former, as these were relatively higher in concentration in the top 30 cm of SM LM soil (appendix M, table 32). The effect might have been more pronounced in spring, leading to the significant difference, while being hidden when production of CH_4 was larger in the other season, or when other variables became limiting to support the same uptake rate of atmospheric CH_4.

4.4 Nitrous oxide land-atmosphere fluxes from Elbe tidal wetland soils

All three PZ acted as small sources of N_2O to the atmosphere when considering the average hourly fluxes over the complete measurement period. Flux magnitudes ranged between 0.0084 to 0.0270 mg N_2O m^{-2} h^{-1} (table 15) and per meteorological season, ranging 0.0033 to 0.0712 mg N_2O m^{-2} h^{-1} (table 16). Although, net uptake of N_2O was incidentally observed at each of the PZ too (appendix S table 39). Similarly, Sun and colleagues (2014) found *Suaeda salsa* dominated marshes in the Yellow River estuary acting as small N_2O sources on seasonal average too, with flux sizes ranging 0.0035 to 0.0257 mg N_2O m^{-2} h^{-1}. Additionally, they observed uptake as well in the summer and autumn months (Z. Sun et al., 2014). Whereas, Moseman-Valtierra and colleagues (2011) reported net uptake of N_2O as daily flux of -0.033 ± 0.021 mmol N_2O m^{-2} day^{-1} from their *Spartina patens* dominated tidal marsh in Massachusetts, United States of America, in July. Chmura and colleagues (2011) observed net uptake of N_2O with a near zero uptake flux of -0.002 ± 0.026 mg N_2O m^{-2} h^{-1} from their *Spartina patens* dominated macrotidal marsh in the Bay of Fundy, Canada, and net emission of 0.013 ± 0.030 mg N_2O m^{-2} h^{-1} from their *Spartina patens* dominated microtidal marsh at Gulf of St. Lawrence, Canada during late August and early September. The hourly N_2O fluxes from the studied tidal wetlands reported here are within the same magnitude range as observed by these referenced studies on salt marshes. Furthermore, our calculated fluxes showed large standard errors compared to the flux magnitudes, which

is also in line with these referenced studies (table 15, 16). Currently, there is to my knowledge no comparable data available from other studies that quantified N_2O land-atmosphere fluxes at oligohaline tidal marshes.

The SM PZ soil emitted a significantly smaller hourly N_2O flux compared to FM PZ and BM PZ in summer and compared to FM PZ in winter. The smaller N_2O fluxes might result from the difference in tidal flood water characteristics. The estuary section of the Elbe receives high dissolved inorganic nitrogen (DIN) concentrations at its the entry, just upstream of the port of Hamburg, in winter and this riverine input decreases towards the summer (Schulz, Sanders, Voynova, Bange, & Dähnke, 2023). From early spring to summer, the nitrate concentration in the river water increased from Hamburg port to river kilometer 700, which is located roughly between the SM and BM, and drops towards the sea (Schulz et al., 2023). Therefore, the flood water reaching FM PZ and BM PZ is expected to have a higher DIN load compared to flood water reaching SM PZ. The larger availability of mineral nitrogen, from the larger input through the tidal floods, would support higher microbial N_2O production, based on the well-established positive relation between mineral nitrogen availability and N_2O production (K. Dobbie et al., 1999; Ji, Babbin, Peng, Bowen, & Ward, 2015; Livesley & Andrusiak, 2012; Moseman-Valtierra et al., 2011; Sgouridis & Ullah, 2017). The combination of higher temperatures and more supportive reducing conditions in summer, with the nitrate supply peaking at the brackish marsh site, as well as the high soil organic nitrogen contents in the fresh water marsh could all together cause the higher hourly fluxes at the FM PZ and BM PZ compared to SM PZ. While in winter, the peak nitrate supply at the FM could have supported the significantly larger hourly FM PZ N_2O fluxes compared to the BM PZ and SM PZ, which received less easily available nitrate for the metabolic activity of the denitrifiers.

The comparable FM PZ and BM PZ hourly N_2O fluxes are likely the result of differences in soil, vegetation and flooding characteristics. While, the conditions at the FM PZ suggest higher denitrification potential as the soil had a higher organic N and organic C content and stronger reducing conditions (appendix M table 30, table 31), there could be a higher N_2 to N_2O production ratio compared to the BM PZ soil. Furthermore, the BM PZ soil received more regular NO_3^- replenishment, resulting from the more frequent flooding, and a deeper reach of the replenishment, due to the coarser soil texture, compared to the FM PZ soil, which could have supported denitrifying community with more easily available nitrogen for denitrification compared to nitrogen in organic complexes. However, VWC was negatively correlated with BM PZ N_2O fluxes. Possibly, an increase in VWC supported more complete denitrification leading to a higher N_2 to N_2O production ratio and therefore lead to a negative correlation of VWC with N_2O land-atmosphere flux. Alternatively, diffusive transport of N_2O towards the soil surface might be hampered at higher VWC, causing a lag time in N_2O land-atmosphere fluxes related to production and transport rates following a tidal flood (Jørgensen & Elberling, 2012).

The hourly FM PZ N_2O fluxes did not significantly correlate with any of the tested auxiliary variables. Whereas, hourly BM PZ and SM PZ N_2O fluxes were positively correlated with T_{air_in} and with PAR_{in}. Possibly, multiple interacting FM PZ site-specific conditions together steered the variation in N_2O flux sizes, as discussed by Sun and colleagues (2014). Alternatively, another environmental condition that was not included in

the correlation tests acted as a dominant control. Small scale spatiotemporal variability in mineral nitrogen has not been studied in this project and could therefore not be further assessed but is an established driver of N_2O flux (K. E. Dobbie & Smith, 2003; Ji et al., 2015; Livesley & Andrusiak, 2012; Moseman-Valtierra et al., 2011). Vegetation is another untested factor here that is known to drive N_2O flux sizes through her effect on oxygen, substrate and mineral nitrogen availability in the rhizosphere soil (Abalos, van Groenigen, & De Deyn, 2018; Drew, 1992; Husson, 2013; Megonigal et al., 2004; Yousaf et al., 2021). Although the N_2O land-atmosphere fluxes did not significantly differ between the flux replicate plots of FM PZ when considering all observations over time, differences in vegetation community composition and productivity could have acted as the interactive control that affected the responses of N_2O land-atmosphere to changes in the environmental conditions differently and obscuring the relations between for example temperature and PAR in the correlation tests.

The SM PZ soil emitted also a significantly smaller hourly N_2O land-atmosphere flux compared to the other three flooding frequency zones within the salt marsh during spring and summer. This finding agrees with the findings of Sun and colleagues (2014), whom observed significantly smaller N_2O flux magnitudes from a pioneer zone species inhabited irregularly flooded marsh. In contrast, Yang and Silver (2016), observed highest N_2O fluxes from their low marsh, N_2O uptake at their mid marsh and smaller positive fluxes at their high marsh. However, their low marsh was flooded for a longer time period than the pioneer zone of this study, and their middle marsh received regular flooding with each high tide (Yang & Silver, 2016). With regard to flooding frequency, the mid marsh in the study of Yang and Silver (2016) is more similar to that of SM PZ of this study. The lower hourly SM PZ N_2O land-atmosphere fluxes can be the result of stronger reducing soil conditions that possibly support higher N_2 to N_2O production rates compared to the other three soils (appendix M table 30). Another explanation could lie in the lower soil nitrate content of the SM PZ soil, that would support a lower N_2O production rate and therefore a lower land-atmosphere flux (appendix M table 31). The positive, albeit weakly, correlations of hourly SM PZ fluxes with microbial metabolic activity enhancing associated variables suggest the importance of the production of N_2O over consumption in driving the land-atmosphere exchange.

4.5 Methane and nitrous oxide flux calculations uncertainties and flux data set assessment

Since calculated fluxes retrieved from closed manual chamber methods are an approximation of the real occurring land-atmosphere flux, it is essential to assess the quality of the representation. In this project, the calculated fluxes were categorized into quality levels to reflect the performance of measurement and calculative methods. The statistical testing was conducted purely with QL1 and QL2 flagged observation, which were associated with smallest uncertainties, but the full dataset is available in appendix S, table 39.

Both CH_4 and N_2O flux data were non-normally distributed, as is commonly found for repeated GHG measurements (Arias-Ortiz et al., 2024; Chmura et al., 2016; Dhanoa et al., 2020; Livesley & Andrusiak, 2012). Multiple extreme outlier flux magnitudes were identified for both gases. Generally, these were extreme in the positive direction and were often observed on either the same day in case of N_2O or for the same replicate plots in case of CH_4. Such hot spots or hot moments have been identified in other studies and linked to transport and transformation of elements limiting the gas production (Loick et al., 2017; McClain et al., 2003). There were also some negative CH_4 land-atmosphere fluxes at the SM sites that categorized as extreme outliers in comparison to the other flux observations of the respective flooding frequency zones. These can also be considered hot moments, but for CH_4 oxidation. The conditions during these cases were likely more favorable for higher CH_4 oxidation rates and possible less favorable for high CH_4 production rates in comparison to the general reigning conditions. Although these observations are statistically considered outliers, there were no fundamental process-based reasons to remove them from the dataset.

Some flux replicate plots were significantly different in CH_4 land-atmosphere flux magnitudes compared to their fellow replicates. Significant larger CH_4 fluxes were observed at FM PZ plot 4 in comparison to plot 2 and could be the result of the difference in vegetation cover at the two plots. Plot 4 was characterized by lower aboveground biomass (979 g DW), number of species (2) and coverage of the present species (*Typha angustifolia*, 8 %, and *Myosotis palustris,* 1 %) as well as a much higher share of bare soil (90 %) compared to plot 2 (respectively 1870 g DW, 3 species, *Caltha palustris* 35%, *Typha angustifolia* 10% and *Myosotis palustris* 2%, bare soil 55%). Part of the explanation could be the presence of a gas accumulation layer from the larger number of roots and rhizomes in the more intensively vegetated plots (Chen & Slater, 2015). Chen and Slater (2015) showed that CH_4 bubbles were intercepted at the interface of highly decomposed peat layer located below a more undecomposed peat layer. The effect of the chamber placement and changes in environmental conditions, for example headspace air pressure, on ebullition transport might translate to a quicker reaction in the lesser vegetated plots where such an interface between different layers of different bulk densities and pore structures is less developed or absent. Whereas in the more intensively vegetated plots ebullition might occur less frequent but possible with larger bubble sizes. Bare soil coverage and above ground biomass results would suggest more frequent ebullition at plot 4 followed by 1, 5, 2 and finally 3, due to their respective bare soil coverages of 90 %, 80 %, 80 %, 55 % and 15% and above ground biomasses of 979 g DW, 1227g DW, 1261 g DW, 1870 g DW and 1916 g DW. The CH_4 headspace concentrations changes did indicate more frequent ebullition events at plot 4, 1 and 5 compared to plot 2 and 3 (data not shown). A second part of the explanation could be the difference in species composition at the plots. While both *Typha angustifolia* and *Caltha palustris* can grow aerenchyma tissue and rhizomes, they differ in their morphological traits and phenological cycles (Tornberg, Bendix, & Brix, 1994; Visser, Colmer, Blom, & Voesenek, 2000). Consequently, their effect on CH_4 production and transport, through root oxygen loss, substrate supply and root hair growth, might be timed differently and expressed at different soil depths.

The significant larger CH_4 fluxes observed at plot 5 compared to plot 1 and 2 in the SM PZ could also be related to differences in plant community composition and plant coverage. The share of bare soil within the flux replicate plots was highest for plot 5 (20 %, appendix U table 41). Furthermore, plot 5 was more dominantly covered by *Spartina anglica* (80 %) compared to the other plots (45 % to 70 %). The dominance of *Spartina anglica* could offer one explanation for the higher CH_4 land-atmosphere fluxes at plot 5. Soils inhabited by *Spartina anglica* have been found to emit larger CH_4 fluxes compared to soils inhabited with native species at US west coast and China (Fuchs et al., 2025; Kim et al., 2020; Tong et al., 2018; Yuan et al., 2019). This difference was associated with enhanced methylotrophic methanogenesis (Kim et al., 2020), methanogenesis using trimethylamine from *Spartina anglica* osmolytes (Yuan et al., 2019) and increased acetate concentrations in the soil pores (Tong et al., 2018). The potential beneficial effect of *Spartina anglica* might not be the only aspect causing the significant differences but her presence increased from flux replicate plot 1 to 2 to 3 to 4 and finally 5. Therefore, plot 1 and 2 would be expected to express smaller CH_4 land-atmosphere fluxes compared to plot 5. It is likely that multiple plot specific conditions and their interacting effects caused the significant differences.

Two flux calculation variables were assessed to further identify uncertainties in the data and include the findings in the interpretation of the results. The adaptation of headspace volume to correct for vegetation and soil surface unevenness had only a small effect on established flux magnitudes. The effect of the correction showed to be larger for larger headspace volumes and larger GHG flux magnitudes. Furthermore, the combined effect of two considered volume corrections expressed bidirectional on CH_4 flux magnitudes. Since headspace volume gain or loss from erosion, sedimentation and vegetation growth has a spatial and temporal variability, it is highly relevant to determine plot and measurement-specific headspace volumes to prevent potential falsely assigned differences within or between treatments or underestimations of differences.

The switch in input temperature also resulted in a small response of flux magnitudes, in a similar magnitude range as caused by the volume adaptation. Generally, the flux magnitude increased when using $T_{initial}$, as the headspace temperature was lower at the start of the measurement and increased over the course of a measurement. The change in temperature depends on the chamber deployment time and chamber size, which were respectively short and large in this project. The observed temperature difference was no larger than ± 4 °C, for the 25 assessed fluxes measured in June and July of 2023. However, six of the assessed fluxes showed a decrease in magnitude, which was associated with a net cooling of the headspace air. This unexpected cooling could be the result of changes in cloud cover, affecting the solar radiation reaching the flux chamber. It could also be a consequence of phase changes of water present in the headspace, due to condensation or evaporation of soil moisture and intercepted water. Furthermore, it could be due to incomplete mixing of air within the headspace due to late activation of the fans or to insufficient flushing of the chamber in between the measurements. The choice of input temperature should made taking these processes into consideration.

The combined effect of adapting headspace volume and switching input temperature led also to small responses of the flux magnitudes. The magnitude changes fell within the calculated flux error, albeit a few exceptions (table 19 A and B). These exceptions were the

SM HMu CH_4 flux of plot 1 on 2023-06-27, SM HMu N_2O flux of plot 4 on 2023-06-15 and 2023-06-27. However, the flux calculation variables were also assessed with regard to their uncertainties and showed that their propagated effects suggested potentially too narrow errors for peak growing season fluxes (chapter 3.4.7). Recalculating flux errors with the propagated uncertainties resulted in relative changes of 0.02 for flux errors associated with the measurements conducted at the SM HMu up to 4.7 for flux errors associated with the measurements conducted at the FM PZ. Ultimately, the temporal and spatial variability of the land-atmosphere fluxes observed at the tidal wetland zones was larger than the flux magnitude changes in reaction to real-case, but deemed maximum, headspace volume and temperature variation. While the flux error magnitude change in reaction to the propagated uncertainty was in the same range as the spatiotemporal variability of the tidal wetland land-atmosphere fluxes, these were also determined for the most extreme cases.

When the data and findings reported here are used for further research of tidal wetland soil greenhouse gas land-atmosphere fluxes, it is crucial that the fluxes are considered within the setting of the dominantly low tide, midday centered measurements. I advise against using this data for upscaling to daily flux rates or seasonal and yearly emissions as the diurnal and tidal cycles are not representatively covered in this project.

Chapter 5 Conclusions

The tidal wetland soils in the Elbe estuary classify as Gleysols, which indicates the important role of groundwater in their formation. Furthermore, the higher salt marsh soil classified as gleyic Solonchak, reflecting the high concentration of soluble salts in addition to the groundwater dynamics driven soil formation. The variation in the considered tidal wetland soil physicochemical characteristics is mainly driven by textural differences caused by tidally steered sedimentation and erosion processes, affected by human interventions to the estuary, plant species inhabiting the wetlands and extreme weather events. The salt marsh soils were further characterized by marine water dominated floods, reflected in its physicochemical characteristics even though the soils in the more frequent flooded zones did not classify as Solonchaks. In addition, the results here point to the importance of the tidal wetland soils' situation in the estuary with respect to the riverbed morphology in determining its characteristics.

The soil redox conditions shifted towards more strongly reducing conditions upstream the Elbe river, down the flooding frequency zones and down soil depth. These trends are linked to soil organic carbon content, soil texture, the flooding frequency characteristics and pH. Characterization of soil redox through soil redox associated diagnostics, the IRIS method and with soil redox sensors lead to corresponding results when aggregating the data over the 10 meters covered with the five replicates and the 11 sampling campaigns or time windows. However, the different methods have limitations that should be considered when relying on only one to characterize soil redox conditions in tidal wetland soils. The exceptions to the general observed trends and the discrepancies between the three characterization methods emphasize the complexity, variability and heterogeneity of soil redox conditions.

The dominantly senses-based soil descriptions are prone to uncertainties in the assessments as the observational performance differs among people. Furthermore, soil matrix and feature colors can be masked by other soil constituents, making it hard to determine if contrasts are strong enough to meet the criteria. Additionally, indicative features can be relicts and not reflect the recent occurring conditions. However, as the soil descriptive characterization method represents conditions over longer spatiotemporal scales, it can proof its worth especially in studies on biogeochemical functioning of ecosystems, such as this project. The IRIS method relies on the metabolic activity of iron reducers and therefore reflects the integrated effect of the controlling conditions on that activity. The method does not yield insights in other redox reactions or differentiate among the controlling conditions. However, it supports the characterization of redox conditions as a proxy reflecting on smaller spatiotemporal scales compared to the soil descriptive characterization method. The redox potential sensors act on the smallest spatiotemporal scales among these three methods. The timeseries datasets of replicate sensors are complex and challenging to interpret when characterizing soil redox characteristics. Local variation in soil temperature, pH, organic carbon and electron acceptors that drive the redox reaction rates can limit the replicate function of multiple sensors installations. In this work, 25 % of the dataset total variance was assigned to the sensors in the predictive mixed

effects model. However, the redox potential sensors offer the opportunity to gain detailed insights on short time scales and could be especially supportive in ecosystem manipulative experiments. The presented comparison tool, based on the conversion to rH value presented in the WRB (2022), offers a way to aggregate the sensor retrieved data to compare with information retrieved with the other two methods.

Average hourly methane land-atmosphere fluxes showed a strong significant magnitude increase towards the less saline zones in the estuary. This increase also coincided with the increasing soil reducing conditions. Furthermore, correlation data indicated a connection of CH_4 land-atmosphere flux with CO_2 land-atmosphere flux, received photosynthetic active radiation, soil temperature, soil volumetric water content, headspace air temperature at the brackish marsh pioneer zone. These correlations could reflect the role of vegetation in gas transport and substrate supply but also directly of the microbial metabolic activity. The average hourly methane land-atmosphere did not significantly differ between the four flooding frequency zones in the salt marsh. However, the seasonal aggregated flux results showed negative spring CH_4 fluxes in the low marsh which were significantly different from the net emissions of the pioneer zone and unmanaged high marsh CH_4 fluxes. The higher nitrate and manganese levels in the low marsh soil could have supported larger anaerobic methane oxidation rates. The oxidation rates might have been smaller during the other seasons and might partly have been obscured by simultaneous production of CH_4.

The average hourly nitrous oxide land-atmosphere fluxes also increased in magnitude upstream the Elbe river but were not significantly different between the fresh water and brackish marshes. The switch of more terrestrial water dominated floods landing at the fresh water and brackish marshes to the more marine water dominated floods landing at the salt marsh offers one explanation for the observed change in flux magnitude along the estuary. The higher mineral nitrogen load, dominantly existing of nitrate, of the river water present in the river sections abutting the fresh and brackish marshes can supply the denitrifying community with more nitrate through tidal flooding. The soil conditions in the brackish marsh suggest potential for a more hot moment characterized denitrification process, while the fresh water marsh soil conditions suggest more durable supportive conditions and likely larger denitrification potentials. It is expected that denitrification plays the main role in N_2O production in these soils and the overlap in N_2O flux magnitudes between these two tidal wetland zones could be related to differences in N_2 to N_2O production ratios. The significantly smaller summer and spring SM PZ N_2O fluxes can also be related to N_2O production rates and N_2 to N_2O production ratios, suggested by lower soil nitrate content, stronger reducing conditions and positive correlation coefficients with soil and air temperature. The data collected and presented here does not provide enough insights to explain the hourly flux magnitude differences that were observed among the flooding frequency zones within the salt marsh.

The calculated GHG land-atmosphere fluxes represent an approximation of the real occurring fluxes. It is crucial to discuss and interpret the findings with knowledge of the quality of the approximations. The sensitivity analyses proofed that correcting the headspace volume for vegetation and soil surface unevenness as well as the switching of the used headspace air temperature from measurement average to starting temperature

resulted in changes in the calculated flux magnitudes. The adaptations to the input variables resulted in increases and decreases of the flux magnitude, which could lead to overestimation or underestimation of difference in fluxes over space and time. Although these magnitude changes were smaller than the observed spatiotemporal variability within the tidal wetland zones. Especially studies that upscale fluxes for budget or annual emission calculations are sensitive for the cascading effect of ignoring measurement specific conditions, such as plant growth over the seasons. The fluxes presented in this work represent hourly fluxes focused roughly three hours before and after low tide during day time conditions. It is highly appreciated to use the data and results presented here for further research, but strongly advised not to upscale the presented values to daily, seasonal or annual representations of the GHG exchange in the tidal wetland soils of the Elbe estuary. GHG land-atmosphere exchange research focusing on tidal wetlands would benefit from more flux quantification, especially covering different tidal stages and day times. As well as, that it should aim for collecting more observations to link changes in flux magnitudes to biotic and abiotic conditions. The results presented here point to the importance of a soils position in the estuary with respect to distance to sea, river morphology, flooding frequency and their indirect effects on the inhabiting vegetation, soil physicochemical characteristics and redox conditions in driving GHG fluxes, but more research is required to elucidate the fundamental processes and effect of interactions among the environmental drivers.

List of publications

Peer reviewed papers

Co-authored papers

Oester, R., Branoff, B., Biederbick, J., Grüterich, L., Koll, R., Lexmond, F., ... & Jensen, K. (2026). Ecotonal gradients shape biodiversity of multiple estuarine taxa. Estuarine, Coastal and Shelf Science, 110042. https://doi.org/10.1016/j.ecss.2026.110042

References

Abalos, D., van Groenigen, J. W., & De Deyn, G. B. (2018). What plant functional traits can reduce nitrous oxide emissions from intensively managed grasslands? *Global change biology, 24*(1), e248-e258.

Anisfeld, S. C., & Benoit, G. (1997). Impacts of flow restrictions on salt marshes: an instance of acidification. *Environmental science & technology, 31*(6), 1650-1657.

Anthony, W., Hutchinson, G., & Livingston, G. (1995). Chamber measurement of soil-atmosphere gas exchange: Linear vs. diffusion-based flux models. *Soil Science Society of America Journal, 59*(5), 1308-1310.

Arias-Ortiz, A., Wolfe, J., Bridgham, S. D., Knox, S., McNicol, G., Needelman, B. A., . . . Oikawa, P. Y. (2024). Methane fluxes in tidal marshes of the conterminous United States. *Global change biology, 30*(9), e17462.

Armour, K., Forster, P., Storelvmo, T., Collins, W., Dufresne, J.-L., Frame, D., . . . Watanabe, M. (2021). *The Earths energy budget, climate feedbacks, and climate sensitivity.* Paper presented at the AGU Fall Meeting Abstracts.

Bai, J., Gao, H., Xiao, R., Wang, J., & Huang, C. (2012). A review of soil nitrogen mineralization as affected by water and salt in coastal wetlands: issues and methods. *CLEAN–Soil, Air, Water, 40*(10), 1099-1105.

Bakker, J. P. (2014). *Ecology of Salt Marshes: 40 Years of Research*: Waddenacademie.

Balderston, W., & Payne, W. (1976). Inhibition of methanogenesis in salt marsh sediments and whole-cell suspensions of methanogenic bacteria by nitrogen oxides. *Applied and Environmental Microbiology, 32*(2), 264-269.

Bartlett, K. B., Bartlett, D. S., Harriss, R. C., & Sebacher, D. I. (1987). Methane emissions along a salt marsh salinity gradient. *Biogeochemistry, 4*(3), 183-202.

Bartlett, K. B., & Harriss, R. C. (1993). Review and assessment of methane emissions from wetlands. *Chemosphere, 26*(1-4), 261-320.

Bastviken, D., Treat, C. C., Pangala, S. R., Gauci, V., Enrich-Prast, A., Karlson, M., . . . Sawakuchi, H. O. (2023). The importance of plants for methane emission at the ecosystem scale. *Aquatic botany, 184*, 103596.

Beal, E. J., House, C. H., & Orphan, V. J. (2009). Manganese-and iron-dependent marine methane oxidation. *Science, 325*(5937), 184-187.

Bethke, C. M., Sanford, R. A., Kirk, M. F., Jin, Q., & Flynn, T. M. (2011). The thermodynamic ladder in geomicrobiology. *American Journal of Science, 311*(3), 183.

Blume, H., & Schwertmann, U. (1969). Genetic evaluation of profile distribution of aluminum, iron, and manganese oxides. *Soil Science Society of America Journal, 33*(3), 438-444.

Boschker, H., De Brouwer, J., & Cappenberg, T. (1999). The contribution of macrophyte-derived organic matter to microbial biomass in salt-marsh sediments: Stable carbon isotope analysis of microbial biomarkers. *Limnology and oceanography, 44*(2), 309-319.

Butterbach-Bahl, K., Baggs, E. M., Dannenmann, M., Kiese, R., & Zechmeister-Boltenstern, S. (2013). Nitrous oxide emissions from soils: how well do we understand the processes and their controls? *Philosophical Transactions of the Royal Society B: Biological Sciences, 368*(1621), 20130122.

Cadier, C., Waltham, N. J., Canning, A., Fry, S., & Adame, M. F. (2023). Tidal restoration to reduce greenhouse gas emissions from freshwater impounded coastal wetlands. *Restoration Ecology, 31*(8), e13829.

Capooci, M., Seyfferth, A. L., Tobias, C., Wozniak, A. S., Hedgpeth, A., Bowen, M., . . . Vargas, R. (2024). High methane concentrations in tidal salt marsh soils: Where does the methane go? *Global change biology, 30*(1), e17050.

Capooci, M., & Vargas, R. (2022). Trace gas fluxes from tidal salt marsh soils: implications for carbon–sulfur biogeochemistry. *Biogeosciences, 19*(19), 4655-4670.

Castenson, K. L., & Rabenhorst, M. C. (2006). Indicator of Reduction in Soil (IRIS) Evaluation of a New Approach for Assessing Reduced Conditions in Soil. *Soil Science Society of America Journal, 70*(4), 1222-1226.

Chanton, J. P., Martens, C. S., & Kelley, C. A. (1989). Gas transport from methane-saturated, tidal freshwater and wetland sediments. *Limnology and oceanography, 34*(5), 807-819.

Chen, X., & Slater, L. (2015). Gas bubble transport and emissions for shallow peat from a northern peatland: The role of pressure changes and peat structure. *Water Resources Research, 51*(1), 151-168.

Chmura, G. L. (2013). What do we need to assess the sustainability of the tidal salt marsh carbon sink? *Ocean & Coastal Management, 83*, 25-31.

Chmura, G. L., Anisfeld, S. C., Cahoon, D. R., & Lynch, J. C. (2003). Global carbon sequestration in tidal, saline wetland soils. *Global Biogeochemical Cycles, 17*(4).

Chmura, G. L., Kellman, L., & Guntenspergen, G. R. (2011). The greenhouse gas flux and potential global warming feedbacks of a northern macrotidaland microtidal salt marsh. *Environmental Research Letters, 6*(4), 044016.

Chmura, G. L., Kellman, L., Van Ardenne, L., & Guntenspergen, G. R. (2016). Greenhouse gas fluxes from salt marshes exposed to chronic nutrient enrichment. *PloS one, 11*(2), e0149937.

Cowardin, L. M. (1979). *Classification of wetlands and deepwater habitats of the United States*: Fish and Wildlife Service, US Department of the Interior.

Denmead, O. (2008). Approaches to measuring fluxes of methane and nitrous oxide between landscapes and the atmosphere. *Plant and soil, 309*(1), 5-24.

Derby, R. K., Needelman, B. A., Roden, A. A., & Megonigal, J. P. (2021). Vegetation and hydrology stratification as proxies to estimate methane emission from tidal marshes. *Biogeochemistry*, 1-17.

Dhanoa, M. S., Louro, A., Cardenas, L. M., Shepherd, A., Sanderson, R., Lopez, S., & France, J. (2020). A strategy for modelling heavy-tailed greenhouse gases (GHG) data using the generalised extreme value distribution: Are we overestimating GHG flux using the sample mean? *Atmospheric Environment, 237*, 117500.

Dobbie, K., McTaggart, I., & Smith, K. (1999). Nitrous oxide emissions from intensive agricultural systems: variations between crops and seasons, key driving variables, and mean emission factors. *Journal of Geophysical Research: Atmospheres, 104*(D21), 26891-26899.

Dobbie, K. E., & Smith, K. A. (2003). Nitrous oxide emission factors for agricultural soils in Great Britain: The impact of soil water-filled pore space and other controlling variables. *Global change biology, 9*(2), 204-218.

Drew, M. C. (1992). Soil aeration and plant root metabolism. *Soil Science, 154*(4), 259-268.

Duarte, C. M., Middelburg, J. J., & Caraco, N. (2005). Major role of marine vegetation on the oceanic carbon cycle. *Biogeosciences, 2*(1), 1-8.

Fiedler, S., & Sommer, M. (2000). Methane emissions, groundwater levels and redox potentials of common wetland soils in a temperate-humid climate. *Global Biogeochemical Cycles, 14*(4), 1081-1093.

Fiedler, S., Vepraskas, M. J., & Richardson, J. (2007). Soil redox potential: importance, field measurements, and observations. *Advances in agronomy, 94*, 1-54.

Firestone, M. K., & Davidson, E. A. (1989). Microbiological basis of NO and N 2 O production and consumption in soil. *Exchange of trace gases between terrestrial ecosystems and the atmosphere, 47*, 7-21.

Freeman, C., Ostle, N., & Kang, H. (2001). An enzymic'latch'on a global carbon store. *Nature, 409*(6817), 149-149.

Fuchs, A., Davidson, I. C., Megonigal, J. P., Devaney, J. L., Simkanin, C., Noyce, G. L., . . . Cott, G. M. (2025). Stronger increase of methane emissions from coastal wetlands by non-native Spartina alterniflora than non-native Phragmites australis. *Plants, People, Planet, 7*(1), 62-79.

Gorham, C., Lavery, P., Kelleway, J. J., Salinas, C., & Serrano, O. (2021). Soil carbon stocks vary across geomorphic settings in Australian temperate tidal marsh ecosystems. *Ecosystems, 24*(2), 319-334.

Greenacre, M., Groenen, P. J., Hastie, T., d'Enza, A. I., Markos, A., & Tuzhilina, E. (2022). Principal component analysis. *Nature Reviews Methods Primers, 2*(1), 100.

Gupta, V., Smemo, K. A., Yavitt, J. B., Fowle, D., Branfireun, B., & Basiliko, N. (2013). Stable isotopes reveal widespread anaerobic methane oxidation across latitude and peatland type. *Environmental science & technology, 47*(15), 8273-8279.

Hallam, S. J., Putnam, N., Preston, C. M., Detter, J. C., Rokhsar, D., Richardson, P. M., & DeLong, E. F. (2004). Reverse methanogenesis: testing the hypothesis with environmental genomics. *Science, 305*(5689), 1457-1462.

Hartman, W. H., Bueno de Mesquita, C. P., Theroux, S. M., Morgan-Lang, C., Baldocchi, D. D., & Tringe, S. G. (2024). Multiple microbial guilds mediate soil methane cycling along a wetland salinity gradient. *Msystems, 9*(1), e00936-00923.

Holm Jr, G. O., Perez, B. C., McWhorter, D. E., Krauss, K. W., Johnson, D. J., Raynie, R. C., & Killebrew, C. J. (2016). Ecosystem level methane fluxes from tidal freshwater and brackish marshes of the Mississippi River Delta: Implications for coastal wetland carbon projects. *Wetlands, 36*(3), 401-413.

Huertas, I. E., Flecha, S., Navarro, G., Perez, F. F., & de la Paz, M. (2018). Spatio-temporal variability and controls on methane and nitrous oxide in the Guadalquivir Estuary, Southwestern Europe. *Aquatic Sciences, 80*, 1-16.

Husson, O. (2013). Redox potential (Eh) and pH as drivers of soil/plant/microorganism systems: a transdisciplinary overview pointing to integrative opportunities for agronomy. *Plant and soil, 362*, 389-417.

Jahn, R., Blume, H., Asio, V., Spaargaren, O., & Schad, P. (2006). *Guidelines for soil description*: FAO.

Jain, P. C. (1993). Greenhouse effect and climate change: scientific basis and overview. *Renewable energy, 3*(4-5), 403-420.

Jenkinson, B. (2002). Indicators of Reduction in Soils (IRIS): A visual method for the identification of hydric soils. *Agronomy. Purdue Univ., West Lafayette, IN*, 77.

Jenkinson, B., & Franzmeier, D. (2006). Development and evaluation of iron-coated tubes that indicate reduction in soils. *Soil Science Society of America Journal, 70*(1), 183-191.

Ji, Q., Babbin, A. R., Peng, X., Bowen, J. L., & Ward, B. B. (2015). Nitrogen substrate–dependent nitrous oxide cycling in salt marsh sediments.

Jørgensen, C. J., & Elberling, B. (2012). Effects of flooding-induced N2O production, consumption and emission dynamics on the annual N2O emission budget in wetland soil. *Soil Biology and Biochemistry, 53*, 9-17.

Kelleway, J. J., Saintilan, N., Macreadie, P. I., & Ralph, P. J. (2016). Sedimentary factors are key predictors of carbon storage in SE Australian saltmarshes. *Ecosystems, 19*, 865-880.

Kiehl, K., Esselink, P., & Bakker, J. (1997). Nutrient limitation and plant species composition in temperate salt marshes. *Oecologia, 111*, 325-330.

Kim, J., Lee, J., Yun, J., Yang, Y., Ding, W., Yuan, J., & Kang, H. (2020). Mechanisms of enhanced methane emission due to introduction of Spartina anglica and Phragmites australis in a temperate tidal salt marsh. *Ecological Engineering, 153*, 105905.

Klüber, H. D., & Conrad, R. (1998). Effects of nitrate, nitrite, NO and N2O on methanogenesis and other redox processes in anoxic rice field soil. *FEMS Microbiology Ecology, 25*(3), 301-318.

Koontz, E. L., Parker, S. M., Stearns, A. E., Roberts, B. J., Young, C. M., Windham-Myers, L., . . . Buskey, E. J. (2024). Controls on spatial variation in porewater methane concentrations across United States tidal wetlands. *Science of the Total Environment, 957*, 177290.

Kroeger, K. D., Crooks, S., Moseman-Valtierra, S., & Tang, J. (2017). Restoring tides to reduce methane emissions in impounded wetlands: A new and potent Blue Carbon climate change intervention. *Scientific reports, 7*(1), 11914.

Kutzbach, L., Schneider, J., Sachs, T., Giebels, M., Nykänen, H., Shurpali, N., . . . Wilmking, M. (2007). CO 2 flux determination by closed-chamber methods can be seriously biased by inappropriate application of linear regression. *Biogeosciences, 4*(6), 1005-1025.

Kutzbach, L., Wagner, D., & Pfeiffer, E.-M. (2004). Effect of microrelief and vegetation on methane emission from wet polygonal tundra, Lena Delta, Northern Siberia. *Biogeochemistry, 69*(3), 341-362.

Le Mer, J., & Roger, P. (2001). Production, oxidation, emission and consumption of methane by soils: a review. *European journal of soil biology, 37*(1), 25-50.

Levy, P. E., Gray, A., Leeson, S., Gaiawyn, J., Kelly, M., Cooper, M., . . . Sheppard, L. (2011). Quantification of uncertainty in trace gas fluxes measured by the static chamber method. *European Journal of Soil Science, 62*(6), 811-821.

Li, J., Qu, W., Han, G., Lu, F., Zhou, Y., Song, W., . . . Eller, F. (2020). Effects of drying-rewetting frequency on vertical and lateral loss of soil organic carbon in a tidal salt marsh. *Wetlands, 40*(5), 1433-1443.

Livesley, S. J., & Andrusiak, S. M. (2012). Temperate mangrove and salt marsh sediments are a small methane and nitrous oxide source but important carbon store. *Estuarine, Coastal and Shelf Science, 97*, 19-27.

Loick, N., Dixon, E., Abalos, D., Vallejo, A., Matthews, P., McGeough, K., . . . Cardenas, L. M. (2017). “Hot spots” of N and C impact nitric oxide, nitrous oxide and nitrogen gas emissions from a UK grassland soil. *Geoderma, 305*, 336-345.

Macreadie, P. I., Anton, A., Raven, J. A., Beaumont, N., Connolly, R. M., Friess, D. A., . . . Lavery, P. S. (2019). The future of Blue Carbon science. *Nature communications, 10*(1), 3998.

Maier, M., Weber, T. K., Fiedler, J., Fuß, R., Glatzel, S., Huth, V., . . . Schäfer, K. (2022). Introduction of a guideline for measurements of greenhouse gas fluxes from soils using non-steady-state chambers. *Journal of Plant Nutrition and Soil Science, 185*(4), 447-461.

Marjoribanks, T. I., Lague, D., Hardy, R., Boothroyd, R., Leroux, J., Mony, C., & Puijalon, S. (2019). Flexural rigidity and shoot reconfiguration determine wake length behind saltmarsh vegetation patches. *Journal of Geophysical Research: Earth Surface, 124*(8), 2176-2196.

McClain, M. E., Boyer, E. W., Dent, C. L., Gergel, S. E., Grimm, N. B., Groffman, P. M., . . . Mayorga, E. (2003). Biogeochemical hot spots and hot moments at the interface of terrestrial and aquatic ecosystems. *Ecosystems*, 301-312.

Mcleod, E., Chmura, G. L., Bouillon, S., Salm, R., Björk, M., Duarte, C. M., . . . Silliman, B. R. (2011). A blueprint for blue carbon: toward an improved understanding of the role of vegetated coastal habitats in sequestering CO2. *Frontiers in Ecology and the Environment, 9*(10), 552-560.

Megonigal, J. P., Hines, M., & Visscher, P. (2004). Anaerobic metabolism: linkages to trace gases and aerobic processes. *Biogeochemistry*.

Megonigal, J. P., & Neubauer, S. C. (2019). Biogeochemistry of tidal freshwater wetlands. In *Coastal wetlands* (pp. 641-683): Elsevier.

Mittmann-Goetsch, J., Wilson, M., Jensen, K., & Mueller, P. (2024). Root-driven soil reduction in wadden sea salt marshes. *Wetlands, 44*(8), 112.

Möller, I., Kudella, M., Rupprecht, F., Spencer, T., Paul, M., Van Wesenbeeck, B. K., . . . Miranda-Lange, M. (2014). Wave attenuation over coastal salt marshes under storm surge conditions. *Nature Geoscience, 7*(10), 727-731.

Morton, P. A., & Heinemeyer, A. (2018). Vegetation matters: Correcting chamber carbon flux measurements using plant volumes. *Science of the Total Environment, 639*, 769-772.

Moseman-Valtierra, S., Gonzalez, R., Kroeger, K. D., Tang, J., Chao, W. C., Crusius, J., . . . Shelton, J. (2011). Short-term nitrogen additions can shift a coastal wetland from a sink to a source of N2O. *Atmospheric Environment, 45*(26), 4390-4397.

Munsell, A. H. (2000). *Munsell soil color charts*: Gretagmacbeth.

Murray, R. H., Erler, D. V., & Eyre, B. D. (2015). Nitrous oxide fluxes in estuarine environments: response to global change. *Global change biology, 21*(9), 3219-3245.

Neiske, F., Seedtke, M., Eschenbach, A., Wilson, M., Jensen, K., & Becker, J. N. (2025). Soil organic carbon stocks and stabilization mechanisms in tidal marshes along estuarine gradients. *Geoderma, 456*, 117274.

Oertel, C., Matschullat, J., Zurba, K., Zimmermann, F., & Erasmi, S. (2016). Greenhouse gas emissions from soils—A review. *Geochemistry, 76*(3), 327-352.

Olsen, S. R. (1954). *Estimation of available phosphorus in soils by extraction with sodium bicarbonate*: US Department of Agriculture.

Pérez-Priego, O., López-Ballesteros, A., Sánchez-Cañete, E. P., Serrano-Ortiz, P., Kutzbach, L., Domingo, F., . . . Kowalski, A. S. (2015). Analysing uncertainties in the calculation of fluxes using whole-plant chambers: random and systematic errors. *Plant and soil, 393*, 229-244.

Pihlatie, M. K., Christiansen, J. R., Aaltonen, H., Korhonen, J. F., Nordbo, A., Rasilo, T., . . . Sheehy, J. (2013). Comparison of static chambers to measure CH4 emissions from soils. *Agricultural and forest meteorology, 171*, 124-136.

Poffenbarger, H. J., Needelman, B. A., & Megonigal, J. P. (2011). Salinity influence on methane emissions from tidal marshes. *Wetlands, 31*(5), 831-842.

Ponnamperuma, F. N. (1972). The chemistry of submerged soils. *Advances in agronomy, 24*, 29-96.

Rabenhorst, M. (2013). Using synthesized iron oxides as an indicator of reduction in soils. *Methods in biogeochemistry of wetlands, 10*, 723-740.

Rabenhorst, M., & Parikh, S. (2000). Propensity of soils to develop redoximorphic color changes. *Soil Science Society of America Journal, 64*(5), 1904-1910.

Rochette, P. (2011). Towards a standard non-steady-state chamber methodology for measuring soil N2O emissions. *Animal Feed Science and Technology, 166*, 141-146.

Rochette, P., Ellert, B., Gregorich, E., Desjardins, R., Pattey, E., Lessard, R., & Johnson, B. (1997). Description of a dynamic closed chamber for measuring soil respiration and its comparison with other techniques. *Canadian journal of soil science, 77*(2), 195-203.

Rockström, J., Steffen, W., Noone, K., Persson, Å., Chapin, F. S., Lambin, E. F., ... & Foley, J. A. . (2009). A safe operating space for humanity. *Nature, 461*(7263), 472-475.

Rosentreter, J. A., Al-Haj, A. N., Fulweiler, R. W., & Williamson, P. (2021). Methane and nitrous oxide emissions complicate coastal blue carbon assessments. *Global Biogeochemical Cycles, 35*(2), e2020GB006858.

Roughan, B. L., Kellman, L., Smith, E., & Chmura, G. L. (2018). Nitrous oxide emissions could reduce the blue carbon value of marshes on eutrophic estuaries. *Environmental Research Letters, 13*(4), 044034.

Rozema, J., Lenssen, G., Van de Staaij, J., Tosserams, M., Visser, A., & Broekman, R. (1997). Effects of UV-B radiation on terrestrial plants and ecosystems: interaction with CO 2 enrichment. *Plant Ecology, 128*, 183-191.

Saidy, A., Smernik, R., Baldock, J. A., Kaiser, K., & Sanderman, J. (2013). The sorption of organic carbon onto differing clay minerals in the presence and absence of hydrous iron oxide. *Geoderma, 209*, 15-21.

Sapkota, Y., Duball, C., Vaughan, K., Rabenhorst, M. C., & Berkowitz, J. F. (2022). Indicator of Reduction in Soil (IRIS) devices: A review. *Science of the Total Environment, 852*, 158419.

Schoutens, K., Heuner, M., Minden, V., Schulte Ostermann, T., Silinski, A., Belliard, J. P., & Temmerman, S. (2019). How effective are tidal marshes as nature-based shoreline protection throughout seasons? *Limnology and oceanography, 64*(4), 1750-1762.

Schulte Ostermann, T., Heuner, M., Fuchs, E., Temmerman, S., Schoutens, K., Bouma, T. J., & Minden, V. (2021). Unraveling plant strategies in tidal marshes by investigating plant traits and environmental conditions. *Journal of Vegetation Science, 32*(3), e13038.

Schulz, G., Sanders, T., Voynova, Y. G., Bange, H. W., & Dähnke, K. (2023). Seasonal variability of nitrous oxide concentrations and emissions along the Elbe estuary. *Biogeosciences Discussions, 2023*, 1-21.

Schulze, D., Rupprecht, F., Nolte, S., & Jensen, K. (2019). Seasonal and spatial within-marsh differences of biophysical plant properties: implications for wave attenuation capacity of salt marshes. *Aquatic Sciences, 81*(4), 65.

Schulze, D. G., Nagel, J. L., Van Scoyoc, G. E., Henderson, T. L., Baumgardner, M. F., & Stott, D. (1993). Significance of organic matter in determining soil colors. *Soil color, 31*, 71-90.

Schweingruber, F. H., Kučerová, A., Adamec, L., Doležal, J., Schweingruber, F. H., Kučerová, A., . . . Doležal, J. (2020). Stem anatomy in monocotyledonous aquatic and wetland plants. *Anatomic Atlas of Aquatic and Wetland Plant Stems*, 466-478.

Segers, R. (1998). Methane production and methane consumption: a review of processes underlying wetland methane fluxes. *Biogeochemistry, 41*(1), 23-51.

Seyfferth, A. L., Bothfeld, F., Vargas, R., Stuckey, J. W., Wang, J., Kearns, K., . . . Sparks, D. L. (2020). Spatial and temporal heterogeneity of geochemical controls on carbon cycling in a tidal salt marsh. *Geochimica et Cosmochimica Acta, 282*, 1-18.

Sgouridis, F., & Ullah, S. (2017). Soil greenhouse gas fluxes, environmental controls, and the partitioning of N2O sources in UK natural and seminatural land use types. *Journal of Geophysical Research: Biogeosciences, 122*(10), 2617-2633.

Shukla, P., Skea, J., Calvo Buendia, E., Masson-Delmotte, V., Pörtner, H., Roberts, D., . . . Van Diemen, R. (2019). IPCC, 2019: Climate Change and Land: an IPCC special report on climate change, desertification, land degradation, sustainable land management, food security, and greenhouse gas fluxes in terrestrial ecosystems.

Skiba, U., & Smith, K. (2000). The control of nitrous oxide emissions from agricultural and natural soils. *Chemosphere-global change science, 2*(3-4), 379-386.

Steffen, W., Richardson, K., Rockström, J., Cornell, S. E., Fetzer, I., Bennett, E. M., . . . De Wit, C. A. (2015). Planetary boundaries: Guiding human development on a changing planet. *Science, 347*(6223).

Sun, L., Song, C., Miao, Y., Qiao, T., & Gong, C. (2013). Temporal and spatial variability of methane emissions in a northern temperate marsh. *Atmospheric Environment, 81*, 356-363.

Sun, X., Jayakumar, A., Tracey, J. C., Wallace, E., Kelly, C. L., Casciotti, K. L., & Ward, B. B. (2021). Microbial N2O consumption in and above marine N2O production hotspots. *The ISME Journal, 15*(5), 1434-1444.

Sun, Z., Wang, L., Mou, X., Jiang, H., & Sun, W. (2014). Spatial and temporal variations of nitrous oxide flux between coastal marsh and the atmosphere in the Yellow River estuary of China. *Environmental Science and Pollution Research, 21*, 419-433.

Täumer, J., Kolb, S., Boeddinghaus, R. S., Wang, H., Schöning, I., Schrumpf, M., . . . Marhan, S. (2021). Divergent drivers of the microbial methane sink in temperate forest and grassland soils. *Global change biology, 27*(4), 929-940.

Tong, C., Morris, J. T., Huang, J., Xu, H., & Wan, S. (2018). Changes in pore-water chemistry and methane emission following the invasion of Spartina alterniflora into an oliogohaline marsh. *Limnology and oceanography, 63*(1), 384-396.

Tornberg, T., Bendix, M., & Brix, H. (1994). Internal gas transport in Typha latifolia L. and Typha angustifolia L. 2. Convective throughflow pathways and ecological significance. *Aquatic botany, 49*(2-3), 91-105.

Trifunovic, B., Vázquez-Lule, A., Capooci, M., Seyfferth, A. L., Moffat, C., & Vargas, R. (2020). Carbon dioxide and methane emissions from a temperate salt marsh tidal creek. *Journal of Geophysical Research: Biogeosciences, 125*(8), e2019JG005558.

Van Beusekom, J. E., Carstensen, J., Dolch, T., Grage, A., Hofmeister, R., Lenhart, H., . . . Rick, J. (2019). Wadden Sea Eutrophication: long-term trends and regional differences. *Frontiers in marine science, 6*, 370.

Velthof, G., & Oenema, O. (1995). Nitrous oxide fluxes from grassland in the Netherlands: II. Effects of soil type, nitrogen fertilizer application and grazing. *European Journal of Soil Science, 46*(4), 541-549.

Veneman, P., Spokas, L., & Lindbo, D. (1998). Soil moisture and redoximorphic features: a historical perspective. *Quantifying soil hydromorphology, 54*, 1-23.

Vepraskas, M., & Richardson, J. (2001). Morphological features of seasonally reduced soils. *Wetland soils: Genesis, hydrology, landscapes, and classification*, 163-182.

Visser, E. J., Colmer, T., Blom, C., & Voesenek, L. (2000). Changes in growth, porosity, and radial oxygen loss from adventitious roots of selected mono-and dicotyledonous wetland species with contrasting types of aerenchyma. *Plant, Cell & Environment, 23*(11), 1237-1245.

Von Fischer, J. C., & Hedin, L. O. (2007). Controls on soil methane fluxes: Tests of biophysical mechanisms using stable isotope tracers. *Global Biogeochemical Cycles, 21*(2).

Vuik, V., Jonkman, S. N., Borsje, B. W., & Suzuki, T. (2016). Nature-based flood protection: The efficiency of vegetated foreshores for reducing wave loads on coastal dikes. *Coastal engineering, 116*, 42-56.

Wagner, D., Pfeiffer, E.-M., & Bock, E. (1999). Methane production in aerated marshland and model soils: effects of microflora and soil texture. *Soil Biology and Biochemistry, 31*(7), 999-1006.

Wang, C., Tong, C., Chambers, L. G., & Liu, X. (2017). Identifying the salinity thresholds that impact greenhouse gas production in subtropical tidal freshwater marsh soils. *Wetlands, 37*(3), 559-571.

Wiesmeier, M., Urbanski, L., Hobley, E., Lang, B., von Lützow, M., Marin-Spiotta, E., . . . Garcia-Franco, N. (2019). Soil organic carbon storage as a key function of soils-A review of drivers and indicators at various scales. *Geoderma, 333*, 149-162.

WRB, I. W. G. (2022). *World Reference Base for Soil Resources. International soil classification system for naming soils and creating legends for soil maps* (4th ed. Vol. 4th edition). Vienna, Austria: International Union of Soil Sciences.

Xin, P., Wilson, A., Shen, C., Ge, Z., Moffett, K. B., Santos, I. R., . . . Moore, W. (2022). Surface water and groundwater interactions in salt marshes and their impact on plant ecology and coastal biogeochemistry. *Reviews of Geophysics, 60*(1), e2021RG000740.

Yang, W. H., & Silver, W. L. (2016). Gross nitrous oxide production drives net nitrous oxide fluxes across a salt marsh landscape. *Global change biology, 22*(6), 2228-2237.

Yousaf, A., Khalid, N., Aqeel, M., Noman, A., Naeem, N., Sarfraz, W., . . . Khalid, A. (2021). Nitrogen dynamics in wetland systems and its impact on biodiversity. *Nitrogen, 2*(2), 196-217.

Ysebaert, T., Yang, S.-L., Zhang, L., He, Q., Bouma, T. J., & Herman, P. M. (2011). Wave attenuation by two contrasting ecosystem engineering salt marsh macrophytes in the intertidal pioneer zone. *Wetlands, 31*, 1043-1054.

Yuan, J., Liu, D., Ji, Y., Xiang, J., Lin, Y., Wu, M., & Ding, W. (2019). Spartina alterniflora invasion drastically increases methane production potential by shifting methanogenesis from hydrogenotrophic to methylotrophic pathway in a coastal marsh. *Journal of Ecology, 107*(5), 2436-2450.

Zheng, J., RoyChowdhury, T., Yang, Z., Gu, B., Wullschleger, S. D., & Graham, D. E. (2018). Impacts of temperature and soil characteristics on methane production and oxidation in Arctic tundra. *Biogeosciences, 15*(21), 6621-6635.

Software

R R Core Team (2020). R: A language and environment for statistical computing. R Foundation for Statistical Computing, Vienna, Austria. URL https://www.R-project.org/

RStudio RStudio Team (2021). RStudio: Integrated Development Environment for R. RStudio, PBC, Boston, MA URL http://www.rstudio.com/.

Pandas The pandas development team. (2025). pandas-dev/pandas: Pandas (v2.3.1). Zenodo. https://doi.org/10.5281/zenodo.15831829
All versions https://doi.org/10.5281/zenodo.3509134

Python Python Software Foundation URL https://www.python.org/

MATLAB The MathWorks Inc, 2022, MATLAB Version: 9.12.0.1884302 (R2022a), Natick, Massachusetts: The MathWorks Inc. https://www.mathworks.com.

“chamberflux” Eckhardt, Tim; Kutzbach, Lars (2016): MATLAB code to calculate gas fluxes from chamber-based methods [dataset]. Institut für Bodenkunde,

Universität Hamburg, PANGAEA, https://doi.org/10.1594/PANGAEA.857799. Version V15 D. Holl, 2022-11, addition of N_2O flux calculation.

"stats" R Core Team (2020). R: A language and environment for statistical computing. R Foundation for Statistical Computing, Vienna, Austria. https://www.R-project.org/

"rstatix" Alboukadel Kassambara (2021). rstatix: Pipe-Friendly Framework for Basic Statistical Tests. R package version 0.7.0. https://CRAN.R-project.org/package=rstatix

"ggplot2" H. Wickham. ggplot2: Elegant Graphics for Data Analysis. Springer-Verlag New York, 2016. isbn 978-3-319-24277-4, https://ggplot2.tidyverse.org

"ggeffects" Lüdecke D (2018). "ggeffects: Tidy Data Frames of Marginal Effects from Regression Models." _Journal of Open Source Software_, *3*(26), 772. doi: 10.21105/joss.00772

"lmerTest" Kuznetsova A, Brockhoff PB, Christensen RHB (2017). "lmerTest Package: Tests in Linear Mixed Effects Models." _Journal of Statistical Software_, *82*(13), 1-26. doi: 10.18637/jss.v082.i13

"lme4" Douglas Bates, Martin Maechler, Ben Bolker, Steve Walker (2015). Fitting Linear Mixed-Effects Models Using lme4. Journal of Statistical Software, 67(1), 1-48. doi: 10.18637/jss.v067.i01.

"factoextra" Alboukadel Kassambara and Fabian Mundt (2020). factoextra: Extract and Visualize the Results of Multivariate Data Analyses. R package version 1.0.7. https://CRAN.R-project.org/package=factoextrafactoextra

"corrplot" Taiyun Wei and Viliam Simko (2021). R package 'corrplot': Visualization of a Correlation Matrix (Version 0.92). Available from https://github.com/taiyun/corrplot

"viridis/viridisLite" Simon Garnier, Noam Ross, Robert Rudis, Antônio P. Camargo, Marco Sciaini, and Cédric Scherer (2021). Rvision - Colorblind-Friendly Color Maps for R. R package version 0.4.0. doi: 10.5281/zenodo.4679424, https://sjmgarnier.github.io/viridis/

"ggpubr" Alboukadel Kassambara (2020). ggpubr: 'ggplot2' Based Publication Ready Plots. R package version 0.4.0. https://CRAN.R-project.org/package=ggpubr

Manuals and books

DETR1, Volcraft, EAN, 4016138518740, Voltcraft® Multimeter, Ladegerät, Multitester, https://www.conrad.de/de/marken/voltcraft.html

HMP45C, Campbell Scientific, Inc. (2011) HMP45C Temperature and Relative Humidity Probe https://www.campbellsci.com/hmp45c-l

LI-7810 CH_4 / CO_2 / H_2O LI-COR Environmental (2024) LI-7810 CH4 / CO2 / H2O Trace Gas Analyzer Instruction Manual. LI-COR, Inc. Publication Number: 984-17414 https://www.licor.com/support/LI-7810/manuals.html

LI-7820 N_2O / H_2O LI-COR Environmental (2020) LI-7820 N_2O / H_2O Trace Gas Analyzer Instruction Manual. LI-COR, Inc. Publication Number: 984-19432 https://www.licor.com/support/LI-7820/manuals.html

Munsell Soil Color Charts. Munsell Color Co. Inc. Baltimore 18, Maryland 21218, USA.

VDLUFA (1991): Bestimmung von Phosphor und Kalium im Doppellactat (DL)-Auszug. Methodenbuch I, Ziffer A 6.2.1.2, 12 S.

Reports

IPCC, 2007: Climate Change 2007: The Physical Science Basis. Contribution of Working Group I to the Fourth Assessment Report of the Intergovernmental Panel on Climate Change [Solomon, S., D. Qin, M. Manning, Z. Chen, M. Marquis, K.B. Averyt, M. Tignor and H.L. Miller (eds.)]. Cambridge University Press, Cambridge, United Kingdom and New York, NY, USA, 996 pp.

IPCC, 2007: *Summary for Policymakers*. In: Climate Change 2007: The Physical Science Basis. Contribution of Working Group I to the Fourth Assessment Report of the Intergovernmental Panel on Climate Change [Solomon, S., D. Qin, M. Manning, Z. Chen, M. Marquis, K.B. Averyt, M. Tignor and H.L. Miller (eds.)]. Cambridge University Press, Cambridge, United Kingdom and New York, NY, USA.

ABP Marine Environmental Research Ltd. Hamburg Port Authority and Federal Waterways and Shipping Administration: River Elbe River Engineering and Sediment Management Concept. Review of sediment management strategy in the context of other European estuaries from a morphological perspective. Report R.1805, May 2011. [Whitehead, P., Houghton, A., Brown, C.]

Maps

Burbaum B., Gehrt E., Janetzko P., Sponagel H., Eckelmann W., Stegger U. (2018), Bodenübersichtskarte 1:200 000 [map], CC2318 Neumünster, Bundesanstalt für Geowissenschaften und Rohstoffe, in Zusammenarbeit mit den Staatlichen Geologischen Diensten. Stilleweg 2, 30655 Hannover, Germany.
UUID : 3E80DA1A-A9A7-45A3-9CC7-79796FE9ABA4

Online sources

Lan, X., K.W. Thoning, and E.J. Dlugokencky: Trends in globally-averaged CH4, N2O, and SF6 determined from NOAA Global Monitoring Laboratory measurements. Version 2025-06, https://doi.org/10.15138/P8XG-AA10. Accessed on 07.06.2025

Preprints

B. B. Branoff, L. Grüterich, M. Wilson, S. P. Tobias-Hunefeldt, Y. Saadaoui, J. Mittmann-Goetsch, F. Neiske, F. Lexmond, J. N. Becker, H.-P. Grossart, P. Porada, W. R. Streit, A. Eschenbach, L. Kutzbach, K. Jensen (2024). Partitioning biota along the Elbe River estuary: where are the community transitions? *bioRxiv* https://doi.org/10.1101/2024.05.13.593883

Appendices

A. Contributions to this dissertation

Research site preparations

The board walks, present at the research stations set up at each tidal wetland zones, were constructed by PhD candidates, post doctoral employees, student assistants and technicians associated with the RTG2530, as well as by employees and interns of the Landesbetrieb für Küstenschutz, Nationalpark und Meeresschutz Schleswig-Holstein (LKN.SH). The preparation, organization of the board walk installation, the general site management and maintenance, as well as experimental site access and work permits were prepared, maintained and led by L. Kutzbach and F. Lexmond. The research stations hosted various research projects within the overarching “Biota-mediated effects on Carbon cycling in Estuaries” project of the RTG2530. This project relied on data stored on logger masts that were set-up at the entrance of each research station for data storage from the various sensors. Its installation was led and maintenance performed by V. Kleinschmidt. Once a year plant community surveys and above ground biomass measurements were performed at the research sites led by M. Wilson and K. Jensen, the raw data collected during these surveys have been used in this dissertation.

Characterization of soils and soil redox conditions

The results of the soils and soil redox condition characterization included in this dissertation will be part of the co-authored manuscript: “Soils and redox conditions in estuaries” by F. N. Lexmond, F. Neiske, J. Mittmann-Goetsch et al. (planned 2026). Contributions declared here are according to its current state in July 2025.

The soil morphological descriptions were led by L. Kutzbach (general characterization), F.N Lexmond (general and chemical characterization), F. Neiske (physical characterization and sensors data) and M. Wilson (vegetation characterization). The field work was supported by W. Putri, P. Tutiyasarn, O. Kaufmann, M. Seedtke, D. Schwarze, C. Skotorzick, S. Undeutsch, C. Wefels, D. Holl, B. Grabellus. The soil sample chemical analyses were conducted or overseen by B. Grabellus. The soil sample physical properties analyses were conducted or overseen by D. Harms. The soil classification, result visualization and statistical testing and interpretation of findings were done by F.N. Lexmond. The IRIS experiment was designed by F.N. Lexmond and F. Neiske, with advice from P. Mueller and J. Mittmann-Goetsch. The IRIS material preparation was done by J. Mittmann-Goetsch, F. Neiske and V. Kleinschmidt. Installations and retrieval of the IRIS material in the field was conducted by F.N Lexmond and F. Neiske. The IRIS stick analyses, scanning and data acquisition was conducted and overseen by J. Mittmann-Goetsch. The here presented IRIS results were statistically analysed and visualized by F. N. Lexmond. The soil redox sensor installations, maintenance and data collection was conducted by V. Kleinschmidt and F. Neiske. The redox sensor data preprocessing was performed by D. Holl. Redox sensor data

statistical analyses and visualization was performed by by F. N. Lexmond. The development, testing, visualisation of the redox conditions characterization method comparison (RC-RI-Rh) system were done by F. N. Lexmond. Results interpretation and discussion and the manuscript writing are being performed by F. N. Lexmond; with input from D. Holl, L. Kutzbach, J. Becker, F. Neiske.

Manual flux chamber development and flux data analyses

The collar and flux chambers were designed by N. Rüggen, construction of the collars was done by F. Lexmond and technicians from the CEN Workshop of University Hamburg. Flux chamber constructions were done by F. N. Lexmond, D. Holl and Heindrich Feinmechanik, Lentföhrden, Germany. The conversion script for the raw trace gas analyzer data was provided by D. Holl.

Written text

The written Zusammenfassung has been reviewed by T. Sodenkamp and her feedback and suggestions on grammar and sentence construction have been incorporated in the present text. Additionally, I relied on the DeepL free version (DeepL.com) for the occasional specific German jargon or unfamiliar words in the Zusammenfassung.

B. Collar installation and collar details

Figure 24 Installation of soil collars. On the left collar installation at the salt marsh (SM), picture taken on 2022-01-25, and on the right collar installation at the fresh water marsh (FM), picture taken on 2022-02-09, by F. N. Lexmond.

Figure 25 Soil collar detail pictures. PVC plate corners riveted together with alumina L-shaped profiles and PVC–aluminia contact was sealed with silicon. Pictures on the left from 2022-02-24, picture on the right from 2022-01-10, taken by F. N. Lexmond.

Table 20 Collar dimensions used for surface area calculation.

collar element	size dimension X (cm)	size dimension Y (cm)
PVC-U plane	0.795	0.795

C. Manual closed flux chamber design of Chamber1

Figure 26 Manual closed flux chamber Chamber1 at the grazed high salt marsh (SM HMg), picture taken on 2022-07-27 by F. N. Lexmond.

Table 21 Chamber1 dimensions per flux chamber element used for headspace volume calculation.

chamber element	size dimension l (cm)	size dimension w (cm)	size dimension h (cm)
top	NA	NA	NA
base	80.5	80.5	82.7
bottom	77.5	77.5	3.2

D. Manual closed flux chamber design of Chamber2

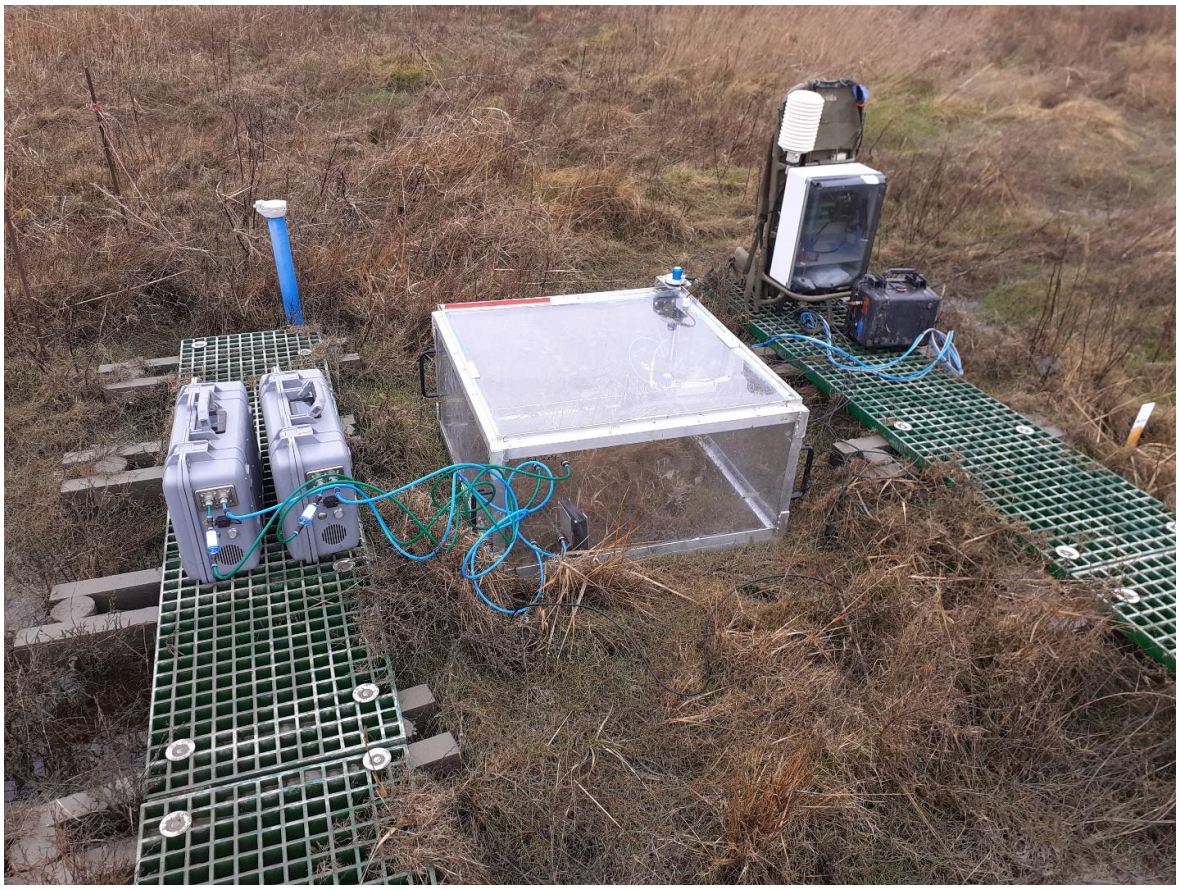

Figure 27 Manual closed chamber flux measurement with Chamber2 at low salt marsh, taken on 2023-02-22, picture by F. N. Lexmond.

Table 22 Chamber2 dimensions per flux chamber element used for headspace volume calculation.

chamber element	size dimension l (cm)	size dimension w (cm)	size dimension h (cm)
top	77.5	77.7	1.0
base	82.6	82.6	39.7
bottom	77.9	78.1	3.2

E. Manual closed flux chamber small and large extensions

Figure 28 Manual closed flux chamber extensions. Top left: large extension used at fresh water pioneer zone (FM PZ), picture taken on 2022-06-30. Top right: two small extensions stacked, picture taken on 2022-09-14. Bottom: combination of the large extension and Chamber2 at the fresh water marsh pioneer zone (FM PZ) on 2023-01-17. Pictures by F. N. Lexmond.

Table 23 Extension dimensions per flux chamber element used for headspace volume calculation.

chamber element	size dimension l (cm)	size dimension w (cm)	size dimension h (cm)
large extension top	77.5	77.7	0.4
large extension base	82.5	82.7	80.8
large extension bottom	77.9	78.1	3.2
small extension top	77.5	77.7	0.4
small extension base	82.6	82.6	39.7
small extension bottom	77.9	78.1	3.2

F. Flux chamber measurement dates

Table 24 Overview of dates corresponding to the conducted measurements at the six studied tidal wetland zones.

tidal wetland zone	#days	dates
FM PZ	12	2022-04-26, 2022-05-17, 2022-09-14, 2022-09-27, 2022-10-27 2023-01-17, 2023-02-23, 2023-03-28, 2023-04-18, 2023-05-11, 2023-06-16, 2023-07-11
BM PZ	11	2022-04-27, 2022-05-11, 2022-05-23, 2022-06-30 2023-01-18, 2023-02-23, 2023-03-27, 2023-04-20, 2023-05-12, 2023-06-14, 2023-06-28
SM PZ	19	2022-04-28, 2022-05-12, 2022-05-25, 2022-06-03, 2022-06-05, 2022-07-12, 2022-07-27, 2022-08-02, 2022-08-10, 2022-08-30, 2022-09-12, 2022-10-26 2023-01-26, 2023-02-22, 2023-04-13, 2023-05-10, 2023-06-01, 2023-06-15, 2023-06-27
SM LM	17	2022-04-28, 2022-05-12, 2022-05-25, 2022-06-03, 2022-06-13, 2022-07-28, 2022-08-02, 2022-08-25, 2022-08-31, 2022-09-13, 2022-10-26 2023-02-20, 2023-02-22, 2023-04-11, 2023-05-10, 2023-06-01, 2023-06-15
SM HMu	19	2022-04-28, 2022-05-12, 2022-05-25, 2022-06-03, 2022-06-13, 2022-07-27, 2022-08-02, 2022-08-10, 2022-08-30, 2022-09-12, 2022-10-26, 2022-12-14 2023-01-26, 2023-02-22, 2023-04-13, 2023-05-10, 2023-06-01, 2023-06-15, 2023-06-27
SM HMg	18	2022-04-28, 2022-05-12, 2022-05-25, 2022-06-03, 2022-06-13, 2022-07-27, 2022-08-02, 2022-08-25, 2022-08-31, 2022-09-13, 2022-10-26, 2022-12-14 2023-01-26, 2023-02-20, 2023-04-11, 2023-05-10, 2023-06-01, 2023-06-15

#days number of measurement days

G. Flux chamber measurement procedure

Preparation of a chamber measurement consisted of the following steps: turning on the portable analysers during travel to the experimental sites, to allow them to heat up and stabilize the laser conditions. Upon arrival at a research station the collars and vegetation were inspected. Followed by the installation of the soil probes. Each time, the installation point of each probe was noted down with respect to river, dike and station entrance. The flux chamber (and extensions) was placed on top of the soil collar after sorting out the inward and outward leaning vegetation. Chamber1 would additionally require flattening of the attached plastic sheet onto the soil surface and placing the metal chain on top. Then the flux chamber was strapped to the board walk or tent pegs with bungy-cords. Finally, the pressure vents would be closed with the stops and the cables and tubing were connected to the power sources and the gas analyser in- and outlets. The moment of flux chamber connection to the gas analyser marked the start of a measurement. The start time in UTC was noted down and for Chamber1 measurements $T_{air_in_man}$ was noted too. During measurements with Chamber1 the temperature was checked after each minute and noted down in addition to the start temperature.

A measurement was finished the moment the end time was noted down, after which the system was prepared for removal. First, the tubes and cables between flux chamber, portable trace gas analysers and loggerbox were disconnected, then the soil probes were removed, finally the extensions and chamber were lifted from the collar and aired out. A picture was made of each collar to track vegetation and ponding on the plot after the five replicate plots were measured. The recorded data was downloaded from the portable trace gas analysers and the data logger at the end of each measurement day.

H. Example plot of (potential) false negative flux

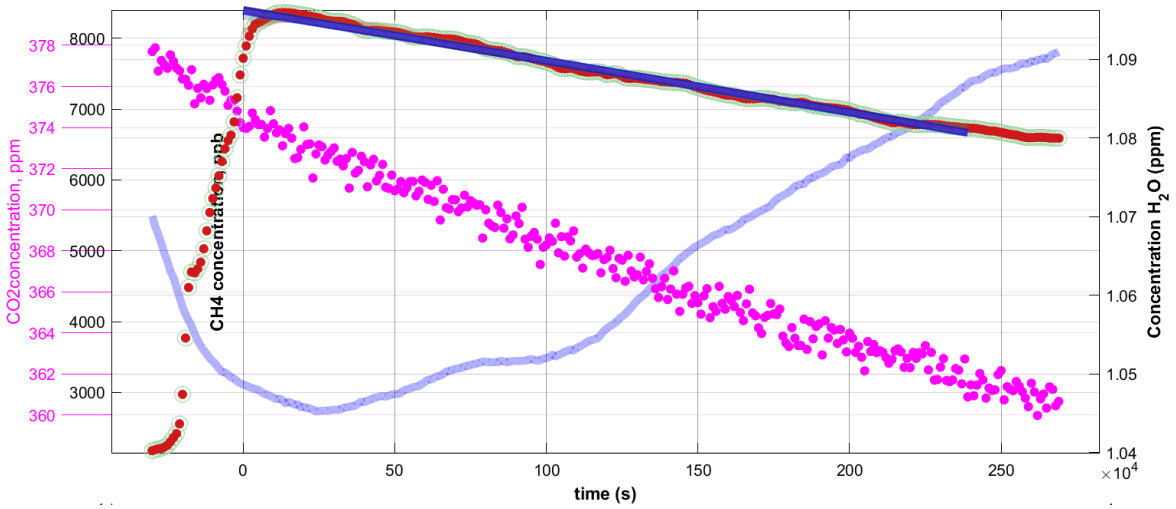

Figure 29 Plot of gas concentration change (pink ppm CO_2, red ppb CH_4, purple ppm H_2O) over the four minute window within five minute measurement. Flux measurement example from fresh water marsh pioneer zone on 2023-04-18. The calculated linear flux was -2.30 (± 0.06) µg CH_4 m^{-2} s^{-1}, with R^2 of 0.98, RMSE of 75.22, but the intercept of the regression model was 8397.7 ppb compared to expected ambient of about 2100 ppb.

I. RMSE details for CH_4 and N_2O full data sets

Table 25 Mean RMSE with standard errors (ppb) from linear CH_4 flux regression model per quality level group per salinity zone.

salinity zone	QL1	QL2	QL3	QL4
FM	38.0 ± 6.1	315 ± 139.0	192 ± 48.4	81.3 ± 36.6
BM	2.7 ± 0.5	6.3 ± 2.0	5.5 ± 1.9	25.3 ± 20.3
SM	$0.2 \pm 5.6*10^{-3}$	$0.4 \pm 2.9*10^{-2}$	0.5 ± 0.1	0.3 ± 0.1

Table 26 Mean CH_4 land-atmosphere fluxes with standard error (mg m^{-2} h^{-1}) calculated with linear regression model per quality level group per salinity zone.

salinity zone	QL1	QL2	QL3	QL4
FM	12.8 ± 1.4	37.2 ± 11.6	13.3 ± 13.0	3.2 ± 5.7
BM	$9.0*10^{-1} \pm 1.7*10^{-1}$	$1.9 \pm 5.5*10^{-1}$	$2.9*10^{-1} \pm 3.4*10^{-1}$	$-6.1*10^{-1} \pm 4.5*10^{-1}$
SM	$4.6*10^{-3} \pm 1.3*10^{-3}$	$8.2*10^{-3} \pm 4.5*10^{-3}$	$-5.5*10^{-2} \pm 3.0*10^{-2}$	$-9.1*10^{-3} \pm 4.5*10^{-3}$

Table 27 Mean RMSE with standard errors (ppb) from linear N_2O flux regression model per quality level group per salinity zone.

salinity zone	QL1	QL2	QL3	QL4
FM	$2.3*10^{-1} \pm 9.4*10^{-3}$	$1.9*10^{-1} \pm 16.7*10^{-3}$	$2.1*10^{-1} \pm 28.8*10^{-3}$	$8.0*10^{-1} \pm 566*10^{-3}$
BM	$2.1*10^{-1} \pm 11.5 *10^{-3}$	$2.7*10^{-1} \pm 19.4*10^{-3}$	$2.4*10^{-1} \pm 16.7*10^{-3}$	$1.5*10^{-1} \pm 0.8*10^{-3}$
SM	$2.0*10^{-1} \pm 3.7*10^{-3}$	$3.2*10^{-1} \pm 10.7*10^{-3}$	$2.1*10^{-1} \pm 9.4*10^{-3}$	$3.0*10^{-1} \pm 59.7*10^{-3}$

Table 28 Mean N_2O land-atmosphere fluxes with standard error (mg m^{-2} h^{-1}) calculated with linear regression model per quality level group per salinity zone.

salinity zone	QL1	QL2	QL3	QL4
FM	$1.3*10^{-2} \pm 2.72*10^{-3}$	$2.2*10^{-2} \pm 5.90*10^{-3}$	$1.1*10^{-2} \pm 12.4*10^{-3}$	$-13.8*10^{-2} \pm 135*10^{-3}$
BM	$2.4*10^{-2} \pm 4.2*10^{-3}$	$2.7*10^{-2} \pm 7.8*10^{-3}$	$0.1*10^{-2} \pm 1.9*10^{-3}$	$0.8*10^{-2} \pm 5.0*10^{-3}$
SM	$2.0*10^{-2} \pm 1.9*10^{-3}$	$3.1*10^{-2} \pm 5.2*10^{-3}$	$1.8*10^{-2} \pm 3.5*10^{-3}$	$0.9*10^{-2} \pm 10.1*10^{-3}$

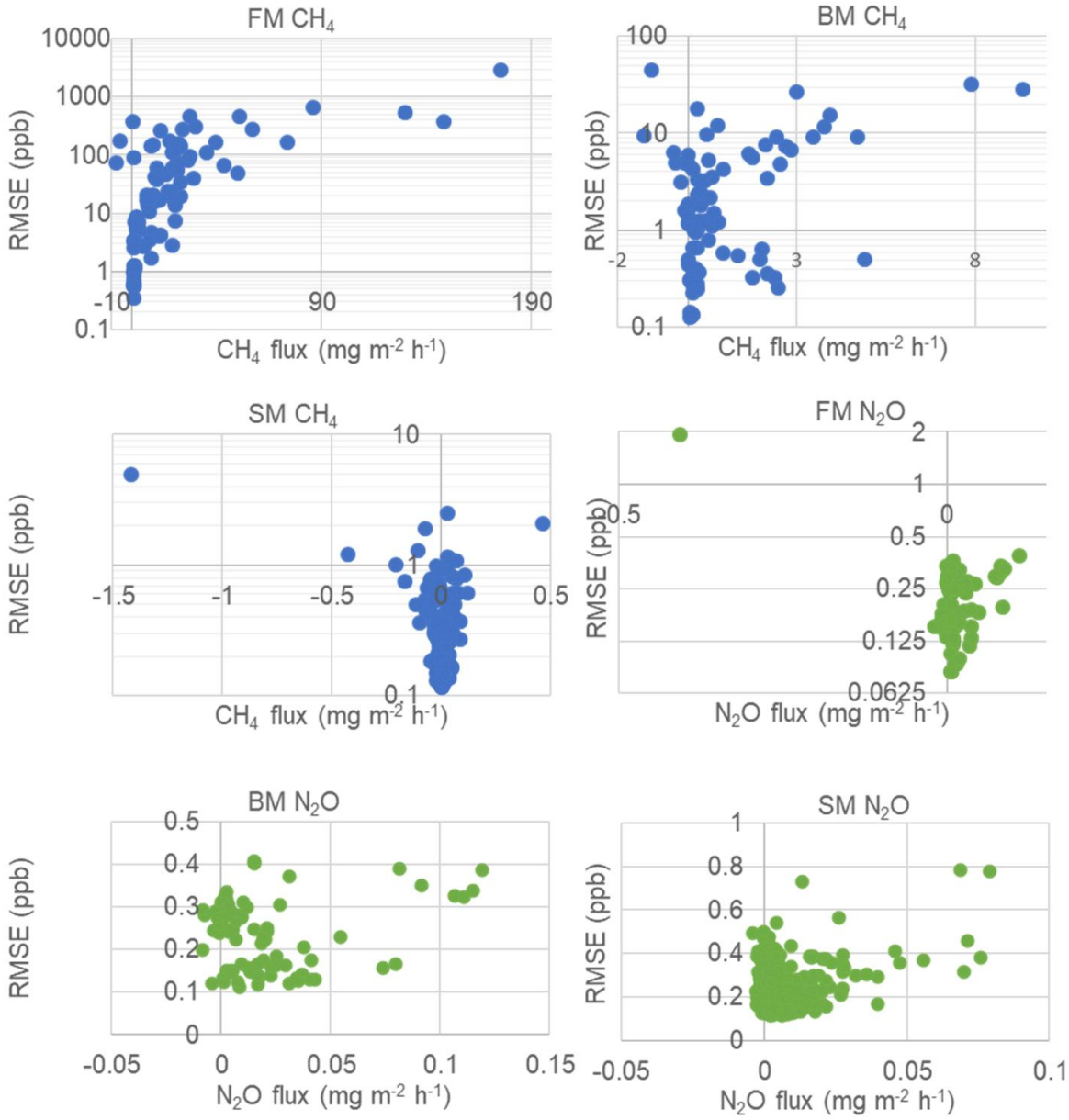

Figure 30 Scatter plots of RMSE (ppb) and calculated land-atmosphere flux magnitude for methane (blue) and nitrous oxide (green) at the three salinity zones including all data points (QL1, QL2, QL3, QL4) from all flux replicate plots, tidal wetland zones and measurement campaigns.

J. Example of deformed collar

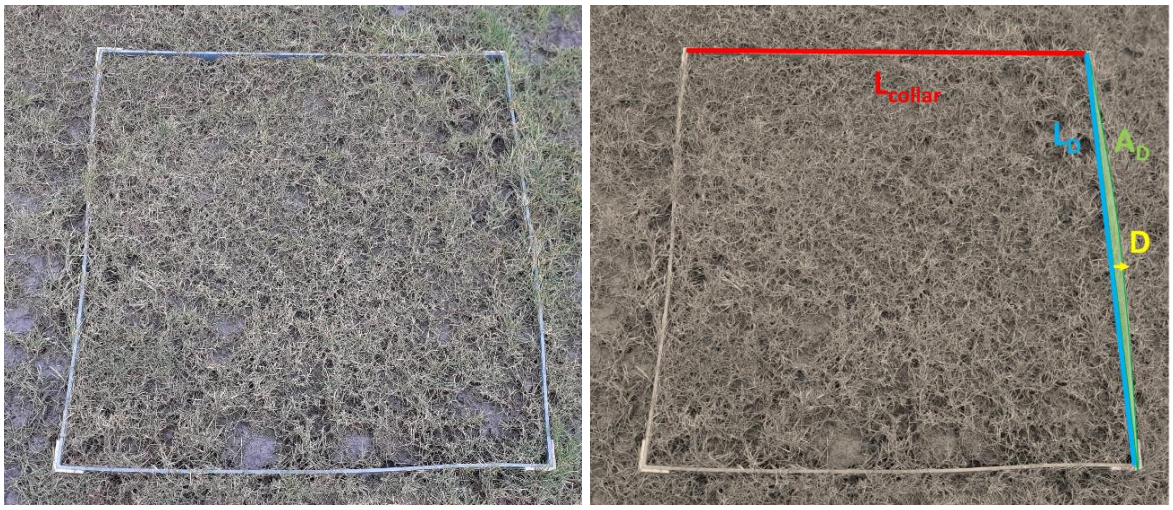

Figure 31 Picture on the left: a deformed collar at salt marsh' managed high marsh (SM HMg). Picture on the right: visualization of collar deforment variables used to calculate the propagated error for surface area in the flux calculation. Pictures by F. N. Lexmond.

K. Friedman tests covered measurement days

Table 29 Overview of day of the year (DOY) included in Friedman tests, corresponding date and season, tidal wetland zone and greenhouse gases sampled.

DOY	**118**	**132**	**145**	**154**	**164**	**208**	**214**
date	2022-04-28	2022-05-12	2022-05-25	2022-06-03	2022-06-13	2022-07-27	2022-08-02
season	spring	spring	spring	summer	summer	summer	summer
tidal wetland zone	SM HMu	SM PZ SM LM SM HMu SM HMg	SM PZ SM HMg	SM PZ	SM HMu SM HMg	SM PZ SM HMg	SM PZ SM HMu
gases	CH_4 N_2O	CH_4 N_2O	CH_4 N_2O	CH_4 N_2O	CH_4 N_2O	CH_4	CH_4 N_2O

DOY	**242**	**256**	**257**	**270**	**299**	**348**	**382**
date	2022-08-30	2022-09-13	2022-09-14	2022-09-27	2022-10-26	2022-12-14	2023-01-17
season	summer	autumn	autumn	autumn	autumn	winter	winter
tidal wetland zone	SM PZ SM HMu	SM HMg	FM PZ	FM PZ	SM LM SM HMg	SM HMg	FM PZ
gases	CH_4 N_2O	CH_4	CH_4 N_2O	CH_4 N_2O	CH_4 N_2O	CH_4	CH_4 N_2O

DOY	**391**	**416**	**419**	**466**	**468**	**495**	**496**
date	2023-01-26	2023-02-20	2023-02-23	2023-04-11	2023-04-13	2023-05-10	2023-05-11
season	winter	winter	winter	spring	spring	spring	spring
tidal wetland zone	SM PZ	SM LM SM HMg	FM PZ	SM LM SM HMg	SM PZ	SM LM SM HMu	FM PZ
gases	CH_4 N_2O	CH_4 N_2O	CH_4 N_2O	CH_4 N_2O	CH_4 N_2O	CH_4 N_2O	CH_4 N_2O

DOY	**517**	**531**	**532**	**543**
date	2023-06-01	2023-06-15	2023-06-16	2023-06-27
season	summer	summer	summer	summer
tidal wetland zone	SM PZ SM LM SM HMu SM HMg	SM PZ SM HMu	FM PZ	SM PZ SM HMu
gases	CH_4 N_2O	CH_4 N_2O	CH_4 N_2O	CH_4 N_2O

L. Soil description forms

Soil morphological descriptions of soils at tidal wetland zones fresh water marsh (FM), brackish marsh (BM) and salt marsh (SM) and respective pioneer zone (PZ), low marsh (LM), unmanaged high marsh (HMu) and managed high marsh (HMg). Horizon descriptions focussed on redox related morphological characteristics. Soil color according to Munsell color charts for matrix color, color mottles, and color reducing features (Munsell, 2000). Soil structures indicated as [type, size] with codes: SB = subangular blocky, GR= granular, AB = angular blocky, MA= massive, SA=sub-/and angular blocky, SG=single grain, structure sizes are VF=very fine, FI=fine/thin, ME=medium, FM=fine and medium, CO=coarse/thick, as described in FAO guidelines for soil description (Jahn et al., 2006). Roots indicated as [size, abundance] with codes: VF= very fine, F= fine, FF= very fine and fine, M=medium, FM= fine and medium, C=coarse and V =very few, F=few, C=common, M=many as described in FAO guidelines for soil description (Jahn et al., 2006).

Profile number			Date of description		Authors			Lat/Lon (UTM 32U)	Elevation (GPS)		Location	
FM PZ			22.02.2022		Maria. S, Lars K.			0536502, 5946448			Pioneer zone in fresh water marsh	
Present weather			Former weather		Soil Temperature Regime			Soil Moisture Regime	Parent Material		Age of the Landsurface	
OV			WC5		ME			AQ	UM2		Yn	
Major landform			Position		Slope form			Slope gradient and orientation	Erosion		Surface sealing and cracks	
LP			-		-			-	W		-	
Land use			Crops		Human influence			Vegetation	Rock outcrops		Coarse surface fragments	
PN			-		-			HT, Prhagmites	-		-	
No.	Depth	Horizon Symbol	Color	Mottling				Reducing conditions	Roots		Soil structure	
				Color	Abund-ance	Size	Contrast		Diameter	Abundance	Type	Size Class
1	0-3	Ah	5GY 4/1	10YR5/8	A	M	C	N 2.5/.	FF	F	PM	
2	3-15	Ahr1	5GY 4/1	-	-	-	-	N 2.5/.	FF	VF	MA	
3	15-30	Ahr2	5GY 4/1	-	-	-	-	N 2.5/.	FF	C	SB, GR	FM
4	30-55	Ahr3	5GY 4/1	-	-	-	-	N 2.5/.	VF	C	SB, GR	FM
5	55-65	Ahr4	5GY 4/1	-	-	-	-	N 2.5/.	VF	C	SB, GR	FM
Remarks		Reducing colors N 2.5/. is dominant in Ahr2 and Ahr4, 5GY 4/1 is dominant in Ahr1 and Ahr3										
Classification		Fluvic, Reductigleyic, Stagnic, Tidalic, Reductic Gleysol (clayic, humic, laxic)										

Profile number		Date of description	Authors	Lat/Lon (UTM 32U)	Elevation (GPS)	Location
FM LM		22.02.2022	Maria. S, Lars K.	0536552, 5946462		Low mars in fresh water marsh
Present weather		Former weather	Soil Temperature Regime	Soil Moisture Regime	Parent Material	Age of the Landsurface
PC		WC5	ME	AQ	UM2	Yn
Major landform		Position	Slope form	Slope gradient and orientation	Erosion	Surface sealing and cracks
LP		-	-	-	W	-
Land use		Crops	Human influence	Vegetation	Rock outcrops	Coarse surface fragments
PN1		-	-	HT, Prhagmites	-	-

No.	Depth	Horizon Symbol	Color	Mottling				Reducing conditions	Roots		Soil structure	
				Color	Abund-ance	Size	Contrast		Diameter	Abundance	Type	Size Class
1	0-18	Ah	10YR 3/2	2.5YR3/4			D,S	N 3/.	VF	M	SB, GR	FI,ME
2	18-24	Ahl	10YR 3/2	2.5YR3/4				N 3/.	VF	M	SB, GR	FI,ME
3	24-34	Ahr1	10YR 3/2					N 2.5/.	FF	C	SB	CO
4	34-48	Ahr2	10YR 3/2					N 2.5/.	FM	F	SB	CO
5	48-80+	Ahr3	10Y 2.5/.								MA	

Remarks	Top 18cm rhizomes vertically orientated, 18-24cm horizontal rhizomes
Classification	Fluvic, Reductigleyic, Stagnic, Mollic, Reductic Gleysol (loamic, humic, panpaic)

Profile number			Date of description		Authors			Lat/Lon (UTM 32U)		Elevation (GPS)		Location	
FM HMu			23.02.2022		Widhi P., Monica W.			0536602, 5946455				Unmanaged high marsh in fresh water marsh	
Present weather			Former weather		Soil Temperature Regime			Soil Moisture Regime		Parent Material		Age of the Landsurface	
PC			WC5		ME			AQ		UM2		Yn	
Major landform			Position		Slope form			Slope gradient and orientation		Erosion		Surface sealing and cracks	
LP			-		-			-		W		-	
Land use			Crops		Human influence			Vegetation		Rock outcrops		Coarse surface fragments	
PN2			-		N			HT, Prhagmites		-		-	
No.	Depth	Horizon Symbol	Color	Mottling				Reducing conditions	Roots		Soil structure		
				Color	Abundance	Size	Contrast		Diameter	Abundance	Type	Size Class	
1	0-12	Ah	10YR 3/1	-	V	F	F	-	VF	C			
2	12-20	Ah	10YR 4/1	-	V	F	D	-	VF, F	C, V			
3	20-30	Ah	10YR 3/2	5YR 4/6	F	F	D	-	M, F	C			
4	30-40	Ahr	10YR 4/2	5YR 3/4	C	M	D	-	VF, F, M	F			
5	40-60	Br	10YR 4/2	5YR 3/4	M	M	D	-	VF	V			
Remarks													
Classification			Fluvic, Stagnic, Somerimollic Gleysol (siltic, humic, laxic, sideralic, ferric)										

Profile number	Date of description	Authors	Lat/Lon (UTM 32U)	Elevation (GPS)	Location
BM PZ	02.03.2022	Selina U.	0524326, 5965031	-5 m	Pioneer zone in brackish marsh
Present weather	Former weather	Soil Temperature Regime	Soil Moisture Regime	Parent Material	Age of the Landsurface
Major landform	Position	Slope form	Slope gradient and orientation	Erosion	Surface sealing and cracks
Land use	Crops	Human influence	Vegetation	Rock outcrops	Coarse surface fragments

No.	Depth	Horizon Symbol	Color	Mottling				Reducing conditions	Roots		Soil structure	
				Color	Abundance	Size	Contrast		Diameter	Abundance	Type	Size Class
1	0-1	A	10YR 4/3	2.5Y 3/1	V	F	D/S		FF	F	MA(+GR)	GR:CO
2	1-30	Ab/B1?	N 2.5/.	-	-	-	-		All	F	MA(+GR)	GR:CO
3	30-37	B2	N 3/.	-	-	-	-		All	C	MA(+GR)	GR:CO
4	37-55	G	N 3/.	-	-	-	-		VF, C	V	MA(+GR)	GR:CO
5	55-70	G2	N 3/.	-	-	-	-		VF	V	MA(+GR)	GR:CO

Remarks	
Classification	Fluvic, Reductigleyic, Tidalic, Reductic Gleysol (loamic, sideralic)

Profile number			Date of description		Authors		Lat/Lon (UTM 32U)		Elevation (GPS)		Location	
BM LM			24.02.22		Widhi A. P.		0524416, 5965136		-5 m		Low marsh in brackish marsh	
Present weather			Former weather		Soil Temperature Regime		Soil Moisture Regime		Parent Material		Age of the Landsurface	
PC			WC4		ME		DU		UM2		Yn	
Major landform			Position		Slope form		Slope gradient and orientation		Erosion		Surface sealing and cracks	
LP			-		-		-		W		-	
Land use			Crops		Human influence		Vegetation		Rock outcrops		Coarse surface fragments	
PN1 (FFH)			-		N		HT		-		-	
No.	Depth	Horizon Symbol	Color	Mottling				Reducing conditions	Roots		Soil structure	
				Color	Abundance	Size	Contrast		Diameter	Abundance	Type	Size Class
1	0-16	Ahl1	10YR 4/1	5YR 3/1	C	M	D		FF	M	GR, SB	FI, CO
2	16-19	Ahl2	10YR 4/1	2.5YR 2.5/4	A	F	P		FF	M	SA	VF
3	19-24	Ahr	Gley12.5/10Y	-	-	-	-		FF	M	MA(GR)	VF
4	24-70	Ahrb	Gley12.5/N &	-	-	-	-		FF	C	MA(GR)	VF
5			Gley 13/10Y									
6	70-75	Cr	Gley14/N	-	-	-	-		F	V	SG	-
Remarks												
Classification			Fluvic, Stagnic, Reductic Gleysol (loamic, humic, protosalic, ferric, panpaic)									

Profile number		Date of description	Authors	Lat/Lon (UTM 32U)	Elevation (GPS)	Location
BM HMu		24.02.22	Widhi A. P., Friederike N.	0524504, 5965171	0 m	Unmanaged high marsh in brackish marsh
Present weather		Former weather	Soil Temperature Regime	Soil Moisture Regime	Parent Material	Age of the Landsurface
PC		WC4	ME	UD	UM2	Yn
Major landform		Position	Slope form	Slope gradient and orientation	Erosion	Surface sealing and cracks
LP		-	-	-	W	-
Land use		Crops	Human influence	Vegetation	Rock outcrops	Coarse surface fragments
PN 1(FFH)		-	N	HT	-	-

No.	Depth	Horizon Symbol	Color	Mottling				Reducing conditions	Roots		Soil structure	
				Color	Abundance	Size	Contrast		Diameter	Abundance	Type	Size Class
1	0-23	Ah	5YR 2.5/2	-	-	-	-		FF	C	SB,GR	CO,ME
2	23-43	Bl	10YR 4/2	5YR 4/6	M	F	D		FM	V	SB	CO
3	43-80	Ahrb	10Y 2.5/1	-	-	-	-		VF	V	SB	CO
Remarks		23-43 lowest 2 cm pure (fine) sand color 2.5Y 5/2; also contained a stone (ø ≤ 2cm) | 15-40cm rhizomes (1/dm2) | 43-80cm lot of undecomposed root/ sedge peat										
Classification		Fluvic, Stagnic, Mollic, Reductic Gleysol (loamic, humic, ferric)										

Profile number			Date of description		Authors		Lat/Lon (UTM 32U)		Elevation (GPS)		Location	
SM PZ			24.11.2021		Panunporn T., Widhi A. P.		0494514, 5975228				Pioneer zone in salt marsh	
Present weather			Former weather		Soil Temperature Regime		Soil Moisture Regime		Parent Material		Age of the Landsurface	
PC 7 °C			WC4		ME		PQ		UM		Yn	
Major landform			Position		Slope form		Slope gradient and orientation		Erosion		Surface sealing and cracks	
LP			BO		SS		03		W		None	
Land use			Crops		Human influence		Vegetation		Rock outcrops		Coarse surface fragments	
PN1			None		N		HM		N		N	
No.	Depth	Horizon Symbol	Color	Mottling				Reducing conditions	Roots		Soil structure	
				Color	Abundance	Size	Contrast		Diameter	Abundance	Type	Size Class
1	0-30	Ahlr	10YR 3/3	10R 4/6	M	M	P	2.5Y 4/1	VF, F	C	SB, GR	FI, VF
2	30-50	Cr1	N 3/.	-	-	-	-	N 2.5/.	VF, F	V	MA	-
3	50-63	Cr2	N 3/.	-	-	-	-	N 2.5/.	VF, F	V	MA	-
Remarks		Top 30 cm has H_2S smell;										
Classification		Fluvic, Reductigleyic, Stagnic, Mollic, Tidalic, Reductic Gleysol (loamic, humic, salic)										

Profile number		Date of description	Authors	Lat/Lon (UTM 32U)	Elevation (GPS)	Location
SM LM		23.11.2021	Panunporn T., Monica W.	0494369, 5975490	0 m	Low marsh in salt marsh
Present weather		Former weather	Soil Temperature Regime	Soil Moisture Regime	Parent Material	Age of the Landsurface
OV 7 °C		WC3	ME	PQ	UM2	Yn
Major landform		Position	Slope form	Slope gradient and orientation	Erosion	Surface sealing and cracks
LP		BO		02	WD	None
Land use		Crops	Human influence	Vegetation	Rock outcrops	Coarse surface fragments
PN		None	N	HM	N	N

No.	Depth	Horizon Symbol	Color	Mottling				Reducing conditions	Roots		Soil structure	
				Color	Abundance	Size	Contrast		Diameter	Abundance	Type	Size Class
1	0-2	Ah	5Y 3/1	x	x	x			VF	V	MA	
2	2-31	Cr	5Y 4/2	10YR 3/6	C	M			VF, F	M	SB	FM
3	31-45	Ahb	5Y 4/1	10YR 3/6	C	F			VF, F, M	M, F	AB	FM
4	45-60	Brbl	5Y 4/2	2.5YR 3/6	M	C			VF, F	M	SB	ME

Remarks	Carbonates: 0-2cm N | 2-31cm MO | 31-45cm N | 45-60cm SL Swelling & Shrinking clays
Classification	Fluvic, Stagnic, Pisoplinthic, Gleysol (loamic, humic, laxic, protosalic)

Profile number	Date of description	Authors	Lat/Lon (UTM 32U)	Elevation (GPS)	Location
SM HMu	24.11.2021	Panunporn T., Widhi A. P.	0494628, 5975286		Ungrazed high marsh in salt marsh
Present weather	Former weather	Soil Temperature Regime	Soil Moisture Regime	Parent Material	Age of the Landsurface
OV 7 °C	WC4	ME	PQ	UM	Yn
Major landform	Position	Slope form	Slope gradient and orientation	Erosion	Surface sealing and cracks
LP	BO	SS	03	W	N
Land use	Crops	Human influence	Vegetation	Rock outcrops	Coarse surface fragments
PN1	None	N	HM	N	N

No.	Depth	Horizon Symbol	Color	Mottling				Reducing conditions	Roots		Soil structure	
				Color	Abundance	Size	Contrast		Diameter	Abundance	Type	Size
1	0-4	Ahlr	10YR 4/1	10YR 3/6	M	M	P	N 2.5/.	VF, F	C	SB	ME
2	4-18	Bl1	10YR 4/1	5YR 4/3	M	F	P	-	F	C	SB, GR	FI/ME,FI
3			10YR 5/1	5YR 4/3	M	F	P	-	F	C	SB, GR	FI/ME,FI
4	18-58	Bl2	2.5Y 5/1	7.5YR 3/4	M	F	D	-	VF	F	SB, AB	ME, FI
5	58-63	Cr	10Y/5 5GY/5	2.5YR 3/6	C	M	D	-	VF	V	MA	
6	63-70	Bl3	5Y 5/1	7.5YR 5/6	F	F	D	-	-	-	SB, AB	ME, FI

Remarks	4-18 layered horizon, 2 colors, 2 structures (also platy) | at 40cm ground water leaked into soil pit | at 55cm dead roots | at 61cm sand layer starts | 63cm> coarse pore (2mm) of dead rhizome
Classification	Fluvic, Stagnic, Gleyic Solonchak (loamic, humic, panpaic, ferric, laxic)

M. Soil horizon characteristics

Table 30 Soil horizon descriptions of redox related diagnostics per tidal wetland zone. Textures indicated as [type, size] with codes: SB = subangular blocky, GR = granular, AB = angular blocky, MA = massive, SA = sub- / and angular blocky, SG = single grain, structure sizes are VF = very fine, FI = fine, ME = medium, FM = fine and medium, CO = coarse as described in FAO guidelines for soil description (Jahn et al., 2006). Roots indicated as [size, abundance] with codes: VF = very fine, F = fine, FF = very fine and fine, M = medium, FM = fine and medium, C = coarse and V = very few, F = few, C = common, M = many as described in FAO guidelines for soil description (Jahn et al., 2006). $RC_{morphology}$ codes assigned as described in table 2. pH values reported from H_2O extractions of fresh soil samples. EC_{se} values calculated as described in WRB (2022), chapter 8.4.28.

tidal wetland zone	nr	horizon	depth (cm)	texture	roots [size, abundance]	soil structure [Type, Size]	$RC_{morphology}$	C_{org} (%w/w)	pH_{H2O}	Bulk density (g cm^{-3})	EC_{se} (dS m^{-1})
SM HMu	5	Ahlr	0-4	Silt Loam	VF+F, C	SB, ME	R4	5.19	7.84	0.86	12.40
	6	Bl1 (layered)	4-18	Silt Loam / Silty Clay Loam	F, C	SB/GR, FI/ME	R4	1.60 / 3.04	8.18 8.02	1.00	17.40 13.10
	7	Bl2	18-58	Loam	VF, F	SB/AB, ME/FI	R4	1.67	8.20	0.80	17.50
	8	Cr	58-63	Sandy Loam	VF, V	MA	R3	0.61	7.78	0.85	51.00
	9	Bl3	63-70	Loam	-	SB/AB, ME/FI	R4	29.35	7.84	NA	17.20
SM LM	10	Ah	0-2	Silty Clay Loam	VF, V	MA	R5+	4.90	8.17	0.82	4.90
	11	Cr	2-31	Silty Clay Loam	VF+F, M	SB, FM	R3	2.78	8.37	0.87	7.60
	12	Ahb	31-45	Silt Loam	VF+F+M, M+F	AB, FM	R4	2.18	8.39	0.74	12.40
	13	Brbl	45-60	Silt Loam	VF+F, M	SB, ME	R3	2.04	8.33	0.82	12.60
SM PZ	14	Ahlr	0-30	Silty Clay Loam	VF+F, C	SB/GR, FI/VF	R3	2.80	7.26	0.92	17.00
	15	Cr1	30-50	Loam	VF+F, V	MA	R2-	1.82	7.87	1.15	27.00
	16	Cr2	50-63	Loam	VF+F, V	MA	R2-	1.73	8.01	1.16	25.30
BM HMu	17	Ah	0-23	Sandy Loam	FF, C	SB/GR, CO/ME	R5+	4.19	7.56	0.85	1.36
	18	Bl	23-43	Loamy Sand	FM, V	SB, CO	R4 (+ R3)	0.59	7.53	1.37	1.76
	19	Ahrb	43-80	Loam	VF, V	SB, CO	R3	3.37	7.69	1.12	1.70
			75-…	Loam			-	3.38	7.48	NA	1.77
LM	20	Ahl1	0-16	Silt Loam	FF, M	GR/SB, FI, CO	R5+R4	1.47	7.26	NA	3.66
	21	Ahl2	16-19	Silt Loam	FF, M	SA, VF	R4	3.98	7.38	NA	3.77
	22	Ahr	19-24	Sandy Loam	FF, M	MA (GR), VF	R3	0.84	7.65	NA	8.00
	23	Ahrb	24-70	Loam	FF, C	MA (GR), VF	R3 (up) R2 (low)	1.39	7.60 7.33	NA	5.17 5.18
	24	Cr	70-75	Sand	F, V	SG	R2	0.24	8.14	NA	12.0
PZ	25	A	0-1	Silt Loam	FF, F	MA(GR),GR /CO	R5	0.74	7.95	1.31	3.06
	26	B	1-30	Sandy Loam	All, F	MA(GR), GR/CO	R2	0.64	8.48	1.32	2.32
	27	Ab	30-37	Loamy Sand	All, C	MA(GR), GR/CO	R2	0.29	8.59	1.43	2.70

tidal wetland zone	nr	horizon	depth (cm)	texture	roots [size, abundance]	soil structure [Type, Size]	$RC_{morphology}$	C_{org} (%w/w)	pH_{H2O}	Bulk density (g cm^{-3})	EC_{se} (dS m^{-1})
	28	G	37-55	Loamy Sand	VF/C, V	MA(GR), GR/CO	R2	0.22	8.71	NA	2.70
	29	G2	55-…	Loamy Sand	VF, V	MA(GR), GR/CO	R2	0.32	8.46	NA	4.08
FM HMu	30	Ah1	0-12	Silt Loam	VF, C		R5	4.96	7.72	0.58	0.93
	31	Ah2	12-20	Silt Loam	VF/F, C/V		R5	2.80	7.63	0.68	1.01
	32	Ah3	20-30	Silt Loam	M + F, C		R4	2.08	7.70	0.77	1.25
	33	Ahr	30-40	Silt Loam	VF+F+M, F		R3	1.21	7.83	0.94	2.26
	34	Br	40-60	Silt Loam	VF, V		R3	0.93	8.07	1.30	2.86
LM	35	Ah	0-18	Loam	VF, M	SB/GR, FI/ME	R4	4.82	7.18	0.62	1.54
	36	Ahl	18-24	Sandy Loam	VF, M	SB/GR, FI/ME	R4	2.00	7.1	0.90	2.99
	37	Ahr1	24-34	Sandy Loam	FF, C	SB/GR, CO	R3	1.08	7.87	1.08	1.73
	38	Ahr2	34-48	Loam	FM, F	SB/GR, CO	R3	1.02	7.92	1.12	1.37
	39	Ahr3	48-80	Silt Loam	-	MA,	R3	1.92	7.48	1.12	1.56
PZ	40	Ah	0-3	Silty Clay	FF, F	PM	R4	3.91	7.35	0.42	0.79
	41	Ahr1	3-15	Silty Clay	FF, VF	MA	R2	4.94	7.19	0.51	0.89
	42	Ahr2	15-30	Silty Clay	FF, C	SB/GR	R2	4.41	7.05	0.57	1.09
	43	Ahr3	30-55	Silty Clay Loam	VF, C	SB/GR	R2	4.43	7.06	0.51	0.87
	44	Ahr4	55-65	Silty Clay Loam	VF, C	SB/GR	R2	4.22	7.22	0.42	0.78

Table 31 Chemical analyses results of soil samples collected from each described soil horizons at the fresh marsh pioneer zone (FM PZ), low marsh (FM LM) and high marsh (FM HMu), at the brackish marsh pioneer zone (BM PZ), low marsh (BM LM) and high marsh (BM HMu) and at the salt marsh pioneer zone (SM PZ), low marsh (SM LM) and two high marshes (SM HMu, SM HMg). EC_{ms} electrical conductivity of fresh soil sample, C_{tot}, N_{tot} and TIC in % w/w, pH measured in the 0.01 M $CaCl_2$ extraction of air dried soil sample, NH_4^+-N and NO_3^-N, NO_3^- in mg kg^{-1} dry soil, P_{olsen} Olsen-method extracted phosphorus in mg per kg dry soil.

tidal wetland zone	horizon	depth (cm)	EC_{ms} (dSm^{-1})	C_{tot} (% w/w)	N_{tot} (% w/w)	TIC (% w/w)	pH_{CaCl2}	CEC ($mmol_c$ kg^{-1})	NH_4-N (mg kg^{-1})	NO_3-N (mg kg^{-1})	NO_3^- (mg kg^{-1})
SM HMu	Ahlr	0-4	3.07	5.90	0.36	0.71	7.88	107.60	13.79	0.48	16.52
	Bl1	4-18	2.57	2.58	0.12	0.97	8.36	76.04	2.66	0.43	14.75
	(layered)		3.29	3.96	0.26	0.92	8.16	151.24	2.95	1.55	14.94
	Bl2	18-58	2.38	2.53	0.13	0.85	8.20	94.43	0.85	<DL	11.75
	Cr	58-63	3.47	1.26	0.03	0.65	8.61	13.86	2.91	0.17	<DL
	Bl3	63-70	4.00	30.21	0.17	0.86	8.21	106.44	4.76	0.63	13.87
SM LM	Ah	0-2	1.57	5.64	0.39	0.75	8.24	155.23	16.03	10.07	80.07
	Cr	2-31	1.91	3.81	0.24	1.03	8.18	119.53	4.69	3.84	25.48
	Ahb	31-45	2.29	3.21	0.19	1.03	8.54	108.29	2.48	1.00	13.07
	Brbl	45-60	2.31	3.05	0.17	1.01	8.52	114.55	1.87	0.55	16.81
SM PZ	Ahlr	0-30	4.28	3.61	0.22	0.81	7.65	127.7	12.51	0.08	5.61
	Cr1	30-50	3.67	2.55	0.14	0.73	8.08	71.97	2.43	0.18	2.48
	Cr2	50-63	3.44	2.54	0.12	0.80	8.06	49.99	1.34	0.05	<DL
BM HMu	Ah	0-23	0.30	4.34	0.34	0.15	6.89	185.09	11.68	2.33	34.69
	Bl	23-43	0.12	0.64	0.05	0.05	6.83	17.59	1.49	<DL	3.27
	Ahrb	43-80	0.29	3.70	0.29	0.33	7.11	114.54	2.27	0.65	6.43
LM	Ahl1	0-16	0.54	2.38	0.12	0.92	7.52	45.24	2.19	0.11	3.24
	Ahl2	16-19	0.69	4.60	0.34	0.63	7.52	162.46	1.86	0.33	5.11
	Ahr	19-24	0.54	1.43	0.06	0.59	7.62	10.29	0.99	0.39	<DL
	Ahrb	24-70	0.70	2.03	0.10	0.68	7.53	29.51	1.26	0.27	<DL
	Cr	70-75	0.71	2.03	0.10	0.64	7.34	21.29	1.35	0.40	<DL
PZ	A	0-1	0.42	1.53	0.06	0.79	7.53	12.73	3.39	0.35	10.87
	B	1-30	0.66	1.32	0.05	0.68	7.54	4.61	0.91	<DL	<DL
	Ab	30-37	0.53	0.68	0.02	0.39	7.47	3.05	0.69	0.03	<DL
	G	37-55	0.26	0.66	0.01	0.44	7.57	4.03	0.66	0.15	<DL
	G2	55-…	0.66	0.77	0.02	0.45	7.60	5.19	0.49	0.04	<DL
FM HMu	Ah1	0-12	0.23	5.41	0.46	0.45	7.17	203.01	7.07	2.83	41.39
	Ah2	12-20	0.19	3.24	0.27	0.44	7.16	140.86	1.72	0.81	19.64
	Ah3	20-30	0.23	2.57	0.18	0.49	7.31	75.29	1.07	<DL	5.54
	Ahr	30-40	0.23	1.73	0.11	0.52	7.45	40.38	0.97	0.05	4.52
	Br	40-60	0.23	1.45	0.08	0.52	7.51	26.26	0.63	<DL	7.37
LM	Ah	0-18	0.36	5.08	0.39	0.26	6.91	168.74	7.02	0.28	4.63
	Ahl	18-24	0.26	2.19	0.15	0.19	6.21	43.45	2.86	0.93	<DL
	Ahr1	24-34	0.15	1.33	0.08	0.25	5.57	7.05	0.83	0.07	<DL
	Ahr2	34-48	0.19	1.13	0.08	0.11	6.67	50.43	0.66	0.12	<DL
	Ahr3	48-80	0.23	2.41	0.14	0.49	6.90	112.55	2.55	0.09	<DL
PZ	Ah	0-3	0.26	4.81	0.34	0.90	7.28	202.13	9.15	0.07	6.93
	Ahr1	3-15	0.37	5.90	0.46	0.96	7.23	227.35	17.9	0.33	4.04
	Ahr2	15-30	0.44	5.39	0.41	0.98	7.24	209.74	17.84	<DL	2.82
	Ahr3	30-55	0.36	5.12	0.40	0.69	7.16	211.94	4.86	<DL	3.87
	Ahr4	55-65	0.32	5.05	0.36	0.83	7.17	155.85	2.99	<DL	2.83

Table 32 Chemical analyses results of soil samples collected from each described soil horizons at the fresh marsh pioneer zone (FM PZ), low marsh (FM LM) and high marsh (FM HMu), at the brackish marsh pioneer zone (BM PZ), low marsh (BM LM) and high marsh (BM HMu) and at the salt marsh pioneer zone (SM PZ), low marsh (SM LM) and two high marshes (SM HMu, SM HMg). clay, silt and sand in % w/w, K_{calac} and P_{calac} (Ca^{2+}-lactate extracted), Fe_{dit} and Mn_{dit} (dithionite extracted) in mg kg^{-1} dry soil, SO_4^{2-}, Cl^- and Br^- (H_2O extracted) in mg kg^{-1} fresh soil sample.

tidal wetland zone	horizon	depth (cm)	clay (% w/w)	silt (% w/w)	sand (% w/w)	K_{calac} (mg kg^{-1})	P_{calac} (mg kg^{-1})	P_{Olsen} (mg kg^{-1})	Fe_{dit} (mg kg^{-1})	Mn_{dit} (mg kg^{-1})	SO_4^{2-} (mg kg^{-1})	Cl^- (mg kg^{-1})	Br (mg kg^{-1})
SM HMu	Ahlr	0-4	21.59	68.18	10.23	645	23.72	57.88	7958	341	<DL	5080.20	22.35
	Bl1	4-18	15.13	68.52	16.34	2989	14.28	38.64	5554	294	625.90	2507.41	9.82
	(layered)		36.47	56.02	7.51	475	19.60	52.07	9691	808	715.46		
	Bl2	18-58	18.88	49.72	31.40	397	18.74	50.04	8215	399	356.47	3712.37	15.27
	Cr	58-63	5.07	36.44	58.49	143	17.20	14.06	3698	698	774.37	2156.03	8.33
	Bl3	63-70	19.29	47.39	33.32	413	62.12	52.25	7726	368	734.70	4104.30	17.76
SM LM	Ah	0-2	30.23	62.78	6.99	570	46.18	69.22	10864	1246	406.44	2051.70	8.25
	Cr	2-31	28.39	62.51	9.10	401	20.80	45.28	8861	1059	378.46	2205.36	9.45
	Ahb	31-45	25.12	60.68	14.20	365	10.34	38.24	9325	1099	398.03	2083.74	8.27
	Brbl	45-60	21.95	56.21	21.84	337	14.11	51.63	8996	1109	489.98	2378.44	11.70
SM PZ	Ahlr	0-30	31.76	47.50	20.74	750	31.09	29.44	9679	680	1534.87	7520.78	21.37
	Cr1	30-50	18.83	47.68	33.49	356	26.29	27.80	5651	274	1132.92	5528.75	20.58
	Cr2	50-63	15.97	42.35	41.68	456	10.00	3.05	6395	193	1387.57	5336.23	16.14
BM HMu	Ah	0-23	14.54	22.58	62.88	93	95.20	35.80	4529	986	87.30	111.98	1.01
	Bl	23-43	4.96	11.84	83.20	32	31.41	9.44	1984	169	25.61	44.60	0.40
	Ahrb	43-80	18.29	48.52	33.19	31	116.40	36.73	6903	670	554.82	181.20	0.47
BM LM	Ahl1	0-16	12.87	69.60	17.54	46	10.20	41.21	7159	384	123.88	382.05	1.38
	Ahl2	16-19	18.46	56.75	24.79	50	24.28	81.03	21480	502	96.80	868.29	2.12
	Ahr	19-24	5.11	28.61	66.28	18	47.92	26.40	2844	85	210.97	360.45	0.79
	Ahrb	24-70	8.96	49.63	41.41	30	88.07	36.73	3556	333	801.57	632.17	0.94
	Cr	70-75	9.80	46.68	43.52	5	17.15	3.57	1659	40	389.08	560.61	1.07
BM PZ	A	0-1	5.28	58.62	36.10	70	12.64	16.52	3869	231	331.66	41.17	0.36
	B	1-30	4.19	49.44	46.37	50	7.20	4.50	2916	156	684.15	35.81	0.32
	Ab	30-37	1.67	17.94	80.39	33	10.02	1.70	1710	69	483.65	39.13	0.27
	G	37-55	1.47	24.03	74.50	34	11.33	2.23	1264	68	175.90	56.65	0.01
	G2	55-…	2.32	25.22	72.45	40	14.14	3.83	1653	102	732.20	137.84	0.43
FM HMu	Ah1	0-12	17.95	69.25	12.80	81	128.79	23.74	10382	1826	114.69	83.03	0.86
	Ah2	12-20	18.22	61.57	20.21	31	90.88	20.90	8760	1176	62.99	66.57	0.54
	Ah3	20-30	10.08	63.31	26.61	17	46.23	8.91	7788	745	61.55	63.24	0.42
	Ahr	30-40	7.59	57.54	34.88	14	21.65	6.29	6247	599	65.51	66.39	0.38
	Br	40-60	5.79	55.71	38.51	15	20.90	8.41	5481	565	67.51	75.82	0.33
FM LM	Ah	0-18	19.44	48.88	31.68	127	97.45	24.21	12658	1440	516.08	292.92	1255.00
	Ahl	18-24	9.32	33.32	57.36	38	59.18	5.62	3655	225	658.38	146.80	0.45
	Ahr1	24-34	5.40	27.74	66.86	24	17.52	<DL	4702	93	1854.05	64.90	0.01
	Ahr2	34-48	10.41	44.97	44.61	24	21.84	4.11	4985	284	1107.97	80.06	0.01
	Ahr3	48-80	19.00	65.63	15.37	51	49.04	3.52	13363	2809	964.14	131.81	0.43
FM PZ	Ah	0-3	45.29	51.94	2.78	260	15.64	29.36	12648	939	1375.54	183.05	1397.00
	Ahr1	3-15	54.75	43.68	1.57	246	10.58	17.63	13458	836	1727.44	391.97	1.72
	Ahr2	15-30	44.47	52.99	2.54	90.5	27.28	19.42	13936	1015	1615.74	292.08	0.86
	Ahr3	30-55	34.29	63.89	1.81	127	86.19	19.40	11616	818	1429.95	266.91	0.88
	Ahr4	55-65	39.50	57.62	2.88	125	14.52	16.97	16965	762	1107.97	317.84	1194.00

N. PCA results soil physicochemical analyses

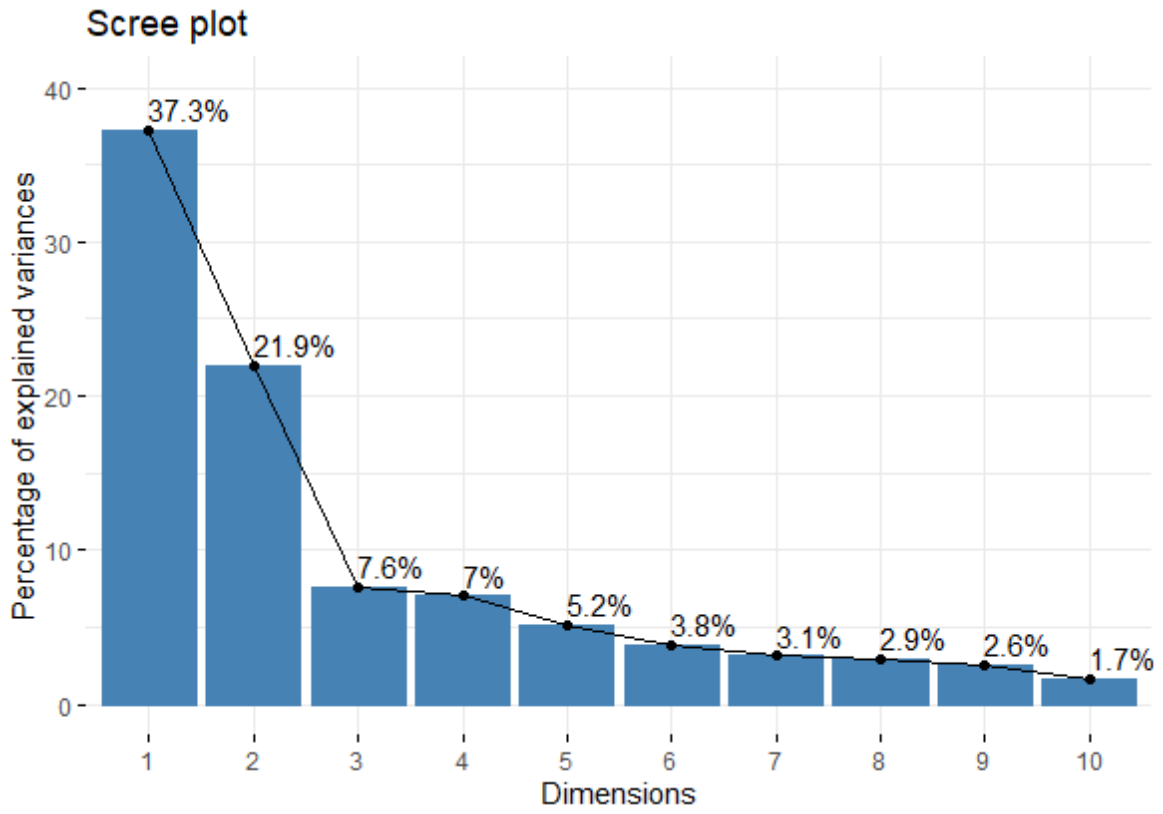

Figure 32 PCA scree plot of first 10 principal components (dimensions) and percentage of explained variance

O. Pearson correlations of physicochemical soil properties

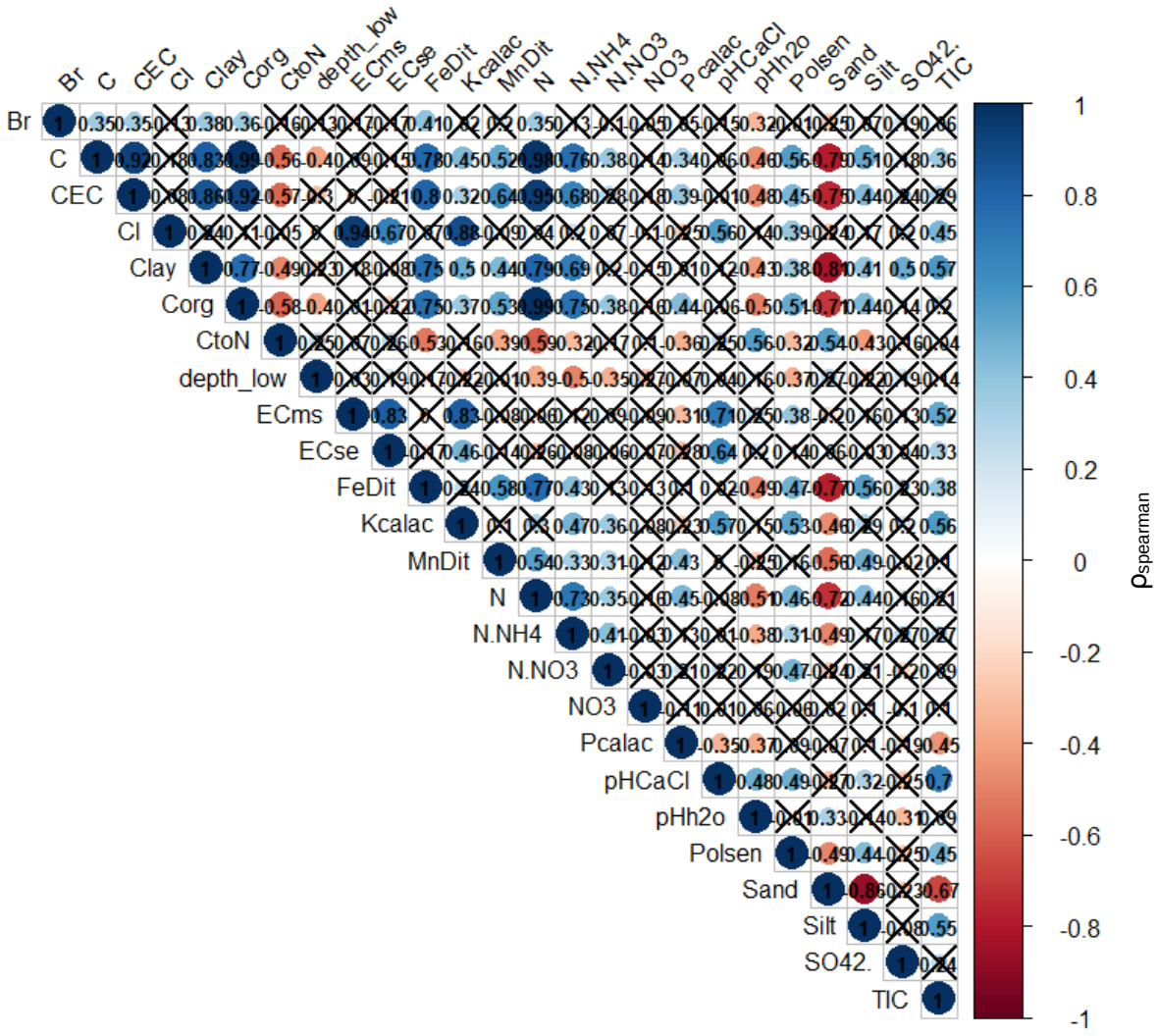

Figure 33 Pearson correlation plot of physicochemical soil properties based on all data-points of the nine studied tidal wetland zones. EC_{se} electrical conductivity of the saturation extract, EC_{ms} electrical conductivity of fresh soil sample, C_{tot}, N_{tot} and TIC in % w/w, pH measured in the 0.01 M $CaCl_2$ extraction of air dried soil sample, NH_4^+-N and NO_3^-N, NO_3^- in mg per kg dry soil, P_{olsen} Olsen-method extracted phosphorus in mg per kg dry soil. Clay, silt and sand as % w/w.

P. Reduction index per soil horizon

Table 33 $RI_{horizon}$ values retrieved from RI_{1cm} with minimum (RImin), maximum (RImax) and median RI (RImed) of the 5 replicate plots over the 11 campaigns are reported as well as the average (RIavg) with standard error (RIse). $RC_{morphology}$ indicating the assigned reduction classes based on soil descriptions.

tidal wet-land zone	horizon	Depth (cm)	RImin (-)	RImax (-)	RIavg (-)	RIse (-)	RImedian (-)	$RC_{morphology}$ (-)
SM HMu	Ahlr	0 – 4	0.00	0.85	0.06	0.02	0.00	R4
	Bl	4 – 18	0.00	0.94	0.11	0.03	0.02	R4
	Bl2	18 – 58	0.03	0.87	0.26	0.03	0.19	R4
	Cr	58 – 60*	0.00	0.68	0.19	0.03	0.12	R3
SM LM	Ah	0 – 2	0.00	0.70	0.08	0.02	0.01	R5
	Cr	2 – 31	0.01	0.87	0.20	0.03	0.15	R3
	Ahb	31 – 45	0.02	0.93	0.31	0.03	0.25	R4
	Brbl	45 – 60	0.03	0.57	0.23	0.02	0.24	R3
SM PZ	Ahlr	0 – 30	0.02	0.50	0.17	0.02	0.11	R3
	Cr1	30 – 50	0.10	0.98	0.47	0.04	0.38	R2
	Cr2	50 – 60*	0.13	0.93	0.62	0.03	0.64	R2
BM HMu	Ah	0 – 23	0.00	0.96	0.10	0.02	0.05	R5
	Bl	23 – 43	0.03	0.98	0.36	0.03	0.36	R4 (+R3)
	Ahrb	43 – 60*	0.02	0.98	0.25	0.03	0.20	R3
BM LM	Ahl1	0 – 16	0.00	0.85	0.15	0.03	0.07	R5 (+R4)
	Ahl2	16 – 19	0.00	0.91	0.35	0.04	0.30	R4
	Ahr	19 – 24	0.05	0.88	0.43	0.03	0.40	R3
	Ahrb1	24 – 40	0.20	0.97	0.67	0.03	0.71	R3
	Ahrb2	40 – 60*	0.37	0.98	0.81	0.02	0.89	R2
BM PZ	A	0 – 1	0.00	0.38	0.04	0.01	0.00	R5
	B	1 – 30	0.01	0.93	0.47	0.03	0.50	R2
	Ab	30 – 37	0.08	1.00	0.78	0.04	0.96	R2
	G	37 – 55	0.09	0.97	0.70	0.04	0.80	R2
FM HMu	Ah1	0 – 12	0.00	0.24	0.04	0.01	0.01	R5
	Ah2	12 – 20	0.00	0.47	0.15	0.02	0.12	R5
	Ah3	20 – 30	0.02	0.68	0.29	0.03	0.30	R4
	Ahr	30 – 40	0.05	0.77	0.34	0.03	0.33	R3
	Bl	40 – 60	0.03	0.78	0.33	0.03	0.32	R3
FM LM	Ah	0 – 18	0.00	0.51	0.11	0.02	0.06	R4
	Ahl	18 – 24	0.00	0.99	0.34	0.04	0.25	R4
	Ahr1	24 – 34	0.02	0.99	0.63	0.04	0.62	R3
	Ahr2	34 – 48	0.13	1.00	0.70	0.03	0.75	R3
	Ahr3	48 – 60*	0.03	0.99	0.60	0.04	0.65	R3
FM PZ	Ah	0 – 3	0.00	0.78	0.06	0.02	0.00	R4
	Ahr1	3 – 15	0.00	0.92	0.29	0.04	0.23	R2
	Ahr2	15 – 30	0.13	0.99	0.74	0.03	0.86	R2
	Ahr3	30 – 55	0.15	0.99	0.85	0.02	0.90	R2
	Ahr4	55 – 60*	0.01	0.94	0.61	0.03	0.63	R2

Q. Sensor redox potential (Eh) and partial hydrogen pressure (rH)

Table 34 A) Salt marsh' pioneer zone (SM PZ) redox sensor results per sensor depth and campaign (table 3) showing the mean and standard error of the redox potential (Eh), soil temperature and pH of the corresponding soil depth and the resulting rH values.

tidal wetland zone	depth (cm)	campaign	mean Eh (mV)	se Eh (mV)	mean T_{soil} (°C)	pH_{H2O} (-)	rH (-)
SM PZ	5	1	-168.18	2.04	17.1	7.3	8.9
	5	2	-136.36	20.83	18.2	7.3	10.0
	5	3	-53.80	105.99	18.8	7.3	12.8
	5	4	-29.83	107.44	16.6	7.3	13.6
	5	5	-42.28	126.06	12.3	7.3	13.2
	5	6	-30.28	122.52	11.7	7.3	13.6
	5	7	-15.17	125.56	5.1	7.3	14.1
	5	8	-18.16	130.37	4.2	7.3	14.0
	5	9	-27.16	130.22	4.1	7.3	13.7
	5	10	-38.12	133.56	4.5	7.3	13.3
	5	11	-35.84	143.2	5.8	7.3	13.4
	10	1	-162.38	11.03	16.9	7.3	9.1
	10	2	-141.59	21.61	18.2	7.3	9.8
	10	3	-28.26	101.96	18.9	7.3	13.6
	10	4	26.72	105.02	16.8	7.3	15.5
	10	5	-29.10	117.14	12.5	7.3	13.6
	10	6	-28.49	120.21	11.8	7.3	13.6
	10	7	-32.05	117.75	5.3	7.3	13.5
	10	8	-25.90	123.77	4.3	7.3	13.7
	10	9	-26.40	125.96	4.3	7.3	13.7
	10	10	-26.93	130.14	4.6	7.3	13.7
	10	11	-21.35	136.75	5.9	7.3	13.9
	30	1	-150.04	26.16	15.2	7.6	10.1
	30	2	-131.11	13.23	17.0	7.6	10.8
	30	3	-19.28	113.69	17.7	7.6	14.5
	30	4	46.48	97.42	16.7	7.6	16.8
	30	5	76.84	141.15	12.9	7.6	17.8
	30	6	10.06	123.51	12.2	7.6	15.5
	30	7	10.24	124.57	7.2	7.6	15.5
	30	8	1.66	134.34	5.1	7.6	15.3
	30	9	1.46	140.14	5.3	7.6	15.2
	30	10	2.29	135.4	5.1	7.6	15.3
	30	11	8.10	144.53	5.8	7.6	15.5
	60	1	-181.95	11.36	13.5	8.0	9.8
	60	2	-153.44	18.9	15.5	8.0	10.8
	60	3	-34.49	124.89	16.3	8.0	14.8
	60	4	-31.34	128.97	16.3	8.0	14.9
	60	5	-40.33	122.32	13.4	8.0	14.6
	60	6	-35.61	122.39	12.5	8.0	14.8
	60	7	-34.19	117.95	9.0	8.0	14.8
	60	8	-27.46	121.52	6.2	8.0	15.1
	60	9	-27.87	122.43	6.3	8.0	15.1
	60	10	-28.66	124.06	5.7	8.0	15.0
	60	11	-25.16	132.46	5.9	8.0	15.1

Table 34 B) Salt marsh' low marsh (SM LM) redox sensor results per sensor depth and campaign (table 3) showing the mean and standard error of the redox potential (Eh), soil temperature and pH of the corresponding soil depth and the resulting rH values.

tidal wetland zone	**depth** (cm)	**campaign**	**mean Eh** (mV)	**se Eh** (mV)	**mean T_{soil}** (°C)	**pH_{H2O}** (-)	**rH** (-)
SM LM	5	1	67.73	272.53	18.1	8.2	18.7
	5	2	180.24	359.41	19.0	8.2	22.5
	5	3	392.91	279.62	19.7	8.2	29.7
	5	4	409.85	207.81	17.1	8.2	30.3
	5	5	-120.00	114.73	12.5	8.2	12.3
	5	6	41.45	155	11.8	8.2	17.8
	5	7	-86.76	107.18	5.4	8.2	13.5
	5	8	143.32	165.93	4.3	8.2	21.3
	5	9	-76.28	92.21	4.2	8.2	13.8
	5	10	40.64	161.5	4.6	8.2	17.8
	5	11	20.45	199.18	6.0	8.2	17.1
	10	1	3.38	141.1	17.7	8.4	16.9
	10	2	63.27	259.52	18.9	8.4	18.9
	10	3	448.58	258.86	19.5	8.4	32.0
	10	4	468.25	220.79	17.3	8.4	32.7
	10	5	-33.31	168.29	12.6	8.4	15.7
	10	6	-6.01	98.15	11.9	8.4	16.6
	10	7	-53.48	122.92	5.9	8.4	15.0
	10	8	192.56	181.65	4.5	8.4	23.3
	10	9	-66.12	104.45	4.4	8.4	14.6
	10	10	-109.34	96.99	4.7	8.4	13.1
	10	11	-76.13	90.17	6.0	8.4	14.2
	30	1	15.83	143.71	16.4	8.4	17.3
	30	2	-80.55	93.21	18.0	8.4	14.1
	30	3	319.34	268.12	18.7	8.4	27.6
	30	4	426.13	209.02	17.5	8.4	31.2
	30	5	-69.80	107.65	13.1	8.4	14.4
	30	6	-90.41	114.47	12.3	8.4	13.7
	30	7	-103.22	122.34	7.2	8.4	13.3
	30	8	-69.82	95.28	5.2	8.4	14.4
	30	9	-104.25	105.1	5.2	8.4	13.3
	30	10	-131.73	123.64	5.1	8.4	12.3
	30	11	-104.14	99.72	6.0	8.4	13.3
	60	1	0.93	162.52	14.5	8.3	16.6
	60	2	-74.69	81.07	16.5	8.3	14.1
	60	3	3.99	165.46	17.3	8.3	16.7
	60	4	157.81	269.08	17.1	8.3	21.9
	60	5	-52.32	98.46	13.7	8.3	14.8
	60	6	-72.23	107.02	12.7	8.3	14.2
	60	7	-76.95	103.09	9.0	8.3	14.0
	60	8	-70.67	96.07	6.2	8.3	14.2
	60	9	-83.55	85.66	6.2	8.3	13.8
	60	10	-92.7	81.44	5.7	8.3	13.5
	60	11	-97.97	84.93	6.0	8.3	13.3

Table 34 C) Salt marsh' high marsh (SM HMu) redox sensor results per sensor depth and campaign (table 3) showing the mean and standard error of the redox potential (Eh), soil temperature and pH of the corresponding soil depth and the resulting rH values.

tidal wetland zone	depth (cm)	campaign	mean Eh (mV)	se Eh (mV)	mean T_{soil} (°C)	pH_{H2O} (-)	rH (-)
SM HMu	5	1	344.12	158.74	18.6	7.8	27.3
	5	2	556.85	43.77	19.0	7.8	34.5
	5	3	588.43	52.53	19.2	7.8	35.5
	5	4	542.56	25.81	16.6	7.8	34.0
	5	5	129.18	376.13	12.3	7.8	20.0
	5	6	468.44	111.07	11.8	7.8	31.5
	5	7	571.82	44.81	5.2	7.8	35.0
	5	8	327.78	168.65	4.3	7.8	26.7
	5	9	65.05	342.66	4.1	7.8	17.8
	5	10	161.61	357.58	4.6	7.8	21.1
	5	11	256.49	356.72	5.9	7.8	24.3
	10	1	-11.32	181.82	4.2	8.1	15.8
	10	2	205.37	325.3	11.8	8.1	23.2
	10	3	280.02	363.07	5.6	8.1	25.7
	10	4	194.12	177.29	4.4	8.1	22.8
	10	5	57.20	294.32	4.6	8.1	18.1
	10	6	89.35	350.13	5.9	8.1	19.2
	10	7	279.06	236.05	18.6	8.1	25.7
	10	8	582.52	35.69	19.0	8.1	35.9
	10	9	614.56	18.16	19.1	8.1	37.0
	10	10	526.52	28.86	16.6	8.1	34.0
	10	11	50.57	296.78	12.4	8.1	17.9
	30	1	320.75	37.99	17.2	7.8	26.5
	30	2	616.36	27.28	18.2	7.8	36.5
	30	3	635.21	21.97	18.2	7.8	37.1
	30	4	544.51	31.52	16.9	7.8	34.1
	30	5	-117.72	52.51	12.8	7.8	11.6
	30	6	56.77	179.53	12.1	7.8	17.5
	30	7	19.26	218.63	7.2	7.8	16.3
	30	8	340.43	119.48	5.1	7.8	27.1
	30	9	-46.85	83.07	5.2	7.8	14.0
	30	10	-106.20	42.84	5.1	7.8	12.0
	30	11	-127.77	12.08	6.0	7.8	11.3
	60	1	157.49	223.64	15.1	8.2	21.7
	60	2	461.50	246.04	16.5	8.2	32.0
	60	3	658.47	100.11	16.9	8.2	38.7
	60	4	659.16	54.53	16.6	8.2	38.7
	60	5	31.17	116.73	13.4	8.2	17.5
	60	6	-64.77	96.75	12.5	8.2	14.2
	60	7	-63.60	79.49	8.9	8.2	14.2
	60	8	-63.96	66.4	6.2	8.2	14.2
	60	9	-85.36	58.25	6.3	8.2	13.5
	60	10	-92.96	54.94	5.7	8.2	13.2
	60	11	-105.71	50.01	6.2	8.2	12.8

R. Gaussian distribution tests of land-atmosphere flux data

Table 35 Shapiro-Wilk Normality test of CH_4 fluxes for all single observations per plot (1 to 5), per tidal wetland zone (all obs) and as average flux of the five flux replicate plots (avg., n = 5).

tidal wetland zone	plot 1	plot 2	plot 3	plot 4	plot 5	all obs.	avg.
FM PZ	p<0.001	p=0.003	p=0.016	p<0.001	p<0.001	p<0.001	p=0.646
BM PZ	p=0.894	p=0.414	p<0.001	p=0.742	p=0.002	p<0.001	p=0.556
SM PZ	p=0.003	p<0.001	p=0.197	p=0.047	p=0.016	p<0.001	p=0.495
SM LM	p=0.115	p=0.063	p=0.002	p=0.335	p<0.001	p<0.001	p=0.498
SM HMu	p=0.024	p=0.008	p=0.481	p=0.056	p=0.001	p<0.001	p=0.626
SM HMg	p=0.045	p<0.001	p=0.053	p=0.011	p=0.007	p<0.001	p=0.238

Table 36 Shapiro-Wilk Normality test of CH_4 fluxes per meteorological season for all single observations of flux replicate plots per tidal wetland zone (all obs.) and as average flux of the five flux replicate plots (avg., n = 5).

tidal wetland zone	tested data	autumn	spring	summer	winter
FM PZ	All obs.	p<0.001	p<0.001	p=0.006	p=0.049
	Avg. (n=5)	p=0.654	p=0.042	p=0.189	p=0.320
BM PZ	All obs.	NA	p=0.103	p=0.020	p<0.001
	Avg. (n=5)	NA	p=0.024	p=0.719	p=0.049
SM PZ	All obs.	p=0.766	p=0.094	p<0.001	p=0.323
	Avg. (n=5)	p=0.009	p=0.210	p=0.347	p=0.300
SM LM	All obs.	p=0.976	p=0.001	p<0.001	p<0.001
	Avg. (n=5)	p=0.185	p=0.973	p=0.071	p=0.001
SM HMu	All obs.	p=0.634	p=0.001	p<0.001	p=0.503
	Avg. (n=5)	p=0.572	p=0.149	p=0.895	p=0.260
SM HMg	All obs.	p=0.170	p=0.006	p<0.001	p=0.004
	Avg. (n=5)	p=0.904	p=0.748	p=0.157	p=0.191

Table 37 Shapiro-Wilk Normality test N_2O fluxes for all single observations per plot (1 to 5), per tidal wetland zone (all obs) and as average flux of the five flux replicate plots (avg., n = 5).

tidal wetland zone	plot 1	plot 2	plot 3	plot 4	plot 5	all obs.	avg.
FM PZ	p<0.001	p<0.001	p=0.117	p<0.001	p=0.179	p<0.001	p=0.193
BM PZ	p=0.003	p=0.170	p<0.001	p=0.218	p=0.002	p<0.001	p=0.541
SM PZ	p=0.670	p=0.006	p=0.363	p=0.153	p=0.009	p<0.001	p=0.786
SM LM	p=0.008	p=0.018	p=0.038	p=0.003	p=0.079	p<0.001	p=0.192
SM HMu	p<0.001	p=0.018	p<0.001	p=0.002	p<0.001	p<0.001	p=0.121
SM HMg	p=0.016	p=0.041	p=0.026	p=0.120	p=0.108	p<0.001	p=0.559

Table 38 Shapiro-Wilk Normality test N_2O fluxes per meteorological season for all single observations of flux replicate plots per tidal wetland zone (all obs.) and as average flux of the five flux replicate plots (avg., n = 5).

tidal wetland zone	tested data	autumn	spring	summer	winter
FM PZ	All obs.	p=0.075	p=0.380	p=0.061	p=0.041
	Avg. (n=5)	p=0.374	p=0.566	p=0.285	p=0.207
BM PZ	All obs.	NA	p=0.593	p=0.195	p=0.216
	Avg. (n=5)	NA	p=0.426	p=0.602	p=0.636
SM PZ	All obs.	p=0.999	p=0.524	p=0.017	p=0.306
	Avg. (n=5)	p=0.855	p=0.158	p=0.035	p=0.709
SM LM	All obs.	p=0.072	p<0.001	p=0.005	p=0.614
	Avg. (n=5)	p=0.200	p=0.868	p=0.136	p=0.833
SM HMu	All obs.	p=0.369	p=0.001	p<0.001	p=0.001
	Avg. (n=5)	p=0.404	p=0.928	p=0.263	p=0.220
SM HMg	All obs.	p=0.440	p<0.001	p=0.010	p<0.001
	Avg. (n=5)	p=0.425	p=0.077	p=0.421	p=0.116

S. Methane and nitrous oxide land-atmosphere flux data

Table 39 Overview of calculated methane, nitrous oxide and carbon dioxide land-atmosphere fluxes and respective absolute flux errors (abs err). QL indicates the assigned quality level (QL1 to QL4), doy indicates day of the year with 2022 < 365 and 2023 > 366 (see tables 29 a, b, c), ID reflects salinity zone, flooding frequency zone and plot number of respective fluxes.

QL	doy	ID	CH_4 (mg m^{-2} h^{-1})	CH_4 abs err (mg m^{-2} h^{-1})	N_2O (mg m^{-2} h^{-1})	N_2O abs err (mg m^{-2} h^{-1})	CO_2 (mg m^{-2} h^{-1})	CO_2 abs err (mg m^{-2} h^{-1})
1	118	SMLM1	1.46E-02	7.88E-04	4.51E-02	1.45E-03	5.63E+01	3.44E+00
1	118	SMLM2	-2.39E-02	4.65E-04	1.90E-02	1.07E-03	-5.42E+02	7.85E+00
3	118	SMLM3	-2.18E-02	3.84E-04	1.39E-02	7.90E-04	-3.41E+02	6.07E+00
3	118	SMLM4	-2.26E-02	4.51E-04	9.37E-03	1.01E-03	-7.97E+01	4.70E+00
3	118	SMLM5	-1.02E-02	3.00E-04	3.78E-02	8.76E-04	-2.75E+02	6.75E+00
3	118	SMHMg4	-7.59E-03	3.63E-04	8.93E-03	7.54E-04	-2.37E+02	6.49E+00
1	118	SMHMg1	1.81E-02	5.27E-04	1.44E-01	2.06E-03	-3.38E+01	9.83E+00
1	118	SMHMg2	-4.91E-03	6.06E-04	4.12E-02	1.36E-03	-8.66E+01	1.02E+01
1	118	SMHMg5	1.44E-03	5.71E-04	2.25E-02	9.54E-04	-5.25E+02	1.05E+01
2	118	SMHMg3	1.59E-03	1.05E-03	2.07E-02	8.52E-04	-3.99E+02	1.08E+01
3	118	SMPZ1	-4.25E-04	4.10E-04	-3.53E-04	7.48E-04	1.98E+01	3.26E+00
1	118	SMPZ2	-6.07E-03	4.66E-04	7.88E-03	9.32E-04	-1.67E+01	4.32E+00
3	118	SMPZ3	-4.30E-03	2.51E-04	9.81E-03	8.57E-04	1.14E+01	2.99E+00
1	118	SMPZ5	1.84E-02	4.71E-04	1.17E-02	7.94E-04	7.83E+01	3.13E+00
1	118	SMPZ4	2.07E-02	4.17E-04	9.45E-03	7.78E-04	9.44E+01	3.27E+00
1	118	SMHMu1	-3.81E-03	2.87E-04	3.88E-02	1.09E-03	-1.32E+02	5.52E+00
1	118	SMHMu5	-8.10E-04	2.61E-04	1.00E-02	7.34E-04	-3.60E+02	8.01E+00
1	118	SMHMu4	1.60E-03	2.57E-04	2.76E-02	7.65E-04	-6.00E+02	1.05E+01
1	118	SMHMu2	1.68E-03	2.35E-04	9.13E-03	6.88E-04	-8.22E+01	7.22E+00
1	118	SMHMu3	5.43E-04	2.51E-04	3.76E-02	9.22E-04	3.58E+02	8.22E+00
1	132	SMHMg2	-2.06E-02	4.23E-04	5.03E-02	1.16E-03	-2.18E+02	7.11E+00
1	132	SMHMg1	-1.70E-03	2.80E-04	6.30E-02	1.19E-03	-3.49E+02	9.03E+00
1	132	SMHMg5	-9.00E-03	3.35E-04	1.86E-02	8.35E-04	-4.78E+02	8.82E+00
1	132	SMHMg3	-1.67E-03	2.66E-04	2.34E-02	8.16E-04	-5.21E+02	9.00E+00
1	132	SMHMg4	-1.64E-03	2.53E-04	1.66E-02	9.37E-04	-4.30E+02	8.22E+00
1	132	SMLM4	7.66E-04	3.41E-04	9.69E-02	1.77E-03	-1.77E+01	4.58E+00
1	132	SMLM5	-1.75E-03	3.11E-04	4.98E-02	1.15E-03	-4.57E+02	8.89E+00
1	132	SMLM2	4.94E-04	2.94E-04	6.10E-02	1.48E-03	-2.81E+02	1.05E+01
1	132	SMLM3	1.13E-03	2.66E-04	3.38E-02	1.25E-03	9.44E+01	6.23E+00
1	132	SMLM1	8.24E-07	2.42E-04	9.52E-02	1.71E-03	3.34E+01	4.61E+00
2	132	SMHMu2	-4.79E-03	3.02E-04	9.24E-02	3.22E-03	-5.02E+02	9.34E+00
2	132	SMHMu5	1.86E-02	6.02E-04	4.72E-02	9.93E-04	-1.09E+03	3.31E+01
2	132	SMHMu1	7.47E-03	4.85E-04	2.47E-01	5.22E-03	-1.42E+02	1.10E+01
2	132	SMHMu4	3.78E-03	2.96E-04	1.64E-01	3.04E-03	-4.18E+02	1.01E+01
2	132	SMHMu3	-1.51E-03	3.26E-04	2.83E-01	5.49E-03	9.56E+01	7.76E+00
1	132	SMPZ5	8.24E-03	3.37E-04	8.47E-03	1.17E-03	-5.81E+01	3.61E+00
1	132	SMPZ1	9.21E-03	3.24E-04	8.72E-03	9.17E-04	-1.58E+02	4.63E+00
1	132	SMPZ2	-5.50E-03	4.36E-04	-1.02E-03	1.09E-03	-4.65E+01	3.70E+00
1	132	SMPZ4	-3.85E-03	6.81E-04	3.15E-03	1.35E-03	-1.95E+00	3.67E+00
1	132	SMPZ3	-3.29E-03	4.75E-04	3.17E-03	1.46E-03	-3.32E+01	4.18E+00
2	145	SMLM1	-2.32E-02	4.63E-04	-2.30E-03	8.98E-04	-2.06E+02	9.77E+00
2	145	SMLM3	-4.81E-02	1.64E-03	-2.32E-03	1.02E-03	-9.61E+02	1.60E+01
2	145	SMLM5	-6.19E-02	1.51E-03	1.43E-03	8.12E-04	-7.13E+02	1.63E+01
2	145	SMLM2	-2.30E-02	1.12E-03	2.64E-02	1.05E-03	-8.20E+02	1.86E+01

QL	doy	ID	CH_4 (mg m^{-2} h^{-1})	CH_4 abs err (mg m^{-2} h^{-1})	N_2O (mg m^{-2} h^{-1})	N_2O abs err (mg m^{-2} h^{-1})	CO_2 (mg m^{-2} h^{-1})	CO_2 abs err (mg m^{-2} h^{-1})
3	145	SMLM4	-3.69E-03	5.99E-04	7.98E-03	8.71E-04	-6.60E+02	1.24E+01
1	145	SMHMg1	1.82E-02	5.50E-04	1.62E-02	7.58E-04	-3.58E+02	1.14E+01
2	145	SMHMg3	-3.50E-02	1.13E-03	1.65E-02	7.55E-04	-3.99E+02	9.35E+00
1	145	SMHMg5	-7.73E-03	4.12E-04	1.89E-02	7.59E-04	-2.25E+02	1.09E+01
1	145	SMHMg2	1.42E-02	4.22E-04	1.38E-02	7.74E-04	-5.79E+02	9.62E+00
1	145	SMHMg4	-3.44E-02	7.43E-04	2.37E-02	8.50E-04	-2.10E+02	8.68E+00
1	145	SMHMu1	-5.06E-03	3.34E-04	7.60E-02	1.68E-03	-1.65E+03	2.58E+01
1	145	SMHMu3	1.05E-02	4.24E-04	4.68E-02	1.19E-03	-9.44E+02	1.64E+01
1	145	SMHMu2	-2.70E-03	3.98E-04	1.43E-01	2.41E-03	-1.20E+03	1.95E+01
2	145	SMHMu4	4.13E-02	8.31E-04	7.37E-02	2.22E-03	-6.42E+02	3.85E+01
3	145	SMHMu5	-2.06E-02	7.54E-04	9.53E-02	1.66E-03	-2.25E+03	3.83E+01
1	145	SMPZ2	3.55E-02	6.08E-04	1.11E-02	9.58E-04	-9.46E+02	1.47E+01
1	145	SMPZ3	2.39E-04	8.80E-04	-9.58E-03	8.64E-04	-7.55E+02	1.30E+01
2	145	SMPZ4	6.38E-03	1.06E-03	1.41E-02	9.39E-04	-5.62E+02	8.61E+00
1	145	SMPZ5	2.74E-02	6.62E-04	-4.96E-04	8.68E-04	-9.66E+01	4.37E+00
1	145	SMPZ1	1.40E-02	4.23E-04	1.01E-02	8.73E-04	-1.04E+03	1.75E+01
3	154	SMHMu3	-3.72E-02	8.46E-04	6.23E-03	1.01E-03	-1.24E+03	2.32E+01
3	154	SMHMu2	-6.91E-03	3.22E-04	6.87E-03	1.13E-03	-1.38E+03	2.16E+01
2	154	SMHMu5	-9.53E-03	3.54E-04	1.62E-02	1.15E-03	-1.84E+03	3.08E+01
2	154	SMHMu4	-5.85E-03	5.32E-04	1.97E-02	1.43E-03	-1.50E+03	3.09E+01
1	154	SMHMu1	8.05E-03	5.88E-04	1.16E-02	8.65E-04	-1.55E+03	2.37E+01
1	154	SMPZ4	5.22E-02	8.93E-04	2.67E-02	1.22E-03	-1.29E+03	1.89E+01
2	154	SMPZ2	2.43E-02	4.63E-04	3.98E-02	1.08E-03	-1.07E+03	1.57E+01
1	154	SMPZ3	2.99E-02	6.75E-04	1.36E-02	9.32E-04	-1.04E+03	1.54E+01
1	154	SMPZ5	8.30E-02	1.28E-03	2.06E-02	1.08E-03	-6.64E+02	1.03E+01
1	154	SMPZ1	3.33E-02	5.06E-04	5.33E-03	8.83E-04	-7.63E+02	1.05E+01
1	154	SMHMg1	2.54E-02	6.65E-04	1.20E-02	1.44E-03	-5.13E+02	1.23E+01
3	154	SMHMg3	-4.40E-04	3.91E-04	6.90E-02	1.81E-03	-5.13E+02	1.26E+01
3	154	SMHMg4	-1.34E-02	4.44E-04	-4.73E-03	8.82E-04	-3.15E+02	8.05E+00
2	154	SMHMg2	4.61E-01	9.41E-03	3.78E-02	1.10E-03	-5.74E+02	1.20E+01
3	154	SMHMg5	-4.71E-02	1.03E-03	7.29E-03	9.78E-04	-6.84E+02	1.18E+01
3	154	SMLM3	-6.94E-03	2.86E-04	-5.04E-03	1.21E-03	-9.23E+02	1.84E+01
1	154	SMLM4	1.14E-03	2.96E-04	-8.92E-03	1.05E-03	-6.88E+02	1.31E+01
1	154	SMLM5	4.71E-03	2.85E-04	-8.95E-03	9.02E-04	-8.62E+02	1.42E+01
1	154	SMLM1	5.77E-03	3.05E-04	1.27E-02	1.13E-03	-8.20E+02	1.40E+01
1	154	SMLM2	2.20E-02	4.90E-04	2.73E-03	8.98E-04	-1.16E+03	1.88E+01
1	164	SMHMg5	-3.06E-03	2.53E-04	7.56E-04	9.17E-04	-1.10E+02	7.19E+00
1	164	SMHMg4	1.90E-03	2.57E-04	9.86E-03	7.45E-04	-4.35E+02	1.26E+01
1	164	SMHMg3	-1.46E-03	2.62E-04	-3.38E-03	7.55E-04	-4.87E+02	1.33E+01
1	164	SMHMg2	1.94E-03	2.57E-04	-7.62E-04	8.39E-04	-5.48E+02	1.39E+01
1	164	SMHMg1	-2.29E-03	8.03E-04	-8.13E-03	8.57E-04	-7.69E+02	1.60E+01
1	164	SMLM5	9.59E-03	3.45E-04	1.10E-02	1.14E-03	-8.13E+02	2.10E+01
3	164	SMLM4	-3.44E-03	1.06E-03	-1.67E-03	1.12E-03	-1.18E+03	3.35E+01
1	164	SMLM3	1.17E-03	2.51E-04	9.94E-04	1.10E-03	-7.69E+01	1.27E+01
2	164	SMLM2	-1.29E-03	2.85E-04	-7.78E-03	1.09E-03	2.32E+02	2.11E+01
1	164	SMLM1	4.87E-04	3.37E-04	1.74E-03	9.64E-04	6.72E+00	1.13E+01
2	164	SMHMu5	3.83E-03	2.73E-04	2.19E-02	1.28E-03	-1.73E+03	3.59E+01
1	164	SMHMu4	1.78E-03	6.09E-04	3.90E-03	1.03E-03	-1.94E+03	3.55E+01
2	164	SMHMu3	-3.94E-03	2.95E-04	8.39E-03	1.08E-03	-5.43E+02	2.26E+01
2	164	SMHMu2	4.14E-03	2.76E-04	2.05E-02	9.11E-04	-8.93E+02	2.46E+01
2	164	SMHMu1	-9.84E-03	3.74E-04	1.71E-02	9.27E-04	-1.07E+03	2.93E+01
1	186	SMPZ2	4.08E-03	5.49E-04	2.65E-02	9.29E-04	-6.43E+02	1.28E+01

QL	doy	ID	CH_4 (mg m^{-2} h^{-1})	CH_4 abs err (mg m^{-2} h^{-1})	N_2O (mg m^{-2} h^{-1})	N_2O abs err (mg m^{-2} h^{-1})	CO_2 (mg m^{-2} h^{-1})	CO_2 abs err (mg m^{-2} h^{-1})
2	186	SMPZ4	4.80E-03	6.87E-04	1.95E-02	8.60E-04	-3.34E+02	2.03E+01
1	186	SMPZ1	-1.01E-01	2.01E-03	2.60E-02	1.82E-03	-1.04E+03	2.01E+01
3	186	SMPZ5	-2.37E-02	1.91E-03	3.60E-02	1.02E-03	-7.50E+02	1.12E+01
1	186	SMPZ3	3.95E-03	6.98E-04	1.50E-02	8.18E-04	-7.74E+02	2.04E+01
2	193	SMPZ5	7.45E-02	1.55E-03	5.01E-03	8.29E-04	-3.19E+01	3.69E+00
2	193	SMPZ4	2.31E-02	5.77E-04	1.23E-03	8.87E-04	2.44E+01	5.08E+00
1	193	SMPZ3	2.03E-02	6.71E-04	1.23E-03	9.95E-04	-1.50E+01	4.08E+00
2	193	SMPZ2	1.24E-02	8.45E-04	4.36E-03	1.09E-03	-2.60E+02	5.24E+00
3	193	SMPZ1	-1.59E-02	4.64E-04	-2.15E-03	9.73E-04	-2.11E+02	5.52E+00
2	208	SMPZ2	1.03E-02	3.05E-04	NA	NA	-4.86E+02	9.02E+00
1	208	SMPZ3	4.04E-03	5.56E-04	4.11E-03	1.04E-03	-3.66E+02	1.58E+01
1	208	SMPZ4	2.52E-03	3.20E-04	5.93E-03	9.54E-04	-1.09E+02	4.78E+00
1	208	SMPZ5	1.91E-02	5.16E-04	8.41E-03	1.16E-03	-3.87E+02	9.97E+00
1	208	SMPZ1	1.37E-02	5.72E-04	1.56E-02	1.09E-03	-5.18E+02	1.05E+01
1	208	SMHMu5	2.22E-04	2.79E-04	3.48E-03	8.74E-04	-1.72E+02	4.66E+00
1	208	SMHMu4	2.14E-04	2.75E-04	9.19E-03	9.46E-04	-2.01E+02	4.91E+00
1	208	SMHMu3	1.02E-03	2.94E-04	8.35E-03	1.43E-03	-5.46E+02	1.07E+01
3	208	SMHMu2	1.04E-03	3.00E-04	1.50E-02	1.80E-03	-6.85E+02	1.21E+01
2	208	SMHMu1	-1.07E-03	2.92E-04	1.49E-02	9.57E-04	-1.22E+02	7.17E+00
1	208	SMHMg1	1.40E-05	2.64E-04	2.28E-02	9.30E-04	2.03E+02	8.04E+00
1	208	SMHMg2	6.26E-04	3.34E-04	1.51E-02	8.62E-04	3.10E+02	7.28E+00
1	208	SMHMg3	1.73E-03	2.57E-04	1.31E-02	8.37E-04	-3.52E+02	5.85E+00
1	208	SMHMg4	-1.15E-03	2.93E-04	6.31E-03	8.55E-04	2.38E+02	7.53E+00
1	208	SMHMg5	-9.23E-04	2.63E-04	2.01E-02	8.10E-04	-6.28E+02	9.72E+00
1	209	SMLM3	-1.17E-02	3.20E-04	3.01E-02	9.08E-04	-2.42E+02	6.67E+00
2	209	SMLM4	9.59E-03	3.96E-04	7.25E-03	1.46E-03	-2.02E+02	5.26E+00
3	209	SMLM5	-1.40E-02	3.37E-04	1.42E-02	1.03E-03	-1.05E+03	1.56E+01
1	209	SMLM2	1.88E-02	5.45E-04	3.09E-02	1.35E-03	-1.06E+02	5.46E+00
1	209	SMLM1	4.27E-03	3.30E-04	2.12E-02	1.31E-03	3.26E+00	6.72E+00
1	214	SMHMg1	-1.25E-02	3.44E-04	2.73E-02	9.36E-04	-2.89E+02	5.74E+00
1	214	SMHMg2	-1.44E-02	4.90E-04	3.50E-02	1.48E-03	-8.75E+01	6.57E+00
3	214	SMHMg3	-7.01E-03	6.51E-04	7.12E-03	8.18E-04	-1.26E+02	5.74E+00
1	214	SMHMg4	-8.49E-03	4.91E-04	2.65E-02	9.09E-04	1.70E+02	4.92E+00
1	214	SMHMg5	7.46E-03	4.64E-04	1.85E-02	9.00E-04	-4.33E+00	7.76E+00
3	214	SMLM1	-6.66E-03	7.16E-04	4.31E-02	1.22E-03	-1.31E+02	1.08E+01
3	214	SMLM2	-7.35E-03	5.80E-04	2.90E-02	8.81E-04	-1.78E+02	4.29E+00
2	214	SMLM3	4.62E-02	1.04E-03	1.83E-02	7.27E-04	-5.77E+02	8.92E+00
1	214	SMLM4	-8.03E-03	4.32E-04	2.86E-02	8.77E-04	-4.26E+02	7.63E+00
1	214	SMLM5	1.44E-02	5.97E-04	2.19E-02	6.49E-04	-2.17E+02	4.50E+00
1	214	SMHMu1	4.95E-03	2.91E-04	1.84E-02	9.69E-04	-6.87E+01	4.24E+00
1	214	SMHMu2	1.34E-02	4.80E-04	1.74E-02	9.14E-04	-7.94E+02	2.00E+01
1	214	SMHMu3	2.58E-03	2.60E-04	1.18E-02	7.02E-04	-4.54E+02	1.09E+01
1	214	SMHMu4	1.60E-02	4.37E-04	1.35E-02	7.61E-04	-7.43E+01	3.94E+00
1	214	SMHMu5	-6.01E-03	7.24E-04	5.18E-03	6.50E-04	1.53E+02	3.57E+00
1	214	SMPZ1	3.54E-02	8.09E-04	5.11E-03	6.53E-04	-4.29E+02	7.04E+00
2	214	SMPZ2	3.47E-02	9.66E-04	-2.34E-04	6.83E-04	-1.42E+02	7.30E+00
1	214	SMPZ3	4.05E-02	8.82E-04	-2.15E-04	6.98E-04	-2.53E+02	4.84E+00
1	214	SMPZ4	2.23E-02	6.58E-04	1.56E-02	7.88E-04	-6.72E+02	9.58E+00
2	214	SMPZ5	1.07E-01	2.14E-03	-4.28E-04	6.87E-04	-3.63E+02	6.04E+00
2	222	SMPZ5	1.19E-01	1.92E-03	4.03E-02	1.36E-03	-9.06E+02	1.24E+01
1	222	SMPZ1	1.42E-02	7.34E-04	2.40E-02	8.95E-04	-8.56E+02	1.29E+01
3	222	SMPZ2	-3.54E-04	5.54E-04	3.25E-02	9.81E-04	-9.51E+02	1.38E+01

QL	doy	ID	CH_4 (mg m^{-2} h^{-1})	CH_4 abs err (mg m^{-2} h^{-1})	N_2O (mg m^{-2} h^{-1})	N_2O abs err (mg m^{-2} h^{-1})	CO_2 (mg m^{-2} h^{-1})	CO_2 abs err (mg m^{-2} h^{-1})
1	222	SMPZ3	2.54E-02	6.29E-04	3.14E-02	8.91E-04	-1.10E+03	1.60E+01
2	222	SMPZ4	5.24E-02	1.31E-03	4.01E-02	1.03E-03	-1.06E+03	1.48E+01
2	222	SMHMu1	4.19E-02	1.06E-03	5.06E-03	1.05E-03	3.48E+02	9.57E+01
1	222	SMHMu5	7.00E-03	4.99E-04	1.00E-02	1.22E-03	-1.10E+02	8.12E+00
3	222	SMHMu4	-2.50E-03	2.48E-04	3.45E-02	1.03E-03	-1.22E+02	5.71E+00
1	222	SMHMu3	1.35E-02	3.51E-04	1.65E-02	8.93E-04	9.12E+00	1.33E+01
1	222	SMHMu2	1.55E-02	4.81E-04	2.42E-02	9.23E-04	-2.74E+02	1.23E+01
4	237	SMLM4	-2.23E-02	4.33E-04	3.97E-02	1.36E-03	-2.97E+02	5.46E+00
1	237	SMLM1	-7.03E-04	3.60E-04	7.29E-02	1.52E-03	4.36E+02	8.98E+00
1	237	SMLM2	-2.65E-03	4.28E-04	6.00E-02	1.19E-03	1.26E+02	7.10E+00
1	237	SMLM3	-2.95E-03	3.10E-04	4.87E-02	1.07E-03	-1.04E+02	6.23E+00
1	237	SMLM5	1.77E-02	4.17E-04	6.27E-02	1.06E-03	-1.35E+02	5.98E+00
1	237	SMHMg3	2.23E-02	5.54E-04	7.30E-02	1.29E-03	3.73E+02	1.03E+01
2	237	SMHMg4	-4.49E-02	1.14E-03	4.32E-02	1.03E-03	1.31E+03	3.02E+01
1	237	SMHMg5	-1.15E-03	6.63E-04	5.80E-02	1.59E-03	3.48E+02	6.11E+00
3	237	SMHMg2	-3.06E-02	7.47E-04	8.28E-02	1.65E-03	6.34E+02	9.38E+00
2	237	SMHMg1	5.60E-02	1.31E-03	9.91E-02	2.40E-03	1.17E+03	1.85E+01
2	242	SMPZ5	6.09E-02	1.11E-03	1.60E-02	9.55E-04	-4.63E+02	6.94E+00
1	242	SMPZ3	8.54E-02	1.23E-03	1.11E-02	1.19E-03	-4.88E+02	7.61E+00
1	242	SMPZ4	9.18E-03	6.65E-04	1.21E-02	1.11E-03	-6.04E+02	8.72E+00
2	242	SMPZ2	-1.18E-01	1.82E-03	2.29E-02	1.07E-03	-1.05E+03	1.93E+01
1	242	SMPZ1	1.64E-02	7.53E-04	8.39E-03	1.24E-03	-1.14E+03	2.06E+01
1	242	SMHMu1	3.95E-02	7.53E-04	2.83E-02	1.39E-03	-4.42E+02	1.83E+01
1	242	SMHMu2	3.36E-03	3.44E-04	4.47E-02	9.77E-04	-1.01E+03	1.52E+01
1	242	SMHMu3	1.75E-02	7.15E-04	-2.46E-03	6.81E-04	-5.32E+02	1.05E+01
1	242	SMHMu4	5.72E-03	3.64E-04	4.82E-03	7.99E-04	7.20E+01	4.82E+00
1	242	SMHMu5	4.46E-03	7.67E-04	1.02E-02	8.53E-04	-9.77E+02	1.61E+01
3	243	SMLM3	-4.92E-02	9.13E-04	4.29E-02	1.27E-03	-7.68E+02	1.38E+01
3	243	SMLM4	-1.63E-02	3.57E-04	4.62E-02	1.14E-03	-5.14E+01	4.64E+00
1	243	SMLM5	2.40E-03	2.83E-04	6.35E-02	1.18E-03	-6.01E+02	9.19E+00
1	243	SMLM2	4.97E-03	2.67E-04	4.80E-02	1.11E-03	-9.22E+01	1.04E+01
3	243	SMLM1	-5.58E-03	4.10E-04	5.32E-02	1.30E-03	-1.19E+02	6.71E+00
1	243	SMHMg5	-6.35E-03	2.67E-04	3.87E-02	9.55E-04	2.21E+02	5.40E+00
3	243	SMHMg4	-1.42E+00	2.08E-02	7.83E-02	1.30E-03	2.36E+01	6.46E+00
3	243	SMHMg3	-4.09E-02	6.42E-04	2.68E-02	1.68E-03	-6.09E+01	7.27E+00
1	243	SMHMg2	4.64E-03	2.59E-04	3.00E-02	7.50E-04	6.88E+02	1.14E+01
1	243	SMHMg1	2.15E-03	2.69E-04	5.24E-02	1.08E-03	1.85E+02	5.58E+00
2	255	SMPZ5	-1.04E-01	2.82E-03	1.61E-02	1.06E-03	1.68E+02	6.65E+00
2	255	SMPZ4	6.47E-02	1.72E-03	2.41E-02	1.07E-03	-1.39E+03	2.09E+01
3	255	SMPZ3	-1.71E-01	2.65E-03	2.23E-02	9.60E-04	-1.64E+03	2.37E+01
1	255	SMPZ2	-2.77E-02	6.69E-04	7.89E-03	9.09E-04	-7.70E+02	1.23E+01
2	255	SMPZ1	-4.68E-02	1.58E-03	1.21E-02	8.70E-04	-8.58E+02	1.18E+01
1	255	SMHMu5	-5.38E-04	3.46E-04	3.72E-02	1.01E-03	-6.80E+02	1.25E+01
1	255	SMHMu4	2.88E-02	5.04E-04	3.57E-02	8.21E-04	-5.17E+02	1.38E+01
3	255	SMHMu3	-4.67E-04	4.57E-04	1.48E-02	7.19E-04	-6.73E+02	1.36E+01
1	255	SMHMu2	4.53E-02	7.19E-04	2.26E-02	8.40E-04	-4.00E+02	1.79E+01
3	255	SMHMu1	-4.29E-01	6.07E-03	1.34E-02	6.72E-04	-3.04E+02	1.29E+01
1	256	SMLM5	-1.28E-02	3.21E-04	3.27E-02	8.64E-04	-6.52E+02	9.13E+00
1	256	SMLM4	-2.63E-03	2.80E-04	1.27E-02	9.68E-04	-7.24E+02	1.25E+01
1	256	SMLM3	-3.59E-03	2.96E-04	1.52E-02	9.90E-04	-5.75E+02	1.17E+01
1	256	SMLM2	4.02E-03	2.75E-04	5.76E-03	9.10E-04	-3.68E+02	6.02E+00
3	256	SMLM1	-5.30E-04	3.54E-04	4.21E-03	7.16E-04	-6.23E+02	9.54E+00

QL	doy	ID	CH_4 (mg m^{-2} h^{-1})	CH_4 abs err (mg m^{-2} h^{-1})	N_2O (mg m^{-2} h^{-1})	N_2O abs err (mg m^{-2} h^{-1})	CO_2 (mg m^{-2} h^{-1})	CO_2 abs err (mg m^{-2} h^{-1})
2	256	SMHMg5	-4.80E-03	3.29E-04	4.54E-02	1.30E-03	3.14E+01	9.26E+00
1	256	SMHMg4	1.29E-03	5.54E-04	2.99E-02	8.69E-04	-2.88E+02	7.45E+00
1	256	SMHMg3	1.96E-03	2.97E-04	4.23E-02	1.04E-03	5.73E+01	3.57E+00
1	256	SMHMg2	-1.46E-03	2.72E-04	4.06E-02	1.07E-03	5.60E+02	1.34E+01
1	256	SMHMg1	4.67E-03	2.85E-04	4.28E-02	9.37E-04	9.72E+02	1.71E+01
3	299	SMHMu3	-1.18E-02	1.12E-03	-1.06E-02	1.27E-03	-6.03E+02	1.86E+01
3	299	SMHMu1	-1.40E-02	6.86E-04	4.50E-02	9.38E-04	2.02E+02	4.40E+00
2	299	SMHMu4	-3.86E-02	1.43E-03	2.26E-02	8.77E-04	-8.08E+01	1.19E+01
2	299	SMHMu5	-5.28E-02	1.41E-03	4.29E-03	8.14E-04	-3.66E+02	5.91E+00
3	299	SMHMu2	-7.86E-02	1.49E-03	7.87E-03	6.36E-04	-2.06E+02	4.43E+00
2	299	SMPZ1	-1.03E-02	1.81E-03	9.35E-03	1.18E-03	-3.58E+02	5.74E+00
2	299	SMPZ2	-3.95E-02	1.14E-03	1.48E-03	1.26E-03	-4.50E+02	7.49E+00
2	299	SMPZ3	-4.44E-02	1.62E-03	-7.12E-03	1.37E-03	-5.60E+02	8.15E+00
3	299	SMPZ4	-2.83E-02	1.39E-03	1.94E-04	1.29E-03	-4.39E+02	6.71E+00
2	299	SMPZ5	1.01E-02	1.13E-03	4.49E-03	1.30E-03	-4.57E+02	7.32E+00
1	299	SMHMg1	-1.99E-02	5.78E-04	6.22E-02	1.38E-03	-4.66E+02	8.46E+00
1	299	SMHMg5	-3.14E-02	8.38E-04	1.26E-02	7.81E-04	-4.74E+02	8.26E+00
1	299	SMHMg2	-2.32E-02	6.25E-04	1.58E-02	7.96E-04	-4.27E+02	7.24E+00
1	299	SMHMg4	-2.17E-03	3.76E-04	1.20E-02	8.01E-04	-2.44E+02	6.08E+00
1	299	SMHMg3	-1.67E-02	4.31E-04	2.82E-02	8.61E-04	-3.05E+02	9.51E+00
1	299	SMLM5	8.74E-06	2.80E-04	1.19E-02	1.03E-03	-3.10E+02	5.31E+00
1	299	SMLM1	-4.51E-03	3.94E-04	2.75E-03	1.39E-03	-1.79E+00	4.99E+00
1	299	SMLM3	-9.40E-03	3.59E-04	5.93E-03	1.08E-03	-1.36E+02	4.04E+00
1	299	SMLM2	1.22E-02	3.59E-04	-1.23E-04	1.07E-03	-1.57E+02	4.02E+00
1	299	SMLM4	6.73E-03	3.08E-04	1.93E-03	9.79E-04	-9.92E+01	3.68E+00
2	348	SMHMg3a	4.00E-02	1.02E-03	1.81E-02	1.13E-03	1.46E+02	4.02E+00
1	348	SMHMg2	-1.37E-02	3.80E-04	4.15E-03	7.63E-04	5.75E+01	2.23E+00
1	348	SMHMg5	-1.27E-02	3.84E-04	4.20E-02	1.27E-03	9.27E+01	2.77E+00
2	348	SMHMg4	4.66E-02	1.17E-03	3.83E-03	9.15E-04	1.01E+02	3.00E+00
1	348	SMHMg3	1.63E-02	4.43E-04	5.62E-03	8.09E-04	1.71E+01	1.62E+00
1	348	SMHMg1	-1.91E-02	5.00E-04	5.80E-03	8.00E-04	-1.95E+01	1.73E+00
2	348	SMHMu1	3.98E-02	1.17E-03	-1.48E-02	1.86E-03	1.57E+01	2.38E+00
2	348	SMHMu2	3.36E-02	1.51E-03	-8.40E-04	1.19E-03	-2.06E+01	1.71E+00
3	348	SMHMu5	-1.78E-03	4.59E-04	2.55E-03	1.04E-03	-5.49E+01	2.03E+00
3	348	SMHMu3	-2.07E-01	5.15E-03	-4.44E-03	8.57E-04	5.49E+00	1.82E+00
2	391	SMPZ4	5.21E-03	1.98E-04	1.42E-02	1.68E-03	2.92E+01	1.67E+00
2	391	SMPZ1	-5.87E-03	3.27E-04	4.74E-03	1.43E-03	-3.08E+01	1.78E+00
2	391	SMPZ2	4.34E-03	3.09E-04	3.89E-03	1.06E-03	1.79E+01	1.70E+00
1	391	SMPZ3	8.70E-03	2.70E-04	1.26E-03	8.69E-04	4.25E+01	1.85E+00
1	391	SMPZ5	2.54E-02	6.77E-04	2.74E-03	8.56E-04	3.08E+01	1.75E+00
1	391	SMHMu2	9.02E-03	2.83E-04	-6.82E-04	7.69E-04	-2.77E-01	1.57E+00
1	391	SMHMu5	-1.33E-02	3.71E-04	3.26E-04	6.53E-04	-9.01E+01	2.83E+00
1	391	SMHMu1	1.43E-02	3.90E-04	-1.26E-03	6.28E-04	7.58E+01	2.50E+00
4	391	SMHMu4	-2.83E-03	1.86E-04	-1.53E-03	1.42E-03	7.10E+01	2.64E+00
4	391	SMHMu3	-5.34E-03	7.44E-04	-5.32E-04	6.21E-04	-1.43E+01	1.66E+00
2	391	SMHMu3	-1.66E-02	4.64E-04	4.14E-04	1.59E-03	-4.35E+01	4.55E+00
1	391	SMHMg5	2.25E-03	1.64E-04	5.21E-03	6.37E-04	-2.30E+02	5.88E+00
3	391	SMHMg1	-8.52E-04	1.30E-04	2.37E-04	6.18E-04	-3.03E+02	7.67E+00
1	391	SMHMg3	-1.40E-03	1.36E-04	2.45E-03	5.58E-04	-1.76E+02	4.61E+00
1	391	SMHMg4	1.81E-03	1.44E-04	1.79E-03	5.94E-04	-1.47E+02	4.23E+00
1	391	SMHMg2	-6.42E-04	1.33E-04	1.35E-03	6.26E-04	-1.16E+02	3.23E+00
2	416	SMHMg4	-1.57E-03	1.59E-04	3.78E-03	1.18E-03	-1.07E+02	3.75E+00

QL	doy	ID	CH_4 (mg m^{-2} h^{-1})	CH_4 abs err (mg m^{-2} h^{-1})	N_2O (mg m^{-2} h^{-1})	N_2O abs err (mg m^{-2} h^{-1})	CO_2 (mg m^{-2} h^{-1})	CO_2 abs err (mg m^{-2} h^{-1})
2	416	SMHMg5	-5.45E-03	2.07E-04	9.12E-04	1.14E-03	-1.27E+02	4.45E+00
2	416	SMHMg1	-5.14E-03	1.95E-04	-3.45E-03	1.10E-03	-1.23E+02	5.44E+00
2	416	SMHMg2	-8.78E-04	1.58E-04	3.45E-03	1.22E-03	-1.66E+02	4.74E+00
2	416	SMHMg3	3.52E-04	1.59E-04	7.90E-04	9.61E-04	-7.56E+01	2.65E+00
2	416	SMLM1	3.48E-02	9.96E-04	1.96E-03	2.28E-03	1.74E+02	5.10E+00
2	416	SMLM2	-1.80E-03	1.74E-04	-3.69E-03	1.23E-03	4.80E-01	1.96E+00
2	416	SMLM3	2.41E-03	1.60E-04	-5.23E-03	1.10E-03	-1.18E+01	1.91E+00
2	416	SMLM4	3.78E-03	1.83E-04	-1.59E-04	1.02E-03	-1.19E+02	3.36E+00
2	416	SMLM5	7.45E-04	1.42E-04	-3.24E-03	1.09E-03	-1.13E+02	3.73E+00
3	418	SMLM5	-1.26E-03	1.57E-04	5.13E-03	8.10E-04	1.73E+01	1.69E+00
2	418	SMLM3	2.06E-03	1.51E-04	4.72E-03	9.18E-04	-2.45E+01	1.64E+00
1	418	SMLM4	3.65E-03	1.63E-04	1.14E-02	8.21E-04	-1.36E+02	3.62E+00
1	418	SMLM2	4.51E-03	1.91E-04	3.50E-03	6.85E-04	-9.08E+01	2.73E+00
1	418	SMPZ1	5.09E-03	1.94E-04	8.25E-04	7.05E-04	-7.18E+01	2.27E+00
1	418	SMPZ5	2.35E-02	6.01E-04	6.72E-03	8.88E-04	-4.66E+01	1.97E+00
1	418	SMPZ4	1.18E-03	2.69E-04	4.46E-04	7.47E-04	-4.56E+01	2.18E+00
4	418	SMPZ3	-5.77E-03	2.83E-04	-3.18E-04	7.55E-04	8.43E+00	1.61E+00
1	418	SMPZ2	1.07E-02	3.11E-04	-2.88E-03	8.36E-04	-3.15E+01	1.65E+00
1	418	SMHMu5	-8.32E-03	3.66E-04	8.17E-04	7.05E-04	3.49E+01	1.95E+00
1	418	SMHMu3	5.08E-03	2.00E-04	3.60E-03	7.19E-04	-7.10E+01	2.35E+00
3	418	SMHMu1	4.94E-02	1.50E-03	1.01E-02	7.60E-04	-3.16E+01	1.79E+00
3	418	SMHMu2	-3.57E-03	2.04E-04	-1.32E-03	6.75E-04	-3.18E+01	1.80E+00
3	418	SMHMu4	-2.40E-03	2.91E-04	2.98E-03	7.24E-04	-5.07E+01	1.99E+00
2	466	SMLM1	-7.55E-04	2.24E-04	2.59E-03	8.50E-04	-1.44E+02	4.20E+00
1	466	SMLM2	2.34E-03	1.40E-04	-2.92E-04	7.01E-04	-2.00E+02	5.15E+00
1	466	SMLM3	1.47E-03	1.42E-04	1.95E-03	7.91E-04	-1.21E+02	3.33E+00
1	466	SMLM5	1.09E-03	1.40E-04	4.69E-04	7.09E-04	-2.87E+02	7.59E+00
2	466	SMLM4	-3.65E-03	2.52E-04	1.24E-03	9.04E-04	-1.64E+02	4.87E+00
1	466	SMHMg5	-7.43E-04	1.71E-04	-1.20E-03	8.07E-04	-2.22E+02	5.91E+00
2	466	SMHMg4	8.65E-04	1.47E-04	-3.12E-03	9.00E-04	-5.56E+01	3.18E+00
1	466	SMHMg3	1.52E-03	2.11E-04	-4.17E-03	8.64E-04	-3.44E+01	2.43E+00
1	466	SMHMg2	-1.77E-03	1.60E-04	2.62E-03	7.41E-04	-1.50E+02	4.05E+00
2	466	SMHMg1	6.22E-03	2.37E-04	4.30E-03	9.48E-04	-3.19E+02	1.02E+01
2	468	SMPZ2	6.99E-03	2.49E-04	1.56E-02	1.18E-03	-1.16E+02	4.02E+00
2	468	SMPZ5	1.15E-02	3.36E-04	1.03E-03	1.04E-03	-1.05E+02	3.24E+00
1	468	SMPZ1	-4.24E-03	1.95E-04	-1.51E-03	7.74E-04	-2.88E+02	7.96E+00
1	468	SMPZ3	3.11E-03	3.99E-04	7.39E-03	7.49E-04	-1.72E+02	4.72E+00
1	468	SMPZ4	-3.26E-03	3.22E-04	-3.77E-03	7.56E-04	-9.71E+01	3.70E+00
1	468	SMHMu2	2.40E-03	4.25E-04	8.79E-03	8.11E-04	-1.97E+02	8.64E+00
3	468	SMHMu1	2.73E-02	4.83E-03	7.87E-03	1.38E-03	-5.72E+02	1.62E+01
3	468	SMHMu3	-9.33E-03	4.00E-04	-7.54E-03	9.37E-04	-1.45E+02	1.85E+01
1	468	SMHMu5	-6.88E-03	2.69E-04	1.62E-03	7.61E-04	-3.11E+02	1.20E+01
1	468	SMHMu4	8.18E-03	4.17E-04	-6.14E-03	8.28E-04	-6.53E+01	6.48E+00
3	495	SMPZ1	-7.18E-03	2.63E-04	-7.11E-03	8.82E-04	-3.95E+01	2.49E+00
2	495	SMPZ5	2.72E-02	1.42E-03	1.21E-03	8.61E-04	1.87E+01	1.53E+00
1	495	SMPZ3	2.78E-02	7.48E-04	-2.75E-03	8.65E-04	-7.83E+01	2.74E+00
2	495	SMPZ2	1.01E-02	3.16E-04	-7.05E-04	9.30E-04	6.42E+01	2.35E+00
2	495	SMPZ4	4.02E-02	9.93E-04	-8.79E-05	1.09E-03	2.21E+01	1.77E+00
2	495	SMHMu5	2.29E-03	1.63E-04	8.19E-04	9.64E-04	-4.33E+01	1.03E+01
1	495	SMHMu2	1.32E-02	3.64E-04	9.15E-03	9.06E-04	5.48E+01	2.34E+00
2	495	SMHMu1	1.19E-02	4.42E-04	9.71E-02	2.58E-03	3.58E+02	9.36E+00
2	495	SMHMu3	1.34E-02	3.62E-04	1.93E-02	1.10E-03	-6.77E+02	1.66E+01

QL	doy	ID	CH_4 (mg m^{-2} h^{-1})	CH_4 abs err (mg m^{-2} h^{-1})	N_2O (mg m^{-2} h^{-1})	N_2O abs err (mg m^{-2} h^{-1})	CO_2 (mg m^{-2} h^{-1})	CO_2 abs err (mg m^{-2} h^{-1})
2	495	SMHMu4	1.81E-03	3.02E-04	7.60E-02	2.16E-03	-1.56E+02	5.33E+00
1	495	SMLM2	8.05E-03	3.08E-04	2.33E-03	8.32E-04	-1.70E+02	5.79E+00
2	495	SMLM5	1.14E-03	2.00E-04	3.60E-03	1.03E-03	-4.60E+02	1.15E+01
1	495	SMLM3	1.32E-03	2.18E-04	2.18E-03	8.30E-04	1.51E+02	4.17E+00
2	495	SMLM1	2.14E-02	5.86E-04	-7.86E-04	1.47E-03	6.81E+01	3.86E+00
2	495	SMLM4	-1.15E-02	4.27E-04	2.14E-03	1.05E-03	7.67E+01	2.93E+00
2	495	SMHMg1	8.67E-03	3.64E-04	1.69E-02	1.02E-03	-1.91E+02	5.44E+00
2	495	SMHMg4	6.50E-02	1.96E-03	1.78E-03	8.76E-04	-1.68E+02	4.70E+00
2	495	SMHMg2	1.71E-02	7.26E-04	5.27E-03	9.23E-04	-5.60E+02	1.45E+01
3	495	SMHMg3	-7.37E-04	3.00E-04	6.44E-04	1.18E-03	-7.67E+02	1.95E+01
2	517	SMLM2	5.80E-05	1.29E-04	5.73E-02	1.79E-03	-1.62E+02	4.68E+00
1	517	SMLM5	4.36E-04	1.58E-04	5.71E-03	8.58E-04	-3.57E+02	1.09E+01
2	517	SMLM3	-8.14E-04	1.42E-04	6.41E-03	9.36E-04	-2.60E+02	6.91E+00
2	517	SMLM2a	2.92E-04	1.45E-04	1.60E-02	1.15E-03	-1.93E+02	5.46E+00
2	517	SMLM1	-1.18E-03	1.45E-04	1.29E-01	3.25E-03	-3.08E+02	7.94E+00
2	517	SMLM4	-1.65E-03	1.51E-04	1.76E-02	1.04E-03	-3.45E+02	8.85E+00
1	517	SMHMg5	-2.85E-03	1.52E-04	1.02E-02	8.70E-04	-1.64E+02	5.36E+00
2	517	SMHMg4	-5.77E-04	1.37E-04	-6.73E-04	8.79E-04	-2.27E+02	8.73E+00
2	517	SMHMg3	-7.94E-04	1.33E-04	3.76E-03	8.88E-04	-2.08E+02	6.56E+00
2	517	SMHMg2	-3.45E-04	1.33E-04	4.50E-03	9.74E-04	1.07E+02	3.83E+00
2	517	SMHMg1	3.05E-04	1.36E-04	2.95E-03	9.32E-04	-9.72E+01	4.75E+00
2	517	SMHMu4	-1.35E-03	3.00E-04	1.71E-01	2.94E-03	-1.58E+03	2.08E+01
1	517	SMHMu2	-2.81E-03	2.68E-04	7.78E-02	1.86E-03	-8.08E+02	1.07E+01
2	517	SMHMu3	-1.69E-04	2.78E-04	2.55E-01	4.08E-03	-7.86E+02	1.19E+01
2	517	SMHMu1	-1.59E-04	2.94E-04	3.29E-02	2.00E-03	-1.25E+03	2.89E+01
2	517	SMHMu5	9.54E-04	2.55E-04	1.99E-01	3.24E-03	-1.98E+03	2.58E+01
2	517	SMPZ4	1.69E-02	4.82E-04	-1.24E-03	1.03E-03	-1.55E+02	5.38E+00
2	517	SMPZ3	4.49E-02	1.20E-03	-1.41E-03	8.87E-04	1.71E+02	4.93E+00
2	517	SMPZ2	9.83E-03	2.89E-04	3.50E-03	9.08E-04	-2.42E+02	6.32E+00
2	517	SMPZ5	8.83E-03	4.74E-04	-1.71E-03	1.22E-03	-1.09E+01	1.84E+00
2	517	SMPZ1	1.03E-03	1.59E-04	-7.52E-04	1.16E-03	-2.26E+02	7.84E+00
2	531	SMPZ3	1.65E-02	4.57E-04	1.89E-02	1.20E-03	-2.19E+02	5.67E+00
2	531	SMPZ5	5.91E-02	1.53E-03	1.35E-02	1.24E-03	-2.00E+02	6.98E+00
2	531	SMPZ2	1.46E-02	4.97E-04	6.78E-03	1.15E-03	5.03E+01	4.38E+00
2	531	SMPZ4	2.58E-02	1.14E-03	6.72E-03	1.18E-03	7.32E+01	2.47E+00
2	531	SMPZ1	-1.41E-02	8.38E-04	1.62E-03	7.64E-04	7.08E+01	2.98E+00
2	531	SMHMu3	-1.09E-03	3.35E-04	4.73E-02	4.16E-03	-9.33E+02	1.19E+01
1	531	SMHMu1	-5.44E-03	3.11E-04	4.98E-02	1.78E-03	-7.94E+02	1.12E+01
2	531	SMHMu5	6.48E-03	2.66E-04	2.50E-01	3.53E-03	-1.42E+03	1.77E+01
2	531	SMHMu4	1.31E-02	3.30E-04	2.73E-01	3.95E-03	-1.69E+03	2.17E+01
1	531	SMHMu2	9.27E-03	3.38E-04	1.16E-01	2.18E-03	-1.31E+03	1.71E+01
3	531	SMHMg3	-9.23E-03	2.99E-04	1.34E-02	8.92E-04	-5.17E+01	2.90E+00
2	531	SMHMg1	-4.17E-03	1.99E-04	3.34E-02	1.47E-03	-4.06E+02	1.32E+01
2	531	SMHMg2	-7.09E-02	1.78E-03	2.01E-02	9.42E-04	2.34E+02	9.76E+00
2	531	SMHMg5	2.67E-03	3.38E-04	5.98E-02	1.82E-03	-6.28E+01	4.69E+00
2	531	SMHMg4	-2.67E-02	7.45E-04	1.14E-02	8.74E-04	-1.36E+02	4.88E+00
1	531	SMLM5	-3.66E-03	1.71E-04	3.01E-02	1.09E-03	-7.16E+02	1.81E+01
2	531	SMLM1	1.44E-03	1.65E-04	9.90E-02	2.57E-03	8.86E+01	4.31E+00
2	531	SMLM3	-7.62E-02	2.70E-03	8.35E-03	7.91E-04	1.26E+02	5.53E+00
1	531	SMLM4	2.43E-02	7.07E-04	4.04E-02	1.27E-03	2.95E+02	7.35E+00
2	543	SMPZ5	2.07E-02	5.71E-04	1.42E-02	1.20E-03	-9.19E+02	2.47E+01
2	543	SMPZ4	1.55E-02	4.50E-04	5.77E-03	1.25E-03	-1.04E+03	3.69E+01

QL	doy	ID	CH_4 (mg m^{-2} h^{-1})	CH_4 abs err (mg m^{-2} h^{-1})	N_2O (mg m^{-2} h^{-1})	N_2O abs err (mg m^{-2} h^{-1})	CO_2 (mg m^{-2} h^{-1})	CO_2 abs err (mg m^{-2} h^{-1})
2	543	SMPZ3	4.20E-03	2.06E-04	-8.46E-03	1.18E-03	3.78E+02	3.93E+01
2	543	SMPZ2	4.50E-03	2.05E-04	4.34E-03	1.21E-03	-5.46E+02	1.70E+01
2	543	SMPZ1	3.21E-03	1.83E-04	-1.03E-02	1.13E-03	-2.11E+02	1.03E+01
2	543	SMHMu5	-7.62E-04	2.73E-04	1.01E-01	2.25E-03	-4.60E+02	1.00E+01
2	543	SMHMu4	-1.62E-03	2.66E-04	6.24E-02	1.83E-03	-1.11E+03	1.54E+01
2	543	SMHMu3	4.68E-03	2.85E-04	5.88E-02	2.24E-03	-1.67E+03	3.53E+01
2	543	SMHMu2	1.30E-03	2.91E-04	8.42E-02	2.23E-03	-2.21E+03	3.96E+01
2	543	SMHMu1	1.55E-02	3.57E-04	1.43E-02	2.20E-03	-4.08E+02	1.91E+01
3	117	BMLM1	2.99E+00	6.61E-02	-8.62E-03	1.08E-03	-2.71E+01	7.91E+00
1	117	BMLM2	4.70E+00	6.35E-02	1.91E-02	9.74E-04	-1.02E+03	1.56E+01
2	117	BMLM3	3.93E+00	5.91E-02	2.36E-03	8.18E-04	-9.51E+01	4.34E+00
1	117	BMLM4	3.78E+00	5.39E-02	2.25E-02	9.64E-04	-8.13E+02	1.40E+01
1	117	BMLM5	2.84E+00	3.91E-02	-4.39E-03	6.54E-04	-1.86E+01	4.19E+00
2	117	BMHM1	3.56E-01	6.61E-03	1.21E-02	8.66E-04	-8.01E+02	1.33E+01
1	117	BMHM2	3.06E-01	5.39E-03	3.70E-02	9.12E-04	-1.00E+03	1.50E+01
1	117	BMHM3	1.47E-01	2.76E-03	4.29E-02	8.88E-04	-1.12E+03	1.94E+01
1	117	BMHM4	8.41E-02	1.28E-03	3.46E-02	8.45E-04	-6.10E+02	1.29E+01
1	117	BMHM5	2.64E-01	4.21E-03	3.49E-02	8.15E-04	-1.84E-01	5.65E+00
2	131	BMHM5	2.12E-01	3.02E-03	1.97E-02	1.19E-03	-9.11E+02	1.98E+01
1	131	BMHM1	1.64E+00	2.44E-02	4.05E-02	8.68E-04	-9.96E+02	1.80E+01
1	131	BMHM2	6.75E-01	9.23E-03	2.27E-02	9.08E-04	-1.57E+03	2.24E+01
2	131	BMHM4	1.84E-01	2.51E-03	2.93E-02	9.35E-04	-2.42E+03	3.78E+01
1	131	BMHM3	4.74E-01	6.59E-03	3.76E-02	1.18E-03	-2.38E+03	3.73E+01
2	131	BMLM4	2.69E+00	3.76E-02	2.07E-02	1.30E-03	-6.41E+02	2.30E+01
2	131	BMLM2	9.29E+00	1.32E-01	9.39E-03	8.78E-04	-6.33E+02	1.92E+01
3	131	BMLM5	3.43E+00	4.78E-02	1.65E-02	9.08E-04	-3.42E+02	1.55E+01
2	131	BMLM1	7.88E+00	1.18E-01	2.53E-02	1.01E-03	-5.97E+02	1.66E+01
1	131	BMLM3	2.42E+00	3.61E-02	2.46E-02	9.23E-04	-9.15E+02	1.77E+01
2	131	BMPZ4	4.08E-01	8.19E-03	1.83E-02	1.15E-03	-1.61E+02	1.44E+01
2	131	BMPZ3	3.26E-02	3.44E-03	1.40E-02	8.33E-04	-9.46E+02	1.43E+01
2	131	BMPZ1	4.92E-01	1.91E-02	4.67E-03	7.69E-04	-6.05E+02	1.21E+01
4	131	BMPZ2	-1.67E-01	9.48E-03	1.32E-02	7.85E-04	-3.52E+02	7.71E+00
4	131	BMPZ5	-1.06E+00	8.95E-02	3.13E-03	7.89E-04	-4.71E+01	5.91E+00
1	143	BMHM5	5.37E-01	1.22E-02	1.88E-02	1.22E-03	-1.51E+03	2.28E+01
1	143	BMHM4	6.31E-01	8.44E-03	3.09E-02	8.11E-04	-2.65E+03	3.95E+01
1	143	BMHM3	8.20E-01	1.09E-02	1.75E-02	7.49E-04	-1.87E+03	2.97E+01
1	143	BMHM1	2.14E+00	3.14E-02	4.89E-03	7.85E-04	-1.39E+03	2.19E+01
1	143	BMLM5	2.56E+00	3.43E-02	8.41E-03	5.88E-04	-1.30E+03	2.16E+01
1	143	BMPZ1	2.37E-01	3.67E-03	1.64E-02	6.37E-04	-2.27E+03	3.73E+01
1	143	BMPZ3	2.17E-01	5.26E-03	7.80E-03	6.58E-04	-7.09E+02	1.92E+01
1	143	BMPZ2	1.76E-01	2.96E-03	1.66E-02	7.38E-04	-1.41E+03	2.71E+01
3	143	BMPZ4	-4.97E-02	3.47E-03	6.53E-04	6.96E-04	-9.35E+02	1.97E+01
3	143	BMPZ5	-4.30E-01	1.32E-02	1.32E-03	6.52E-04	-2.65E+02	1.45E+01
1	181	BMPZ1	5.76E-01	9.05E-03	7.43E-02	1.79E-03	-2.59E+03	3.26E+01
1	181	BMPZ2	6.48E-01	1.39E-02	4.10E-02	1.84E-03	-1.87E+03	3.13E+01
1	181	BMPZ3	1.77E+00	2.45E-02	5.39E-02	2.46E-03	-2.46E+03	4.51E+01
1	181	BMPZ4	9.49E-01	1.77E-02	7.94E-02	1.82E-03	-3.45E+03	4.16E+01
1	383	BMPZ3	3.74E-04	2.07E-03	-2.17E-03	8.75E-04	1.43E+01	1.68E+00
1	383	BMPZ4	3.47E-02	1.63E-03	1.55E-03	9.77E-04	-8.93E+00	1.62E+00
2	383	BMPZ5	2.00E-01	2.05E-02	9.62E-03	8.72E-04	1.05E+01	1.47E+00
1	383	BMPZ5	5.31E-01	1.30E-02	2.05E-02	9.10E-04	2.50E+00	1.53E+00
3	383	BMPZ4	-9.24E-04	1.35E-03	4.13E-03	8.86E-04	-3.15E+00	1.58E+00

QL	doy	ID	CH_4 (mg m^{-2} h^{-1})	CH_4 abs err (mg m^{-2} h^{-1})	N_2O (mg m^{-2} h^{-1})	N_2O abs err (mg m^{-2} h^{-1})	CO_2 (mg m^{-2} h^{-1})	CO_2 abs err (mg m^{-2} h^{-1})
1	383	BMPZ3	8.47E-02	2.08E-03	5.43E-03	7.67E-04	-1.90E+01	1.52E+00
3	383	BMPZ1	-7.32E-03	5.53E-03	2.30E-03	9.36E-04	-6.17E+00	1.73E+00
3	419	BMPZ1	-1.07E-01	3.11E-03	-4.82E-04	7.36E-04	-1.65E+01	1.63E+00
1	419	BMPZ5	7.48E-03	3.82E-04	3.66E-03	7.30E-04	-2.76E+01	1.62E+00
1	419	BMPZ3	1.71E-02	4.38E-04	6.22E-03	6.89E-04	-3.62E+01	1.69E+00
1	419	BMPZ5	6.58E-02	1.65E-03	5.38E-03	7.39E-04	-5.30E+01	1.99E+00
1	419	BMPZ3	1.67E-02	4.35E-04	7.70E-03	8.68E-04	-5.27E+01	2.02E+00
3	451	BMPZ1	-1.64E-02	6.86E-04	-7.49E-03	8.68E-04	-1.11E+01	1.72E+00
1	451	BMPZ5	2.74E-01	6.73E-03	4.97E-04	7.48E-04	-1.00E+02	2.84E+00
1	451	BMPZ3	8.67E-02	2.12E-03	1.41E-03	8.42E-04	-8.31E+01	2.47E+00
1	451	BMPZ5	7.69E-01	2.31E-02	4.94E-03	8.69E-04	-1.13E+02	3.18E+00
2	451	BMPZ3	9.75E-02	2.38E-03	1.52E-02	1.25E-03	-1.44E+02	4.02E+00
2	451	BMPZ1	1.66E-02	5.22E-04	2.56E-03	9.66E-04	-7.64E+01	2.37E+00
2	475	BMPZ1	-2.36E-01	6.63E-03	2.17E-03	1.04E-03	-1.73E+01	1.59E+00
3	475	BMPZ2	-5.64E-03	1.32E-03	1.50E-03	9.51E-04	4.76E+00	1.55E+00
1	475	BMPZ3	6.97E-02	1.70E-03	1.18E-03	8.40E-04	5.97E+00	1.64E+00
3	475	BMPZ4	-8.26E-04	4.80E-04	2.10E-04	7.79E-04	-8.32E+00	1.54E+00
1	497	BMPZ2	1.09E-01	2.63E-03	3.08E-02	1.31E-03	-1.25E+03	3.09E+01
3	497	BMPZ2	-5.68E-02	2.00E-03	-2.68E-04	9.10E-04	-8.75E+02	2.25E+01
1	497	BMPZ3	2.20E-01	5.37E-03	1.17E-02	8.79E-04	-1.19E+03	2.95E+01
1	497	BMPZ3	2.24E-01	5.45E-03	9.22E-03	7.90E-04	-1.19E+03	2.92E+01
3	497	BMPZ4	-1.25E+00	3.23E-02	-3.31E-03	6.73E-04	-3.00E+02	1.37E+01
3	497	BMPZ4	-3.54E-01	1.01E-02	-1.37E-03	6.98E-04	-9.08E+02	2.30E+01
3	497	BMPZ5	-4.07E-02	6.07E-03	1.49E-02	7.74E-04	-7.05E+02	1.76E+01
1	497	BMPZ5	2.82E-01	7.35E-03	6.64E-03	7.52E-04	-7.04E+02	1.75E+01
2	497	BMPZ1	7.87E-02	4.78E-03	-8.37E-03	8.62E-04	-4.61E+02	1.20E+01
2	497	BMPZ1	1.91E-01	5.79E-03	-1.95E-03	7.90E-04	-2.92E+02	7.26E+00
1	530	BMPZ2	9.15E-01	7.59E-03	1.15E-01	2.90E-03	-2.60E+03	2.65E+01
2	530	BMPZ5	2.06E+00	1.70E-02	9.10E-02	2.93E-03	-2.09E+03	1.99E+01
2	530	BMPZ5	1.96E+00	1.62E-02	1.06E-01	2.78E-03	-2.26E+03	1.94E+01
2	530	BMPZ4	1.75E+00	1.45E-02	1.19E-01	3.27E-03	-1.81E+03	1.65E+01
2	530	BMPZ3	2.18E+00	2.07E-02	1.49E-02	3.31E-03	-5.54E+02	1.87E+01
1	530	BMPZ3	1.34E+00	1.12E-02	1.10E-01	2.80E-03	-1.12E+03	1.06E+01
2	544	BMPZ5	4.88E+00	4.02E-02	8.10E-02	3.26E-03	-2.99E+03	2.59E+01
2	544	BMPZ4	2.18E+00	1.81E-02	9.80E-03	2.59E-03	-1.89E+03	1.74E+01
1	544	BMPZ3	2.49E+00	2.04E-02	2.63E-02	2.53E-03	-3.42E+03	3.05E+01
1	544	BMPZ3	2.39E+00	1.96E-02	2.81E-03	2.52E-03	-2.43E+03	2.08E+01
1	116	FMPZ1	6.42E+00	8.96E-02	1.04E-02	9.48E-04	-8.71E+01	3.53E+00
1	116	FMLM1	6.17E-01	1.03E-02	1.37E-02	9.79E-04	8.45E+00	3.26E+00
1	116	FMLM2	2.20E+00	3.03E-02	7.16E-04	1.55E-03	2.19E+02	4.26E+00
4	116	FMLM3	8.53E+00	3.05E-01	-5.22E-03	1.09E-03	2.49E+02	4.98E+00
1	116	FMLM4	9.80E-01	1.88E-02	6.03E-03	9.46E-04	2.65E+02	5.65E+00
1	116	FMLM5	1.82E+00	2.87E-02	8.26E-03	1.89E-03	1.12E+02	3.45E+00
1	116	FMHMu1	1.40E+00	1.89E-02	7.40E-02	1.79E-03	5.73E+01	4.18E+00
1	116	FMHMu2	5.98E-01	7.94E-03	4.79E-02	1.15E-03	3.15E+02	5.05E+00
1	116	FMHMu3	1.12E+00	1.59E-02	8.38E-02	1.49E-03	-3.74E+02	7.04E+00
2	116	FMHMu4	4.02E-01	5.74E-03	2.47E-02	1.03E-03	-4.77E+00	1.57E+01
2	116	FMHMu5	1.39E+00	2.09E-02	3.53E-02	1.11E-03	4.75E+01	1.77E+01
3	137	FMPZ1	2.40E+01	6.18E-01	-3.71E-03	7.70E-04	-2.90E+02	4.92E+00
3	137	FMPZ2	-1.66E-02	7.37E-01	-8.80E-03	9.16E-04	-2.13E+02	4.30E+00
2	137	FMPZ4	1.76E+02	6.17E+00	1.52E-02	9.71E-04	-9.86E+01	5.42E+00
2	137	FMPZ5	2.66E+01	9.94E-01	6.66E-04	7.86E-04	-2.07E+02	4.01E+00

QL	doy	ID	CH_4 (mg m^{-2} h^{-1})	CH_4 abs err (mg m^{-2} h^{-1})	N_2O (mg m^{-2} h^{-1})	N_2O abs err (mg m^{-2} h^{-1})	CO_2 (mg m^{-2} h^{-1})	CO_2 abs err (mg m^{-2} h^{-1})
3	137	FMPZ3	8.33E-02	1.81E-01	-1.78E-03	7.64E-04	-1.05E+03	1.58E+01
1	137	FMLM2	7.22E-01	9.65E-03	-2.00E-03	8.72E-04	1.47E+00	3.46E+00
1	137	FMLM3	1.07E+00	1.41E-02	-3.79E-03	7.87E-04	1.03E+02	3.54E+00
1	137	FMLM4	1.82E+00	2.83E-02	-3.56E-03	8.58E-04	5.48E+01	4.27E+00
1	137	FMLM5	1.73E+00	2.48E-02	-2.19E-03	9.66E-04	-1.68E+01	3.47E+00
1	137	FMLM1	4.39E-01	8.65E-03	7.75E-04	8.20E-04	-2.66E+02	5.54E+00
2	137	FMHMu1	2.36E-01	3.63E-03	9.59E-04	7.78E-04	-3.43E+02	7.39E+00
2	137	FMHMu4	2.54E-01	3.62E-03	1.45E-02	9.89E-04	-5.38E+02	1.15E+01
2	137	FMHMu3	2.91E-01	3.97E-03	3.58E-02	9.41E-04	-1.06E+03	2.53E+01
2	137	FMHMu5	3.02E-01	4.38E-03	1.21E-02	8.25E-04	-1.26E+03	2.83E+01
2	137	FMHMu2	2.21E-01	3.08E-03	6.99E-03	6.97E-04	-6.72E+02	1.14E+01
1	257	FMPZ1	2.64E+01	3.78E-01	1.11E-02	1.04E-03	-9.72E+02	8.76E+00
1	257	FMPZ2	2.06E+01	2.52E-01	3.36E-02	1.32E-03	-1.05E+03	1.27E+01
1	257	FMPZ3	1.91E+01	1.38E-01	3.54E-02	1.46E-03	-9.37E+02	1.07E+01
2	257	FMPZ4	1.31E+01	1.07E+00	7.58E-03	1.34E-03	-1.65E+02	6.36E+00
1	257	FMPZ5	1.17E+01	2.55E-01	1.35E-02	1.04E-03	-2.27E+02	6.39E+00
2	257	FMHMg1	5.45E-01	8.68E-03	5.61E-03	4.50E-04	-5.58E+02	9.83E+00
1	257	FMHMg2	1.07E+00	1.41E-02	3.05E-03	4.52E-04	1.91E+01	4.38E+00
1	257	FMHMg3	3.08E+00	4.12E-02	4.86E-03	5.70E-04	-3.64E+02	7.08E+00
2	257	FMHMg4	2.44E+00	3.35E-02	1.72E-02	5.72E-04	-2.09E+02	6.70E+00
1	270	FMPZ3	8.76E+00	5.74E-02	-2.06E-02	1.73E-03	2.09E+02	6.36E+00
1	270	FMPZ1	2.20E+01	6.79E-01	6.88E-03	2.33E-03	-4.19E+01	6.17E+00
1	270	FMPZ4	3.98E+01	7.30E-01	7.13E-03	1.68E-03	-5.79E+01	6.24E+00
1	270	FMPZ2	7.68E+00	6.54E-02	3.78E-03	1.96E-03	-4.00E+01	6.53E+00
2	270	FMPZ5	8.56E+01	2.89E+00	1.71E-02	1.83E-03	9.87E+01	6.36E+00
1	270	FMHMg1	2.80E-01	3.79E-03	-7.35E-03	1.00E-03	6.33E+01	3.32E+00
1	270	FMHMg3	3.64E-01	4.76E-03	-4.94E-03	8.10E-04	1.67E+02	4.25E+00
1	270	FMHMg2	5.21E-01	6.83E-03	1.31E-03	9.01E-04	1.76E+02	4.00E+00
1	270	FMHMg4	3.63E-01	4.84E-03	-1.24E-03	8.95E-04	1.56E+02	3.92E+00
2	300	FMPZ3	2.83E+01	2.41E-01	6.10E-03	1.83E-03	4.04E+02	7.98E+00
4	300	FMPZ1	9.35E+00	1.04E-01	-4.08E-01	3.71E-02	1.32E+02	8.55E+00
1	300	FMPZ2	1.54E+01	2.15E-01	-2.00E-03	1.48E-03	1.43E+02	6.38E+00
2	300	FMPZ4	1.75E+01	7.52E-01	7.02E-03	1.39E-03	1.88E+02	6.95E+00
1	300	FMPZ5	9.71E+00	1.01E-01	8.52E-03	1.47E-03	8.98E+01	6.92E+00
1	382	FMPZ2	6.28E+00	8.46E-02	1.84E-02	2.87E-03	4.83E+01	6.75E+00
1	382	FMPZ3	1.03E+01	1.62E-01	6.18E-04	2.61E-03	8.60E+01	4.45E+00
2	382	FMPZ1	5.70E+01	9.61E-01	2.97E-02	2.46E-03	7.10E+01	4.63E+00
2	382	FMPZ4	5.08E+01	1.54E+00	2.79E-02	2.10E-03	5.71E+01	5.17E+00
1	382	FMPZ5	1.32E+01	1.09E-01	2.63E-02	2.43E-03	8.00E+01	4.35E+00
1	382	FMPZ5	1.25E+01	1.04E-01	4.08E-02	2.37E-03	5.36E+01	4.54E+00
1	382	FMPZ3	7.95E+00	6.62E-02	2.50E-02	2.41E-03	5.98E+01	4.59E+00
1	382	FMPZ1	1.29E+01	1.19E-01	4.28E-03	2.13E-03	9.47E+01	4.29E+00
1	382	FMPZ4	2.09E+01	4.78E-01	1.23E-02	2.28E-03	6.19E+01	5.00E+00
1	382	FMPZ2	5.29E+00	4.43E-02	1.44E-03	2.20E-03	2.28E+01	4.76E+00
1	419	FMPZ1	2.71E+01	6.66E-01	4.68E-03	7.21E-04	-1.31E+02	3.50E+00
1	419	FMPZ3	3.51E+01	8.63E-01	4.53E-03	7.22E-04	-3.68E+01	1.68E+00
1	419	FMPZ2	2.13E+01	5.24E-01	6.01E-03	7.36E-04	-6.97E+01	2.22E+00
1	419	FMPZ4	2.23E+01	5.45E-01	3.30E-03	7.23E-04	1.60E+01	1.63E+00
2	419	FMPZ5	2.97E+01	8.00E-01	8.48E-03	7.71E-04	-6.01E+01	2.24E+00
1	452	FMPZ4	1.89E+01	4.75E-01	4.71E-03	8.77E-04	-1.28E+01	1.54E+00
1	452	FMPZ5	9.79E+00	2.88E-01	7.50E-03	9.29E-04	-1.83E+02	4.74E+00
1	452	FMPZ1	2.26E+01	5.73E-01	2.01E-03	7.71E-04	-1.19E+02	3.36E+00

QL	doy	ID	CH_4 (mg m^{-2} h^{-1})	CH_4 abs err (mg m^{-2} h^{-1})	N_2O (mg m^{-2} h^{-1})	N_2O abs err (mg m^{-2} h^{-1})	CO_2 (mg m^{-2} h^{-1})	CO_2 abs err (mg m^{-2} h^{-1})
1	452	FMPZ2	7.32E+00	1.79E-01	3.04E-03	7.32E-04	-2.24E+02	5.64E+00
1	473	FMPZ2	2.88E+00	7.04E-02	7.07E-03	9.18E-04	-5.31E+02	1.31E+01
3	473	FMPZ4	-6.66E+00	2.53E-01	1.11E-03	7.16E-04	-1.05E+02	2.95E+00
4	473	FMPZ5	-8.26E+00	2.16E-01	-1.25E-03	7.98E-04	-1.67E+02	4.36E+00
3	473	FMPZ1	-1.11E+01	2.77E-01	5.57E-03	8.31E-04	-2.49E+02	6.27E+00
1	496	FMPZ5	2.27E+01	2.80E-01	1.33E-02	1.76E-03	-2.85E+02	4.79E+00
1	496	FMPZ5	1.94E+01	2.42E-01	4.38E-03	1.95E-03	-9.58E+01	3.50E+00
1	496	FMPZ4	1.98E+01	3.46E-01	3.38E-03	1.76E-03	-2.72E+02	4.45E+00
1	496	FMPZ4	1.95E+01	4.00E-01	5.29E-03	1.69E-03	-2.31E+02	4.24E+00
1	496	FMPZ3	9.97E+00	1.26E-01	3.68E-04	1.68E-03	-1.01E+03	1.26E+01
2	496	FMPZ3	1.19E+01	1.76E-01	8.25E-05	1.61E-03	-3.87E+02	8.33E+00
1	496	FMPZ2	1.14E+01	1.62E-01	-2.54E-03	1.97E-03	-3.55E+02	5.21E+00
1	496	FMPZ2	8.18E+00	9.97E-02	5.85E-03	1.76E-03	-4.94E+02	6.67E+00
1	496	FMPZ1	1.98E+01	2.42E-01	4.48E-03	1.93E-03	-7.50E+02	9.64E+00
1	496	FMPZ1	1.90E+01	2.31E-01	4.04E-03	1.74E-03	-6.04E+02	8.16E+00
1	532	FMPZ3	8.35E+00	8.88E-02	2.80E-02	2.98E-03	-2.90E+03	2.07E+01
1	532	FMPZ5	1.88E+01	2.68E-01	1.84E-02	2.83E-03	-8.84E+02	8.47E+00
1	532	FMPZ4	2.06E+01	2.70E-01	6.49E-03	2.76E-03	-1.51E+02	6.14E+00
1	532	FMPZ2	1.62E+01	1.39E-01	1.34E-02	2.97E-03	-1.88E+02	5.46E+00
1	532	FMPZ1	1.97E+01	1.32E-01	1.02E-02	2.79E-03	4.34E+01	5.89E+00
3	557	FMPZ5	7.36E+01	8.87E-01	7.20E-02	4.01E-03	-1.84E+03	2.38E+01
2	557	FMPZ4	1.30E+02	2.72E+00	8.11E-02	4.23E-03	-1.96E+03	1.31E+01
1	557	FMPZ3	4.31E+01	3.84E-01	8.00E-02	4.58E-03	-1.52E+03	1.28E+01
1	557	FMPZ2	5.01E+01	3.41E-01	8.56E-02	4.39E-03	-1.44E+03	1.23E+01
2	557	FMPZ1	1.48E+02	1.97E+00	1.10E-01	5.29E-03	-2.11E+03	1.39E+01

T. Spearman's correlations of methane and nitrous oxide land-atmosphere fluxes and tidal wetland environmental variables

Table 40 Overview of Spearman's correlation test results with variable A and B as tested variables, $\rho_{spearman}$ as Spearman's rho, p as p value of the tests. The column 'dataset' reflects the tested tidal wetland zones (salinity zone and flooding frequency zone). n(i) reports the number of observations tested.

var. A	var. B	$\rho_{spearman}$	p value	dataset	n(i)
CH_4	CO_2	-0.06	0.20	ALL	458
	N_2O	-0.02	0.70	ALL	458
	T_{air_in}	-0.04	0.58	ALL	253
	PAR_{in}	-0.10	0.13	ALL	253
N_2O	CO_2	-0.31	9.45E-12	ALL	457
	T_{air_in}	0.50	< 2.2E-16	ALL	252
	PAR_{in}	0.50	< 2.2E-16	ALL	252
CO_2	T_{air_in}	-0.45	7.26E-14	ALL	253
	PAR_{in}	-0.56	< 2.2E-16	ALL	253
T_{air_in}	PAR_{in}	0.78	< 2.2E-16	ALL	253
CH_4	CO_2	-0.10	0.48	FM PZ	56
	N_2O	0.32	0.01	FM PZ	56
	VWC	0.07	0.69	FM PZ	40
	EC	0.12	0.46	FM PZ	40
	T_{soil}	0.10	0.56	FM PZ	40
	T_{air_in}	0.25	0.12	FM PZ	39
	PAR_{in}	0.07	0.68	FM PZ	39
N_2O	CO_2	-0.21	0.12	FM PZ	56
	CH_4	0.32	0.01	FM PZ	56
	VWC	0.05	0.74	FM PZ	40
	EC	0.26	0.10	FM PZ	40
	T_{soil}	-0.03	0.83	FM PZ	40
	T_{air_in}	0.15	0.35	FM PZ	39
	PAR_{in}	0.22	0.18	FM PZ	39
CH_4	CO_2	-0.74	1.68E-08	BM PZ	42
	N_2O	0.64	4.69E-06	BM PZ	42
	VWC	-0.40	0.01	BM PZ	42
	EC	0.68	7.18E-07	BM PZ	42
	T_{soil}	0.65	3.33E-06	BM PZ	42
	T_{air_in}	0.56	8.34E-04	BM PZ	32
	PAR_{in}	0.53	1.78E-03	BM PZ	32
N_2O	CO_2	-0.69	4.70E-07	BM PZ	42
	CH_4	0.64	4.69E-06	BM PZ	42
	VWC	-0.44	3.34E-03	BM PZ	42
	EC	0.53	3.02E-04	BM PZ	42
N_2O	T_{soil}	0.65	3.85E-06	BM PZ	42
	T_{air_in}	0.59	4.24E-04	BM PZ	32
	PAR_{in}	0.63	1.01E-04	BM PZ	32
CH_4	CO_2	-0.13	0.25	SM PZ	86
	N_2O	0.18	0.10	SM PZ	86
	VWC	0.06	0.62	SM PZ	72
	EC	0.12	0.31	SM PZ	72
	T_{soil}	0.24	0.04	SM PZ	72
	T_{air_in}	0.16	0.23	SM PZ	54
	PAR_{in}	-0.06	0.64	SM PZ	54
N_2O	CO_2	-0.53	1.70E-07	SM PZ	85
	CH_4	0.18	0.10	SM PZ	85
	VWC	0.35	2.99E-03	SM PZ	71
	EC	0.17	0.15	SM PZ	71
	T_{soil}	0.37	1.54E-03	SM PZ	71
	T_{air_in}	0.45	8.28E-04	SM PZ	53
	PAR_{in}	0.39	4.37E-03	SM PZ	53
CH_4	CO_2	0.16	0.19	SM LM	69
	N_2O	-0.04	0.73	SM LM	69
	VWC	0.04	0.79	SM LM	59
	EC	0.35	0.01	SM LM	59
	T_{soil}	-0.05	0.73	SM LM	59
	T_{air_in}	-0.13	0.41	SM LM	41
	PAR_{in}	-0.21	0.18	SM LM	41
N_2O	CO_2	0.03	0.81	SM LM	69
	CH_4	-0.04	0.73	SM LM	69
	VWC	0.24	0.07	SM LM	59
	EC	-0.28	0.03	SM LM	59
	T_{soil}	0.44	5.69E-04	SM LM	59
	T_{air_in}	0.76	7.67E-09	SM LM	41
	PAR_{in}	0.78	1.96E-09	SM LM	41

var. A	var. B	$\rho_{spearman}$	p value	dataset	n(i)	var. A	var. B	$\rho_{spearman}$	p value	dataset	n(i)
CH_4	CO_2	0.15	0.21	SM HMu	76	CH_4	CO_2	0.05	0.68	SM HMg	79
	N_2O	-0.07	0.54	SM HMu	76		N_2O	-0.06	0.57	SM HMg	79
	VWC	-0.16	0.21	SM HMu	61		VWC	-0.06	0.64	SM HMg	67
	EC	-0.18	0.18	SM HMu	61		EC	-0.03	0.81	SM HMg	67
	T_{soil}	0.23	0.07	SM HMu	61		T_{soil}	-0.09	0.47	SM HMg	67
	T_{air_in}	0.06	0.70	SM HMu	41		T_{air_in}	-0.23	0.12	SM HMg	46
	PAR_{in}	-0.01	0.95	SM HMu	41		PAR_{in}	-0.29	0.05	SM HMg	46
N_2O	CO_2	-0.49	6.82E-06	SM HMu	76	N_2O	CO_2	0.24	0.03	SM HMg	79
	CH_4	-0.07	0.54	SM HMu	76		CH_4	-0.06	0.57	SM HMg	79
	VWC	-0.34	0.01	SM HMu	61		VWC	-0.29	0.02	SM HMg	67
	EC	-0.44	4.57E-04	SM HMu	61		EC	-0.20	0.11	SM HMg	67
	T_{soil}	0.47	1.14E-04	SM HMu	61		T_{soil}	0.53	3.77E-06	SM HMg	67
	T_{air_in}	0.56	1.27E-04	SM HMu	41		T_{air_in}	0.62	4.00E-06	SM HMg	46
	PAR_{in}	0.65	4.38E-06	SM HMu	41		PAR_{in}	0.73	1.11E-08	SM HMg	46

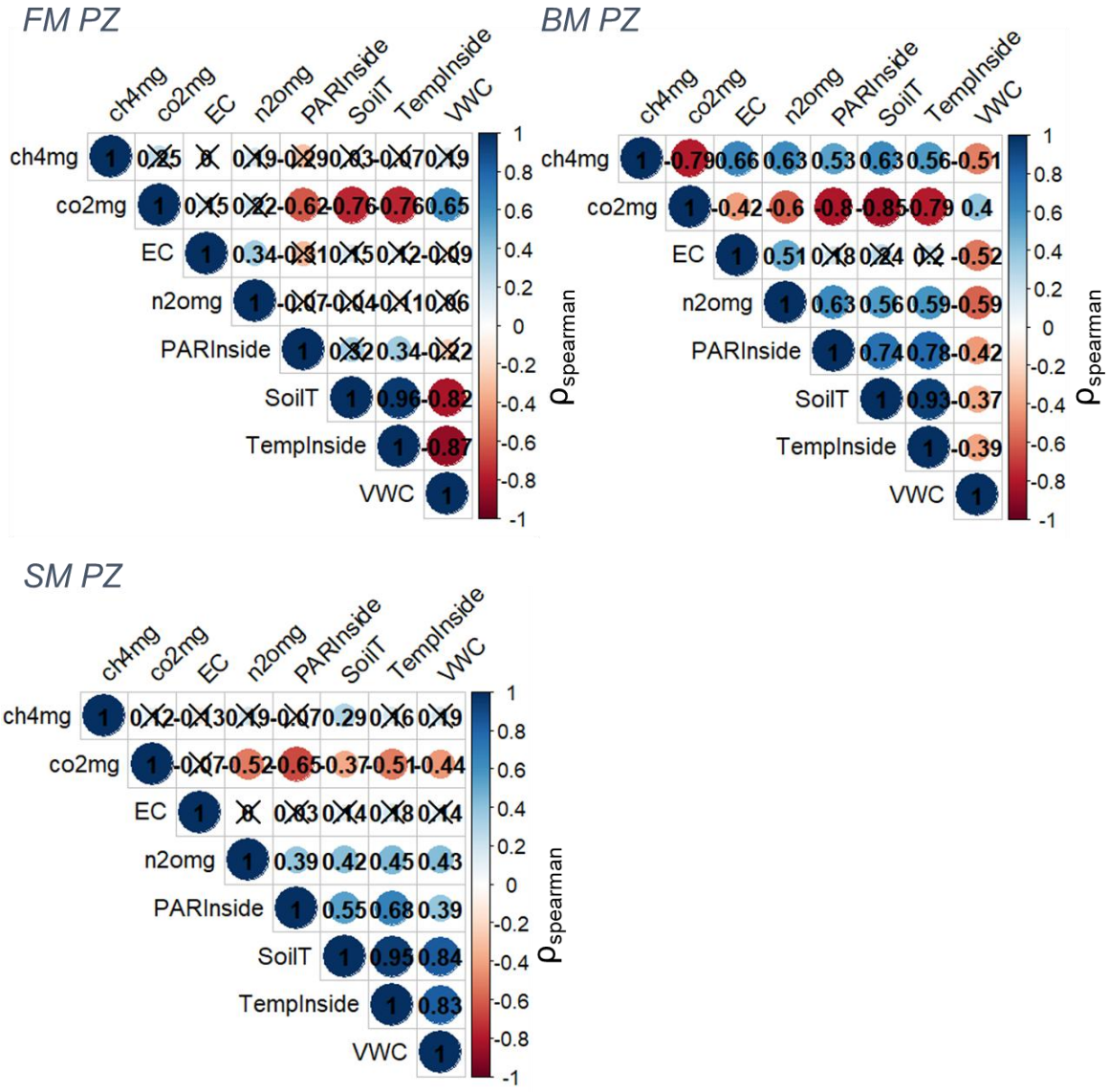

Figure 34 Spearman's correlation plots for observations at pioneer zones along the Elbe river. Left to right fresh marsh pioneer zone (FM PZ) with 34 complete cases, brackish marsh pioneer zone (BM PZ) with 33 complete cases and salt marsh pioneer zone (SM PZ) with 52 complete cases.

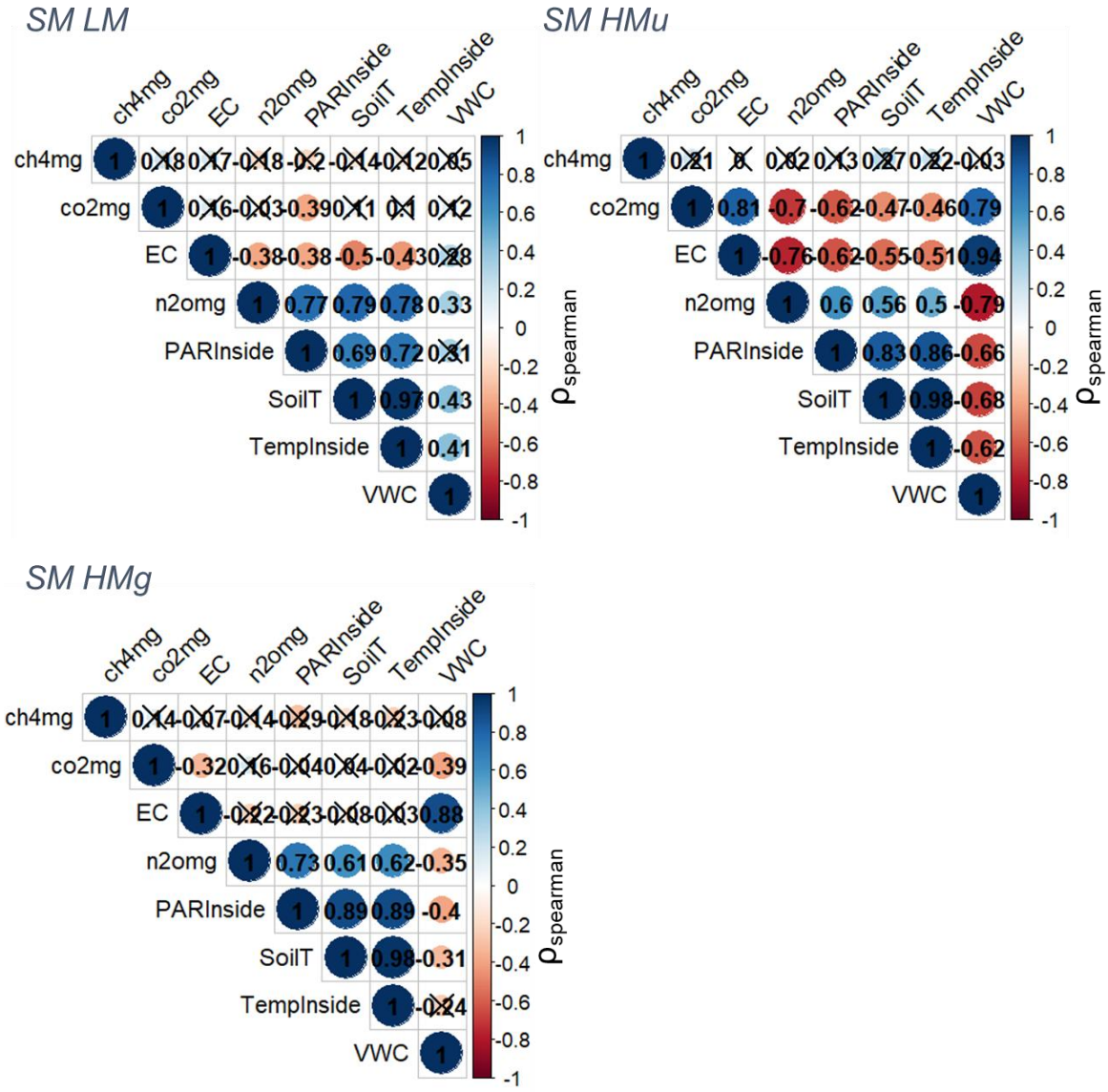

Figure 35 Spearman's correlation plots for observations at the salt marsh flooding frequency zones (left to right) salt marsh low marsh (SM LM) with 40 complete cases, salt marsh unmanaged high marsh (HMu) with 39 complete cases and salt marsh managed high marsh (SM HMg) with 46 complete cases.

U. Vegetation community composition and details

Table 41 Plant community composition per flux replicate plot per tidal wetland zone with fresh water marsh (FM), brackish marsh (BM), salt marsh (SM), pioneer zone (PZ), low marsh (LM), unmanaged high marsh (HMu), managed high marsh (HMg). Plant species are Typha a. Typha angustifolia, Caltha p. Caltha palustris, Myosotis p. Myosotis palustris, Bolboschoenus m. Bolboschoenus maritimus, Spartina a. Spartina anglica, Puccinellia m. Puccinellia maritima, Aster t. Aster tripolium, Atriplex p. Atriplex prostrata, Atriplex l. Atriplex littoralis, Suaeda m. Suaeda maritima, Halimione p. Halimione portulacoides, Triglochin m. Triglochin maritima, Salicornia e. Salicornia europaea, Agrostis s. Agrostis stolonifera, Plantago m. Plantago maritima, Festuca r. Festuca rubra, Glaux m. Glaux maritima, Lolium p. Lolium perenne. Plant specie per flux replicate plot expressed in number of individuals present or in % surface coverage. Bare soil coverage per flux replicate plot expressed % and above ground biomass expressed in grams dry weight (fp: flux plot).

tidal wetland zone	**fp**	**plant species** (n or %)	**bare soil** (%)	**above ground biomass** (g)
FM PZ	1	*Typha a.* (n = 15); *Caltha p.* (1%), *Myosotis p.* (5%)	80%	1227
	2	*Typha a.* (n = 10); *Caltha p.* (35%), *Myosotis p.* (2%)	55%	1870
	3	*Typha a.* (n = 13); *Caltha p.* (80%)	15%	1916
	4	*Typha a.* (n = 9); *Caltha p.* (0%), *Myosotis p.* (1%)	90%	979
	5	*Typha a.* (n = 19); *Caltha p.* (0%), *Myosotis p.* (7%)	80%	1261
BM PZ	1	*Bolboschoenus m.* (83%)	17%	1100
	2	*Bolboschoenus m.* (78%)	21%	1034
	3	*Bolboschoenus m.* (75%)	25%	994
	4	*Bolboschoenus m.* (80%)	20%	1061
	5	*Bolboschoenus m.* (56%)	44%	676
SM PZ	1	*Spartina a.* (45%), *Puccinellia m.* (10%), *Aster t.* (12%), *Suaeda m.* (9%), *Triglochin m.* (15%)	8%	637
	2	*Spartina a.* (55%), *Puccinellia m.* (10%), *Aster t.* (9%), *Suaeda m.* (7%), *Halimione p.* (5%), *Triglochin m.* (2%)	8%	637
	3	*Spartina a.* (60%), *Puccinellia m.* (8%), *Aster t.* (5%), *Atriplex p.* (1%), *Suaeda m.* (10%), *Salicornia e.* (1%)	15%	555
	4	*Spartina a.* (70%), *Puccinellia m.* (7%), *Aster t.* (15%), *Suaeda m.* (1%), *Salicornia e.* (1%)	8%	609
	5	*Spartina a.* (80%), *Puccinellia m.* (5%), *Aster t.* (1%), *Atriplex p.* (1%)	20%	592

tidal wetland zone	**fp**	**plant species** (n or %)	**bare soil** (%)	**above ground biomass** (g)
SM LM	1	*Spartina a.* (2%), *Puccinellia m.* (45%), *Aster t.* (20%), *Atriplex p.* (4%), *Atriplex l.* (1%), *Suaeda m.* (10%), *Halimione p.* (5%), *Salicornia e.* (3%), *Plantago m.* (1%), *Festuca r.* (5%)	10%	441
	2	*Puccinellia m.* (50%), *Aster t.* (8%), *Atriplex p.* (5%), *Atriplex l.* (1%), *Suaeda m.* (1%), *Halimione p.* (5%), *Triglochin m.* (12%), *Salicornia e.* (1%), *Plantago m.* (1%), *Festuca r.* (20%)	10%	579
	3	*Spartina a.* (12%), *Puccinellia m.* (50%), *Aster t.* (10%), *Atriplex p.* (4%), *Atriplex l.* (2%), *Suaeda m.* (7%), *Salicornia e.* (3%), *Agrostis s.* (1%), *Plantago m.* (5%), *Festuca r.* (8%)	10%	549
	4	*Spartina a.* (3%), *Puccinellia m.* (40%), *Aster t.* (8%), *Atriplex p.* (10%), *Atriplex l.* (1%), *Suaeda m.* (10%), *Triglochin m.* (1%), *Salicornia e.* (10%), *Agrostis s.* (3%), *Plantago m.* (10%), *Festuca r.* (15%)	5%	573
	5	*Puccinellia m.* (24%), *Aster t.* (10%), *Atriplex p.* (11%), *Suaeda m.* (2%), *Triglochin m.* (25%), *Salicornia e.* (3%), *Agrostis s.* (3%), *Plantago m.* (1%), *Festuca r.* (18%)	8%	577
SM HMu	1	*Aster t.* (5%), *Atriplex p*. (15%), *Elymus a.* (75%)	8%	1071
	2	*Aster t.* (15%), *Atriplex p.* (25%), *Elymus a.* (50%)	10%	971
	3	*Aster t.* (25%), *Atriplex p.* (15%), *Elymus a.* (45%)	10%	584
	4	*Aster t.* (5%), *Atriplex p.* (5%), *Elymus a.* (85%)	5%	833
	5	*Aster t.* (1%), *Atriplex p.* (1%), *Elymus a.* (95%)	5%	788
SM HMg	1	*Puccinellia m.* (7%), *Aster t.* (3%), *Agrostis s.* (10%), *Festuca r.* (70%), *Glaux m.* (10%)	5%	195
	2	*Puccinellia m.* (12%), *Agrostis s.* (37%), *Festuca r.* (35%), *Glaux m.* (4%)	5%	230
	3	*Puccinellia m.* (8%), *Aster t.* (2%), *Agrostis s.* (37%), *Festuca r.* (51%), *Glaux m.* (2%)	5%	210
	4	*Aster t.* (2%), *Agrostis s.* (13%), *Festuca r.* (60%), *Lolium p.* (22%)	2%	227
	5	*Aster t.* (2%), *Agrostis s.* (6%), *Festuca r.* (75%), *Lolium p.* (17%)	2%	223

V. Greenhouse gas flux uncertainty and sensitivity analyses

Table 42 Uncertainty (e_{Vdim}) in the flux chamber headspace volumes resulting from chamber dimensions.

label	**headspace volume** (m^3)	$\mathbf{e_{Vdim}}$ (m^3)
Chamber1	0.555	0.00516 *
Chamber2	0.296	0.00119
Chamber1 + 2 x small Extension	1.151	0.00543 *
Chamber1 + large Extension	1.146	0.00536 *
Chamber2 + small extension	0.589	0.00168
Chamber2 + large extension	0.869	0.00187
Chamber2 + small + large extension	1.162	0.00222
Chamber2 + 2 x small + large extension	1.455	0.00252

* Includes uncertainty from concaving chamber sheets due to high winds.

Table 43 Uncertainty ($e_{Vdim_SSE_BM}$) in the flux chamber headspace volume from combining chamber dimensions and soil-surface-to-collar rim volume at pioneer zone of the brackish marsh. Standard error (se) of the 9 reference cells used for correcting chamber volume reported as se ref cell volumes. $e_{Vdim_SSE_BM}$ Chamber2 gives the headspace volume uncertainty when measuring with Chamber 2 at the respective plot. Similarly, $e_{Vdim_SSE_BM}$ Chamber2 + large extension, $e_{Vdim_SSE_BM}$ Chamber1 and $e_{Vdim_SSE_BM}$ Chamber1 + large extension gives headspace volume uncertainty for the respective construction combinations at respective plots.

tidal wetland zone flux replicate plot	**se reference cell volumes** (m^3)	$\mathbf{e_{Vdim_SSE_BM}}$ **Chamber2** (m^3)	$\mathbf{e_{Vdim_SSE_BM}}$ **Chamber2 + large extension** (m^3)	$\mathbf{e_{Vdim_SSE_BM}}$ **Chamber1** (m^3)	$\mathbf{e_{Vdim_SSE_BM}}$ **Chamber1 + large extension** (m^3)
BM PZ 1	$6.14 * 10^{-4}$	0.00134	0.00197[A]	0.00520*	0.00540*
BM PZ 2	$3.49 * 10^{-4}$	0.00124	0.00190	0.00518*	0.00537*
BM PZ 3	$1.68 * 10^{-4}$	0.00120	0.00188	0.00517*	0.00537*
BM PZ 4	$3.49 * 10^{-4}$	0.00124	0.00190	0.00518*	0.00537*
BM PZ 5	$4.99 * 10^{-4}$	0.00129	0.00194	0.00519*[A]	0.00539*[A]

* Includes uncertainty from concaving chamber sheets due to high winds.

[A] Combination that did not occur in the final data set due to flux calculation quality filtering.

Table 44 Uncertainty in headspace volume from soil-surface-to-collar-rim (V_{sse_SM}), approximated uncertainty ($e_{Vdim_sse_SM}$) from chamber dimension and V_{sse} for pioneer zone (PZ), low marsh (LM), unmanaged high marsh (HMu) and managed high marsh (HMg) at the salt marsh (SM) per replicate plot as indicated by numbers 1 to 5. The flux replicate plots of the SM HMu were occasionally measured with the addition of the small chamber extension and addressed with a second uncertainty.

tidal wetland zone flux replicate plot	V_{sse_SM} (m^3)	$V_{Chamber2_corr_SSE}$ (m^3)	$e_{Vdim_sse_SM}$ **Chamber2 / + small extension** (m^3)
SM PZ 1	0.004	0.301	0.00606
SM PZ 2	-0.002	0.294	0.00599
SM PZ 3	0.001	0.297	0.00154
SM PZ 4	0.005	0.302	0.00436
SM PZ 5	0.000	0.296	0.00470
SM LM 1	0.019	0.316	0.02703
SM LM 2	0.018	0.316	0.01731
SM LM 3	0.015	0.312	0.00987
SM LM 4	0.017	0.314	0.02206
SM LM 5	0.017	0.315	0.01599
SM HMu 1	0.014	0.312	0.00774 / 0.00783
SM HMu 2	0.002	0.298	0.00801 / 0.00810
SM HMu 3	0.012	0.309	0.00725 / 0.00735
SM HMu 4	0.016	0.314	0.00899 / 0.00907
SM HMu 5	0.001	0.298	0.00682 / 0.00693
SM HMg 1	-0.002	0.294	0.00884
SM HMg 2	-0.009	0.287	0.00657
SM HMg 3	-0.005	0.291	0.01205
SM HMg 4	-0.004	0.292	0.01232
SM HMg 5	-0.006	0.290	0.01612

Table 45 Vegetation properties for propagated uncertainty approximation.

tidal wetland zone **flux replicate plot**	**species**	**individuals**	**leaf volume** **min : max** (cm^3)	**stem volume** **min : max** (cm^3)
FM PZ 1	*Thypha angustifolia*	15	305 : 441	458 : 1036
FM PZ 2		10	203 : 294	305 : 690
FM PZ 3		13	264 : 382	397 : 898
FM PZ 4		9	183 : 265	275 : 621
FM PZ 5		19	386 : 559	580 : 1312
		DW (g)		
FM PZ 1	*Lythrum salicaria*;	116	186 : 474	108 : 155
FM PZ 2	*cirsium arvense*;	1317	2106 : 5367	1220 : 1757
FM PZ 3	*myostis scorpioides*	1674	2675 : 6819	1550 : 2232
FM PZ 4		0	0	0
FM PZ 5		1	1 : 3	1 : 1
		DW (g)		
BM PZ 1	*Bolboschoenus*	1100.41	606 : 2282	NA
BM PZ 2	*maritimus*	1034.12	560 : 2144	1236 : 1470
BM PZ 3		994.35	548 : 2062	1189 : 1414
BM PZ 4		1060.64	584 : 2199	1268 : 1508
BM PZ 5		676.43	373 : 1402	814 : 968
		individuals (min : max)		
SM HMu 1	*Elymus athericus*	399 : 801	4333 : 4391	1197 : 2404
SM HMu 2		266 : 726	3928 : 3981	798 : 2180
SM HMu 3		239 : 437	2365 : 2396	718 : 1312
SM HMu 4		421 : 623	3370 : 3415	1265 : 1870
SM HMu 5		435 : 589	3190 : 3232	1307 : 1770

Table 46 Uncertainty in headspace volume from combining chamber dimensions, soil surface elevation and vegetation at pioneer zones (PZ) of the fresh marsh (FM) and brackish marsh (BM) and for the unmanaged high marsh (HMu) at the salt marsh (SM). V_{veg} reports the calculated vegetation standing stock volume. $e_{Vdim_SSE_Veg}$ July 2023 gives headspace volume uncertainty in July 2023 for the specific measurements conducted with respective chamber construction, at respective plot in July 2023.

tidal wetland zone **flux replicate plot**	**V_{veg} ± sd** (m^3)	**$e_{Vdim_SSE_Veg}$ July 2023** (m^3)
FM PZ 1	$1.58 * 10^{-3} \pm 7.42 * 10^{-4}$	0.00262
FM PZ 2	$5.97 * 10^{-3} \pm 3.02 * 10^{-3}$	0.00393
FM PZ 3	$7.61 * 10^{-3} \pm 3.58 * 10^{-3}$	0.00460
FM PZ 4	$6.72 * 10^{-4} \pm 3.03 * 10^{-4}$	0.00253
FM PZ 5	$1.42 * 10^{-3} \pm 6.41 * 10^{-4}$	0.00260
BM PZ 1	NA	NA
BM PZ 2	2.71 * 10-3 ± 1.28 * 10-3	0.00229
BM PZ 3	2.61 * 10-3 ± 1.23 * 10-3	0.00225
BM PZ 4	2.78 * 10-3 ± 1.31 * 10-3	0.00231
BM PZ 5	1.78 * 10-3 ± 8.37 * 10-4	0.00211
SM HMu 1	6.16 * 10-3 ± 8.95 * 10-4	0.00788
SM HMu 2	5.44 * 10-3 ± 1.01 * 10-3	0.00816
SM HMu 3	3.40 * 10-3 ± 4.42 * 10-4	0.00736
SM HMu 4	4.96 * 10-3 ± 4.60 * 10-4	0.00908
SM HMu 5	4.75 * 10-3 ± 3.57 * 10-4	0.00693

Table 47 Four-minute averaged temperature (T_{air_in}) used in base flux calculations and initial temperature ($T_{initial}$) used in sensitivity analysis from automatic thermometer. Standard deviation of the considered fluxes per vegetation zone with fresh marsh pioneer zone (FM PZ), brackish marsh pioneer zone (BM PZ) and salt marsh' unmanaged high marsh (SM HMu).

tidal wetland zone flux replicate	**plot and date**	**T_{air_in}**	**$T_{initial}$**	**sd**
FM PZ 1	11.07.2023	33.4	30.5	2.7
FM PZ 2	11.07.2023	34.5	32.5	
FM PZ 3	11.07.2023	34.8	34.3	
FM PZ 4	11.07.2023	33.3	33.6	
FM PZ 5	11.07.2023	34.3	38.4	
BM PZ 2	14.06.2023	34.8	37.1	1.8
BM PZ 3	14.06.2023	30.6 / 29.0	30.6 / 28.2	
BM PZ 4	14.06.2023	31.3	31.3	
BM PZ 5	14.06.2023	33.9 / 31.3	35.7 / 33.6	
BM PZ 3	28.06.2023	24.9 / 24.8	24.6 / 21.3	
BM PZ 4	28.06.2023	24.0	23.7	
BM PZ 5	28.06.2023	26.4	25.4	
SM HMu	15.06.2023	23.6	22.7	1.5
SM HMu	15.06.2023	28.4	27.6	
SM HMu 3	15.06.2023	23.4	20.1	
SM HMu 4	15.06.2023	27.6	27.1	
SM HMu 5	15.06.2023	26.2	28.1	
SM HMu 1	27.06.2023	21.3	19.9	
SM HMu 2	27.06.2023	28.3	25.4	
SM HMu 3	27.06.2023	29.6	28.4	
SM HMu 4	27.06.2023	28.3	25.8	
SM HMu 5	27.06.2023	25.7	25.0	

Acknowledgements

This PhD project was funded by the Deutsche Forschungsgemeinschaft (DFG) and conducted under the wing of the research training program 2530 “Biota-mediated effects on Carbon cycling in Estuaries”. I would like to thank for the opportunity of working towards this achievement with the granted financial support from the DFG, the guidance from my advisory panel: Lars Kutzbach, Philipp Porada, Kathrin Dausmann (Universität Hamburg) and Klaus Holger Knorr (Universität Münster), the assessment of this written work by my reviewers: Lars Kutzbach and Peter Müller (Rheinland-Pfälzische Technische Universität Kaiserslautern-Landau) and the evaluation and valuable discussion of my research work during the disputation by my exam committee.

There are many people that have supported me, guided me and challenged me in the best possible ways to reach this achievement that is in front of you. I would like to express my sincere thanks to my advisor Lars Kutzbach for the amazing opportunities to study and teach about temperate tidal wetlands. Thank you for all the fun discussions, amazing trips and travels, valuable feedback and your never-ending enthusiasm and support. Additionally, I would like to thank David Holl for all the valuable advice and discussions and your support with my writing and chamber construction attempts. More thanks go out to Birgit Grabellus, Norman Rüggen and Volker Kleinschmidt for taking care of much of the lab analyses and material preparations. I would also like to thank Klaus-Holger Knorr, Julian Mittmann-Götsch and Peter Müller for introducing me to new field methods and support me with the applications.

A (too?) large part of my time working on this research has been spent outside in the tidal wetlands of the Elbe estuary. I like to thank the Amt für Umweltschutz of Kreis Steinburg, Untere Naturschutzbehörde of Pinneberg and the Landesbetrieb für Küstenschutz, Nationalpark und Meeresschutz Schleswig-Holstein for granting the permissions to conduct our research in the tidal wetlands and supporting the preparations of the research sites. Furthermore, I like to thank all the fieldwork assistants that have supported me.

Special thanks to my fellow RTG2530 PhD candidates and Susanne Stirn and Kai Jensen for creating the opportunities and space to grow as a scientist with all the courses, retreats and conversations. Our exchange was insightful and fun. Monica, Widhi, Elly, Rike, Youssef and Raphael, thank you for all the amazing adventures in the marshes and the mountains, for the lovely chats and passionate discussions.

Most of my indoor hours I have spent in the work group Soils in the Climate System at the Institute of Soil Science, university of Hamburg and I am incredible grateful to have been able to work there with such amazing people, thank you Miriam, Lutz, Selina, Oliver, Evan, Tim, David, Lars and all others.

During the four years in Hamburg, I have met many more amazing people that made my time there fun, sportive and adventurous, thank you all. However, the biggest share of love, fun, support and occasional ‘schop onder de kont’, I have received from my family Noa, Bente, Jeroen, Hermi, Ton and friends Evelien and Fleur. Thank you for being you and making me me. Another thank you goes out to all my other friends and family.